The effect of site substitution on the structure and spectroscopy of lead halide perovskites for photovoltaics

Charles, Bethan

Award date:
2020

Awarding institution:
University of Bath

The Effect of Site Substitution on the Structure and Spectroscopy of Lead Halide Perovskites for Photovoltaics

submitted by

Bethan Charles

for the degree of Doctor of Philosophy

of the

University of Bath

Centre for Sustainable Chemical Technologies
Department of Chemistry

October 2019

Abstract

Hybrid lead halide perovskite photovoltaic devices have demonstrated rapid improvements in performance over a decade of development. However, the materials have drawn criticism for lack of stability. Site substitution at any of A, B or X-sites of the ABX_3 perovskite structure has been shown to reduce these instabilities, although there is a need to further understand the effect of these substitutions on fundamental material behaviour. This thesis focuses on the effects of site substitution on the phase behaviour and stability of perovskites in which the A-site is varied between cesium, methylammonium ($CH_3NH_3^+$, MA) and formamidinium ($CH(NH_2)_2^+$, FA), and the X-site between iodide and bromide.

The phase behaviour of Cs-FA and Cs-MA lead halide perovskites is investigated using variable temperature neutron powder diffraction, complemented with X-ray diffraction and photoluminescence spectroscopy. On cooling $Cs_{0.1}FA_{0.9}PbI_3$ a slow, second order cubic ($Pm\bar{3}m$) to tetragonal ($P4/mbm$) transition is observed close to 290 K. An additional orthorhombic ($Pnma$) phase forms below 180 K and transition to a disordered state is observed at the lower temperature of 125 K compared to that seen in $FAPbI_3$ (140 K). $Cs_{0.1}MA_{0.9}PbI_3$ shows similar phase behaviour to $MAPbI_3$, but mixed Cs-FA-I-Br systems maintain a desirable pseudo-cubic structure through to low temperatures.

Degradation pathways and kinetics of lead iodide formation in FA-MA lead iodide thin films are investigated through X-ray diffraction. MA-rich compositions degrade to lead iodide and iodide salts, whereas FA-rich films transition rapidly to the non-perovskite δ-$FAPbI_3$ phase. Kinetic analysis demonstrates that the rate of lead iodide formation decays exponentially up to $x = 0.6$ in $FA_xMA_{1-x}PbI_3$, with the δ-phase forming for $x \geq 0.7$.

Halide exchange in 2 mm^2 perovskite crystals is investigated through photoluminescence, with $MAPbBr_3$ crystals part-exchanged with iodide forming a preferred composition of $MAPb(I_{0.87}Br_{0.13})_3$. However, subsequent chemical analysis using X-ray diffraction and energy-dispersive X-ray spectroscopy reveals Br-I exchange to be inefficient, as iodide fails to diffuse into the bulk of the crystal. Mixed A-site perovskites show a significantly reduced rate of halide exchange, with no exchange observed in Cs-FA and Cs-MA lead iodide systems.

These results demonstrate the importance of understanding the effect of site substitution on structure-property relationships in perovskite materials for photovoltaics.

Acknowledgements

Firstly I would like to thank my supervisor Dr Daniel Wolverson for all his support, from lab work to writing to providing the opportunity for a placement in Germany. I would also like to thank my co-supervisor Prof Chick Wilson for his help with the structural side of this PhD and his enthusiastic help with my work and extracurricular endeavours.

Thank you to Prof Mark Weller for his continued help and support through to the end of this work. And of course to past members of the Weller group, Adam, Mako and especially Oli and Pascaline for showing a physicist around chemistry labs, joining in conference adventures to the USA and great (but hazy) memories from cider festivals.

Thank you to the EPSRC Centre for Doctoral Training in Sustainable Chemical Technologies for funding this work. Thank you also to the Intitute of Physics, Royal Society of Chemistry, Institute Laue Langevin, ISIS neutron and muon source, Institute of Materials Minerals and Mining, University of Bath Doctoral College, SuperGen Super Solar, and the Armourers and Brasiers Company for additional funding for conferences and outreach activities.

Thank you to members of the Wolverson and Wilson groups, especially Lewis (for all the help with spectroscopy measurements) and Lauren (for the single crystal X-ray experiments). Thank you also to Dr Petra Cameron for kindly allowing me to use her lab and members of the Cameron group for their help, as well as Dr Philip Fletcher for his help with some of the characterisation techniques.

Thank you to Jess Dillon and Prof Saiful Islam for their help in my first year work, and to Saiful again for his encouragement with the outreach activities I took part in.

A special thanks go to the NANOPTO group at ICMAB for the great collaboration, especially Prof Alejandro Goñi, Dr Isabel Alonso and Adrián Francisco, it has been an absolute pleasure to work with you all.

Thank you to Prof Jochen Feldmann for kindly giving me the opportunity to work at the Chair for Photonics and Optoelectronics at the LMU. A huge thanks go to Sebastian for all his support during my visit, as well as Alexander and He for all their help, and the entire PhOG group for making me feel so welcome.

Thanks go to Prof Trystan Watson for the invite to SPECIFIC at Swansea University and to Simone for the experience working in the labs. Thank you also to Prof Paul

Henry and Dr James Tellum at the ISIS neutron and muon source for their help in the neutron diffraction work.

To the Doctoral Welcome Team, thank you for the camaraderie and chats at coffee mornings. And thank you especially Dr Eleanor Parker for being a fantastic manager and for making such a difference to the well being and provisions for doctoral students at the University of Bath.

Thank you to Maya for all her time and effort given in the name of setting up Bath Science in Policy, I'll miss our A-team. And of course thanks to the Bath SIP committee who made it possible, especially to Tess, Kat, Alan, Craig and Jean-Michel for helping us grow when we first set up. And thank you to Jemma for introducing me to many more outreach opportunities (and Moles...).

Thank you to the ACN brunch club (Maha, Christine, Anna, Jo and Bea) for many lovely weekends taking me out of the PhD bubble.

Thank you to my family, for all their support when I left my job to take a chance on this PhD, and for the countless weekends spent hopping between Bristol and Bath since.

And finally, thank you to Dan, for being foolish enough to ask me ice skating and who is the reason this PhD is finished.

"Piled Higher and Deeper" by Jorge Cham www.phdcomics.com

Declaration of Authorship

I declare that I am the author of this thesis. The work presented was carried out between October 2016 and September 2019 at the University of Bath, under the supervision of Dr Daniel Wolverson, Prof. Chick Wilson and Prof. Mark Weller (October 2016 to June 2018). Additional work was carried out at the Ludwig-Maximilians University of Munich (LMU), in the Chair for Photonics and Optoelectronics under the supervision of Prof. Jochen Feldmann. Experiments were also carried out at the ISIS neutron and muon source at the Rutherford Appleton Laboratories, in collaboration with instrument scientists.

Neutron powder diffraction (NPD) was carried out on the POLARIS instrument at ISIS neutron and muon source by myself, Mark Weller and Paul Henry. I performed the subsequent analysis of the data with guidance from Mark Weller and Paul Henry.

Single crystal X-ray diffraction (SXRD) experiments were carried out by myself and Lauren Hatcher at the University of Bath. Lauren Hatcher conducted the data analysis.

Energy-dispersive X-ray spectroscopy (EDX) and scanning electron microscope (SEM) measurements were carried out by Philip Fletcher at the University of Bath, I analysed the data.

Photoluminescence (PL) spectroscopy was undertaken at the LMU with guidance from Sebastian Rieger and Alexander Richter. Sebastian Rieger analysed the time resolved PL (TRPL) for data presented in Chapter 4 (Cesium Formamidinium Lead Halide Perovskites), I analysed the remaining TRPL and PL data.

Ab-initio simulation was performed by Jessica Dillon in collaboration with Saiful Islam's Energy Materials Group.

Unless otherwise indicated in the text, all remaining experiments and data analysis presented in this thesis were conducted by myself.

.....

Bethan Charles

October 2019

Publications

The below list of publications were produced as part of this work. Items 1 and 6 are presented in Chapters 4 and 6 respectively. Materials synthesised as part of this work led to the publication of items 3-5, which are not presented in this thesis.

1. **Charles B**, Weller M.T, Hatcher L.E, Rieger S, Henry P.F, Feldmann J, Wolverson D, Wilson C.C, Phase Behaviour and Substitution Limit of Mixed Cesium-Formamidinium Lead Tri-Iodide Perovskites, (submitted)

2. Francisco-López A, **Charles B**, Alonso M. I, Garriga M, Campoy-Quiles M, Weller M. T, Goñi A. R Phase Diagram of Methylammonium/Formamidinium Lead Iodide Perovskite Solid Solutions from Temperature Dependent Photoluminescence and Raman Spectroscopy, (submitted)

3. Alonso M.I, **Charles B**, Francisco-López A, Garriga M, Weller M.T, Goñi A, Spectroscopic Ellipsometry Study of $FA_xMA_{1-x}PbI_3$ Hybrid Perovskite Single Crystals, *J. Vac. Sci. Technol. B*, 2019, **37**, 6, 062901

4. Francisco-López A, **Charles B**, Weber O. J, Alonso M. I, Garriga M, Campoy-Quiles M, Weller M. T, Goñi A. R, Equal Footing of Thermal Expansion and Electron-Phonon Interaction in the Temperature Dependence of Lead Halide Perovskite Band Gaps, *J. Phys. Chem. Lett.*, 2019, **10**, 11, 2971-2977

5. Francisco-López A, **Charles B**, Weber O. J, Alonso M. I, Garriga M, Campoy-Quiles M, Weller M. T, Goñi A, Pressure-Induced Locking of Methylammonium Cations versus Amorphization in Hybrid Lead Iodide Perovskites, *J. Phys. Chem. C*, 2018, **38**, 22073-22082

6. **Charles B**, Dillon J, Weber O. J, Islam M. S, Weller M. T, Understanding the Stability of Mixed A-Cation Lead Iodide Perovskites, *J. Mater. Chem. A*, 2017, **5**, 22495-22499

Conference Presentations

Work described in this thesis was presented at the selected conferences listed below:

- **07/2019 - International Conference on Materials Chemistry (MC14)**
  Poster presentation - University of Birmingham, UK
- **09/2018 - International Conference on Perovskite Solar Cells (PSCO)**
  Oral presentation - EPFL, Lausanne, Switzerland
- **04/2018 - Materials Research Society (MRS-Spring)**
  Poster presentation - Phoenix, Arizona, USA
- **01/2018 - Next Generation Materials for Solar PV**
  Oral presentation - Royal Society of Chemistry (RSC), London, UK
- **12/2017 - RSC Solid State Chemistry Meeting**
  Oral presentation - University of Reading, UK

Awards

Selected awards achieved during my doctoral studies are listed below:

- **09/2018 - Best Oral Presentation**
  PSCO - EPFL, Lausanne, Switzerland
- **05/2018 - Vice Chancellors Award: Public Engagement with Research**
  University of Bath, UK
- **03/2018 - STEM For Britain Finalist**
  Houses of Parliament, London, UK
- **12/2017 - Best Oral Presentation**
  RSC Solid State Chemistry Meeting - University of Reading, UK

Contents

List of Figures

List of Acronyms

ADPs atomic displacement factors.
AFM atomic force microscopy.

c-Si Crystalline silicon.
CB conduction band.

DAC diamond anvil cell.
DFT density functional theory.
DSC differential scanning calorimetry.

EDX energy-dispersive X-ray spectroscopy.

FA formamidinium.
FWHM full width at half maximum.

ICMAB Institute of Materials Science of Barcelona.

JMAK Johnson-Mehl-Avrami-Kolmogorov.

MA methylammonium.

NMR Nuclear Magnetic Resonance imaging.
NPD neutron powder diffraction.

PL photoluminescence.
PV photovoltaic.
PXRD powder X-ray diffraction.

SE secondary electron.
SEM scanning electron microscope.
SXRD single crystal X-ray diffraction.

TCSPC time-correlated single photon counting.

TOF time of flight.
TRPL time resolved photoluminescence.

VB valence band.

XRD X-ray diffraction.

Chapter 1

Introduction

1.1 The Need for New Materials

Adopted by all United Nations member states, the 2030 Agenda for Sustainable Development is built on seventeen core Sustainable Development Goals aiming to reduce inequality and poverty, improve access to education and combat climate change. Goal seven - providing access to affordable, reliable and sustainable modern energy to all - presents a significant challenge.[1] A huge effort is needed in order to succeed in addressing this goal, so entwined with one of the most significant threats of our time, climate change. The world needs to shift away from energy generation using fossil fuels to new cleaner, possibly more local energy generation. Such a shift will require new systems, new technology and crucially new materials.

It is not only the energy sector that benefits from research into new materials. Advances in materials science have helped shrink computers to fit in our pockets, helped ensure we can communicate near instantaneously with the other side of the world and extended our reach into the solar system. Further understanding of the fundamental science of new materials will help the world progress towards the more efficient, equal and smarter society towards which the Sustainable Development Goals aim.

1.2 The Potential of Solar Energy

Harnessing the energy provided by the Sun would meet the world's energy demand many times over. Solar has the potential of providing up to 50,000 EJ (10^{18} Joules) a year, more than capable of meeting the predicted annual global consumption for 2050 of 1000 EJ.[2] Solar energy is so abundant that it would be possible to exceed global demand through the installation of large solar photovoltaic (PV) farms at a small number of key locations around the world, running to a conversion efficiency of as little as 8%.[3]

However, realistically this solar energy remains difficult to capture, store and transport long distances. Solar irradiation also varies significantly throughout the world, from 60 - 250 Wm^{-2} depending on latitude, resulting in the vast potential of this resource not yet being realised. However, the solar industry has experienced rapid growth in recent years, reflected in the astonishing fall in PV module prices, decreasing 69% between 2010 and 2016, making the cost of solar competitive with fossil fuels.[4]

Crystalline silicon (c-Si) currently dominates the PV industry, forming 95% of the

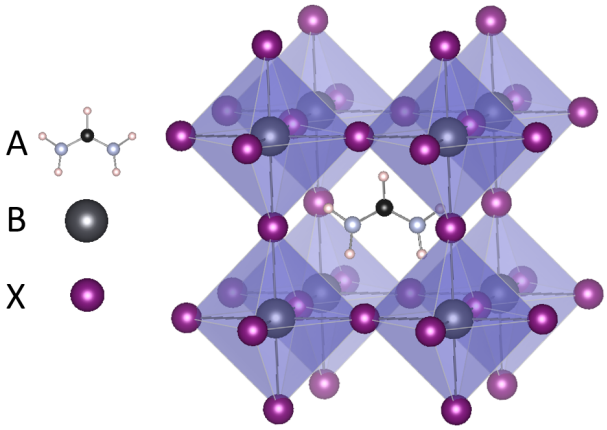

Figure 1-1: Typical atomic structure of an ABX_3 perovskite, represented here by $FAPbI_3$. Where A represents the central cation (in this case the organic $CH(NH_2)_2^+$ formamidinium (FA) ion) with carbon as black, nitrogen as blue and hydrogen as pink. B represents the corner anions (lead, grey) and X the halide anions forming the corner octahedra (iodide, purple). Structure drawn using the software VESTA[8]

market share, although there is increasing demand for new generations of devices.[5] Modern materials can be used to fabricate thin film solar PV which achieve the same power output as c-Si but use far less raw material. Thin films also offer the potential to be integrated within other electronic devices, as well as the on the walls or windows of buildings. But perhaps the most significant development in thin film solar technology for the near future is the fabrication of tandem solar cells, which combine existing c-Si technology with thin film materials in an effort to overcome thermodynamic limit on power conversion efficiencies for single junction devices.[6] Perovskites, the class of material investigated in this thesis, have been increasingly investigated for use in these record-breaking tandem devices.[7]

1.3 Perovskites in Photovoltaics

In 1839 Gustav Rose discovered a mineral in Western Russia which he named after the Russian mineralogist Count Lev Perovski.[9] Over a century later and C.K. Møller of the Royal Veterinary and Agricultural College in Denmark determined the structure of the class of materials we know as perovskites.[10]

The term perovskite commonly refers to any material with the same crystal structure as the original calcium titanate ($CaTiO_3$) discovered by Rose in the 19th century. Although in recent years this definition has been applied rather loosely, the perovskites

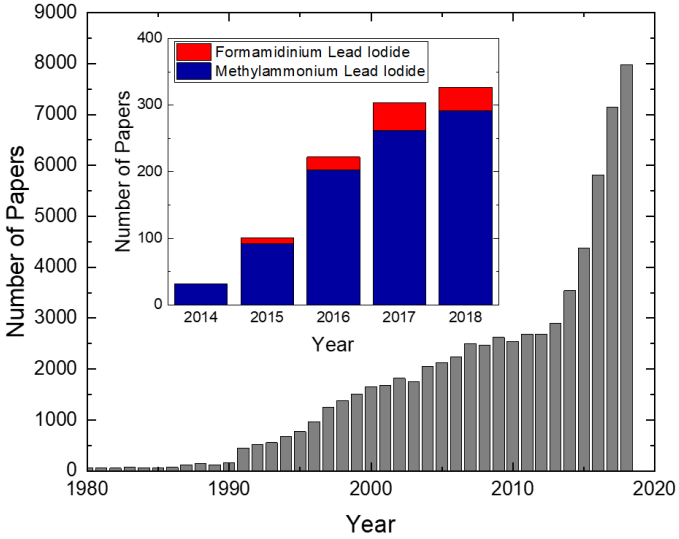

Figure 1-2: Number of papers published containing the key word 'perovskite' in the title and/or abstract between 1980 and 2018. Inset displays number of papers with the key words 'methylammonium' and/or 'formamidinium lead iodide' in the title between 2014 and 2018. Numbers taken from a simple search on Web of Science in March 2018.

investigated in this thesis are of the structure ABX_3, where A is a small organic or inorganic cation sitting in the centre of the void created by four corner B ions forming octahedra with their six nearest X halide ions (see Figure 1-1).

The 20th century saw perovskites used as materials in fuel cells, catalysts, heating elements, lasers and capacitors, and, in 1978, D.Weber developed the first hybrid organic-inorganic halide perovskites by inserting methylammonium (MA) cations ($CH_3NH_3^+$) at the A site.[11] Jumping forward 30 years, T. Miyasaka and colleagues in Japan inserted this hybrid organic-inorganic lead halide perovskite into dye sensitised solar cells, achieving efficiencies of 3.6%.[12]

Just three years later the groups of Grätzel in Switzerland, Park in South Korea and Snaith in the UK fabricated promising solid state perovskite devices, demonstrating the perovskite layer to be capable of both charge generation and transport.[13,14] The field of perovskites has since exploded, seeing an exponential growth in the number of papers published year on year; Figure 1-2 gives an idea of the scale of the growth in the perovskite research community. The result of this huge research effort is that perovskite PV is currently outperforming established technologies such as cadmium telluride thin films and, remarkably, is fast approaching silicon technology efficiencies, which benefit from half a century of research and development.

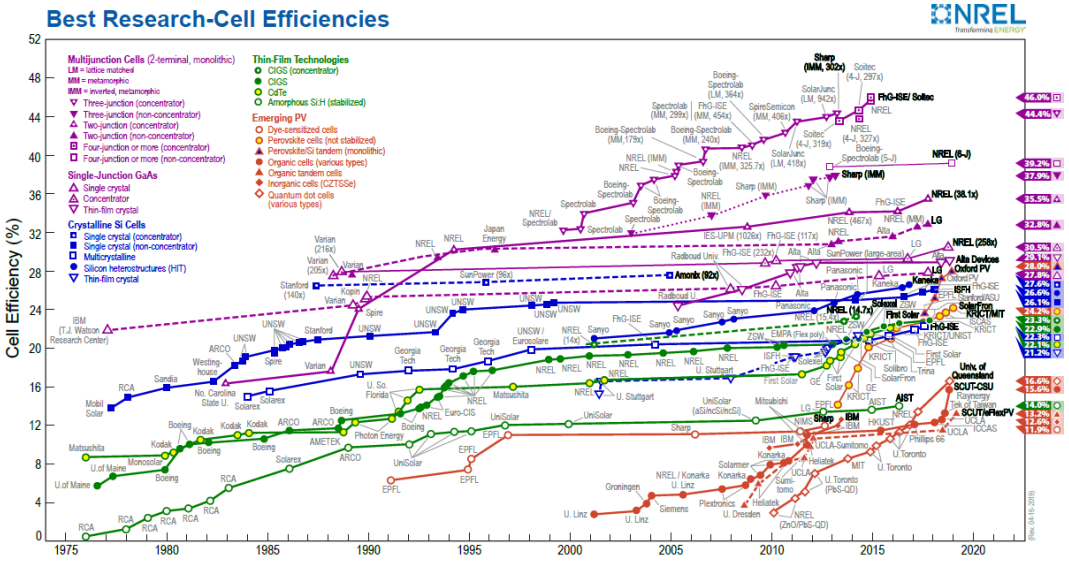

Figure 1-3: The NREL PV device efficiency table.[16]

The National Renewable Energy Laboratory (NREL) tracks the highest efficiencies achieved for all research PV devices. The annual chart is shown in figure 1-3, which displays perovskite solar cell efficiencies as yellow/orange dots. Despite the first record only appearing in 2013, perovskite device efficiencies are now competing with established technologies such as CIGS (copper indium gallium selenide) and silicon cells. The caveat is that many of these high efficiencies have been recorded on small lab scale devices unsuitable for commercial use, although the community is currently turning its head to the large scale manufacture of perovskite PV devices. Scaled up deposition methods compatible with industrial manufacture techniques, such as roll-to-roll deposition and ink jet printing, are currently under development.[15]

Despite the promising progress of perovskite PV a few key issues remain, one being the potential environmental impact of these materials, which seem to favour a core of toxic lead (Pb) for the highest performing materials. However, the most contentious issue surrounding perovskites is undoubtedly stability. Even though significant improvement has been seen in recent years, perovskite device lifetimes remain very low, in part due to the tendency for the perovskite structure to degrade. The most popular perovskite PV material compositions are based on $MAPbI_3$ ($CH_3NH_3PbI_3$), $FAPbI_3$ ($CH(NH_2)_2PbI_3$) and $CsPbI_3$ which all exhibit stability issues. On exposure to oxygen and light the archetypal $MAPbI_3$ degrades into its constituents,[17] while the popular $FAPbI_3$ and $CsPbI_3$ both undergo transitions to a photo-inactive phase at room temperature.[18,19]

One key method to improve fundamental material stability is through site substitution

at any one of the perovskite's A, B or X sites.[20] This thesis does not consider the effect of changing the corner B ions, which are maintained as lead (Pb) throughout, although swapping out the Pb for elements such as tin (Sn) in an effort to reduce material toxicity is an active field of research.[21] Throughout this work the effect of varying the central A cation between cesium (Cs), formamidinium (FA) and MA and the X halide ion between iodine (I) and bromine (Br) is considered.

Site substitution can lead to significant improvements in PV device efficiencies, lifetimes and durability.[20,22,23] However, in order to fully appreciate and so optimise device design a detailed understanding of the complex structure-property relationships exhibited by these intriguing materials on a more fundamental level is needed. This forms the basis of the work presented in this thesis.

1.4 Scope of Work

The focus of this thesis surrounds hybrid halide perovskites with an ABX_3 structure. Throughout this work the cation occupying the central A-site is varied between formamidinium ($CH(NH_2)_2^+$, FA), methylammonium ($CH_3NH_3^+$, MA) and cesium, with compositions including iodide and bromide at the X-site also investigated. The B-site is maintained as the lead anion throughout. This family of materials have captured significant attention over the past decade due to the impressive development of perovskite PV device efficiencies[16] produced via low-cost deposition methods.[24] However, in the excitement of their success, an understanding of fundamental structure-property relationships fell behind device development. If these perovskites are to be optimised for use in commercial devices, a detailed understanding of material behaviour is needed.

As described previously, some of the best performing PV devices include site substituted perovskite materials, where the A and X-sites are occupied by varying ratios of FA, MA and Cs cations and halide anions.[23] Despite the popularity of site substitution in PV device research, its effect on the fundamental structural and spectroscopic properties of perovskites was largely unknown. This motivated the overarching research question addressed in this thesis: *what effect does site substitution have on the structure and spectroscopy of lead halide perovskites for photovoltaics.*

To address this question the work aimed to characterise perovskite material in the form of simple thin films, powder and single crystals, in order to focus on material properties only and mitigate against any effects caused by the type of PV device architecture used.[25–27] Because of the importance of material quality, significant effort was

undertaken to optimise the crystallisation methods presented.

Detailed overviews of the phase behaviour of Cs-FA and Cs-MA lead iodide systems are first presented between 300 K and 100 K using neutron powder diffraction (NPD), complemented with X-ray diffraction (XRD) and variable temperature photoluminescence (PL). The phase behaviour of mixed Cs-FA-I-Br and Cs-MA-I-Br perovskites investigated by NPD is also investigated. Building on work conducted prior to this thesis, trends in the stability of mixed FA-MA lead iodide perovskites are then presented through XRD analysis of the crystallisation of decomposition products. Finally, the possibility of halide exchange in lead iodide and lead bromide crystals is investigated using PL, XRD and energy-dispersive X-ray spectroscopy (EDX).

The work presented in this thesis provides insight into the differences between the behaviour of single cation single halide perovskites and complex site substituted materials. The structure-property investigations at the heart of this thesis contribute towards the development of these materials for use in PV applications across a range of environments.

Chapter 2

Theoretical Background

2.1 Introduction to Semiconductors

Semiconductors are materials with an electrical conductivity between that of insulators and metals. The properties of crystalline semiconductors can be understood through the *band theory of solids*, where the discrete energy levels of single atoms combine in an ordered material to form continuous energy *bands* through which charge carriers can travel.[28] Band theory is discussed in greater detail in Section 2.3 of this chapter. The crystallinity, which describes the long range order of atoms in the semiconductor, describes how the individual atoms are packed together to form these energy bands, therefore the structure and electronic properties of semiconductors are highly correlated.[29]

The charge carriers in semiconductors are commonly released via energy provided by light, an electric field or thermal energy and their behaviour is dictated by external factors, such as temperature, pressure and an applied voltage. In photovoltaic materials charge carriers are generated under illumination. Energy from a wave packet of light (known as a photon) can promote a negative electron from the highest occupied band (valence band) to the lowest unoccupied band (conduction band) across a region in energy known as the *bandgap* and leaving behind an empty electron state, known as a *hole* which carries a positive charge.[29]

Adding small quantities of impurities, or doping a semiconductor can cause substantial changes in material behaviour, changing the intrinsic conductivity. In the familiar case of silicon, doping with a material such as phosphorus adds donor levels below the conduction band (CB) and is known as n-type doping, whereas, adding acceptor levels just above the valence band (VB) using a material such as boron is referred to as p-type doping. Semiconductor devices, including many solar cells, utilise the p-n junction where a p and n type semiconductor are put in contact initiating the diffusion of charge carriers.[30]

Knowledge of semiconducting properties can be traced back as far as the early 19th century; however, it was only well into the 20th century that the full scale of applications were realised with the invention of the transistor in the 1940s transforming our society.[31] Exploiting the vast range of semiconducting behaviours has resulted in the extensive use of semiconductors in electronic devices, for applications in devices as wide-ranging as satellites and solar cells.[32]

2.2 Introduction to Photovoltaics

A solar cell refers to any electronic device capable of converting incident sunlight into electrical power. To do this, a solar device requires a photoabsorber material in which light from the solar spectrum is able to cause an electronic transition from a ground to an excited state. The energy from this transition is then collected via the separation of charges (i.e. the creation of free negative and positive charge carriers) which are transported to contacts. Negative carriers collect at the cathode, while positive carriers collect at the anode. The exciting photon may cause the generation of free electron and hole particles in the photoabsorber, in which case the generation and separation of charge carriers occurs simultaneously. In other materials, a bound excited state known as an *exciton* may be formed, where the binding energy (E_b) of the electron-hole pair needs to be overcome in order to extract the charge carriers for use in a device. In order to extract the maximum number of charge carriers possible for a given material, a detailed understanding of the interaction of these photoabsorber materials with light is required.[33]

Solar cells (referred to as PV devices and cells interchangeably in this thesis) are often named after their semi-conducting photoabsorber layer, such as silicon, and can be categorised into *generations*. First generation solar cells refer to common, commercially available cells usually made out of c-Si. Second generation are generally associated with thin film devices using materials such as amorphous silicon and cadmium telluride (CdTe), while third generation refers to emerging PV materials such as perovskites.[34]

The bandgaps of several commonly used photoabsorber materials are shown on the solar spectrum in Figure 2-1. In theory, the greater proportion of the Sun's spectrum the photoabsorber is able to utilise the better; however, in reality there exist optimum material bandgaps depending on the design of the device.[35,36]

Devices can generally be classed as single junction or multi-junction, so called due to the number of p-type and n-type semiconductor junctions present. Common to all PV device designs, energy from incident light is transferred to exciting an electron leading to the creation of an electron - hole pair. However, only a proportion of these charge carriers can be collected at the contacts due to recombination. In recombination the electron-hole pairs combine, relaxing from an excited state to their preferred equilibrium state, resulting in the loss of energy through either radiative or non-radiative mechanisms,[33] limiting solar cell performance.

In 1961 Shockley and Queisser published their *Detailed Balance Limit* theory on the

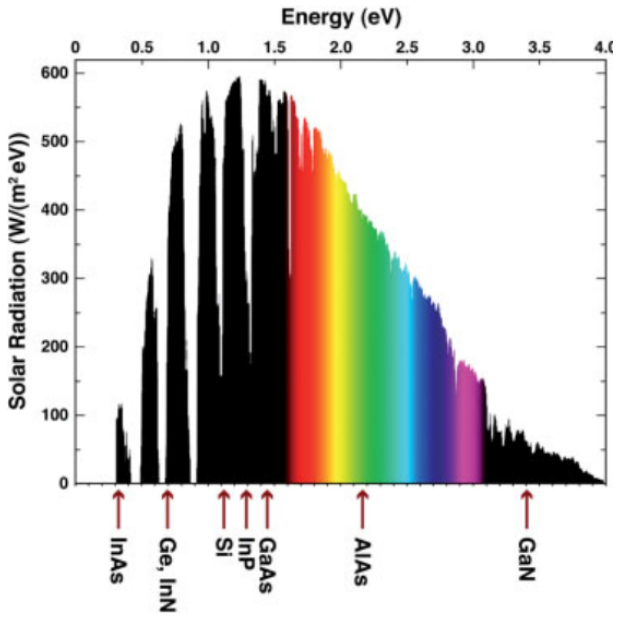

Figure 2-1: The AM 1.5 solar spectrum reproduced from Brown and Wu.[37] AM 1.5 is the standard used when comparing solar cell performance, referring to sunlight hitting the ground at an angle of 48° with a power density of 1 kWm^{-2}. The values of common semiconductor bandgaps are shown in relation to their position on the solar spectrum.

maximum achievable efficiency of a single *p-n* junction solar cell, based on unavoidable recombination processes.[36] For a single junction solar cell a theoretical limit of around 33% efficiency is achievable with an optimal bandgap in the region of 1.5 eV.[35]

Figure 2-2 shows simple schematics of common perovskite PV device architectures. The perovskite thin film is often sandwiched between an electron transport material (ETM), a hole transport material (HTM), a transparent conducting oxide (such as FTO) and a rear contact (such as gold).[23] Planar devices contain layers deposited sequentially, whereas mesoscopic cells contain a mesoporous layer (such as TiO_2) allowing the perovskite layer to diffuse through, thereby improving charge carrier transfer. Numerous other architectures containing different materials have been trialed by research groups around the world[23,38]

A multi-junction device can overcome the Shockley-Queisser limit. Indeed multi-junction devices are currently achieving the highest reported efficiencies, in some cases up to 46%.[16] In 1980 C. Henry calculated the maximum theoretical efficiencies achievable using multiple bandgaps to be 50% and 56% for two and three bandgaps respectively, a considerable improvement on a single junction device.[35] Therefore, new PV materials are often optimised for use in multi-junction device architectures. In per-

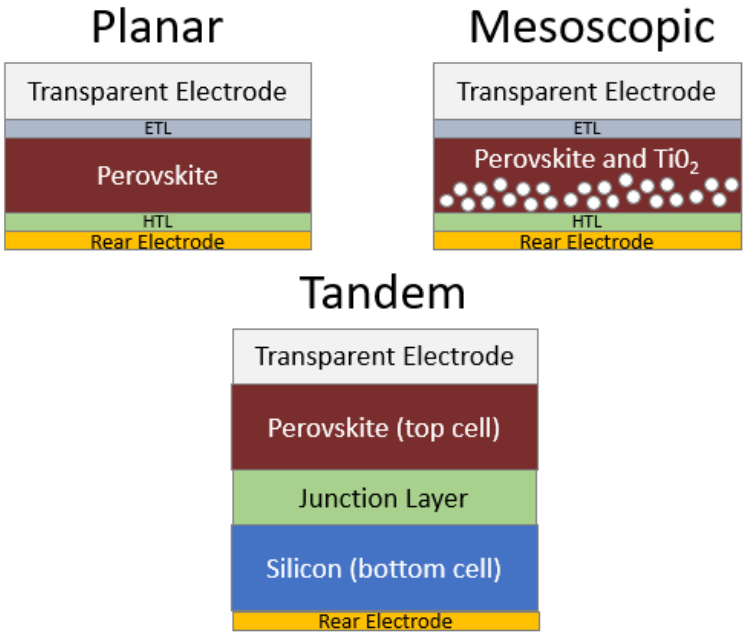

Figure 2-2: Schematics of some common perovskite PV device architectures.

ovskite PV tandem cells are becoming increasingly common, where a perovskite cell forms the top cell of a two (or more) cell device (Figure 2-2). Currently at the forefront of research are silicon-perovskite tandem cells, which achieved efficiencies of 28% in 2018.[39]

2.3 Band Theory

As introduced at the beginning of this chapter in Section 2.1, the properties of semiconductors - such as those used in PV devices - can be understood through the band theory of solids. In order to appreciate the workings of semiconductors, the physical properties of metals (in which valence electrons travel freely) must first be considered. Charge carrier behaviour in metals can be described by the *free electron model* derived from the Schrödinger equation which relates the wavefunction of an electron (ψ), Hamiltonian operator ($\mathcal{H}$) and energy eigenvalue (ϵ) through $\mathcal{H}\psi = \epsilon\psi$. The free particle Schrödinger equation for an electron of wavector $\mathbf{k}$ and mass m is:[29]

$$-\frac{\hbar^2}{2m}\frac{\delta^2}{\delta \mathbf{r}^2}\psi_{\mathbf{k}}(\mathbf{r}) = \epsilon_{\mathbf{k}}\psi_{\mathbf{k}}(\mathbf{r}) \tag{2.1}$$

where $\hbar$ is the Planck constant h divided by 2π. Assuming the electrons are confined to a cube of length a and repeated with a period a, the wavefunctions that satisfy the model are in the form of plane waves such that:

$$\psi_{\mathbf{k}}(\mathbf{r}) = e^{i\mathbf{k}\cdot\mathbf{r}}. \tag{2.2}$$

Substituting 2.2 into 2.1 gives the energy as:

$$\epsilon_{\mathbf{k}} = \frac{\hbar^2\mathbf{k}^2}{2m}. \tag{2.3}$$

This model allows for continuously distributed electron energy values and is a good description for metals (such as lithium and sodium), but it fails to account for the interaction between charge carriers and the ions making up a crystal structure. To account for this, the free electron model is developed into the *nearly free electron model*, where the effect of the periodic potential of the ions making up the crystal is accounted for. The solutions of the Schrödinger equation in a 3D periodic potential are provided by the Bloch function:

$$\psi_{\mathbf{k}}(\mathbf{r}) = u_{\mathbf{k}}(\mathbf{r})e^{i\mathbf{k}\cdot\mathbf{r}} \tag{2.4}$$

where $u_{\mathbf{k}}(\mathbf{r})$ has the periodicity of the lattice. Each Bloch function represents a one-electron wavefunction, but can be grouped into wave packets representing electrons

propagating through the crystal.

Accounting for the periodic potential of the crystal results in the formation of energy *bands* separated by regions in energy where there are no wave-like solutions to the Schrödinger equation. These energy gaps are referred to as *bandgaps*. The band structures of semiconducting materials are commonly plotted as energy vs wavector, such as those shown in Figure 2-3, where the bandgap can be identified. The bandgap of a semiconducting material occurs between the highest occupied band and the lowest unoccupied band, known as the valence band (VB) and conduction band (CB) respectively. These bandgaps are of values such that the transition of electrons between bands can be promoted by the energy input of photons of visible or infra-red light. For example, gallium arsenide (GaAs) - a popular PV material - has a bandgap of 1.52 eV, implying a VB to CB transition can be promoted by infra-red light of wavelength 815 nm.[23] As electrons are excited from the VB to the CB a vacant state is left behind in the VB, referred to as a positively charged hole. Both electrons and holes can contribute to electrical conductivity, and useful PV materials allow the extraction of both types of charge carrier.

Bandgaps can be either direct or indirect, where the highest point of the VB and lowest point of the CB align in k-space directly in the former and are offset in the latter, as shown schematically in Figure 2-3(a). Transitions occurring across a direct bandgap due to the absorption of light of frequency f produce an electron-hole pair separated by an energy $E = hf$. However, transitions across an indirect bandgap must fulfil the conservation of momentum due to the lowest point of the CB and highest point of the VB being offset by a wavector $\mathbf{k}$. Therefore, for an indirect absorption process, additional energy in the form of a lattice vibration (or phonon) is required. The phonon generated has a wavevector $\mathbf{K}$ such that $\mathbf{k} + \mathbf{K} \approx 0$. The energy of this phonon is significantly smaller than the bandgap energy E_g and is often generated thermally. Ideally, photovoltaic materials have direct bandgaps, making the absorption of light and subsequent generation of charge carriers as efficient as possible; this is one property enabling PV materials such as perovskites to exhibit high PV efficiencies with films only nanometres thick.[24]

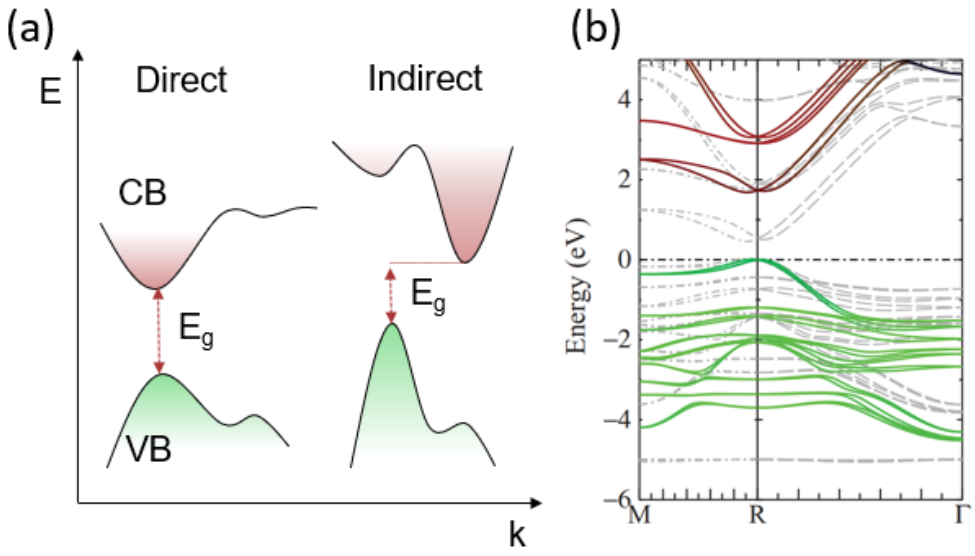

Figure 2-3: (a) Schematic $E-k$ diagram for a direct and indirect bandgap (E_g) between the valence (green) and conduction (red) bands. (b) Real example of an $E-k$ diagram for the band structure for the archetypal PV perovskite $MAPbI_3$ reproduced from Brivio *et al.*[40] Here green represents the I $5p$ band and red the Pb $6p$ band.

2.4 Interaction with Light

2.4.1 Absorption and Emission Spectroscopy

Absorption and emission spectroscopy are experimental tools which can provide a plethora of information on the electronic band structure and charge carrier behaviour. In the case of perovskites, optical spectroscopy can even be used as an indicator of the crystallographic phase (or phases) present in a sample.[41–43] It is also possible for band structures and charge carrier behaviours to be modelled computationally using a variety of methods, the most common being density functional theory (DFT), which can be used to provide information regarding the ground state electronic structure of a material.[44] Although beyond the scope of this thesis, computational methods often provide invaluable references for the interpretation of experimental data.

The energy (E) and wavelength (λ) of a photon in a vacuum are fundamentally linked through the relationship:

$$E = hf = \frac{hc}{\lambda} \tag{2.5}$$

where c the speed of light. This energy can be harnessed in absorption if the energy of the incident photon is equal to or greater than that of the material bandgap. Electrons are excited from the VB to the CB in semiconductors under illumination, forming electron-hole pairs in the process. Luminescence then occurs when the electron-hole pair recombine, releasing energy in the form of another photon. When luminescence is triggered specifically by the absorption of light it is referred to as *photoluminescence (PL)*. The photon emitted as a result of PL will have a different energy to the photon absorbed due to the number of pathways available in the relaxation of the electron to its equilibrium state.[45]

The type of charge carrier formed via photoexcitation has important consequences for PV device operation. If a bound electron and hole pair (an exciton) is formed, an additional binding energy (E_b) must be overcome in order to separate the charges for extraction.[46] Significant effort was invested into the investigation of the photogenerated species in $MAPbI_3$ and similar compounds in order to determine whether the behaviour excitonic or free-carrier in nature.[46–50] Time resolved spectroscopic techniques have suggested free charge carrier densities to dominate in hybrid halide perovskites, which also exhibit high charge carrier mobilities and low recombination rates.[46]

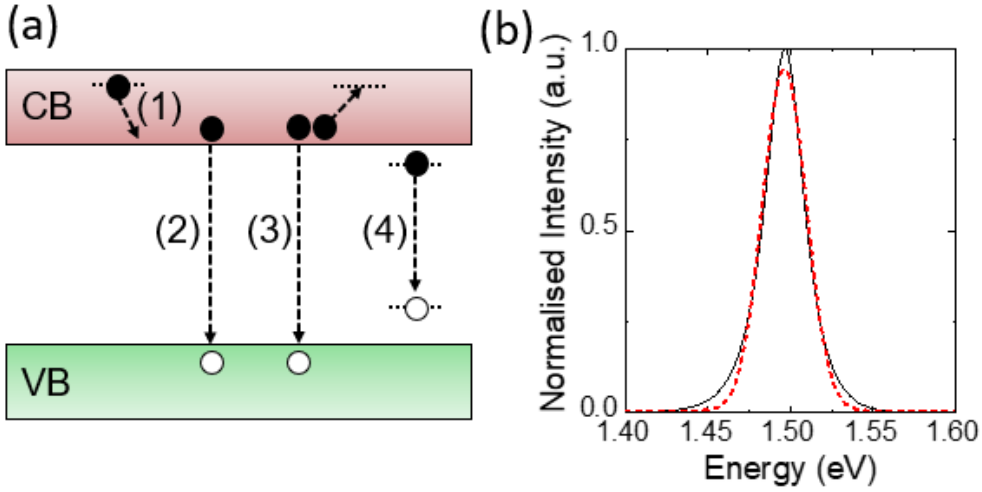

Figure 2-4: (a) Schematic of the recombination pathways discussed in this thesis with electrons and holes represented as black and white dots respectively. (1) Non-radiative transition (2) Radiative recombination (3)Auger recombination (4) trap assisted recombination. (b) Example PL spectrum (black line) taken of the perovskite $Cs_{0.1}FA_{0.9}PbI_3$ investigated in a later chapter, fitted with a Gaussian function (red dashed line).

The recombination pathways referred to in this thesis are non-radiative, radiative, Auger and trap assisted. Non-radiative transitions occur when excited electrons relax to the ground state and do not result in the production of a photon. The excess energy is usually dissipated as phonons (lattice vibrations). Radiative recombination is the direct recombination of an electron-hole pair resulting in the release of a photon. In the three-body Auger process the excess energy from an electron-hole recombination is transferred to another electron in the CB, prompting a transition to a higher energy state. Trap assisted recombination involves the recombination of an electron-hole pair via one or more trap states existing within the energy gap of the material. These trap states are commonly caused by impurities or other material defects.[45,46] Figure 2-4(a) summarises these typical pathways.

The behaviour of these pathways affect the spectroscopic line shapes observed in an experiment, which are generally characterised by either Lorentzian or Gaussian profiles. Lorentzian functions take into account homogeneous (or natural) broadening mechanisms, where the spectroscopic line width (or full width at half maximum, FWHM) is determined by the lifetime of the excited state. However, in crystals composed of multiple different ions, such as those investigated in this work, it is realistic to expect inhomogeneous broadening described by the Gaussian function:

$$G(\omega) = \frac{1}{\sqrt{\pi\Gamma}} e^{-(\omega-\omega_0)^2/\Gamma^2} \tag{2.6}$$

where ω_0 is the centre frequency and Γ is the linewidth.[51] In Figure 2-4 an example PL spectrum (black line) observed for a perovskite sample investigated in this thesis is shown fitted with a single Gaussian function (red dashed line) in the program Origin.

Transient or time resolved photoluminescence (TRPL) can be used in addition to PL to provide greater insight into the recombination pathways present in a material. This is done by examining the luminescence decay which can be subsequently modelled using an appropriate rate equation. For free-charge carriers the rate equation:

$$-\frac{dn}{dt} = k_1 n + k_2 n^2 + k_3 n^3 \tag{2.7}$$

can be used. Here the time dependence of the free-charge carrier density $n(t)$ is written as a function of the rate constants for monomolecular recombination (k_1), bimolecular recombination (k_2) and Auger recombination (k_3).[52] In the case of hybrid perovskites, k_1 is dominated by trap-assisted recombination and bimolecular recombination is predominately radiative.[46] Together these rates form the total recombination rate of the material ($r(n)$), defined as:

$$r(n) = k_1 + k_2 n + k_3 n^2. \tag{2.8}$$

2.4.2 Hybrid Halide Perovskites

PL and absorption spectroscopies have been extensively used to investigate photophysical properties of the hybrid halide perovskites. The behaviours inferred from these measurements have varied widely depending on the type of material measured, for example between polycrystalline thin films or single crystals.[50,53–59]

Shi *et al.* first reported a discrepancy between the absorption onset of thin films and single crystals, reporting absorption edges 0.1 eV lower for the crystals. Samples of $MAPbBr_3$ were deemed to have higher optical bandgaps when deposited as a polycrystalline thin film. The differences were attributed to higher trap state densities and increased disorder present in the thin films.[60] These same observations were reported by other groups, while subsequent investigations also suggested there to be no difference in the optical properties of single crystals and thin films.[61–64] Wu *et al.* postulated

the difference in reported behaviours to be due to the fact that both surface and bulk properties can be present for single crystal measurements, but only surface properties are measured in thin films, and the optical properties of the surface can differ from the bulk.[65]

PL peak shape and position have been other key discrepancies in reported optical measurements on perovskite single crystals, resulting in a range of values suggested for defect densities.[60,66,67] In an effort to rectify these findings, Wenger *et al.* measured $MAPbBr_3$ single crystal PL in front and back illumination configurations, where the detector is placed on the same and opposite side as the excitation spot respectively. In back excitation photo-emitted photons travel through a section of the crystal before being detected, causing a red-shift in observed PL peak due to photon reabsorption.[62] Therefore the relative positions of the excitation spot and detector can have a significant influence on the PL observed.

Similar to PL, reports differ on the behaviours of charge-carrier mobilities and recombination mechanisms as measured through TRPL, leading to a debate on the importance of material processing.[68] It is clear that the method of synthesis does impact material properties such as defect densities and charge carrier mobility, but the extent to which these properties are a result of material processing or intrinsic to the perovskites themselves is unknown.[60,62,67,68]

2.4.3 Variable Temperature PL Behaviour in Perovskites

Photoluminescence Shift

Shifting PL peak position indicates a shifting bandgap. The bandgap (E_g) of some semiconductors are dependant on temperature (T) in a manner often described by the Varshni relationship:[69]

$$E_g = \frac{E_0 - \alpha T^2}{T + \beta} \tag{2.9}$$

where E_0 is the bandgap at 0 K and α and β are constants. This semi-empirical relationship predicts the decrease in material bandgap with increasing temperature due to the effects of lattice expansion.[69] However, in the case of the soft hybrid halide perovskites the temperature dependent behaviour of the electronic states is more complex; dictated by phase transitions, octahedral tilting, lattice thermal expansion and electron-phonon interactions.

In contrast to the trend predicted by Equation 2.9 and the observed behaviour of many semiconductors, hybrid halide perovskites tend to exhibit a blue shift in bandgap energy with increasing temperature.[70] This characteristic has been attributed to the coupling between electronic and vibrational states within the lattice known as electron-phonon (EP) coupling. The change in material bandgap (E_g) with temperature can also be expressed through thermal expansion (TE) effects such that:

$$\frac{dE_g}{dT} = \left[\frac{\delta E_g}{\delta T}\right]_{TE} + \left[\frac{\delta E_g}{\delta T}\right]_{EP} \tag{2.10}$$

with computational work suggesting that the EP term dominates. However, results obtained as part of this work conducted in collaboration with Institute of Materials Science of Barcelona (ICMAB), combining high pressure and variable temperature PL experimental measurements, suggest the TE term has a greater contribution to change in bandgap. The work (not presented in this thesis) was conducted using perovskite crystals grown via the space-confined method described in Chapter 3 and demonstrated thermal expansion effects account for 60% of the observed energy shift in $MAPbI_3$.[70]

Photoluminescence Broadening

Phonon scattering dominates emission line broadening in hybrid halide perovskites, leading to decreased full width at half maximum (FWHM) values in PL spectra at lower temperatures. The temperature dependence of the FWHM ($\Gamma(T)$) can be expressed in terms of the below:

$$\Gamma(T) = \Gamma_o + \Gamma_{AC}(T) + \Gamma_{LO}(T) + \Gamma_{imp}(T) \tag{2.11}$$

where Γ_o is the temperature independent homogeneous broadening term, Γ_{AC} and Γ_{LO} are the broadening terms as a result of acoustic (AC) and longitudinal optical (LO) phonon scattering respectively and Γ_{imp} results from scattering due to ionised impurities. Work by Wright *et al.* on hybrid lead halide perovskites showed the contribution from Γ_{imp} and Γ_{AC} (known as the deformation potential) to be negligible, leading to the temperature dependence of the FWHM being dominated by Γ_o and Γ_{LO}, the latter also known as Fröhlich scattering. This scattering can be expressed in terms of the Bose-Einstein distribution function $N_{LO}(T)$ as below:

$$\Gamma(T) = \Gamma_o + \Gamma_{LO} = \Gamma_o + \gamma_{LO} N_{LO}(T) = \Gamma_o + \frac{\gamma_{LO}}{e^{\frac{E_{LO}}{K_B T}} - 1} \tag{2.12}$$

where γ_{LO} is the charge carrier – LO phonon coupling strength and E_{LO} is the energy for the LO phonon. Understanding these interactions is vital for electronic device applications as electron-phonon interactions dictate charge carrier mobilities.[58]

2.5 Crystal Structure

2.5.1 Crystallography

Crystals are materials in which atoms, ions or molecules are arranged in the lowest energy configuration, causing long range order that can be described by translational symmetry.[71] The whole crystal can be defined by one repeating unit referred to as the unit cell, which constructs the crystal lattice when translational symmetry operators are applied in three dimensions (3D). The fundamental symmetry is categorised into crystal systems defined by the lattice vectors **a**, **b**, **c** and their associated angles α, β, γ. The crystal systems can be subdivided into different cell types according to the number of lattice points they contain, for example primitive (P) and body centred (I). Figure 2-5 shows the crystal systems most commonly associated with the materials discussed in this thesis.

Integer values (n_i) of the primitive lattice vectors (**a**, **b** and **c**) constructing these systems are used to describe the lattice vector ($\mathbf{r}_n$) between lattice points such that:

$$\mathbf{r}_n = n_1\mathbf{a} + n_2\mathbf{b} + n_3\mathbf{c}. \tag{2.13}$$

Unit cells are packed together forming 2D arrays of lattice points known as lattice planes which can be indexed using Miller indices. There are three indices for a 3D structure, h, k and l referring to the reciprocal of the fractional intercept of the lattice plane along the a, b and c axes respectively.[72] For example, the shaded face in Figure 2-5 represents the (001) plane in Miller notation. The geometric symmetry of the lattice points within the cell, generated by the presence of symmetry elements such as inversions or rotations, is described by one of the 32 unique point groups. Taking into account translational, geometric and non-primitive lattice symmetries leads to the 230 unique space groups, which together represent the total number of possible arrangements of symmetry elements within a crystalline material.[72]

Defects, Disorder and Twinning

Real crystals are rarely perfect. Defects can occur which affect the long range order and local environment of atoms in an array. Figure 2-6 summarises some potential defects, including vacancies (atoms 'missing' from unit cells), the presence of interstitial or substitutional impurities, dislocations (generated through stress causing a deformation in the crystal), stacking faults (caused by the disorder in crystal planes) and grain

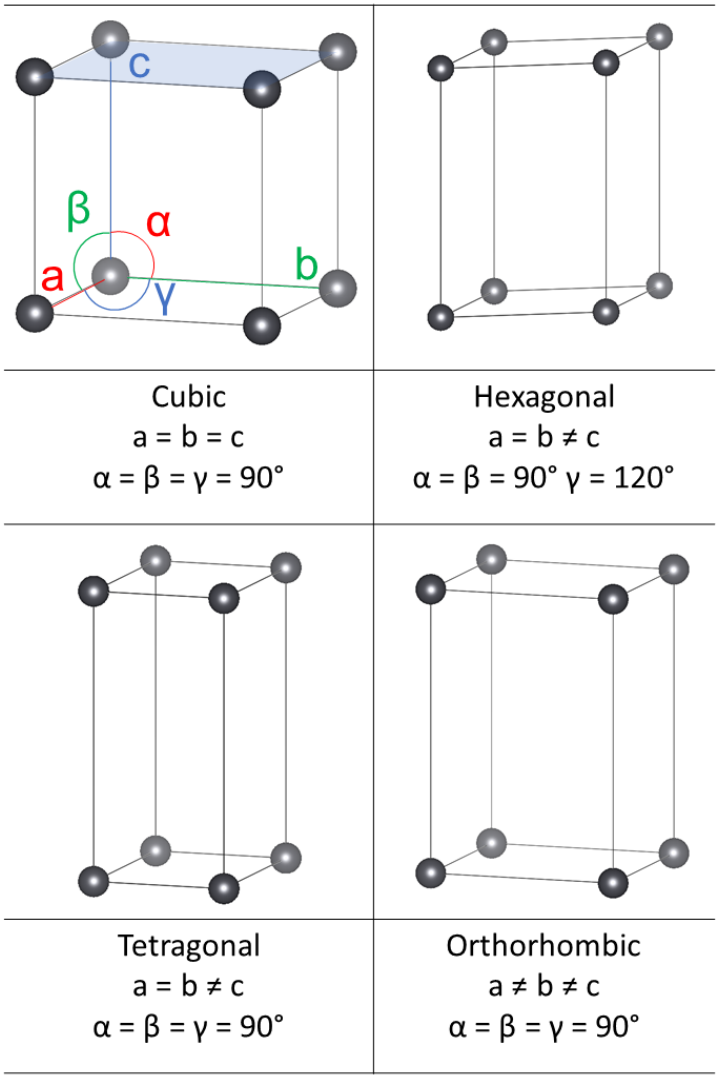

Figure 2-5: The four main crystal systems discussed in this thesis, presented in their primitive form, with definitions of the lattice parameters a, b, c and their associated angles α, β and γ. The shaded area in the cubic system represents the [001] Miller plane.

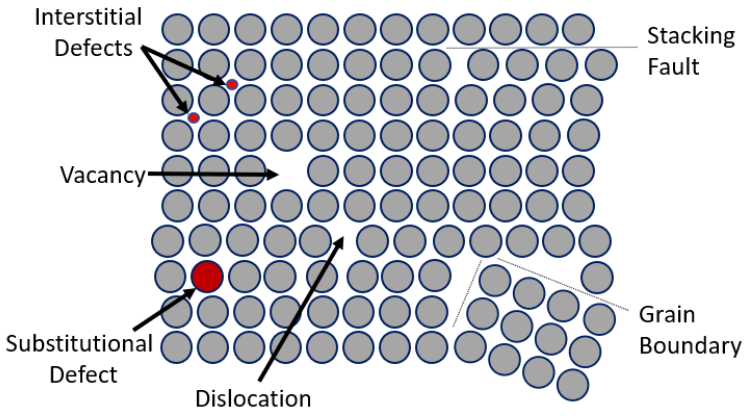

Figure 2-6: Schematic of potential defects which can occur in a crystal.

boundaries (a boundary separating areas of different crystalline orientation).[71,73] Defects can lead to the formation of trap states in the electronic structure of a crystal, causing the recombination of charge carriers.[73]

Disorder is often present within crystalline materials (especially perovskites) and can cause problems determining the true structure of a material. In an ideal system the contents of all unit cells are identical; however, instantaneously this is not the case, as each atom vibrates causing small displacements measured as an atomic displacement factors (ADPs), therefore the measured structure is time-averaged. Large ADPs can be a sign of dynamic or static disorder and, in the some cases, these cannot be differentiated, for example for randomly orientated or tumbling molecules.[71]

Twinning is a commonly observed effect caused by a crystal having two or more orientations of the same structure growing together in a symmetrical manner. Twinning can occur during crystal synthesis caused by the inter-growth of two or more single crystals; the phenomenon can also occur through phase transitions.[72] Some perovskites are known to twin through phase transitions, causing a significant problem to structural determination.[74]

2.5.2 Structure Determination

A crystal structure can be solved experimentally through the use of X-ray and neutron diffraction. These techniques are used to assign a crystal system and space group to an unknown structure, as well as determine the positional co-ordinates and thermal motion of atoms.

In the case of XRD, X-rays are scattered from the electrons associated with the elements present in a unit cell, a process first observed by physicist Max von Laué while at the University of Munich. [1] A path difference exists between the incident and scattered X-rays resulting in constructive or destructive interference depending on the scattering angle. The scattering power as a function of scattering angle is defined by the atomic scattering factor (f) which differs depending on the atom type. At a scattering angle of zero f is equivalent to the number of electrons present, its value then falls with increasing scattering angle in a manner characteristic to that atom.[72]

X-rays scattered from each atom in the crystal combine to create the observed X-ray diffraction pattern, where the intensities and geometry of the maxima are associated with the atomic positions in the unit cell through a Fourier transform. The diffraction pattern as a whole is a Fourier transform of the electron density (ρ). These fundamental mathematical relationships underpin structure determination through diffraction.

The amplitude ($|F_{hkl}|$) and phase (Φ_{hkl}) of each diffracted X-ray from a Miller plane (hkl) can be represented by a complex number known as the structure factor:[71,72]

$$\mathbf{F}_{hkl} = |F_{hkl}|e^{i\Phi_{hkl}} \tag{2.14}$$

where the intensity of the diffracted beams from a Miller plane (I_{hkl}) is directly proportional to $|F_{hkl}|^2$. The structure factor is crucial in determining the atomic positions and electron density (ρ) at each (x, y, z) coordinate. The relevant transform for atomic positions is:

$$\mathbf{F}_{hkl} = \sum_{j=1}^{N} f_j e^{2\pi i(hx_j+ky_j+lz_j)} \tag{2.15}$$

where $(hx_j + ky_j + lz_j)$ are the fractional coordinates of the j^{th} atom in a unit cell containing N atoms. However, in a real crystal the scattering intensity is affected by the thermal motion and occupation factor of atoms in the unit cell. To account for these additional parameters, a correction factor must be applied to the structure factor equation such that:

[1] The photoluminescence work presented in this thesis was undertaken in the very lab Laué first observed X-ray diffraction.

$$\mathbf{F}_{hkl} = \sum_{j=1}^{N} f_j n_j e^{-8\pi^2 U_{iso} sin^2\theta/\lambda^2} e^{2\pi i(hx_j+ky_j+lz_j)} \tag{2.16}$$

where n_j is the occupation of the j^{th} atom in a unit cell, θ is the scattering angle, λ is the wavelength of radiation used and U is the isotropic mean square atomic displacement (units Å^2).[72]

The transformation for electron density (ρ) is:

$$\rho_{xyz} = \frac{1}{V} \sum_{hkl} |F_{hkl}| e^{-2\pi i(hx+ky+lz)} \tag{2.17}$$

where V is the volume of the unit cell. These transformations can be used to construct an electron density map and X-ray diffraction pattern from a known structure, that is, from a structure in which the positions and types of atoms present in a unit cell are defined. However, an important issue to address is the fact that the phase (Φ_{hkl}) cannot be directly measured; this is known as the *phase problem* and complicates structure determination for an unknown material.

To overcome the phase problem *Patterson synthesis* or *direct methods* can be used. In Patterson synthesis values of $|F_{hkl}|^2$ are calculated from observed intensities and the phases Φ_{hkl} are set to 0, whereas direct methods estimate approximate phases. The family of solutions collectively known as direct methods essentially solve the phase problem by assuming positive values of ρ at all points formed by distinct atoms modelled as point-like objects. Alternatively, a known structure can be used as a reference. From the known atom types and positions of the reference model, values for F_{hkl} and ρ_{hkl} can be calculated and compared to measured values. The model can then be refined to minimise the difference.[72]

Bragg Scattering

Bragg's Law provides the geometrical conditions for constructive interference of scattered X-rays and occurs because the wavelength of X-rays (typically 0.1 nm or 1 Å) are of the same order as the spacing between lattice planes in the crystal. X-rays are scattered elastically from the electrons associated with these planes in a manner analogous to the reflection of electromagnetic waves on planar surfaces. Constructive interference of waves *reflected* from planes of the same (hkl) value satisfy the Bragg condition:

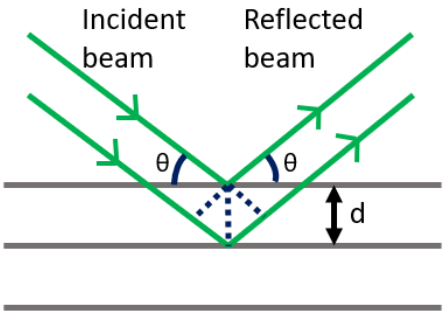

Figure 2-7: Schematic of the diffraction of X-rays from crystal lattice (grey lines) used to construct the Bragg condition.

$$n\lambda = 2d_{hkl}\sin(\theta) \tag{2.18}$$

where n is an integer, λ is wavelength, d_{hkl} is the spacing between the lattice planes and θ is the angle between the incident X-ray beam and atomic plane, as shown in Figure 2-7. Therefore, the Bragg condition directly relates diffraction maxima to d-spacing, from which lattice parameters of the unit cell can be extracted.[75]

Neutron Diffraction

Due to the de Broglie relation:[75]

$$\lambda = \frac{h}{mv} \tag{2.19}$$

a particle of mass m and velocity v has an associated wavelength λ related via the Planck constant h. The wave-particle duality implied by the de Broglie equation results in neutrons being capable of undergoing Bragg reflection. Structure determination through neutron diffraction is often used as a complementary method to XRD, as - unlike X-rays which are scattered by electrons - neutrons are scattered by atomic nuclei. The different process results in neutron diffraction being more sensitive to scattering from lighter elements, such as hydrogen, and less sensitive to heavier elements, such as lead. This is useful in the case of hybrid lead-halide perovskites, where XRD is dominated by the heavy lead and halide anions, obscuring the behaviour of the central organic cation.[72,75]

Figure 2-8 (a) shows the difference between the relative scattering factors for X-rays and neutrons of some elements used in this work. The schematic clearly shows that

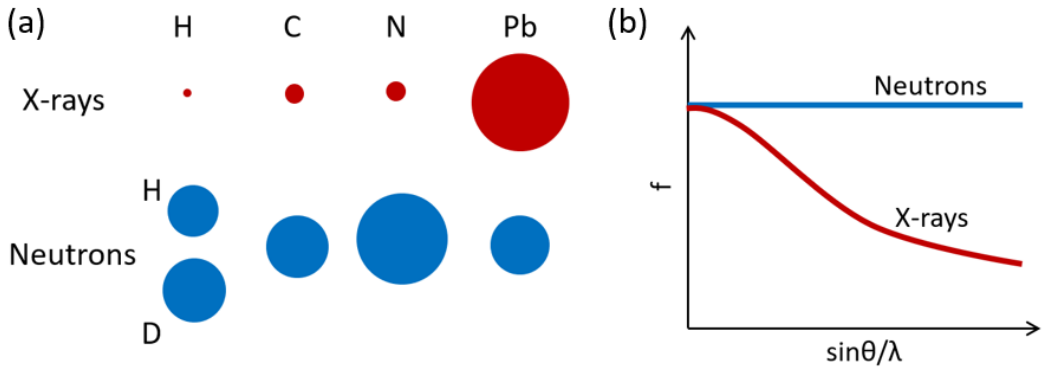

Figure 2-8: (a) Relative scattering factors of H, D, C, N and Pb using X-rays and neutrons adapted from Weller and Young.[75] (b) Variation of scattering f with scattering angle θ for neutrons and X-rays, the neutron scattering factor is unaffected by the value of θ, whereas the X-ray scattering factor weakens at higher angles.

while the scattering from lead dominates when using X-rays, the scattering is more evenly distributed throughout the lighter and heavier atoms when using neutrons. Another key difference in neutron diffraction is the independence of scattering factor f to the scattering angle θ, therefore extending the range of usable data to higher θ (or lower d-spacing) allowing for a more accurate determination of atomic positions.[75] However, diffraction using neutrons is generally less accessible than X-rays, as the principle sources of neutrons are nuclear fission reactors or synchrotron spallation sources. The spallation source at ISIS neutron and muon source in Oxfordshire was used in this work.

2.5.3 General Perovskite Structural Properties

Perovskites are soft materials capable of undergoing structural phase transitions from the ideal cubic system in space group $Pm\bar{3}m$ to a variety of lower symmetry phases. These transitions can occur due to a change in temperature, pressure and composition, although the fundamental ABX_3 stoichiometry remains.[11] For example, the A-site cation in $MAPbI_3$ can be partially substituted with FA to form $FA_{0.5}MA_{0.5}PbI_3$ where the effective A-site cation is now $FA_{0.5}MA^{+}_{0.5}$.

The formation of perovskites depends on three major factors: charge neutrality between the cations and anions, the stability of the corner BX_6 octahedra and the ratio of the A, B and X ionic radii as defined by the Goldschmidt tolerance factor (t).[76] The factor t is defined as the ratio of the radii of the B-site cation (r_B) and the X-site halide anion

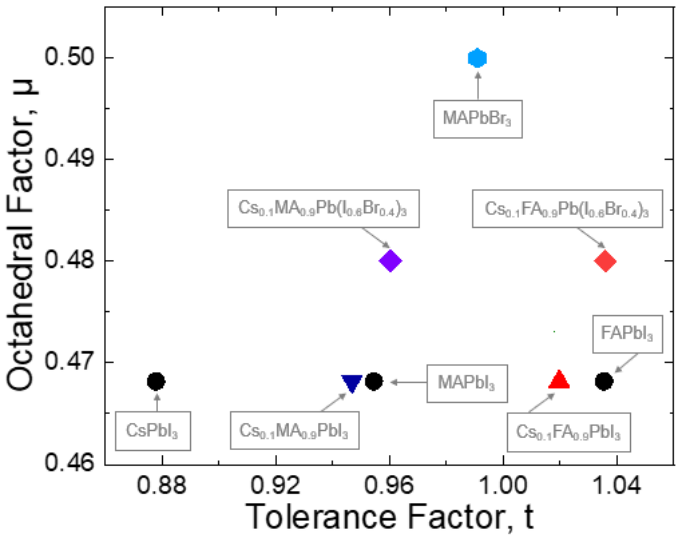

Figure 2-9: Tolerance (t) and octahedral (μ) factors plotted for the hybrid halide perovskites investigated in this thesis.

(r_X) by:

$$t = \frac{(r_A + r_X)}{\sqrt{2}(r_B + r_X)} \tag{2.20}$$

with r_A the ionic radius of the A-site cation. Each of these radii can be averaged to produce effective radii (r_{eff}) in mixed cation/halide systems; for example, in the case of $FA_{0.5}MA_{0.5}PbI_3$ the effective r_A would be given by:

$$r_{A(eff)} = \frac{1}{2}(r_{FA} + r_{MA}) \tag{2.21}$$

where $r_{FA} + r_{MA}$ are the radii of the FA and MA cations respectively. Tolerance factor values where $0.87 \leq t \leq 1.06$ are generally accepted to generate perovskite-like structures; however, this is not a definitive rule.[77–79] In general t values of 1 indicate the ideal cubic structure, whereas a value of $t < 0.8$ indicates an A cation with an effective radius too small to form the perovskite structure.

Additionally, the octahedral factor (μ) can be used to predict the stability of the BX_6 octahedra, as defined by:

$$\mu = \frac{r_B}{r_X}. \tag{2.22}$$

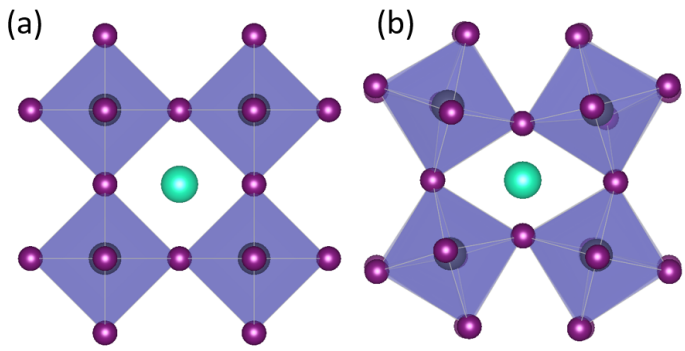

Figure 2-10: (a) Ideal cubic perovskite structure with central organic or inorganic cation (green) surrounded by PbI_6 octahedra (purple). (b) Octahedral tilting causing a distortion lowering the symmetry.

Perovskite structures are generally stable with $0.44 \leq \mu \leq 0.55$.[80] Calculating values for t and μ are useful in predicting material properties, however the suggested limits on the values of these factors cannot act as definitive predictions of material structure.

Figure 2-9 shows the values of t and μ for materials investigated in this work, as calculated from published ionic radii.[79,81,82] When calculating tolerance factors, care was taken to include the effects of different metal-halide coordination as proposed by Travis *et al.*[79] In this revised system, the ionic radius of Pb^{2+} increases when coordinated with I^- compared to Br^-.

In reality, due to the restrictions on the ideal $Pm\bar{3}m$ system, most perovskites are distorted in one of three ways; (1) with a displaced B-cation, (2) a distorted BX_6 octahedra and/or (3) the relative tilting of the BX_6 octahedra.[83] A schematic of the latter is displayed in Figure 2-10 and is a characteristic commonly referred to in this thesis. Octahedral tilting is often categorised in terms of Glazer notation which describes the tilt of the BX_6 units around each of the a[100], b[010] and c[001] axes. The notation $a^*b^*c^*$ is used, where the superscript $*$ can be 0, + or - indicating no tilt, in-phase or anti-phase tilting of successive octahedra respectively.

The tilting - often caused by changes in temperature, pressure or composition - produces relatively small distortions which can lead to significant differences in the symmetry of the material as well as changes in electronic and magnetic properties.[84] Tilting lowers the symmetry of the structure, contributing to a change in phase from the parent $Pm\bar{3}m$ space group to an allowed subgroup. Howard and Stokes employed group-theoretical analysis to determine 15 perovskite space groups formed through tilting, along with the allowed structural phase transitions between them, shown in Figure 2-11.[83]

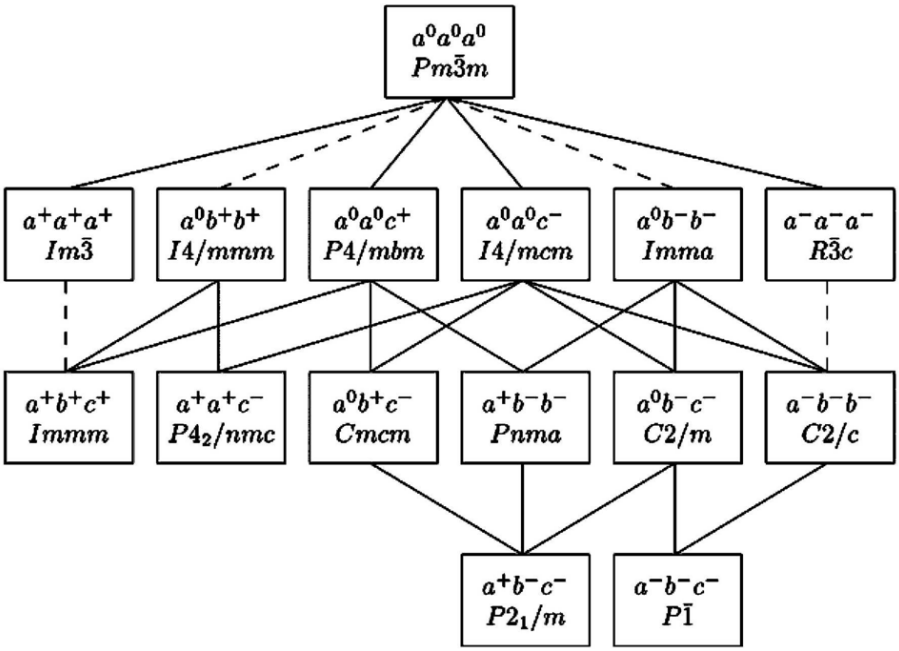

Figure 2-11: Schematic reproduced from Howard and Stokes[83] showing the allowed phase transitions from the perovskite parent phase P$m\bar{3}m$ and associated octahedral tilts in Glazer notation.[85]

2.5.4 Nomenclature

Chapters 4 and 5 of this thesis concern the lowering of perovskite crystal symmetry with the lowering of temperature, as introduced in the previous section (2.5.3). The structure of the perovskite changes on cooling or heating, undergoing reversible phase transitions. These phases are commonly labelled as α, β and γ.

For hybrid halide perovskites the α-phase, representing the highest temperature phase, occupies the cubic space group P$m\bar{3}m$. On cooling this transitions to the β-phase which - for the perovskites of interest in this thesis - is tetragonal. Further cooling may result in formation of a third tetragonal or orthohombic phase labelled as γ[74,86–88] .

An additional complication occurs for compounds which can exist in perovskite or non-perovskite polymorphs, such as $FAPbI_3$ and $CsPbI_3$.[74,88] The non-perovskite polymorphs of these materials are labelled as the δ-phase and have a distinctive yellow colour. The non-perovskite δ-phase is characterised by the material no longer having corner sharing lead-halide octahedra. These reversible phase transitions are summarised in Figure 2-12.

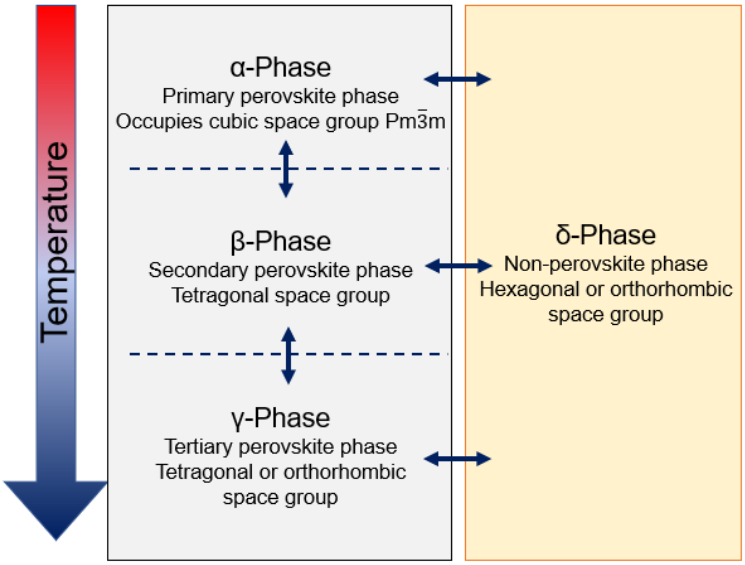

Figure 2-12: Schematic of the nomenclature used to describe perovskite structural phases. The crystal systems associated with each phase are given for the family of hybrid halide perovskites of interest in this thesis.

2.5.5 Hybrid Halide Perovskite Structures

While the properties detailed in Section 2.5.3 relate to all 3D perovskites, this thesis concentrates on the hybrid halide family of materials; namely, 3D ABX_3 perovskites containing an organic and/or inorganic cation at the A site and a halide ion at the X site.

$MAPbI_3$

Methylammonium lead iodide ($CH_3NH_3PbI_3$ shortened to $MAPbI_3$) is arguably the most widely studied material for perovskite PV, with the ability to form efficient devices while remaining relatively easy to synthesise.[16,89] However, at the outset of the explosion in perovskite PV research, while there was a significant drive to form efficient devices, the structure of $MAPbI_3$ was less well known. In 2015 Weller *et al.* produced a detailed report on the structure and cation orientation of $MAPI_3$ between 100 - 352 K, summarised in Figure 2-13.[86] Using neutron powder diffraction it was found that $MAPbI_3$ transitioned from an orthorhombic P*nma* system to tetragonal I4/*mcm* at 165 K and to the cubic P$m\bar{3}m$ system at 327 K.

The degree of tilting of the PbI_6 corner octahedra varies significantly between phases, with an average Pb-I-Pb angle of 154.5°, 165.3° and 180° for the orthorhombic, tetrag-

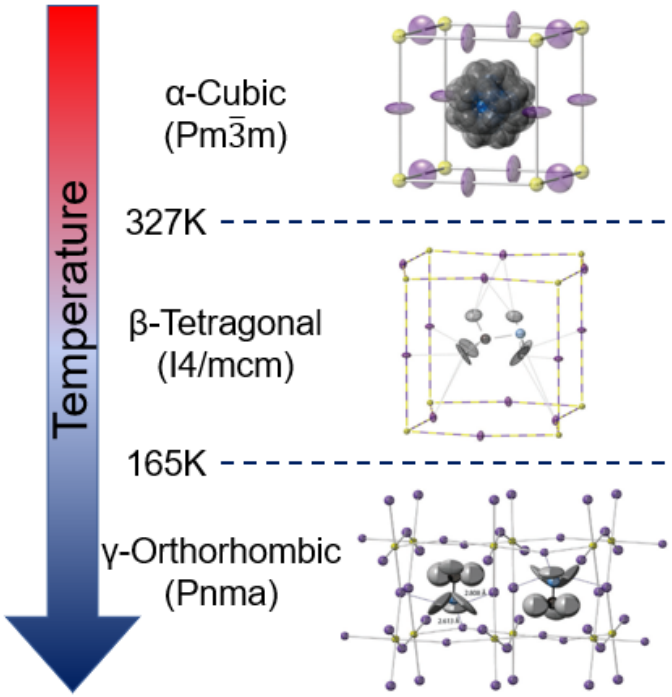

Figure 2-13: Phase transitions of $MAPbI_3$ with unit cell structures as presented by Weller *et al.*[86] Probability ellipsoids directly relate to values of ADPs and give an indication of the thermal motion of atoms. Lead is shown as yellow, iodine as purple, carbon black, nitrogen blue and hydrogen as grey.

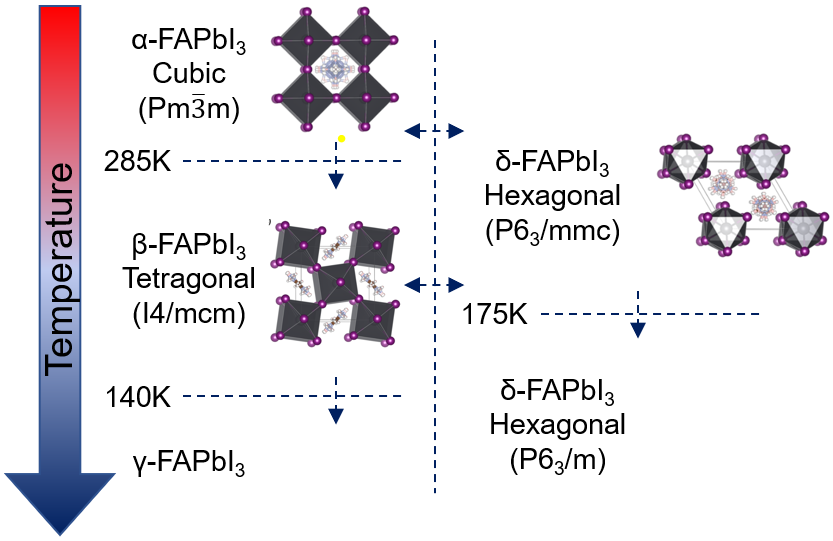

Figure 2-14: Phase transitions of $FAPbI_3$ as summarised in Weber *et al.*[74] Below 325 K the α, β and δ phases are known to readily inter-convert in the presence of moisture while the definitive structure of the γ-phase has not yet been fully determined. Iodine is purple, lead grey, carbon brown and nitrogen blue.

onal and cubic phases respectively. This tilting affects the hydrogen bonding distances between the NH_3 group on the MA cation and the corner I ions, producing stronger bonding in the orthorhombic than in the tetragonal phase.[86] As a result, the MA cation is fixed in the Pb-I cage of the orthorhombic structure. However, with increasing temperature the cation gains thermal energy weakening the hydrogen bonds, resulting in the cation becoming rotationally disordered in the *ab* plane in the tetragonal phase and then freely rotating in the cubic phase.[86,90,91] The high level of MA rotation in tetragonal $MAPbI_3$ may help account for the material's excellent PV performance, although this characteristic has also been linked to the hysteresis observed in devices.[92]

$FAPbI_3$

Formamidinium lead iodide ($CH(NH_2)_2PbI_3$ shortened to $FAPbI_3$) is often preferred over $MAPbI_3$ due to its favourable bandgap and greater heat tolerance.[87] However, due to the larger size of the FA cation putting strain on the Pb-I bonds, $FAPbI_3$ can exist as a cubic black perovskite α-phase or a yellow hexagonal non-perovskite δ-phase at room temperature.[18] The tendency of the α and δ-phases to inter-convert has caused some issues when investigating the temperature dependent behaviour of this material. While the high and mid temperature phases are well understood, the low temperature behaviour is less defined.[42,87] Figure 2-14 summarises the known transitions in $FAPbI_3$, showing the high temperature $Pm\bar{3}m$ cubic phase which can convert to the hexagonal

non-perovskite δ-phase in the presence of moisture or to the tetragonal β-phase upon fast cooling in a dry environment. Previous work by Weller *et al.* found the FA cation to have a rotational motion comparable to that of the MA in $MAPbI_3$ in the high temperature cubic phase.[87]

There exist conflicting reports in the literature over the low temperature phase, commonly referred to as γ-$FAPbI_3$. Using powder X-ray diffraction (PXRD) Fabini *et al.* solved the structure at 91 K in the same P4/*mbm* space group as the β-phase; whereas, at the same temperature, Chen *et al.* found a supercell structure adopting the space group P4*bm*, using neutron diffraction.[42,93] Through the comparison of previous studies, as well as powder neutron diffraction experiments using hydrogenous and partially deuterated $FAPbI_3$, Weber *et al.* found there to be a high level of disorder throughout the material below 140 K.[74] The disorder was attributed to either the growth of a super-cell similar to that found by Chen *et al.* or to the formation of domains of the β and δ phases.[74,93]

$CsPbI_3$

Similar to $FAPbI_3$, cesium lead iodide ($CsPbI_3$) also readily inter-converts between a black perovskite phase and yellow PV-inactive non-perovskite δ-phase. While the yellow orthorhombic phase is the most stable polymorph of $CsPbI_3$, it is possible to retain the black perovskite structure at room temperature through fast cooling in dry conditions.[88] Previously, this black phase was believed to be the cubic α-$CsPbI_3$ form; however, work by Sutton *et al.* showed that the PV active phase at room temperature is in fact orthorhombic P*nam*.[18,88] Figure 2-15 summarises the known phases in $CsPbI_3$.

$MAPbBr_3$

The iodide based hybrid perovskites are arguably the most intensively researched materials in the community, although bromide based materials have also proven to be highly capable PV materials.[24] Methylammonium lead bromide ($MAPbBr_3$) exhibits greater air and moisture stability than its iodine based counterpart.[94] Similarly to $MAPbI_3$, $MAPbBr_3$ undergoes structural transitions between the cubic, tetragonal and orthorhombic systems with changing temperature, though the space groups and transition temperatures are subtly different. The $MAPbBr_3$ phases are P$m\bar{3}m$ above 235 K, P4/*mmm* between 148 K to 235 K and P*na*21 below 148 K for the cubic, tetragonal and orthorhombic systems respectively.[94]

The structural behaviour of each of these popular perovskites has an important impact on the properties of the material crucial to PV performance, such as the electronic

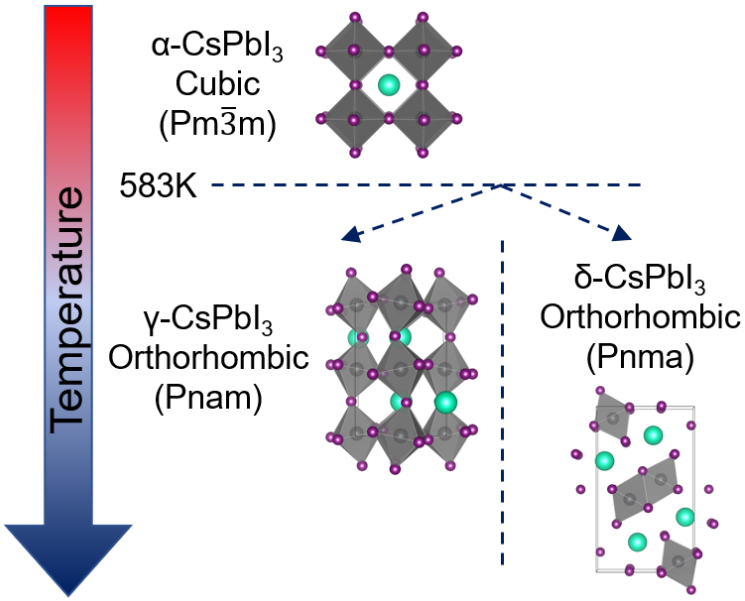

Figure 2-15: Phase transitions of $CsPbI_3$ visualised using the CIF structures published by Sutton *et al.* drawn in the software VESTA. The γ-phase can quickly convert to the non-perovskite δ-phase in the presence of water.[88]

bandgap, charge carrier mobility and thermal stability. However, shortcomings in the desirable PV properties of archetypal materials such as $MAPbI_3$, $FAPbI_3$, $CsPbI_3$ and $MAPbBr_3$ can often be overcome through altering the perovskite structure, for example through site substitution.[23,95,96]

2.6 Site Substitution

2.6.1 Thermodynamics of Mixing

A solid solution can be made when two or more components mix. The behaviour and limit of mixing is determined by the thermodynamics of the system and can be displayed visually using phase diagrams. Phase diagrams are useful because they enable the prediction of phases present at particular temperatures and concentrations. An example diagram is shown in Figure 2-16 which shows a simple binary phase diagram of compounds A and B.[29] The green lines represent solid-to-solid transitions. It should be noted that hybrid halide perovskites tend to decompose before the liquid phase is achieved.[97]

Mixing can be understood by use of internal energy (U), enthalpy (H), entropy (S) and Gibbs free energy (G). A change in internal energy is the sum of changes of potential and kinetic energies:[29]

$$dU = CdT - PdV \tag{2.23}$$

where C is the heat capacity, dT the change in temperature, P the pressure and dV the change in volume. Change in enthalpy is given by:

$$dH = dU + PdV + VdP. \tag{2.24}$$

Entropy is the measure of disorder caused by the arrangement of atoms or molecules in a system as well as their thermal displacements. Change is entropy is defined as:

$$dS \geq \frac{dq}{T} \tag{2.25}$$

where dq is the heat added to the system. These parameters are combined to define the Gibbs free energy (G) which can be used to describe the equilibrium states of a system. A change in G can be written as:

$$dG = dH - TdS - SdT. \tag{2.26}$$

Changes in the free energy of a solid solution (ΔG_{mix}) are subsequently defined as:

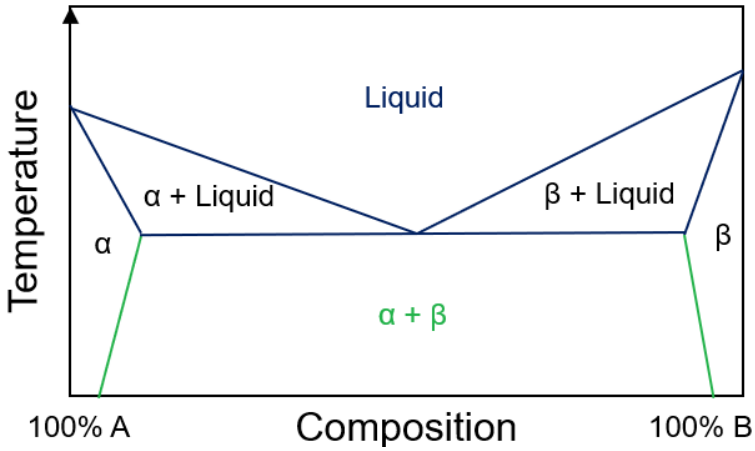

Figure 2-16: Phase diagram of a two component system, A and B. α and β are respectively A and B-rich phases. These labels do not directly refer to the labelling of temperature induced structural variations in perovskites.

$$\Delta G_{mix} = \Delta H_{mix} + T\Delta S_{mix}. \tag{2.27}$$

Considering a two component system made of A and B, the enthalpy and entropy of the mixed system (ΔH_{mix} and ΔS_{mix} respectively) can be written in terms of interaction energies and atomic fractions of the two components. A-A, B-B and A-B interaction energies are written as w_{AA}, w_{BB} and w_{AB} respectively, while x_A and x_B are the fraction of A and B atoms in a system comprising of N atoms, each with a coordination number z . Using these parameters the mixing terms are given by:[98]

$$\Delta H_{mix} = \frac{N z x_A x_B}{2}(2w_{AB} - w_{AA} - w_{BB}) \tag{2.28}$$

$$\Delta S_{mix} = k_B N_A(-x_A ln(x_A) - x_B ln(x_B)) \tag{2.29}$$

where N_A is Avogadro's number.[98] Free energy curves of ΔG_{mix} against composition are often plotted to determine the most stable state (or the lowest free energy) for a particular pressure, temperature and composition. However, it is sometimes the case that the system can reduce its free energy by separating into two different phases, resulting in phase separation. If the mixture lies in an unstable region of the free energy diagram then phase separation can happen spontaneously, known as spinodal decomposition. This instability is common in mixed hybrid halide perovskites, and a

significant challenge in improving material lifetime lies in achieving thermodynamically stable perovskites through successful site substitution[80,99] .

2.6.2 A and X-Site Substitution

The ABX_3 structure of perovskites can be altered to fully or partially substitute ions at any combination of the A, B or X sites. This compositional engineering allows for the tuning of structural and physical properties enabling more stable PV devices capable of achieving higher power conversion efficiencies.[81] For example, Pellet *et al.* first combined the MA and FA cations into mixed A-site perovskite devices; $FA_{1-x}MA_xPbI_3$ demonstrated superior PV performance when compared to the single cation $FAPbI_3$ and $MAPbI_3$ devices.[20] Subsequently, introducing Cs in a triple cation configuration has been shown to produce more thermally stable PV solar cells with improved reproducibility and greater resistance to device defects.[81] Additional substitution at the X halide site has been shown to further improve device stability, with Saliba *et al.* achieving a maximum power conversion efficiency of 21.1% and a consistent power output of 18% for 250 hours using the composition $Cs_{0.1}(MA_{0.17}FA_{0.83})_{0.9}Pb(I_{0.83}Br_{0.17})_3$.[81]

Although not a focus in this work, significant research effort also exists in an attempt to replace the lead in hybrid perovskites in order to create Pb-free devices, removing the toxicity issue that surrounds perovskite PV.[21,23,100,101] Klug *et al.* investigated the effects of substituting the Pb with nine divalent metal alternatives (Co, Cu, Fe, Mg, Ni, Sn, Sr and Zn), however the Pb based perovskites remain the best PV performers.[21]

Despite the effect of site substitution on PV performance being a key area of research for the perovskite community, its effect on the fundamental structural behaviour of these materials was relatively unknown and is subsequently the focus of attention in this thesis.

$\mathbf{FA}_x\mathbf{MA}_{1-x}\mathbf{PbI}_3$

An investigation into the phase behaviour of $FA_xMA_{1-x}PbI_3$ was conducted as part of a Master of Research degree prior to the work presented in this thesis and subsequently published.[95]

Powder samples of $FA_xMA_{1-x}PbI_3$, made through the precipitation method, were measured by PXRD and variable temperature single crystal X-ray diffraction (SXRD) for compositions of $0 \leq x \leq 1$ (in intervals of 0.1). Nuclear Magnetic Resonance imaging (NMR) was used to compare the observed and expected ratios of FA to MA, confirm-

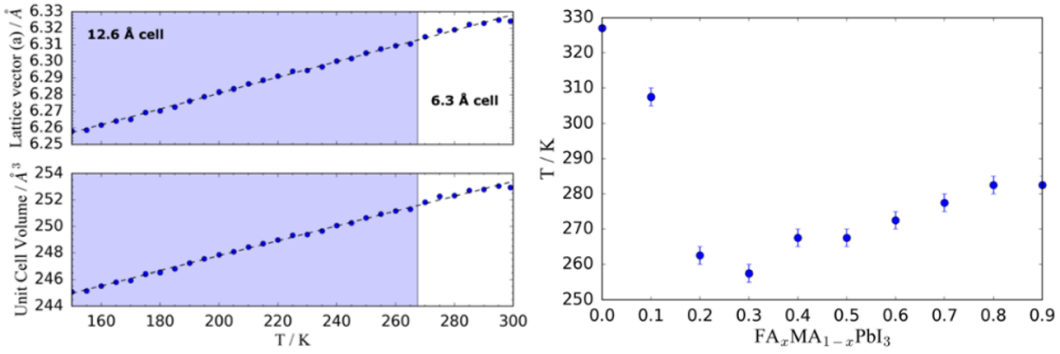

Figure 2-17: (Left) The reduced lattice parameter a and unit cell volume for $FA_{0.5}MA_{0.5}PbI_3$ obtained via variable temperature SXRD between 300 K - 150 K. (Right) Variation in transition temperature between the 6.3 Å to 12.6 Å unit cell depending on composition x in $FA_xMA_{1-x}PbI_3$. Adapted from Weber *et al.*[95]

ing that uptake of the FA and MA ions mirrored the concentrations used in precursor solutions, while the lattice parameters for $FA_xMA_{1-x}PbI_3$ were observed to vary with Vegard's law:[102]

$$a_{A_xB_{1-x}} = xa_A + (1-x)a_B \tag{2.30}$$

where a_A and a_B represent the lattice parameters of $FAPbI_3$ and $MAPbI_3$ respectively. The material remains in the tetragonal $I4/mcm$ $MAPbI_3$ structure for $x \leq 0.1$; however, beyond this the increasing presence of the FA cation forces the structure into the cubic $Pm\overline{3}m$ phase. Variable temperature SXRD measurements also revealed a linear decrease in the pseudo-cubic lattice parameter with decreasing temperature, although below a composition dependent transition temperature the unit cell doubled from 6.3 Å to 12.6 Å (see Figure 2-17). However, this doubled cubic cell, caused by increased octahedral tilts, could also be described by an I-centered tetragonal cell.[95]

$Cs_xFA_{1-x}PbI_3$ and $Cs_xMA_{1-x}PbI_3$

Less extensive studies exist for the phase behaviour of $Cs_xFA_{1-x}PbI_3$ and $Cs_xMA_{1-x}PbI_3$ systems due the substitution limit of cesium within the perovskite structure.[22] The general consensus is that Cs incorporation is limited to $x \leq 0.2$, beyond this phase separation occurs into the FA or MA perovskite and the undesirable δ-$CsPbI_3$.[103] However the vast majority of investigations into mixed $Cs_xFA_{1-x}PbI_3$ and $Cs_xMA_{1-x}PbI_3$ systems are concerned with thin films within different PV devices. Therefore work was needed to understand the detailed structure-property relationships of these materials

without the influence of the vast range of PV device architectures, a motivation for a significant proportion of work presented in this thesis.

$\mathbf{MAPb(I_yBr_{1-y})_3}$

Exchanging the cation at the A-site can have important effects on perovskite properties but site substitution at the X halide site often has a greater influence on the material. For example, in varying the halide between I, Br and Cl, the perovskite colour, structure and stability can be tuned while maintaining desirable PV properties.[104] Tetragonal $MAPbI_3$ turns to the ideal cubic structure with 20% $MAPbBr_3$ substitution, however these mixed systems have shown a tendency to phase separate into I and Br-rich regions due to the high mobility of the halide ions.[105–107] This high level of mobility has other implications, including the potential to create site substituted halide systems simply by mixing $MAPbI_3$ and $MAPbBr_3$ in appropriate ratios.[108] Halide exchange has already been demonstrated in perovskite nanocrystals which motivated work for this thesis investigating I/Br exchange in large single crystals.[108]

2.7 Perovskite Stability

Despite device efficiencies challenging commercially available technology,[16] stability remains a critical issue for perovskite solar cells, with the best devices stable over months, but with most degrading after only a few minutes of use.[16,109] Optimising both material and device design will be crucial in overcoming this significant barrier.

Aristidou *et al.* found that exposing the favoured hybrid perovskite $MAPbI_3$ to light and oxygen can lead to the degradation into lead iodide (PbI_2), MA, I and H_2O.[17] On exposure to light a superoxide (O_2^-) species is formed through the absorption of electrons generated by the light. This species can then react with the photoexcited $MAPbI_3$ ($CH_3NH_3PbI_3^*$) through the reaction:[17]

$$4CH_3NH_3PbI_3^* + O_2^- \rightarrow 4PbI_2 + 2I_2 + 2H_2O + 4CH_3NH_2. \tag{2.31}$$

In the absence of a photoexcited species and superoxide the reaction of $MAPbI_3$ with oxygen is thermodynamically unfavorable, therefore degradation by oxygen is unlikely to occur if the $MAPbI_3$ is stored in the dark, although this is not useful for PV applications. Figure 2-18 shows the result of this decomposition into PbI_2 and precursor salts, explored in more detail in a later chapter.

$MAPbI_3$ is also known to readily hydrolyse to $MAPbI_3{\cdot}H_2O$ in the presence of moisture.[110] Encapsulation provides one method to overcome this and prolong the life of a perovskite device. However, calorimetric measurements by Nagabhushana *et al.* revealed a positive enthalpy of formation in relation to decomposition to precursor materials PbI_2 and MAI, implying $MAPbI_3$ to be thermodynamically unstable.[99] This was also confirmed by Zhang *et al.* through density functional theory (DFT) calculations, showing that $MAPbI_3$ was prone to degrade to PbI_2 and MAI regardless of atmospheric conditions.[106]

Nagabhushana *et al.* went on to suggest substitution at the A and X-sites had the potential to reduce the apparent thermodynamic instability in $MAPbI_3$.[99] Indeed a number of studies have shown improved device stabilities with the incorporation of additional halide anions or organic cations.[7,27,94,109,111,112] Binek *et al.* showed incorporation of only a small amount of MA ($\leq$20%) stabilised $FAPbI_3$, suppressing the formation of the δ-phase at room temperature,[111] while Zhang *et al.* found improved film crystallinity and device performance on the addition of $\leq$10% FA to $MAPbI_3$.[112] Substituting small amounts of Cs into the $MAPbI_3$ and $FAPbI_3$ structures has also

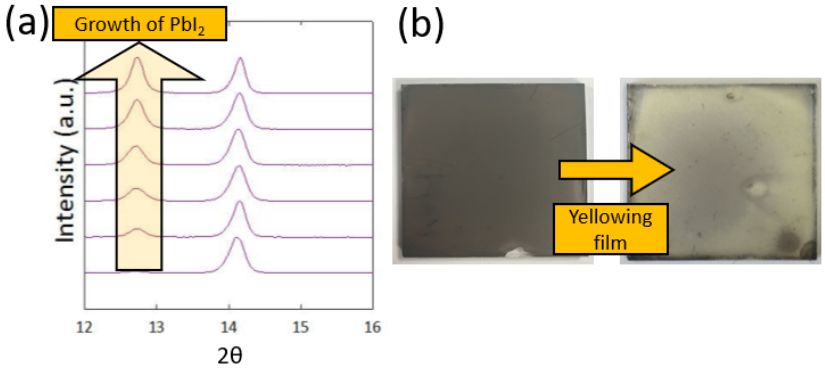

Figure 2-18: (a) Evolution of PXRD patterns for a thin film of $MAPbI_3$ synthesised for work presented in Chapter 6. The bottom trace was measured on the as-made film while the top trace was measured 10 days later. The growing peak represents the increasing presence of PbI_2. (b) As-made black perovskite film yellowing after 10 days.

been shown to improve the thermal and moisture stability of the pure phases, while still demonstrating good PV performance in devices.[99,104,113]

Substitution at the X-site of the perovskite has led to bandgap tuning covering the entire visible spectrum and so enabled material optimisation depending on end use, for example for use in single junction or tandem solar cells.[7] Mixed cation mixed halide compositions, such as $Cs_{0.17}FA_{0.83}Pb(I_{0.83}Br_{0.17})_3$, have shown increased stability when used in PV devices, and $MAPb(Br_yCl_{1-y})_3$ perovskites have been observed to maintain a desirable cubic structure through to 120 K.[94] It was suggested that the suppression of phase transitions to lower symmetry structures with decreasing temperature is inhibited by halide disorder, which affects the tilting of the PbX_6 octahedra driving the phase transitions.[94] The effect of Br substitution in lead iodide perovskites is investigated further in Chapters 4 and 5 using variable temperature neutron diffraction.

One concern of site substitution is that forming mixed halide perovskite compositions introduce an additional instability due to photo-induced phase separation.[114] Under illumination mixed I-Br lead perovskites have been shown to preferentially separate into I and Br rich regions, causing problems for PV devices due to charge carrier trapping occurring in I rich regions.[107] This phenomenon is investigated in large single crystals in Chapter 7.

It is clear the mixed cation/anion perovskites demonstrate superior PV performance; however, the fundamental behaviours and degradation mechanisms of these mixed-site materials were not widely known, prompting the work undertaken in this thesis.

Chapter 3

Material Synthesis and Characterisation

3.1 Perovskite Synthesis

Formamidinium iodide (FAI), methylammonium iodide (MAI), formamidinium bromide (FABr) and methylammonium bromide (MABr) were purchased from GreatCell Solar. Unless specified otherwise, all other reagents were purchased from Merck and solvents were purchased from Alfa Aesar, with purities $> 99\%$. Reactant quantities are detailed in Appendix A, while specific synthetic details, relevant to each chapter, can be found in Appendix B.

3.1.1 Mechanochemical

Mechanochemical synthesis offers an efficient and reproducible method of producing large quantities of perovskite powder, avoiding the hazardous solvents and high temperatures required by other synthetic routes.[115] The method has previously proved successful in the synthesis of metal-organic frameworks (MOFs) and perovskite-type oxides, therefore the approach was extended to the hybrid halide perovskites family.[116,117]

When mixed together perovskite precursors show a tendency to form the black perovskite phase; for example, simply grinding methylammonium iodide (CH_3NH_3I, MAI) and lead iodide (PbI_2) manually using a pestle and mortar for 10 minutes produces $MAPbI_3$ of quality comparable to that produced through more commonly used methods discussed later in this chapter. Therefore the mechanochemical synthesis of mixed cation mixed halide perovskites through manual grinding and automated ball milling was investigated.

To produce 2 g of the material $Cs_{0.1}MA_{0.9}Pb(I_{0.6}Br_{0.4})_3$, 0.0906 g of CsI, 0.4988 g MAI, 0.6429 g PbI_2 and 0.7677 g $PbBr_2$ were manually ground in a pestle and mortar for 30 minutes. The same quantities of Cs, MAI, PbI_2 and $PbBr_2$ were loaded with small stainless steel grinding balls into a 12 ml grinding jar and into a Retsch Planetary Ball Mill PM100. The number of grinding balls, revolutions per minute (rpm) and time were varied to optimise the quality of the resulting powder. All powders were subsequently heated in an oven at 100°C overnight as this significantly improved the quality of the final material.

Despite the promise of a simple, reproducible and efficient method of producing complex mixed cation mixed halide perovskites, it was decided to concentrate on the solvothermal, precipitation and inverse solubility methods described in Sections 3.1.2, 3.1.3 and

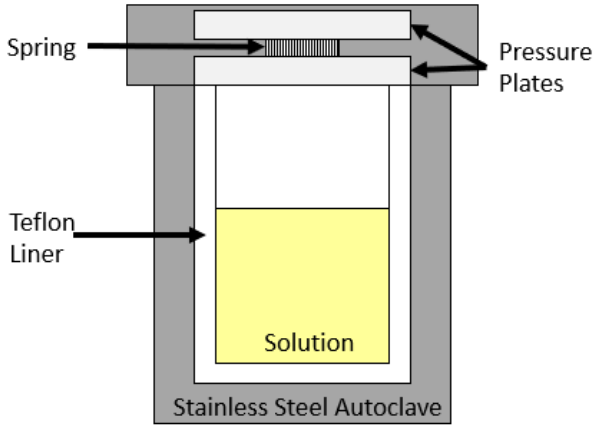

Figure 3-1: Schematic of solvothermal synthesis using a stainless steel autoclave. The perovskite precursor solution was sealed in the autoclave which was heated then slowly cooled in an oven.

3.1.4 respectively. The decision to concentrate on alternative synthetic routes was made largely due to material quality, which - because of grinding effects - proved difficult to characterise through X-ray diffraction.

3.1.2 Solvothermal

The lead iodide perovskites methylammonium lead iodide ($CH_3NH_3PbI_3$, $MAPbI_3$), formamidinium lead iodide ($HC(NH_2)_2PbI_3$, $FAPbI_3$) and the mixed organic cation phases ($FA_xMA_{1-x}PbI_3$, $0 \leq x \leq 1$) were prepared using the method by Poglitsch and Weber.[118]

1.5 wt% of hypophosphorous acid was used to reduce hydriodic acid (HI, 57 wt%) before stoichiometric quantities of MAI, FAI and lead acetate trihydrate ($Pb(CH_3COO)_2{\cdot}3H_2O$, abbreviated to $Pb(OAc)_2{\cdot}3H_2O$) were added to make a 1 molar (1M) solution. The quantities of the precursor materials needed are detailed in Appendix A. The solution was then transferred to a Teflon cup, placed in a stainless steel autoclave and sealed, as shown in Figure 3-1. The autoclave was heated in an oven at 100°C for 12 hours allowing the solid precursors to dissolve completely. The temperature was then gradually lowered to 46°C over 8 hours before the Teflon cup was removed from the autoclave and the perovskite powder filtered. The resulting powder was oven dried at 100°C overnight.

$FA_xMA_{1-x}PbI_3$ tended to phase separate into the black perovskite α-phase and yellow

non-perovskite δ-phase when $x \geq 0.7$. This could be remedied by heating the precursor solution for a further 5 hours at 100°C. However, due to potential decomposition of the MAI and FAI precursor salts at high temperatures[97] and quality of material produced it was decided to focus on synthesis by precipitation for work on cesium and bromine containing perovskites.

Solvothermal synthesis was utilised to obtain results presented in Chapter 6.

3.1.3 Precipitation

Based on the method of Poglitsch and Weber,[118] precipitation from acid provided a similar, yet substantially quicker route for the synthesis of perovskite powders than the solvothermal method described in Section 3.1.2. In this case, the precursor salts MAI, FAI and/or CsI were added to stoichiometric combinations of PbI_2, $PbBr_2$, HI and hydrobromic acid (HBr, 48 wt%) depending on the desired final composition. 1.5 wt% of hypophosphorous acid was used to reduce HI prior to use. Material quantities used to synthesise powders are detailed in Appendix A.

Stoichiometric quantities of precursor salts and lead halide powders were added, as required, to reduced HI and HBr to form a 1 M solution in a 3-necked round bottom flask fitted with a condenser and nitrogen gas inlet as shown in Figure 3-2. Solutions were heated to 100°C under nitrogen and stirring using a hot plate and oil bath. The stirring was stopped and solutions were kept at 100°C for 45 minutes before being cooled to 46°C over 1 hour allowing the precipitation of perovskite powder. The resulting powder was filtered and oven dried at 100°C overnight. The average yield for this synthesis was 55%.

Precipitation from acid was used to obtain results presented in Chapters 4, 5 and 6.

3.1.4 Inverse Solubility

The counter-intuitive property of perovskites to crystallise out of solution at high temperature was used extensively in this work. Inverse temperature crystallisation (referred to as inverse solubility throughout this thesis) was first demonstrated by Saidaminov *et al.* in 2015, who demonstrated a significant reduction in the solubility of $MAPbX_3$ perovskites in the solvents γ-butyrolactone (GBL) and dimethylformamide (DMF) at high temperatures.[66] Exploiting the inverse solubility shown by the $MAPbX_3$ materials, Saidaminov and colleagues were able to grow good quality single crystals on the

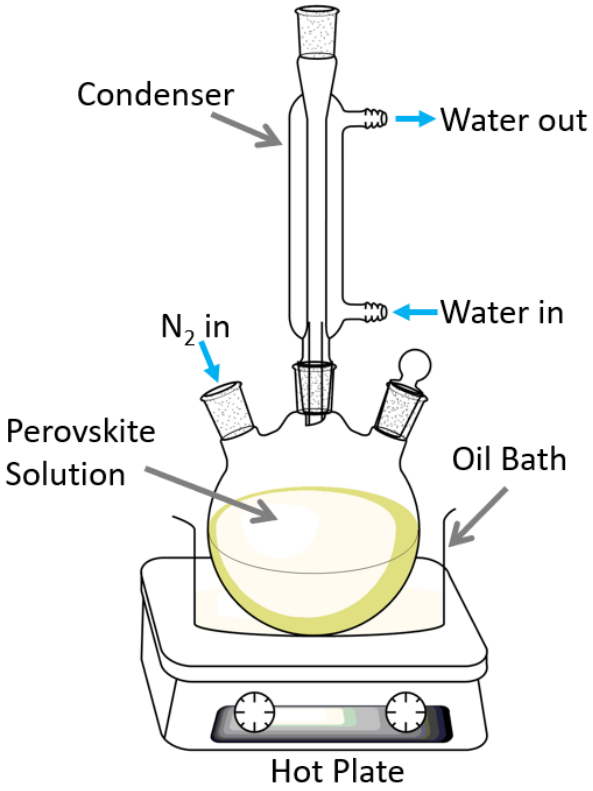

Figure 3-2: Schematic of precipitation of perovskite powder from acid using a three necked round bottom flask flushed with nitrogen and immersed in an oil bath.

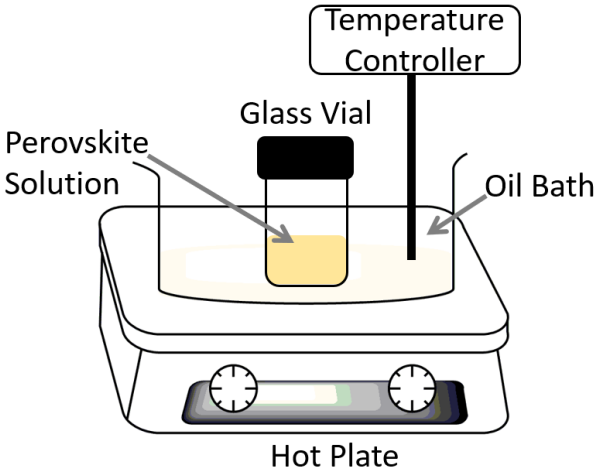

Figure 3-3: Schematic of perovskite crystal growth via inverse solubility. Sealed glass vials containing the precursor solution were placed in an oil bath, the temperature of which was carefully controlled using a Stuart SCT1 controller attached to a hot plate.

millimeter scale in just three hours, significantly shorter than previous attempts growing large perovskite crystals which could take up to one month.[119] The best quality $MAPbI_3$ crystals were achieved by dissolving precursors in GBL and heating to 110°, whereas use of DMF at 80° produced the best quality $MAPbBr_3$ crystals.

The solubility of a 1 M solution of $MAPbI_3$ in GBL was shown to increase up to 60°C but rapidly decrease beyond this, whereas the solubility of $MAPbBr_3$ in DMF continuously decreased on increasing temperature.[25] It was proposed that this unusual behaviour is determined by the formation of complexes in the precursor solutions. In the case of inverse solubility, an increase in temperature induces the dissociation of precursor-solvent complexes formed at 60°C for $MAPbI_3$ in GBL and at room temperature for $MAPbBr_3$ in DMF. This dissociation results in unbound precursor particles which, when supersaturation is reached, precipitate out of solution.[66]

In this work the method of Saidaminov *et al.* was developed to produce crystals of mixed cation lead halide perovskites. The average yield of the inverse solubility method was 10%, significantly less than that achieved by precipitation and solvothermal methods. Crystal growth via inverse solubility was used to obtain results presented in Chapters 4, 5, 7 and 7. Quantities used to synthesise perovskite crystals are detailed in Appendix A.

$\mathbf{FA}_x\mathbf{MA}_{1-x}\mathbf{PbI}_3$ Crystal Growth

Stoichiometric quantities of MAI, FAI and PbI_2 were dissolved at 60°C in dry GBL.

Concentrations of the precursor solutions were kept at 1 M with an exception for the FA rich materials $FA_xMA_{1-x}PbI_3$ ($x \geq 0.8$) where concentrations were lowered to 0.9 M to allow the FAI to fully dissolve. When the precursor salts and lead halide powders had completely dissolved, the solutions were quickly filtered using Millex GS filters (pore size 0.22 μm) and transferred to clean cylindrical glass vials. The solutions were then immediately heated to 110°C using an oil bath, the temperature of which was carefully controlled and monitored using a Stuart SCT1 controller. Solutions were maintained at 110°C for three hours allowing crystallisation, the temperature was then raised to 120°C for a final hour before the remaining solution was filtered and crystals were oven dried at 100°C overnight.

In general this method produced perovskite crystals ranging from 0.5 - 1 mm in diameter, however crystallite size and quality could be improved by careful control of the temperature ramp; for example, slowing the ramp to 10°C $hour^{-1}$ produced crystals over 2 mm in diameter.

$Cs_xFA_{1-x}PbI_3$ and $Cs_xMA_{1-x}PbI_3$ Crystal Growth

Stoichiometric quantities of CsI, FAI, MAI and PbI_2 were dissolved at 80°C in dry GBL and the solutions were then heated to 110°C at a rate of 10°C $hour^{-1}$. The temperature was increased to 110°C for a further hour before the resulting crystals were filtered from the remaining solution and oven dried at 100°C overnight.

$FA_xMA_{1-x}PbBr_3$ Crystal Growth

Stoichiometric quantities of FAI, MAI and $PbBr_2$ were dissolved in dry DMF at room temperature and immediately heated to 80°C. The solution was left undisturbed for three hours allowing crystallisation, the remaining solution was then filtered and resulting crystals were oven dried at 100°C overnight.

3.1.5 Space Confined Crystal Growth

The method of Saidaminov *et al.*[66] was developed in conjunction with the *space confined* method reported by Chen *et al.*[120] in order to produce single crystals of controlled dimensions specifically for high pressure measurements in a diamond anvil cell (DAC) in collaboration with the Institute of Materials Science of Barcelona (ICMAB).

Glass substrates (25 mm x 75 mm) were cleaned sequentially with acetone and ethanol in an ultrasonic bath for 10 minutes before being placed on a clean hotplate at 60°C. Stoichiometric precursor solutions of MAI, FAI, PbI_2 were prepared 60°C in dry GBL

according to the quantities detailed in Appendix A. Once completely dissolved, 100 μL of the precursor solution was transferred onto a glass substrate and a second substrate (also kept at 60°C) was placed on top of the first (Figure 3-4 (a)). The temperature of the hot plate was increased to 110°C at a rate of 10°C hour^{-1}, then maintained at 110°C for 24 hours allowing crystallisation by inverse solubility. The top glass substrate was removed and the resulting crystals were oven dried at 100°C overnight. The crystals were carefully removed from the bottom substrate under an optical microscope.

The thickness of the crystal could be varied by applying an evenly distributed weight of 120 g on top of the substrates sandwiching the precursor solution. Final measurements of the single crystals grown via the space confined method, and subsequently used in the high pressure measurements at ICMAB, averaged dimensions of 2 mm x 30 μm as calculated through parallax measurements from secondary electron (SE) images taken with a scanning electron microscope (SEM).

In order to calculate crystal thickness a plan-view SE image of the desired crystal was taken, before additional images were acquired with the SEM stage tilted at at 60° and 69° creating a parallax (α) of 9°. Three easy to identify features were selected in both images (60° and 69°): an origin (O) and features on the base (A) and top (B) edges of the crystal (as shown schematically in Figure 3-4 (b,c)). The program ImageJ[121] was used to obtain the co-ordinates of each position A and B (in the 60° image) and A' and B' (in the 69° image) with respect to the origin. The co-ordinates were converted from pixels to μm using the scale bar, and the z co-ordinates of A and B (z_a and z_b respectively) were calculated by:[122]

$$z_a = \frac{x_a - x_{a'}}{2\sin(\alpha/2)} \quad \text{and} \quad z_b = \frac{x_b - x_{b'}}{2\sin(\alpha/2)}. \tag{3.1}$$

As the image was tilted about the y axis, $y_{a/b} = y_{a'/b'}$, therefore the y co-ordinates were not used in the calculation for $z_{a/b}$. The thickness (or depth) of the crystal (Z) was then simply calculated by $Z = z_b - z_a$.

Crystal growth via the space confined method was used to produce samples for work in collaboration with the Institute of Materials Science of Barcelona (ICMAB). The work is not presented in this thesis, but can be found in the publications listed at the beginning of this thesis.

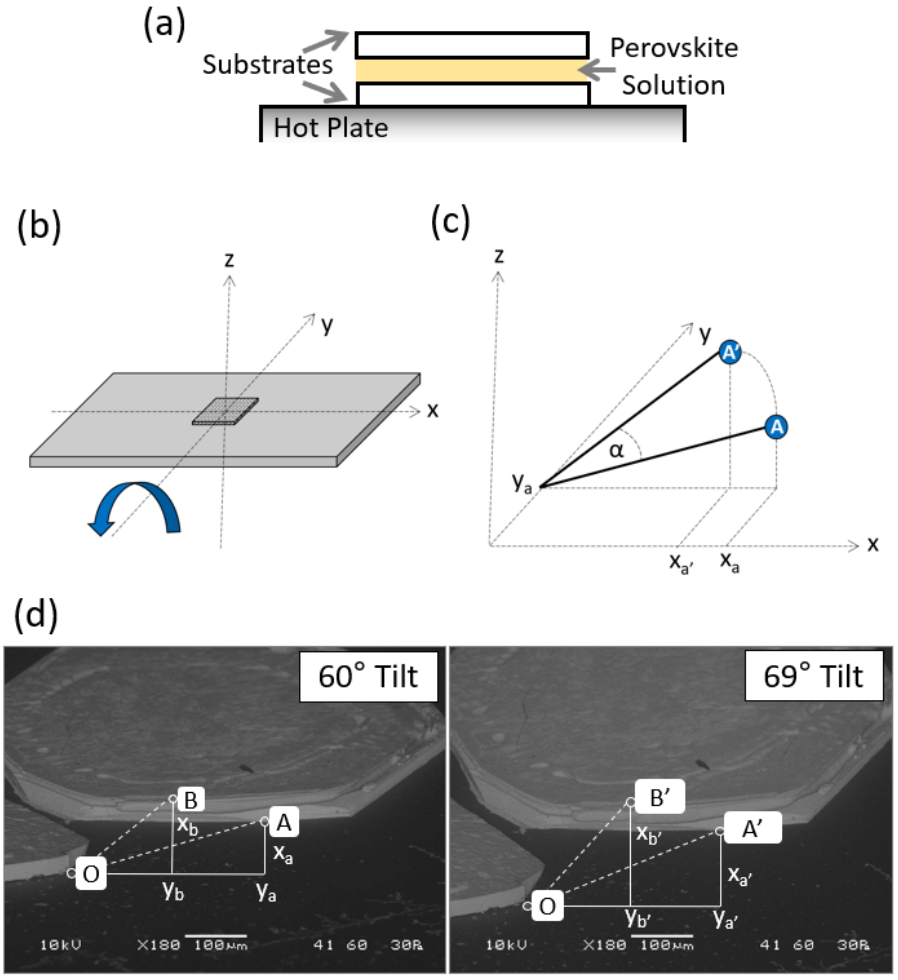

Figure 3-4: (a) Schematic of space confined crystal growth. (b) Sample sitting on an SEM stage capable of tilting around the y-axis. (c) Geometrical relationship between a point A on the sample before (A) and after (A') at an angle α known as the parallax, enabling 3D measurements from 2D images. (d) SEM images of a $MAPbI_3$ crystal grown via the space confined method. The sample stage was tilted at 60° and 69° creating a parallax of 9° enabling crystal thickness to be determined.

3.1.6 Drop Casting

Deuterated perovskite powder samples ($Cs_{0.1}FA_{0.9}PbI_3$-D) were required for a neutron diffraction experiment performed on the POLARIS instrument at the ISIS Neutron and Muon source. Part deuterated FAI ($CH(ND_2)_2I$ referred to as FAI-D) was provided by Dr James Tellam of the ISIS Deuteration Facility.

Perovskite synthesis via inverse solubility was first investigated as, despite low yields, this method produced good quality, impurity free material. CsI and PbI_2 were oven dried at 100°C overnight, while the solvent GBL was dried over calcite ($CaCO_3$) to ensure the complete removal of water and so reduce the risk of H-D exchange during synthesis. CsI, FAI-D and PbI_2 were dissolved in the dried GBL according to the inverse solubility method outlined in Section 3.1.4 and quantities detailed in Appendix A. However, when the temperature of the precursor solutions were heated above 90°C a yellow precipitate crashed out of solution, subsequently preventing crystal growth. The formation of complexes between the solvent molecules and precursor compounds are crucial in the success of the inverse solubility method,[66] therefore it was proposed that presence of the deuterium in the FAI salt prevented the formation of complexes favourable to the crystallisation of the perovskite compound at 110°C.

After the failure of the inverse solubility method it was decided to focus on the drop casting method, which had previously proved successful in the synthesis of deuterated $FAPbI_3$ ($FAPbI_3$-D).[74] To achieve 10 g of $Cs_{0.1}FA_{0.9}PbI_3$-D 0.405 g of dried CsI, 2.412 g of FAI-D and 7.184 g of dried PbI_2 were dissolved in 25.97 ml of dimethyl sulfoxide (DMSO-d_6, 99.9% atom % D) and drop cast onto a preheated glass dish at 150°C on a hot plate in a dry atmosphere. As the solvent evaporated a black solid formed which was subsequently dried on the hotplate for a further 120 minutes. The sample was sealed under nitrogen and stored below 5°C to reduce H-D exchange.

Deuterated perovskite powder synthesised via the drop casting method was used to obtain results presented in Chapter 4.

3.1.7 Thin Film Fabrication

Thin films of $FA_xMA_{1-x}PbI_3$ were deposited onto clean glass substrates via spin coating. The glass substrates (25 mm x 25 mm) were cleaned sequentially using acetone and ethanol in an ultrasonic bath for 10 minutes and then placed in a Bioforce Nanosciences UV/Ozone Procleaner for 20 minutes.

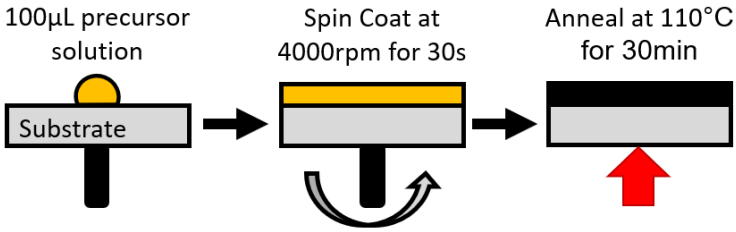

Figure 3-5: Process used to deposit thin films of $FA_xMA_{1-x}PbI_3$ onto glass substrates.

MAI and FAI were measured such that the MAI:FAI ratio varied from 0 to 1 in increments of 0.1, before being dissolved with stoichiometric quantities of PbI_2 in dimethylformamide (DMF) to form 0.6 M precursor solutions. Solutions were stirred for 30 minutes to ensure all solid precursor dissolved, 100 μL of the resulting solutions were then deposited onto the substrates in a dry box and spin coated at 4000 rpm for 30 seconds. The films were then transferred to a hot plate and annealed at 110°C for 30 minutes. Material quantities used in the fabrication of thin films are detailed in Appendix A.

Thin films deposited via spin coating were used to obtain results presented in Chapter 6.

3.2 Sample Characterisation

The theory behind the characterisation methods used in this work is described below. Brief summaries of the measurements performed are also given for each technique, although additional experimental information specific to each chapter, can be found in Appendix B.

3.2.1 Scanning Electron Microscopy

Scanning electron microscopy (SEM) uses a focused beam of electrons to produce detailed images of small features. The human eye can distinguish between objects up to a resolution of approximately 0.1 mm, while an optical microscope can reduce this to approximately 2 x 10^{-4} mm.[123] However, this resolution can be greatly improved by the replacement of light with electrons. The first electron microscope was made in the 1930s, replacing the light source with an electron source, and the condenser lens with an electromagnetic coil.[123] The technique has improved to the point that images of nanometer sized objects can be resolved.[75]

SEM images are achieved via elastic and inelastic interactions between the electron beam and sample. In elastic scattering, incident electrons are deflected by the atomic nucleus or outer shell electrons of the sample material, with electrons deflected through an angle $> 90°$ known as back scattered electrons (BSE). Incident electrons are inelastically scattered through a variety of interactions with the sample material resulting in the ionization of the sample and the subsequent emission of secondary electrons (SE) of energies typically below 50 eV.[123]

Unlike optical imaging, SEM electrons do not reflect off the surface of the sample, but instead penetrate into the material before undergoing scattering. The incident beam of electrons therefore excites a region of the material, the depth of which is dependent on the energy of the incident beam and the density of the sample.[123]

Summary of Measurements

SEM images were taken of mixed Cs/MA/FA lead iodide crystals, $MAPbBr_3$ crystals and mixed MA/FA lead iodide thin films using a Jeol JSM-6480LV SEM. Perovskite crystals were prepared 24 hours before measuring, affixed to SEM stubs using carbon tape and placed under vacuum allowing off-gassing of the tape.

Secondary and backscattered electron images using an accelerating voltage of 20 kV

were taken of $Cs_xFA_{1-x}PbI_3$ (x = 0.1, 0.2), $Cs_xMA_{1-x}PbI_3$ (x = 0.1, 0.15) and $MAPbBr_3$ as presented in Chapters 4, 5 and 7 respectively. Secondary electron images were also taken of $FA_xMA_{1-x}PbI_3$ (x = 0.3, 0.5, 0.6, 0.7) thin films, using an accelerating voltage of 5 kV and presented in Chapter 6.

3.2.2 Energy Dispersive X-ray Spectroscopy

Energy dispersive X-ray spectroscopy (EDX) - also referred to as EDAX or EDS - is a powerful technique enabling elemental composition analysis of a sample. The method makes use of an inelastic scattering process whereby a high energy electron ejects a core electron from an element in the sample. An outer electron subsequently transitions to fill the vacant position left by the core electron, releasing energy in the form of an X-ray characteristic to that transition. Analysis of these characteristic X-rays allow for the identification of elements within a sample.

Castaing's first approximation models a proportional relationship between characteristic X-ray intensities and the mass fraction of elements present within a sample. However, there is some deviation from this linear approximation when compounds containing multiple different elements are examined. Some elements are more absorbing than others resulting in lower X-ray intensities detected, while some may exhibit a strong fluorescent effect leading to greater intensities. To account for these differences corrections (referred to as matrix effects) are applied which take into account atomic number (Z), fluorecence (F) and absorption (A).[124] An accuracy of $\pm 2\%$ for dominant elements can be achieved. One draw back to EDX analysis is the difficulty to distinguish between elements with similar atomic numbers, due to the overlap of characteristic X-ray peaks.[75]

Summary of Measurements

EDX measurements were carried out on $Cs_xFA_{1-x}PbI_3$ (x = 0.1, 0.2), $Cs_xMA_{1-x}PbI_3$ (x = 0.1, 0.15) and $MAPbBr_3$ crystals, the results of which are discussed in Chapters 3, 4 and 7 respectively. All measurements were made with a Jeol JSM-6480LV SEM equipped with an Oxford INCA X-Act SDD X-ray detector using an accelerating voltage of 20 kV. The programs INCA and AZtec by Oxford Instruments were used to analyse chemical composition.

3.2.3 Differential Scanning Calorimetry

In differential scanning calorimetry (DSC) a sample and reference are heated under the same conditions, while the difference in heat flow required to increase (or decrease) the temperature of the two is measured. An event is recorded when the sample undergoes a phase change, such as during melting or crystallisation. The event is recorded as an endotherm or exotherm depending on whether heat flow to the sample was increased or decreased in order to maintain a steady temperature in relation to a reference. Endothermic and exothermic reactions tend to be expressed as negative and positive deviations from the baseline respectively.[75]

Summary of Measurements

DSC measurements were carried out on $Cs_{0.1}FA_{0.9}PbI_3$ samples grown via inverse solubility and precipitation using a TA Instruments DSC Q20. Samples were cycled between 225 K and 420 K at a rate of 2 $Kmin^{-1}$. Data are presented in Chapter 4.

3.3 Structural Characterisation

3.3.1 Single Crystal X-ray Diffraction

As introduced in Chapter 2 Section 2.5.1, the diffraction of X-rays can be used to determine the structure of a crystalline material. In single crystal X-ray diffraction (SXRD) single crystals of sizes up to 0.5 mm are measured.[75] It is essential good quality crystals are used, creating well-defined diffraction spots without problems associated with twinning or other defects; therefore short data sets are quickly collected before experiments to asses crystal suitability.

To generate X-rays a tungsten filament is heated, releasing electrons which are accelerated by an applied voltage to a metal anode (either copper or molybdenum in this work). The electrons interact with the target atoms by slowing and then changing direction, generating X-rays of a broad range of energies known as Bremmsstrahlung radiation. The interactions can also cause the ejection of electrons in the target, resulting in the relaxation of outer electrons, which generate characteristic K_α and K_β X-ray radiation. A monochromotor is used to narrow the range of X-ray energies so only a narrow band centered around the K_α radiation hits the sample.[75]

Samples are mounted onto a goniometer capable of rotating the crystal. If left in a

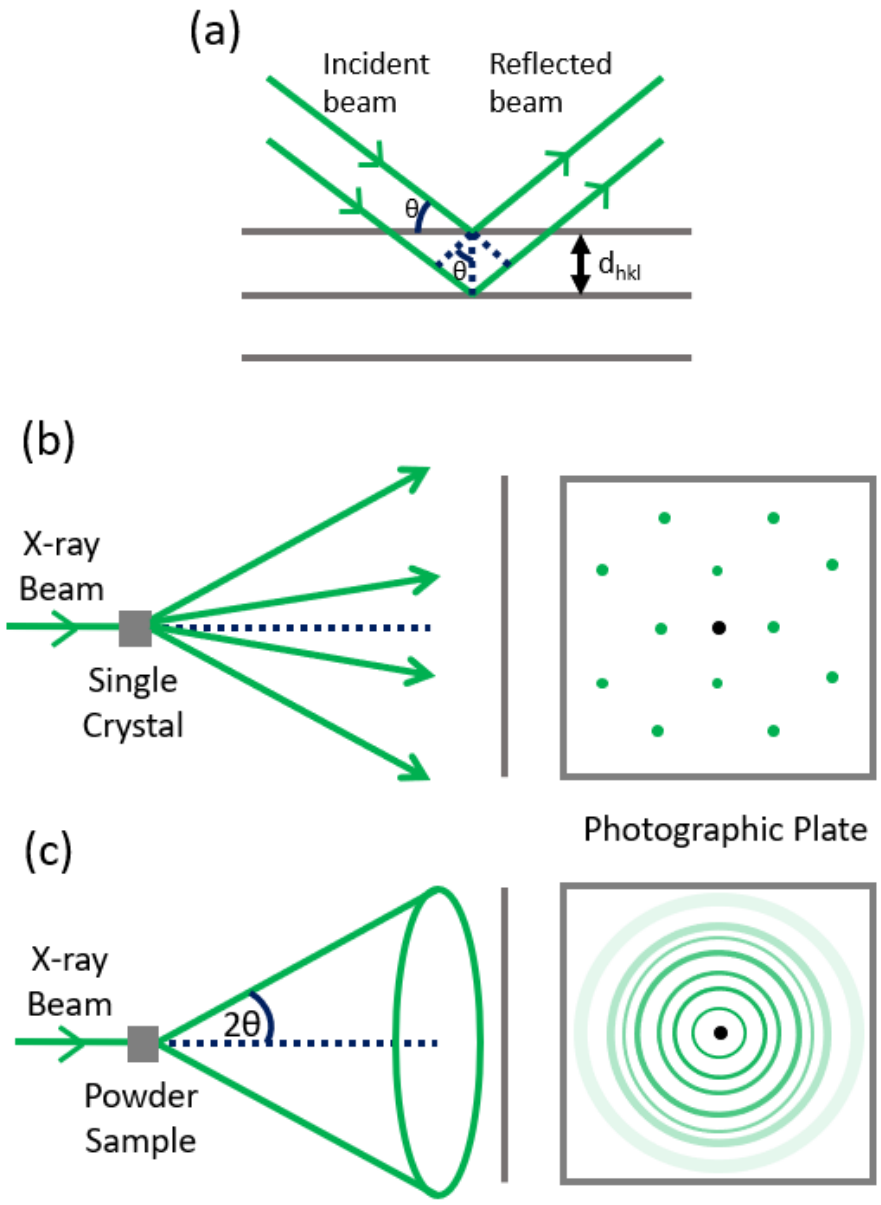

Figure 3-6: (a) Conditions for Bragg's law, two parallel X-rays scattered at an angle θ from neighbouring lattice planes of spacing d_{hkl}. (b) Schematic of SXRD pattern, each spot recorded on the photographic plate represents diffraction by a single plane indexed by the Miller indices (hkl). (c) Schematic of the cone of diffracted X-rays from a polycrystalline powder sample and the resulting pattern recorded on the photographic plate.

single orientation only a small number of lattice planes satisfying the Bragg condition (Figure 3-6 (a)) will be observed, therefore the goniometer rotates the sample to access all required diffracting lattice planes and measure a complete pattern. A CCD records the diffraction pattern as a series of spots with intensities and positions characteristic to the material structure, a schematic of which is shown in Figure 3-6 (b).[71] As detailed in Chapter 2 the diffraction pattern is the Fourier transform of the crystal structure and is solved due to the directly proportional relationship between the intensity of the spots (I_{hkl}) and the structure factor amplitude ($|F_{hkl}|^2$). The phase problem (also introduced in Chapter 2) is addressed through using either Patterson synthesis or direct methods; from these methods an electron density map is created allowing the time averaged structure of the material to be determined.[72]

The quality of the structure determined from the diffraction pattern is assessed by the residual (or R-factor):

$$R = \frac{\sum_{hkl} ||F_{hkl}|^{obs} - |F_{hkl}|^{calc}|}{\sum_{hkl} |F_{hkl}|^{obs}} \tag{3.2}$$

where $|F_{hkl}|^{calc}$ are the structure factors as calculated from the suggested structure and $|F_{hkl}|^{obs}$ are the measured structure factors. The residual should tend towards zero, and can be minimised by refining parameters (such as atomic positions and thermal parameters) in the structural model used to produce the $|F_{hkl}|^{calc}$ values.[72]

Summary of Measurements

SXRD data were collected on a RIGAKU SuperNova dual tube Eos S2 CCD diffractometer using MoKα radiation ($\lambda = 0.7107$ Å). Suitable single crystals of $Cs_{0.1}FA_{0.9}PbI_3$ and $Cs_{0.1}MA_{0.9}PbI_3$ synthesized via inverse solubility were selected and measured at 300 K using an exposure of 10 s/frame, before being cooled and measured at 175 K, 150 K and 120 K using an increased exposure of 20 s/frame. Structures were solved using the programs Olex2,[125] ShelXL[126] and PLATON[127] and results are discussed in Chapters 4 and 5 for FA and MA containing perovskites respectively.

3.3.2 Powder X-ray Diffraction

As in SXRD, PXRD makes use of the diffraction of X-rays from planes in a crystalline material satisfying the Bragg condition: $n\lambda = 2d_{hkl}sin(\theta)$, where n is an integer (required for the constructive interference of X-rays) and λ is the wavelength.[128] However,

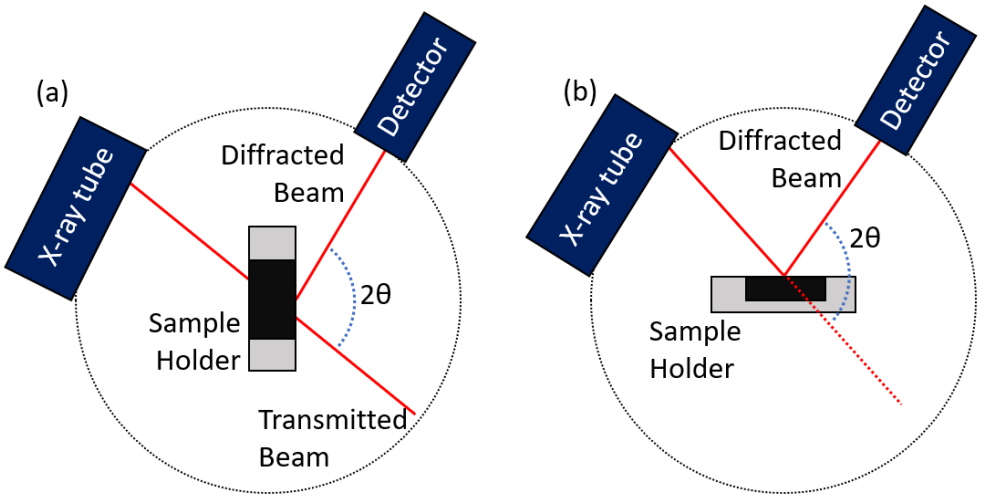

Figure 3-7: (a) PXRD measured using Debye-Scherrer geometry in transmission mode and (b) Bragg-Brentano geometry in reflection mode. The sample is shown in black.

in a powder sample crystallites are orientated in many different directions, therefore, rather than the spots of SXRD, PXRD produces a cone of tightly packed spots, creating a pattern of concentric rings at the detector (Figure 3-6 (c)).[129] Powder diffractometers are able to detect these rings and produce a pattern of reflection intensity against 2θ.[75]

Two different geometries were used to measure PXRD in this work, Bragg-Brentano and Debye-Scherrer. In Debye-Scherrer geometry the beam is parallel to the fully illuminated sample, and the CCD detector is moved at a set radius collecting the diffraction pattern over the desired values of 2θ. In Bragg-Brentano geometry a sample is inserted such that the diffraction vector (the vector bisecting the incident and scattered beam) is normal to the sample surface. Figure 3-7 shows a simple schematic of the two different geometries used in this work.[71,75]

Summary of Measurements

PXRD data of all samples synthesised via solvothermal, precipitation, inverse solubility and drop casting methods were collected on a Bruker Advance D8 diffractometer (Bragg-Brentano geometry) and/or a STOE STADI P (Debye-Scherrer geometry) using CuKα radiation (λ = 1.540 60 Å). Crystals synthesised via inverse solubilty were ground using a pestle and mortar prior to measuring. Collection ranges and resolutions were varied depending on the sample measured. Profile fitting methods - introduced later in this chapter in Section 3.3.4 - were carried out using the program GSAS-II.[130] the structural models used for individual samples are presented in Chapters 4, 5 and 7 for $Cs_{0.1}FA_{0.9}PbI_3$, $Cs_{0.1}MA_{0.9}PbI_3$ and $MAPbBr_3$ respectively.

Thin films of $FA_xMA_{1-x}PbI_3$ ($0 \leq x \leq 1$) were deposited onto glass substrates which were cut to squares 1 cm x 1 cm in size before being measured on a Bruker Advance D8 diffractometer. Diffraction patterns were collected between $10 \leq 2\theta \leq 50$ with a step size of 0.016° and were analysed using the EVA diffraction suite, results of which are presented in Chapter 6.

3.3.3 Neutron Powder Diffraction

As introduced in Chapter 2 2.5.1, neutron diffraction is a complementary technique to X-ray diffraction, capable of providing more information at higher scattering angles with a greater sensitivity to lighter elements. However, neutrons are not as accessible as X-rays, therefore experiments require access to national facilities. The NPD work presented in this thesis was carried out at the ISIS Neutron and Muon Source at the Rutherford Appleton Laboratories in Oxfordshire.

The ISIS facility is a spallation source, meaning neutrons are produced by bombarding a heavy metal target with high energy protons. This process begins with a source of H^- ions being accelerated to 37% the speed of light by a linear accelerator. The ions are then injected into a synchrotron 163 m in circumference, and continue to be accelerated and focused into a high energy beam by powerful magnets. Alumina foil is used to strip away the two electrons of the H^- ions, leaving behind protons which are accelerated further by strong electric fields. Once travelling at 84% the speed of light, magnets kick out a packet of protons which collide with a tungsten target, knocking out neutrons from the tungsten nuclei. This provides a pulse of neutrons of a range of velocities (v) as determined by the de Broglie equation $v = h/m\lambda$, relating the neutron mass (m) and wavelength (λ) to the Planck constant (h).[75] Due to the range of neutron velocities produced in a spallation source, the type of neutron diffraction is known as time of flight (TOF). TOF diffraction relates the velocity (and so wavelength) of a neutron to the time taken to reach a detector; for example, a neutron travelling at 4000 ms^{-1} has a wavelength of 1 Å and takes 10 ms to reach a detector 40 m away from the spallation source.[131]

The de Broglie relationship defining the wavelength of neutrons can be related to the Bragg condition as below:

$$\lambda = \frac{h}{mv} = \frac{ht}{mL} = 2d\sin\theta \tag{3.3}$$

where t is the total time of flight for a neutron along a flight path of length L. Rearranging the above equation produces:

$$t = \frac{2mL}{h} d\sin\theta \tag{3.4}$$

relating d-spacing to t, a relationship used in Chapters 4 and 5 of this thesis to convert neutron TOF data to the more accessible d-spacing format.

The instrument POLARIS was used to collect the NPD data presented in this thesis. POLARIS utilises an intense flux of neutrons to quickly produce medium resolution NPD data sets, allowing for short counting times and smaller sample quantities. For the variable temperature data presented in this work a He cooled cryostat was fitted to the instrument enabling measurements to be carried out between 300 K and 100 K. The diffractometer has 434 ZnS and ^{3}He scintillator detectors arranged into six banks grouped together as Banks A, B, C and D. Banks A and C are positioned at a low angle, while C is positioned to intercept backscattered neutrons. Bank D (also referred to as Bank 4) is located 90° to the sample.[132]

Summary of Measurements

NPD was carried out on the POLARIS instrument at the ISIS Neutron and Muon Source, Rutherford Appleton Laboratories. Approximately 6 g of each material were loaded into 5 mm vanadium sample cans under argon and sealed using indium O-rings. Powder diffraction patterns were measured as a function of temperature between 300 K and 100 K (detailed information on the temperature ramps and exposure times used can be found in the chapters relevant to each material). Profile fitting methods - discussed in Section 3.3.4 - were carried out using the program GSAS-II. Samples of $Cs_{0.1}FA_{0.9}PbI_3$-D synthesised via drop casting, and fully hydrogenous $Cs_{0.1}FA_{0.9}Pb(I_{0.6}Br_{0.4})_3$, $Cs_{0.1}MA_{0.9}PbI_3$ and $Cs_{0.1}MA_{0.9}Pb(I_{0.6}Br_{0.4})_3$ powders synthesised from precipitation were measured. Results are discussed in Chapters 4 and 5 for FA and MA containing perovskites respectively.

3.3.4 Powder Diffraction Fitting Methods

Since the beginning of the 20th century the powder diffraction method has been used in qualitative phase analysis of crystalline samples. However, the field was revolutionised in the 1960s by the introduction of the Rietveld method, which enabled determination of atomic structure from 2D powder diffraction patterns. Bragg reflection intensities

Crystal System	Expression for d_{hkl}
Cubic	$\frac{1}{d_{hkl}^2} = \frac{h^2+k^2l^2}{a^2}$
Tetragonal	$\frac{1}{d_{hkl}^2} = \frac{h^2+k^2}{a^2} + \frac{l^2}{c^2}$
Orthorhombic	$\frac{1}{d_{hkl}^2} = \frac{h^2}{a^2} + \frac{k^2}{b^2} + \frac{l^2}{c^2}$
Hexagonal	$\frac{1}{d_{hkl}^2} = \frac{4}{3}\left(\frac{h^2+hk+k^2}{a^2}\right) + \frac{l^2}{c^2}$

Table 3.1: Expressions for d_{hkl} for the crystal systems of interest in this thesis.

and positions provide information on material composition and atomic positions, and are usually analysed via peak indexing before full profile refinements are attempted.[133]

Indexing

Miller indices (h, k, l) and d-spacings are related as defined by the geometry of the unit cell present, therefore allowing the calculation of lattice parameters (a, b and/or c). For example, the relationship between the Miller indices, d_{hkl} and lattice parameter a in cubic system can be defined as:

$$\frac{1}{d_{hkl}^2} = \frac{h^2 + k^2 + l^2}{a^2} \tag{3.5}$$

which can be substituted into the Bragg equation and rewritten as:

$$sin^2\theta = \frac{\lambda^2}{4a^2}(h^2 + k^2 + l^2). \tag{3.6}$$

This relationship implies each peak in the diffraction pattern of a cubic material can be assigned its associated Miller plane (h, k, l) in a procedure known as indexing. More complex relationships exist for other crystal systems; however, the theory remains the same.[75] The expressions of d_{hkl} for the crystal systems explored in this thesis are listed in Table 3.1. Indexing a powder pattern results in the calculation of likely lattice parameters and space group symmetries which can be used in subsequent structure independent and full profile fitting.

Structure Independent Fitting

In this work the Pawley method was the preferred technique used for structure independent fitting, that is fitting without a structural model.[134] The most likely space group and lattice parameters are extracted from indexing a diffraction pattern, which are used to produce a pattern of calculated intensities. The lattice parameters are then refined along with the background, zero point, peak shape parameters and *all* reflection intensities in order to minimise the difference between the calculated and observed intensities. The zero point is the point at which $2\theta = 0°$ and can shift depending on the alignment of the detector, while the peak shape parameters are also dependent on the properties of the diffractometer.[133]

Rietveld Refinement

The Pawley method refines all diffraction peak intensities; however, a greater understanding of the structure can be achieved through full profile fitting, where the atoms making up the unit cell are used to calculate intensities.[133,135,136] Known as the Rietveld method, the technique uses a predefined structural model producing a calculated profile. The method works by minimising the Rietveld function Φ, given by:[136]

$$\Phi = \sum_{i=1}^{N} w_i (Y_i^{obs} - Y_i^{calc})^2 \tag{3.7}$$

where Y^{obs} and Y^{calc} are the observed and calculated intensities respectively and w_i is the weight assigned to the ith data point carried out over all data points N such that:

$$w_i = \frac{1}{\sigma^2(Y_i^{obs})} \tag{3.8}$$

where σ^2 is the variance of Y_i^{obs}. The value of Y^{calc} is calculated over all Bragg reflections ($\mathbf{s} = (hkl)$) over a phase p, contributing to each position i in the profile as below:[133]

$$Y_i^{calc} = \sum_p \left(S_p \sum_{\mathbf{s}(p)} (|F_{\mathbf{s},p}^{calc}|^2 \phi_{\mathbf{s},p,i} C_{\mathbf{s},p,i}) \right) + B_i \tag{3.9}$$

where S_p is the scaling factor proportional to the amount of phase p present, $|F_{\mathbf{s},p}^{calc}|^2$ are the calculated reflection intensities with a profile function $\phi_{\mathbf{s},p,i}$. $C_{\mathbf{s},p,i}$ is the total correction factor and B_i is the background correction.

The peak positions - representing single or overlapping (hkl) reflections - are determined by the lattice and space-group present, as well as the properties of the diffractometer. For example, in Bragg-Brentano geometry used in PXRD, sample displacement can result in a shift of peak positions. The peak intensities are determined by the time and space averaged crystal structure, for example site occupancy and atomic displacement factors (also known as thermal parameters or ADPs). ADPs are important in the refinement of perovskite structures, in which the dynamic behaviour of the PbX_6 octahedra and central cation often define the physical properties of the material.[86] Peak shape parameters, which help define the profile $\phi_{\mathbf{s},p,i}$, are highly dependent on diffractometer properties, as well as being related to the crystallite size[133]

The quality of the refinement is provided by the weighted R-factor (R_{wp}) and the statistically expected R-factor (R_{exp}):[133]

$$R_{wp} = \Big(\frac{\Phi}{\sum_{i=1}^{n} w_i (Y_i^{obs})^2}\Big)^{\frac{1}{2}} \tag{3.10}$$

$$R_{exp} = \Big(\frac{(N-P)}{\sum_{i=1}^{n} w_i (Y_i^{obs})^2}\Big)^{\frac{1}{2}} \tag{3.11}$$

where P is the number of refined parameters. The ratio of the two - known as the goodness-of-fit or χ^2 - should tend towards one.

In this work, analysis of X-ray and neutron powder diffraction data was carried out using the program GSAS-II developed by Toby and Dreele of Argonne National Laboratory.[130]

3.4 Optical Characterisation

Perovskite crystals grown via inverse solubility were characterised using UV-Visible absorption and photoluminescence spectroscopy; however, mounting the crystals for measurements was, initially, challenging. For measurements presented in this thesis a 40 gml^{-1} solution of the polymer zeonex in toluene was used to securely attach crystals to substrates. Glass or $Si0_2$ substrates were cut to size, then cleaned using isopropanol and dried thoroughly using a nitrogen gun. One drop of zeonex/toluene solution was deposited onto the substrate and left to partially dry for 30 seconds. Suitable crystals were selected and carefully placed in the centre of the polymer solution which was then

left to dry fully for 15 minutes. The samples showed no signed of degradation on contact with the polymer/toluene solution, which was chosen due to its optical transparency in the region of interest for the perovskites investigated.

3.4.1 UV-Visible Absorption

Ultraviolet-Visible spectroscopy (UV-Vis) is a standard technique used to investigate the electronic structure of a material by analysis of its absorption spectra across the UV and/or visible regions of the electromagnetic spectrum. Only one wavelength of a white light source is passed through the instrument at any one time, the absorption or reflectance of the sample is then measured compared to a reference.

The absorbance (A) of a sample is typically measured in transmission configuration, where the transmission ($T(\lambda)$) is measured as a fraction of transmitted intensity through the sample ($I(\lambda)$) to original intensity ($I_0(\lambda)$). A is related to $T(\lambda)$ through:[137]

$$A(\lambda) = \log_{10}(T(\lambda)) = \log_{10}\left(\frac{I(\lambda)}{I_0(\lambda)}\right). \tag{3.12}$$

Transmission measurements are common in the analysis of thin films; however, solid-state materials often present a problem when measuring A due to the short penetration depth of UV and visible light. Measurement in transmission configuration is not possible for most solid-state samples, such as the perovskite powders and crystals investigated in this work. Reflectance provides an alternative to transmission measurements, where reflected, as opposed to transmitted, light is collected. Specular reflectance (light scattered at the same angle as the incident light) and diffuse reflectance (light scattered across all angles) are collected using a highly reflective integrating sphere and measured as the reflectivity (R). The Kubelka-Munk function ($F(R)$) can then be used to transform R into a form that more resembles absorbance through:[75]

$$F(R) = \frac{(1-R)^2}{2R}. \tag{3.13}$$

In this thesis UV-Vis spectroscopy is utilised to investigate the band gap positions of materials. Electrons are promoted from the VB to the CB when the energy of the excitation source is greater than the material band gap (E_g). Therefore, in a plot of λ against absorbance (A) or reflectivity (R), a band gap would appear as a steep change in gradient known as an absorption edge. The position of the band gap can

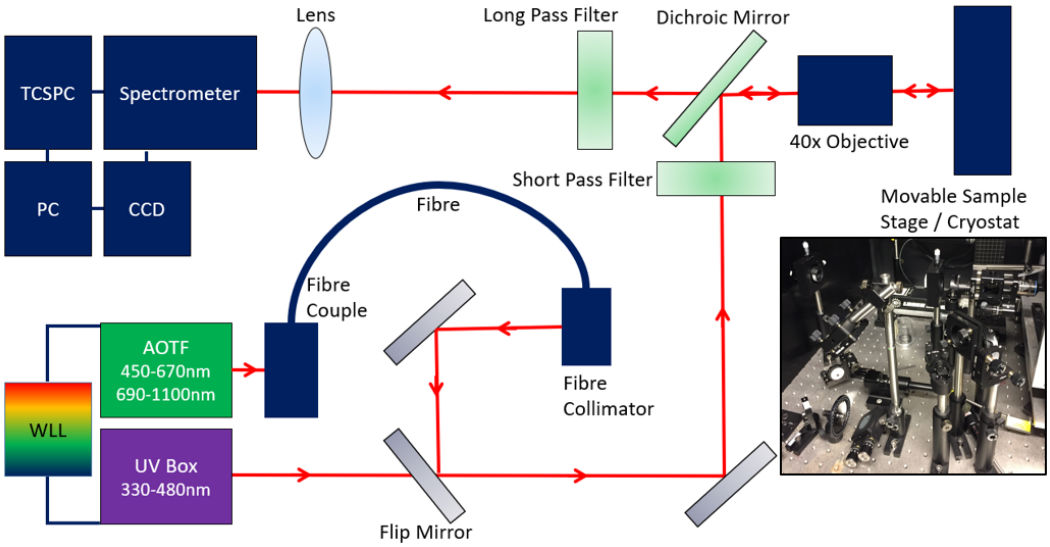

Figure 3-8: Schematic of the layout used for steady state PL and TCSPC measurements at the LMU, and (inset) a photo of the same system.

be determined through extrapolating from the absorption edge to the x-axis intercept, known as a Tauc plot.[75,137] The energy of the band gap (E_g) can then be inferred through the relationship $E_g = hc/\lambda$.

Summary of Measurements

UV-Vis spectra were measured using a Perkin Elmer Lambda 750s spectrophotometer fitted with a 60 mm integrating sphere. The spectrophotometer operated as a double beam, double monochromator system with holographic grating monochromators. A deuterium tungsten bulb, with a range from 190-3300 nm, provided the white light source.

Perovskite crystals were mounted onto clean glass substrates using the polymer glue zeonex. Reference spectra of glass and zeonex were subtracted from the final measurements. Powder samples were mounted using a PTFE sample holder with a fused silica window.

Samples of $Cs_{0.1}FA_{0.9}PbI_3$ and $Cs_{0.1}MA_{0.9}PbI_3$ were measured and the results presented in Chapters 4 and 5.

3.4.2 Steady State and Transient Photoluminescence

As introduced in Chapter 2 Section 2.4, photoluminescence (PL) is caused by the excitation of an electron from the ground state to an excited state through the absorption of a photon, the electron then relaxes to a lower level via a radiative transition. Steady state PL data presented in this thesis were recorded at the Chair for Photonics and Optoelectronics at the Ludwig-Maximillians University of Munich (LMU). The excitation signal was provided by white light and UV pulsed laser sources. Filters were connected to the pulsed sources, enabling the excitation wavelength to be tuned over the near-infrared, visible and UV. PL spectra were collected using CCD detectors.

As the excitation wavelength of the pulsed laser source was varied, suitable optical filters were selected to prevent unwanted wavelengths reaching the sample or detector, in the layout shown schematically in Figure 3-8. Edge pass filters could be used to isolate the desired regions of the spectrum. Short pass filters were used to transmit shorter wavelengths but prevent any additional longer wavelengths from hitting the sample. Long pass filters, which transmit longer wavelengths but block shorter wavelengths, were then used to ensure PL signal was collected without allowing any reflected laser light through. Suitable dichroic mirrors, which exhibit different reflection and transmission properties depending on wavelength, were also used to prevent stray laser light reaching the detector.

As suggested in Figure 3-8, the detector type at the LMU could be switched to allow transient PL measurements via *time-correlated single photon counting (TCSPC)*. This technique uses a short pulse to excite the sample, then measures the number of emitted photons as a function of time. In TCSPC the PL decay is visualised as a histogram, displaying the number of photons arriving at the detector within a particular time interval after excitation, shown schematically in Figure 3-9. TCSPC enables the measurement of fluorescence lifetimes, and the shape of decay can be modelled to deduce charge carrier behaviour.[138]

All PL spectra were collected as a function of wavelength, but are presented as a function of energy, therefore, the recorded intensity (I) is proportional to the number of photons (N) collected in a wavelength interval ($d\lambda$). However, the equivalent intervals in energy (dE) vary in size, implying a correction factor for intensity is needed when converting spectra from a function of wavelength to a function of energy.[139] This correction is applied according to the equation below where the minus sign can be ignored.

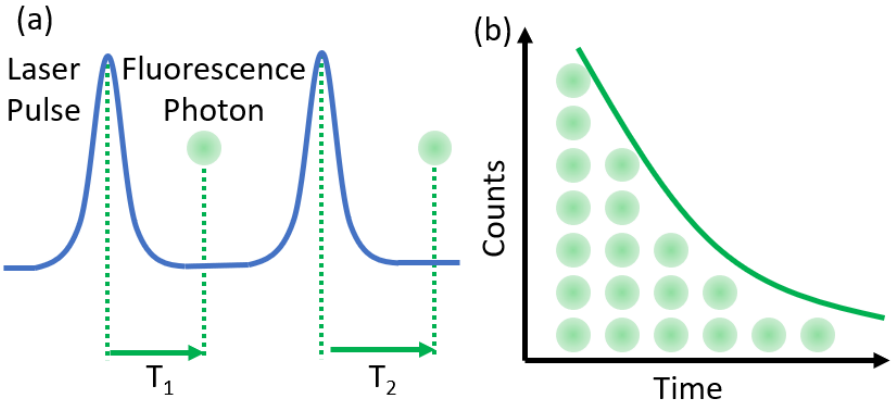

Figure 3-9: (a) Schematic of the principle behind TCSPC, measuring the time between the excitation laser pulses and detection of fluorescence photons. (b) Histogram recording the number of photons recorded at particular times after the laser pulse.

$$I(E) = I(\lambda)\frac{d\lambda}{dE} = I(\lambda)\frac{d}{dE}(\frac{hc}{E}) = -I(\lambda)\frac{hc}{E^2} \tag{3.14}$$

Optimising PL Signal

The 1 μm^2 laser spot was aligned and focused onto perovskite samples using a repetition rate of 77.9 MHz. A suitable integration time and entrance slit size were selected to prevent saturation, while allowing for increased intensity at lower temperatures for variable temperature measurements. As the temperature of the sample was decreased, the position of the sample and the cryostat window would move very slightly. This movement affected the alignment of the white light laser (WLL), therefore the position and intensity of the PL signal was checked and (if necessary) adjusted every 50 K. To improve reproducibility a background spectrum was taken, and to reduce noise PL spectra were averaged over 10 measurements with an exposure time of 1 second each.

Summary of Measurements

Steady state and transient PL measurements were conducted on mixed cation lead halide perovskites within the Chair for Photonics and Optoelectronics at the Ludwig-Maximillians Unviversity of Munich (LMU). An NKT Photonics, SuperK Extreme, EXR-20 white light laser (WLL) together with a SuperK Select acousto-optic tunable filter (AOTF) and SuperK Extend-UV were used to provide and tune the excitation signal and an Olympus SLCPLFL 40x/0.55 long distance objective and CCD were used to collect the PL signal. Additional long pass, short pass and dichroic filters were used to block any remaining laser light, ensuring only the PL signal was recorded.

The detector was calibrated using a xenon lamp. Spectra measured at the LMU and presented for this work were obtained using a repetition rate of 1.22 MHz .

Crystals of $Cs_{0.1}FA_{0.9}PbI_3$ and $Cs_{0.1}MA_{0.9}PbI_3$ grown via inverse solubility were mounted onto silica substrates using the polymer zeonex and fixed in a CryoVac cryostat using Apezion grease before the cryostat pressure was lowered to 10^{-6} mbar using a Turbo-Drag pump. The temperature was varied from 290 K to 10 K via a vacuubrand type ME 4 NT pump circulating liquid helium and nitrogen through a reservoir, cooling the cryostat. Spectra obtained from the FA and MA containing perovskites are presented in Chapters 4 and 5 respectively.

Samples of $FA_xMA_{1-x}PbI_3$ ($x = 0$, 0.6) and $MAPbBr_3$ were also mounted onto silica substrates using the polymer zeonex and measured at room temperature without use of a cryostat; the resulting spectra are discussed in Chapter 7.

Chapter 4

Cesium Formamidinium Lead Halide Perovskites

4.1 Introduction

The majority of work on perovskite photovoltaics has focused methylammonium lead tri-iodide ($CH_3NH_3PbI_3$ or $MAPbI_3$), the material used in the first perovskite device.[12] However, replacing the MA cation with the larger formamidinium ($CH(NH_2)_2^+$ or FA) cation has a number of benefits; including increased thermal stability[140] and a lower bandgap of 1.48 eV, enabling absorption into the infra-red.[141] To appreciate the complex effects of site substitution on this family of perovskites, the behaviour of phase pure $FAPbI_3$ must first be considered in detail.

In 2014, Stoumpos *et al.* investigated the phase behaviour of $FAPbI_3$ using X-ray diffraction, identifying a high temperature α-phase, which can be cooled to form lower symmetry β and γ-phases.[18] However, there has been confusion surrounding the exact form of these phases, with the original study incorrectly assigning the α-phase to the trigonal P3m1 space group and subsequent investigations disagreeing on the behaviour - or even existence - of the low temperature phases.[18,42,93,120]

The structure of α-$FAPbI_3$ is now commonly accepted to be cubic, occupying the typical perovskite P$m\bar{3}m$ space group with lattice parameter $a = 6.3620(8)$ Å. High resolution neutron diffraction data was complemented by *ab initio* calculations performed by Weller *et al.*, suggesting the trigonal FA cations are rotationally active in the α-phase. The presence of weak hydrogen bonds (H-bonds) between the NH_2 groups and I anions of the octahedra was also shown.[87]

Over two years from 2016, the variable temperature behaviour of $FAPbI_3$ was investigated by multiple groups, each with conflicting descriptions depending on the thermal history of the samples used, as described in the points below.

- Fabini *et al.* employed high resolution X-ray diffraction to determine a tetragonal P4/mbm β-phase below 285 K. The $FAPbI_3$ sample was heated *in situ* to form the α phase, before being cooled below 100 K. An additional transition at 140 K was recorded and assigned to a re-emergent tetragonal phase, with the FA cation modelled as a single pseudoatom.[42]

- Chen *et al.* combined neutron and X-ray diffraction studies to investigate hydrogenous and deuterated $FAPbI_3$, heating a quenched sample from 77 K to 300 K. This study determined a tetragonal γ-phase to transition to a tetragonal β-phase (P4/mbm) at 140 K. The low temperature γ-phase was investigated at 100 K and modelled to a 1 x 1 x 6 supercell expansion of the tetragonal β-phase,

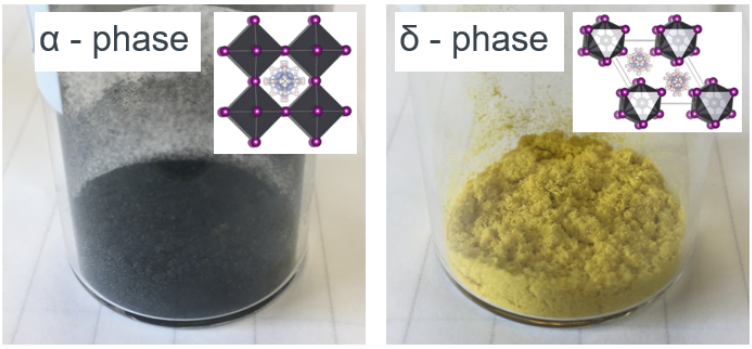

Figure 4-1: Photos of powder $FAPbI_3$ samples, taken in the black α and yellow δ-phases, with (inset) the relevant crystal structures visualised in the program VESTA as reported in Weber *et al.*[74]

lattice parameters $a = 8.8774(1)$ Å and $c = 37.6724(14)$ Å.[93]

- Weber *et al.* did not observe any additional Bragg reflections due to an extended supercell in NPD measurements on deuterated $FAPbI_3$, but instead attributed the < 140 K phase to be caused by a locally disordered γ-phase.[74]

Some of the confusion surrounding the low temperature phase of $FAPbI_3$ can be attributed to the complex behaviour of the FA cation. In a separate study, Fabini *et al.* investigated the dynamics of FA through solid state NMR, concluding that the H-bonds formed between the NH_2 groups and I anions play a crucial role in determining material structure.[142] NMR measurements revealed the rotational motion of the cation to reduce significantly below 100 K, limiting the kinetic energy available for the FA cation to re-orientate, so preventing the preferred octahedral tilting pattern, resulting in a frustrated inorganic framework.[142]

Variable temperature diffraction studies on $FAPbI_3$ agree on the formation of the α-phase above 285 K; however, this is only observed in quench cooled samples or materials stored in an inert atmosphere.[42,74,120] Unfortunately, use of $FAPbI_3$ in PV devices introduces the additional problem of the non-perovskite δ-phase, introduced in Chapter 2 Section 2.5.3. δ-$FAPbI_3$ is the preferred polymorph at room temperature, crystallising in the hexagonal $P6_3mc$ space group with lattice parameters cell $a = 8.6603(14)$ Å and $c = 7.9022(6)$ Å.[18] Unlike α-$FAPbI_3$ which is defined by corner sharing lead iodide octahedra, δ-$FAPbI_3$ consists of face sharing PbI_6 octahedra linked in the [001] direction, with the FA cations occupying the space between PbI_6 chains. Similar to $FAPbI_3$, $CsPbI_3$ also exits as perovskite and non-perovskite polymorphs, forming the undesirable δ-phase at room temperature. Yellow δ-$CsPbI_3$ occupies the orthorhombic space

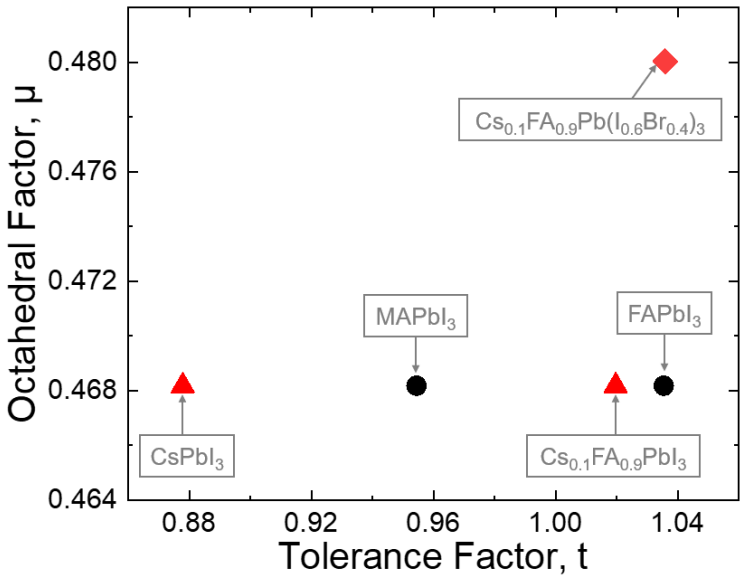

Figure 4-2: Goldschmidt tolerance (t) and octahedral (μ) factors for the FA containing perovskites discussed in this chapter.[79,81,82] All samples lie within the suggested acceptable tolerance range for a perovskite structure. Values for $MAPbI_3$ and $CsPbI_3$ are included for reference.

group Pnma, lattice parameters $a = 10.462(5)$ Å, $b = 4.799(5)$ Å and $c = 17.765(5)$ Å.[88] Conversion between the black α and yellow δ-phases in both compounds are fully reversible on heating above 300 K and 583 K for $FAPbI_3$ and $CsPbI_3$ respectively.[74,88] The materials can become kinetically trapped in the α-phase if quench cooled in a dry environment.[74,88] Examples of trapped α and preferred δ-phase $FAPbI_3$ powders, synthesised as part of this work, are shown Figure 4-1 alongside the relevant crystal structures.

Incorporating small amounts of Cs at the FA site of the $FAPbI_3$ structure can inhibit the formation of the hexagonal δ-$FAPbI_3$ phase. This development has lead to significantly improved device PV lifetimes, as well as enhanced thermal and moisture stabilities of mixed Cs-FA cation thin films when compared to pure $FAPbI_3$.[104] Yi *et al.* attributed the enhanced stability provided by the Cs cation to the improved crystallization of the α-phase, as cation mixing in the α-phase is more energetically favorable than that in the δ-phase for both $CsPbI_3$ and $FAPbI_3$.[113]

The degree of Cs substitution permitted, while maintaining the perovskite structure, is indicated by the Goldschmidt tolerance (t) and octahedral (μ) factors (introduced in Chapter 2 Section 2.5.3). The calculated values of t and μ for materials discussed

in this chapter are shown in Figure 4-2, all of which fall within the accepted region capable of forming the typical perovskite structure of corner sharing octahedra.[79,80,143]

However, there is confusion concerning the structures of the mixed Cs-FA lead iodide perovskites, with contradictory information on whether the composition $Cs_{0.1}FA_{0.9}PbI_3$ adopts a tetragonal or cubic structure at room temperature. Li *et al.* concluded Cs doping to stabilise the cubic α-phase of $FAPbI_3$,[77] while Prathapani *et al.* subsequently identified $Cs_{0.17}FA_{0.83}PbI_3$ as cubic, occupying the $Pm\bar{3}m$ space group with lattice parameter $a = 6.313\,\text{Å}$.[144] However, Prasanna *et al.* indexed $Cs_{0.15}FA_{0.85}PbI_3$ to the tetragonal space group $P4/mbm$, due to the presence of additional superlattice peaks in synchrotron XRD patterns which were attributed to a tetragonal distortion of the PbI_6 framework.[145] This tetragonal distortion was supported by *ab initio* studies performed by Ghosh *et al.*, who suggested substitution of FA with smaller Cs cations causes anisotropic contraction of the unit cell, lowering the crystal symmetry.[146]

The confusion surrounding the room temperature structure of Cs-FA perovskites motivated the PXRD, SXRD and NPD work presented in this thesis, which also aimed to address the poorly understood complex phase behavior of the mixed Cs/FA/I/Br perovskites.[144–147] At the time of this work, the Cs-FA perovskites had not been investigated using neutron diffraction, which evades some of the common limitations of XRD. Unlike XRD - in which the central organic cation is often modelled as a pseudoatom[142] - NPD allows determination of light atom positions, including distinguishing between carbon and nitrogen, and is also less affected by twinning commonly observed in these hybrid perovskites.[87]

The spectroscopic effects of Cs and Br incorporation into the $FAPbI_3$ structure have been widely studied in thin films.[104,141,144,145,148] Structural changes induced by site substitution of the smaller Cs cation and Br anion alter the overlap of outer Pb and halide orbitals, directly affecting the electronic properties of the material, enabling tuning of the bandgap.[70,95,143,145] For example, the bandgap of $FAPbI_yBr_{3-y}$ has been shown to decrease from 2.23 eV to 1.48 eV on increasing y, changing colour from orange to black.[141] The ability to tune bandgap is important in the development of tandem solar cells, in which separate single junction devices, capable of harvesting different energies of the solar spectrum, are stacked together. Champion PV material, $Cs_{0.17}FA_{0.83}Pb(I_{0.83}Br_{0.17})_3$, with a bandgap of 1.63 eV, has been employed in perovskite-silicon tandem cells achieving efficiencies of 23.6%.[7] In 2016, McMeekin *et al.* demonstrated the potential of $Cs_{0.17}FA_{0.83}Pb(I_{0.6}Br_{0.4})_3$ to surpass 25% efficiency in tandem architectures, serving as the motivation for the Cs/FA/I/Br composition investigated in this work.[149] Tandem perovskite-silicon cells are currently being developed

for commercial applications, highlighting the importance of fully understanding the complex structural and optoelectronic properties of mixed cation-halide perovskites.[6]

The majority of studies on mixed cation-halide perovskites focus on compositional phase behaviour, investigating how properties change depending on the level of Cs or Br substitution, very few studies on the variable temperature phase behaviour of these materials exist. Another important point regarding previous studies for mixed Cs/FA/I/Br perovskites, is that measurements are almost exclusively performed on thin films; however, phase behaviour and optical absorption properties of thin films can vary significantly depending on the deposition method used.[26,141] It is crucial that the fundamental structural properties of these mixed Cs-FA cation materials is fully understood in order to appreciate PV device operation across different environments. These factors promoted the work discussed in this chapter, which examines the intrinsic phase behaviour of $Cs_{0.1}FA_{0.9}PbI_3$ and $Cs_{0.1}FA_{0.9}Pb(I_{0.6}Br_{0.4})_3$ perovskites with varying temperature.

4.2 Phase Behaviour of Mixed Cesium Formamidinium Lead Iodide Perovskites

4.2.1 Cesium Substitution Limit

Samples of $Cs_xFA_{1-x}PbI_3$ ($0 \leq x \leq 0.2$) were synthesised as single crystals through the inverse solubility method, and as powder through the precipitation technique.[66,118] The composition $Cs_{0.1}FA_{0.9}PbI_3$ could be successfully synthesised as black powder and single crystals. Cs incorporation into the material was supported by a measured contraction of the unit cell indexed in PXRD to 6.346 Å, compared with 6.362 Å measured for pure cubic $FAPbI_3$.[87] Further investigation on single crystals using EDX determined an average Cs weight percent of 2.42%, leading to the formation of the composition $Cs_{0.12}FA_{0.88}PbI_3$. These results suggest a substitution limit of 12% Cs into the $FAPbI_3$ structure when synthesised through the inverse solubility method. Figure 4-3 shows the EDX maps obtained on a $Cs_{0.1}FA_{0.9}PbI_3$ crystal, displaying the distribution of Cs (yellow), Pb (blue) and I (green) throughout the crystal.

A 12% Cs substitution limit is similar to that found in thin films of $Cs_xMA_{1-x}PbI_3$ and $Cs_xFA_{1-x}PbI_3$.[22,96,149] Using solid state NMR, Kubicki *et al.* determined a 15% limit of Cs incorporation into $FAPbI_3$ powder, observing the appearance of additional δ-$CsPbI_3$ peaks for $x \geq 0.2$. $Cs_{0.15}FA_{0.85}PbI_3$ samples grown via inverse solubility for this work showed some additional peaks in PXRD data attributed to very small amounts of δ-$CsPbI_3$; however, $Cs_{0.2}FA_{0.8}PbI_3$ crystals clearly separated into black α and yellow δ-phases (Figure 4-4). PV performance has been shown to reduce in $Cs_xMA_{1-x}PbI_3$ devices where $x > 0.15$,[77] a trait which can be explained by the Cs substitution limit observed in powder perovskites by Kubicki *et al.*[105] and for single crystals in this work.

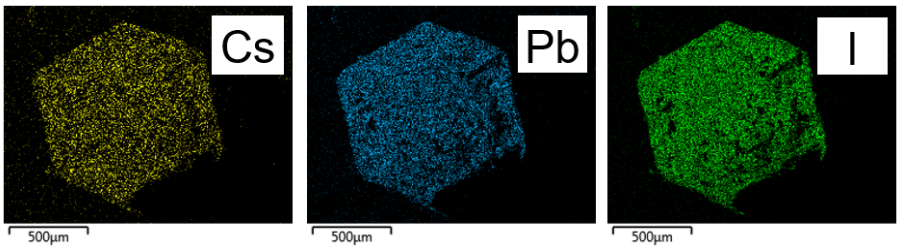

Figure 4-3: EDX maps of mixed Cs/FA lead iodide perovskite crystals grown via inverse solubility showing distribution of Cs (yellow), Pb (blue) and I (green).

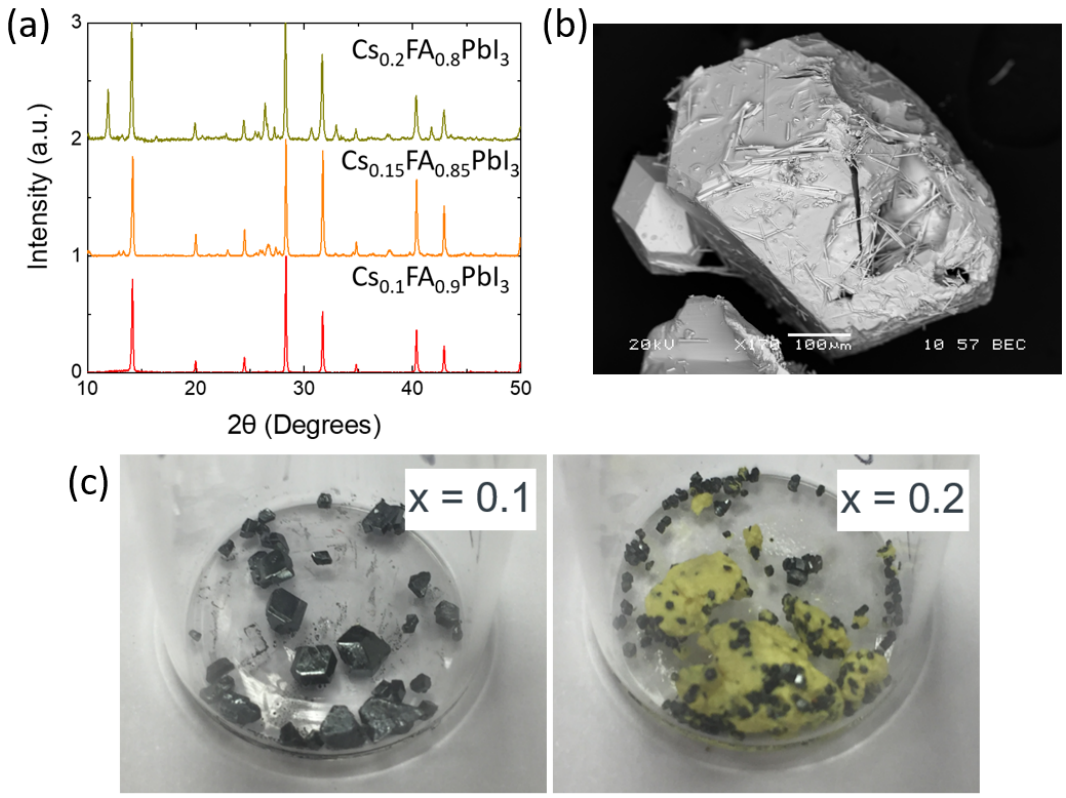

Figure 4-4: (a) PXRD patterns for samples of $Cs_xFA_{1-x}PbI_3$ ($x = 0.1$, 0.15, 0.2), additional peaks in the $x = 0.15$ and 0.2 patterns could be assigned to the non-perovskite δ-phases of $FAPbI_3$ and $CsPbI_3$.(b) Backscattered SEM image of a $Cs_{0.2}FA_{0.8}PbI_3$ crystal grown via inverse solubility, δ-phase needles can be clearly seen. (c) Images of as-made $Cs_xFA_{1-x}PbI_3$ ($x = 0.1$, 0.2) synthesised via inverse solubility, yellow δ-phase appears when $x \geq 0.2$

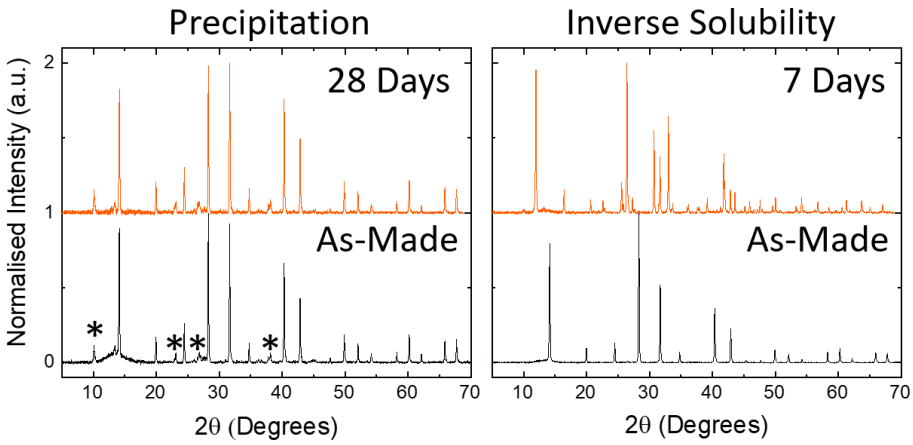

Figure 4-5: PXRD patterns of $Cs_{0.1}FA_{0.9}PbI_3$ samples synthesised by precipitation and inverse solubility. Crystals grown by inverse solubility and ground into powder would fully convert to the δ-$FAPbI_3$ and δ-$CsPbI_3$ phases after 7 days. Powder samples synthesised by precipitation would remain stable in air at 20% humidity over 28 days (* identifies δ-phase impurities in the as-made sample).

On the other hand, Prasanna *et al.* reported 25% Cs incorporation into thin films.[145] It is probable that the 12% Cs limit therefore refers to mixed Cs-FA lead iodide perovskites grown via the inverse solubility method, as crystallisation is highly dependent on the ability to form a supersaturated solution before 110°C, the temperature at which $FAPbI_3$ crystallises.[66]

Inclusion of Cs increases resistance to the formation of the undesirable non-perovskite δ-$FAPbI_3$ and δ-$CsPbI_3$ phases, as observed in previous studies.[81,109,150] However, over time, these perovskites still degrade into the δ-phases. Kubicki *et al.* found $Cs_xFA_{1-x}PbI_3$ powders synthesised mechanochemically to be thermodynamically unstable, releasing δ-$CsPbI_3$ over time.[105] In contrast to the results of Kubicki *et al.*, this work finds powders synthesised by the precipitation method to be stable in air at 20% humidity over 28 days. As seen in PXRD patterns presented in Figure 4-5, there was no increase in peak intensity associated with δ-$CsPbI_3$ impurities already present in the as-made sample. On the other hand, phase pure α-$Cs_{0.1}FA_{0.9}PbI_3$ crystals synthesised by inverse solubility, and ground into powder using a pestle and mortar, converted into the δ-phase over seven days (Figure 4-5). Conversely, $Cs_{0.1}FA_{0.9}PbI_3$ crystals remained in the black α-phase over one month. It is possible Cs loss is favoured in the smaller crystallites produced by grinding crystals grown by inverse solubility,[105] whereas the high temperature process used in the precipitation method is capable of trapping Cs in the structure.

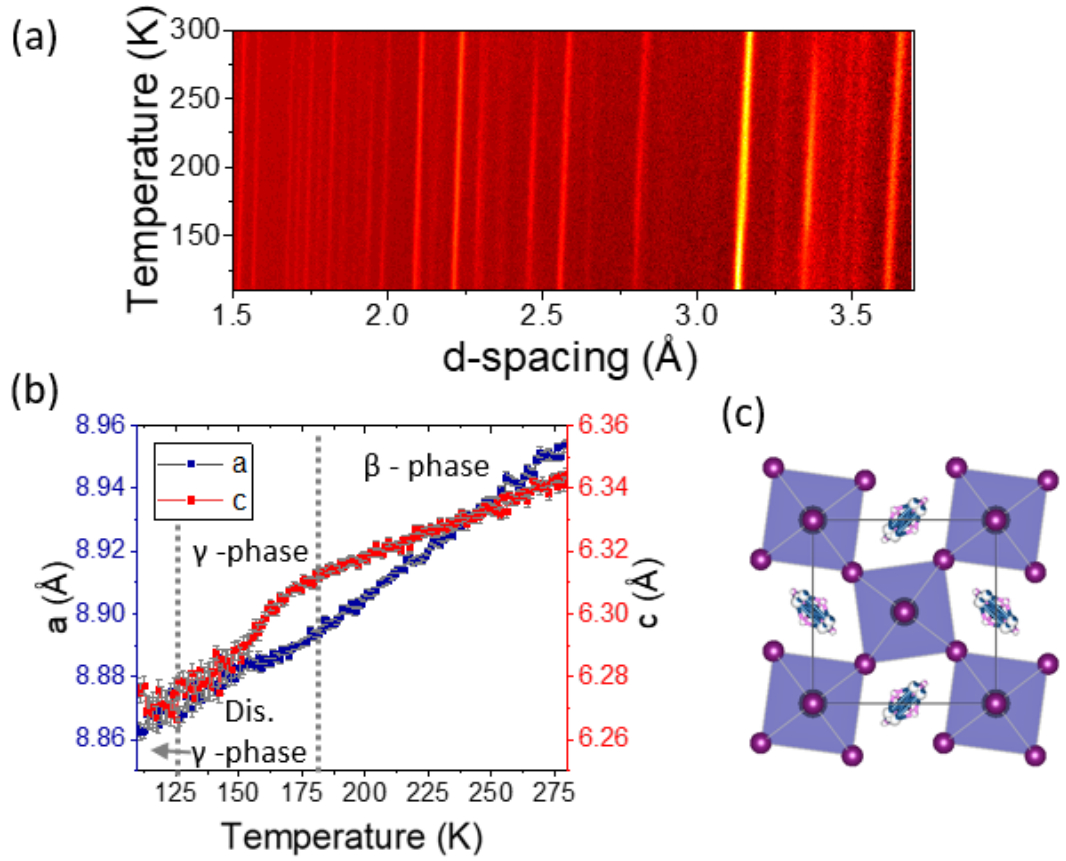

Figure 4-6: (a) Contour plot of neutron powder diffractograms on a $Cs_{0.1}FA_{0.9}PbI_3$-D sample stacked by temperature recorded on POLARIS at ISIS neutron and muon source. (b) Sequential refinement of pseudo-tetragonal cell from 280 K to 110 K with transition temperatures marked by grey lines. (c) Tetragonal model of the β-phase used in the sequential refinement. The model failed to fit data above 280 K coinciding with the gradual second order change to the α-phase.

4.2.2 Variable Temperature Neutron Powder Diffraction

The phase behavior of $Cs_{0.1}FA_{0.9}PbI_3$-D was tracked using variable temperature NPD on the POLARIS instrument at ISIS neutron and muon source. A powder sample of $Cs_{0.1}FA_{0.9}PbI_3$-D was cooled to 100 K and subsequently heated *in situ* at a rate of 0.2 $Kmin^{-1}$ with data collected continuously and binned into 1 K ranges between 100 K and 300 K. Data from the 90° detector bank (Bank 4) were used due to the range in *d*-spacing, resolution and count-rate matching the requirements of the experiment. Patterns with *d*-spacing ranging between 1.5 Å - 3.69 Å are displayed as stacked plots in Figure 4-6 (a).

A continuous shift in peak positions can be seen in Figure 4-6 (a), representing decreasing unit cell volume with decreasing temperature. Figure 4-6 (a) also shows the emergence of additional peaks from 290 K to 180 K indicating decreasing symmetry. The appearance of additional peaks represent the emergence of the tetragonal β-phase. Formation of a tetragonal phase with distinct a and c lattice parameters occurs below 290 K. The intensity of the emergent peaks decreases below 180 K, corresponding to the transformation to an orthorhombic γ-phase.

Trends in the shift and intensity of peaks were investigated using sequential refinement in GSAS II.[130] A pseudo-cubic model was first used from the refinement of NPD data at 300 K; however, it became apparent that a tetragonal model would better describe the structural behaviour over the temperature range investigated. The β-phase tetragonal model, based on that developed by Weber *et al.* for $FAPbI_3$,[74] and obtained from a long collection at 200 K was used. The tetragonal space group P4/*mbm* was used, and the part deuterated FA cation was modelled as a rigid CH-NHD molecule. This model was refined against shorter NPD collections at higher temperatures, but failed to provide a suitable fit above 280 K, corresponding with the slow second order transition to the cubic α-phase. The model was subsequently refined again against the 280 K NPD pattern, which was used as a starting point to the sequential refinement, resulting in the trend in lattice parameters shown in Figure 4-6 (b).

The evolution (positions and halfwidth) of the dominant peak centered at 3.15 Å (Figure 4-7 (a)) was also analysed using sequential peak fitting in GSAS II. The shift in peak position and FWHM correspond to the phase transition points suggested by the earlier sequential refinement of a pseudo-tetragonal structure. Changes in gradient of the peak shift (Figure 4-7(b)) are observed at 290 K, 180 K and 125 K corresponding with the cubic/tetragonal/orthorhombic and low temperature phases respectively. Peak broadening can be used as an indicator for peak splitting corresponding to changing symmetry. Extracted values of the dominant peak FWHM as a function of temperature (Figure 4-7 (c)) indicate clear broadening below 290 K which can be assigned to the formation of distinct peaks indicative to the tetragonal structure. An abrupt change in FWHM shift is observed at 180 K, attributed to a further structural transition from the tetragonal β-phase to an orthorhombic γ-phase.

4.2.3 Cubic Phase

The structure of $Cs_{0.1}FA_{0.9}PbI_3$ above 290 K was investigated via PXRD, SXRD and NPD.

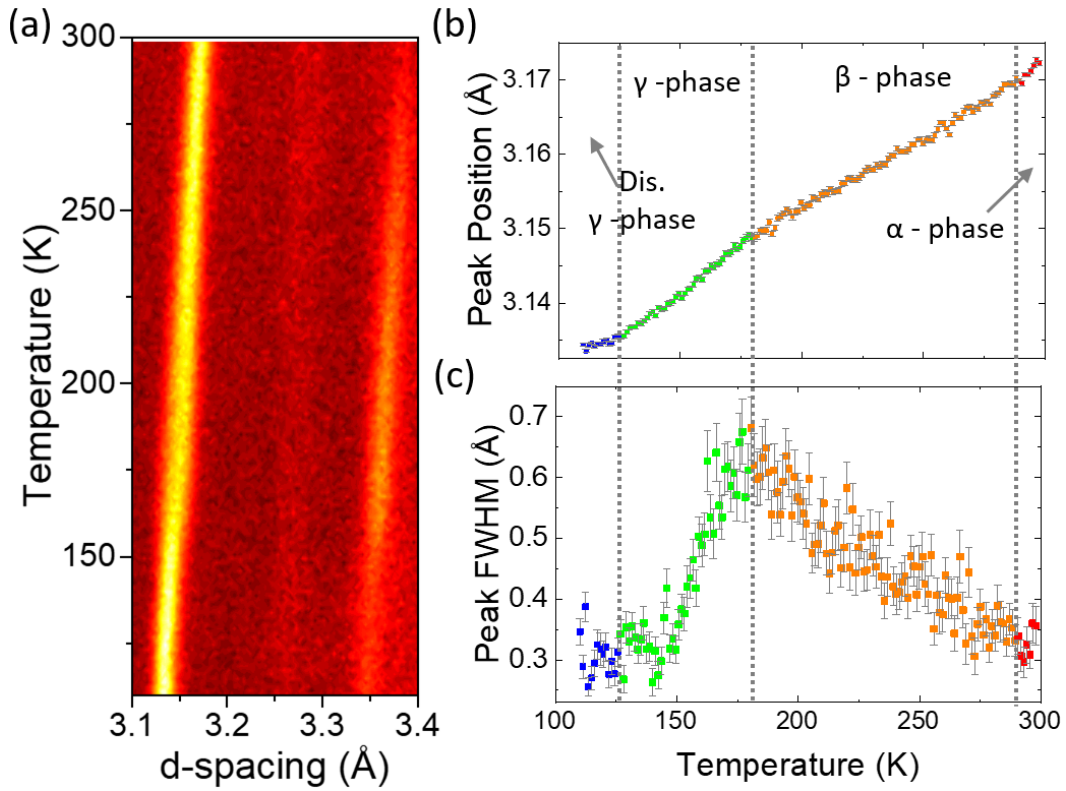

Figure 4-7: (a) Contour plot of neutron powder diffractograms on a $Cs_{0.1}FA_{0.9}PbI_3$-D sample stacked by temperature recorded on POLARIS in the range of 3.1 Å - 3.4 Å. (b) Resulting peak position of sequential peak fit on the dominant peak centered at 3.15 Å. (c) FWHM as a function of temperature of the dominant peak. (a) and (c) are divided into the cubic (red), tetragonal (orange), orthorhombic (green) and low temperature (blue) phases.

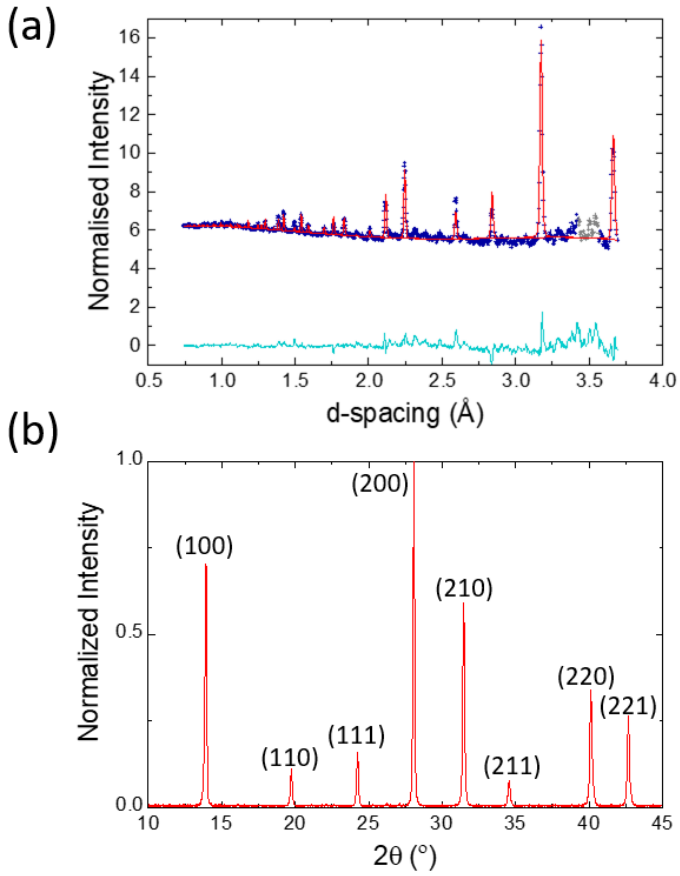

Figure 4-8: (a) Rietveld fit on NPD data collected on POLARIS at 300 K refined to space group P$m\bar{3}m$ with lattice parameter $a = 6.345\,62(24)$ Å, $wR = 1.69\%$. The difference between the observed and calculated values is shown in light blue and regions marked in grey could be assigned to δ-phase impurities. (b) PXRD data indexed to a cubic cell in P$m\bar{3}m$.

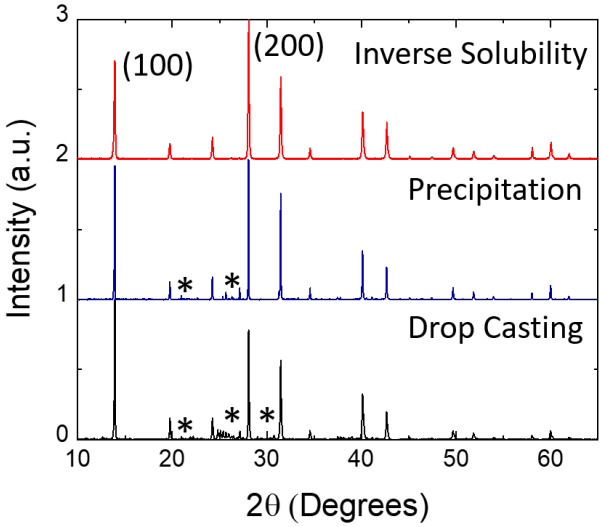

Figure 4-9: PXRD patterns of $Cs_{0.1}FA_{0.9}PbI_3$-H samples synthesized via inverse solubility (red), precipitation (blue) and $Cs_{0.1}FA_{0.9}PbI_3$-D synthesized by drop casting (black). The samples synthesized by the inverse solubility method were identified as phase pure, whereas small quantities of δ-$CsPbI_3$ and δ-$FAPbI_3$ impurities (*) were identified in the other powders.

Fully hydrogenated, phase pure $Cs_{0.1}FA_{0.9}PbI_3$ samples synthesized by the inverse solubility method, and ground using a pestle and mortar, were investigated using PXRD. PXRD patterns indexed best to the cubic $Pm\bar{3}m$ space group and revealed a shift in the (100) peak in comparison to α-$FAPbI_3$ due to an expected contraction of the lattice on Cs incorporation.[147] Figure 4-8 (b) shows the indexed PXRD pattern obtained at 298 K from a STOE STADI P diffractometer. PXRD was also used to check the quality of the part deuterated samples synthesised by the drop casting method for NPD measurements. Impurity peaks were identified and indexed to small quantities ($< 2\%$) of δ-$CsPbI_3$ and δ-$FAPbI_3$ (Figure 4-9).

NPD data obtained from a 2-hour collection at 300 K on POLARIS was fully analyzed using the GSAS II software. Lattice parameters from the indexed PXRD data were used as a starting point for further refinement. Initially the structural description of $FAPbI_3$ at 298 K was used as a model,[87] atomic positions were used as published and only lattice and instrumental parameters were varied at first. The planar part-deuterated FA cation was modelled to a rigid H-C-N-HD molecule, with initial isotropic ADPs of 0.05 $Å^2$ set. As performed by Weller *et al.* for $FAPbI_3$, the C-H atoms were assigned a site occupancy of 0.16, while the single N-HD group was modelled with an occupancy of 0.0833, together describing the 12 orientations of the planar FA cation

300K						
Atom	x	y	z	Occupancy	U_{iso}	Symmetry
Pb1	0	0	0	1.000	0.0255(13)	m3m
I1	0.5	0	0	1.000	0.0806(21)	4/mmm(x)
C1	0.5	0.50(12)	0.5	0.167	0.244(6)	4mm(y)
N1	0.70(11)	0.558(23)	0.5	0.083	= C1 U_{iso}	m(z)
H1	0.5	0.7(4)	0.5	0.167	= C1 U_{iso}	4mm(y)
H2	0.75(5)	0.65(7)	0.5	0.083	= C1 U_{iso}	m(z)
D1	0.7(4)	0.3(4)	0.5	0.083	= C1 U_{iso}	m(z)

Table 4.1: Structural information for partially deuterated α-$Cs_{0.1}FA_{0.9}PbI_3$-D from POLARIS data at 300 K, space group $Pm\bar{3}m$, lattice parameter $a = 6.345\,62(24)$ Å, $wR = 1.68\%$. The central cation was modelled as a CH – NHD rigid molecule.

within the cuboctahedral void.[87] This initial refinement produced a good fit of the data, with a wR of 1.92%. Subsequent refinement of the Pb and I ADPs produced a slightly improved fit, with $wR = 1.89\%$. The ADPs of the C, N, H and D making up the rigid FA cation were constrained to be equal, and when refined the wR improved to 1.72% producing a value of $0.244(6)$ Å^2. The high thermal parameter values indicate significant rotational motion of the FA cation at 300 K. The position of the whole cation was then refined, producing the cubic structural model detailed in Table 4.1, with $wR = 1.69\%$. The Rietveld fit (shown in Figure 4-8 (a)) converged to a lattice parameter of $6.345\,62(24)$ Å in the space group $Pm\bar{3}m$.

Despite some earlier studies suggesting $Cs_{0.1}FA_{0.9}PbI_3$ to adopt a tetragonal structure in ambient conditions,[145] we do not observe peak splitting in the PXRD and high resolution NPD indicative to a tetragonal symmetry. However, the cubic to tetragonal transition is very close to room temperature, with data from differential scanning calorimetry (DSC) measurements further supporting this. Samples synthesised via inverse solubility and precipitation were cycled from 293 K - 225 K - 420 K four times at 2 Kmin^{-1}. A small transition of 0.01 Wg^{-1} was observed centered at 290 K cycling down and 285 K cycling up in temperature corresponding to the phase transition from cubic to tetragonal. A 5 K difference in transition temperature between the down and up temperature cycles demonstrates the presence of a small amount of thermal hysteresis. Figure 4-10 shows a typical DSC trace for a sample of $Cs_{0.1}FA_{0.9}PbI_3$ between 225 K and 310 K.

Single crystals of $Cs_{0.1}FA_{0.9}PbI_3$ grown via inverse solubility also were selected to obtain a structural model at 300 K using SXRD data. Two methods were used; firstly, the established structure for α-$FAPbI_3$ was used as a model, accounting for the low

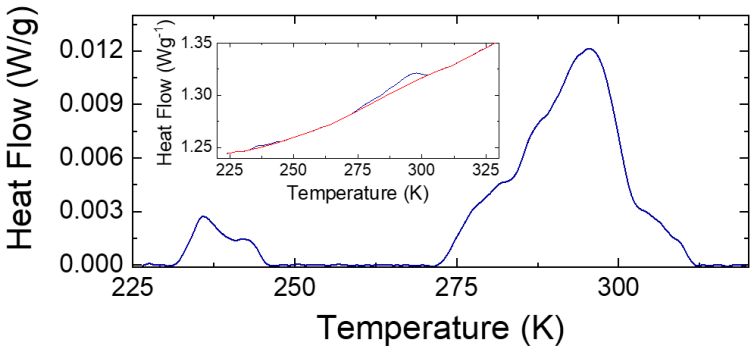

Figure 4-10: Baselined DSC measurement for $Cs_{0.1}FA_{0.9}PbI_3$ samples synthesised via inverse solubility, cycled once between 293 K – 225 K – 420 K at 2 Kmin^{-1}. A very small change in heat flow is centered at 290 K corresponding with the cubic-tetragonal phase transition. (Inset) original data (blue) and baseline (red), the slope is an artifact of the instrument.

scattering and tumbling of the FA cation by modelling the A—site as a single atom with a large ADPs. Secondly, the structure was solved in the low symmetry space group $P\bar{1}$ before the validation software PLATON[127] was used to determine a more suitable space group. In both cases the best solution fit to $Pm\bar{3}m$ with lattice parameter $a = 6.2780(3)$ Å.

Large anisotropic ADPs associated with iodide anions in the SXRD refinement suggest a soft PbI_6 framework. An attempt was made to model the observed spread of electron density to locked octahedral tilts as predicted from *ab initio* methods by Gosh *et al.*,[147] however, any ordered tilting of the PbI_6 octahedra could not be deduced. It was therefore resolved that the time averaged structure of $Cs_{0.1}FA_{0.9}PbI_3$ is cubic at 300 K, although the local structure may contain pseudo-tetragonal domains due to tilted octahedra switching rapidly between preferred orientations.

4.2.4 Tetragonal Phase

Variable temperature NPD was used to investigate the tetragonal β-phase that was found to exist between 290 K and 180 K; the transition to this phase is characterised by the appearance of the tetragonal unit cell (211) reflection as seen centered at $d = 3.37$ Å in Figure 4-11. Rietveld fits were performed on NPD data based on the model developed by Weber *et al.* for pure $FAPbI_3$,[74] with only the lattice and instrumental parameters allowed to vary in the initial refinement.

The part-deuterated FA cation was modelled as a rigid H-C-N-HD molecule with an

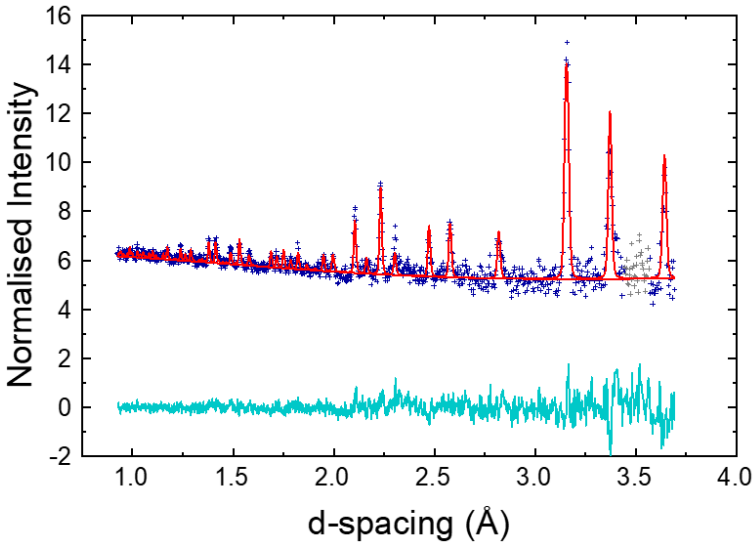

Figure 4-11: Rietveld fit on NPD data collected on POLARIS at 200 K refined to space group P4/*mbm*, $a = 8.9084(8)$ Å, $c = 6.3224(8)$ Å, $wR = 2.90\%$. Regions marked in grey could be assigned to δ-phase impurities.

occupancy of 0.5 for the C atom and 0.25 for the N, H and D, representing the restricted motion of the cation in the tetragonal phase.[74] ADPs for the Pb and I were then refined, producing lower values than those obtained in the cubic phase, suggesting reduced motion of the PbI_6 octahedra. The thermal parameters for C, N, H and D of the FA cation were constrained to be equal, refining to give 0.190(9) Å^2. The position of the rigid cation was then refined to give the tetragonal structural model shown in Table 4.2, in the space group P4/*mbm*, lattice parameters $a = 8.9084(8)$ Å, $c = 6.3224(8)$ Å, with $wR = 2.90\%$. The tetragonal model fits the data well from 180 K to 280 K, above this temperature refinements failed as the material gradually transitioned to the cubic α-phase.

4.2.5 Orthorhombic Phase

Unlike pure $FAPbI_3$, which exists as a tetragonal β-phase through to low temperature, an additional orthorhombic phase was observed in SXRD and NPD data for $Cs_{0.1}FA_{0.9}PbI_3$. SXRD data for a single crystal of $Cs_{0.1}FA_{0.9}PbI_3$ was modeled in the orthorhombic space group P*nma* at 150 K where lattice parameters extracted were $a = 8.8192(12)$ Å, $b = 12.5777(13)$ Å, $c = 8.6274(13)$ Å. However, SXRD data obtained at 175 K could be indexed to either P*nma* or the tetragonal space group P4/*mbm*, with reflections satisfying both solutions appearing due to proximity to a structural

200K						
Atom	x	y	z	Occupancy	U_{iso}	Site
Pb1	0	0	0	1.00	0.0057(22)	4/m(z)
I1	0	0	0.5	1.00	0.035(8)	4/m(z)
I2	0.7879(10)	0.28791	0	1.00	0.059(8)	mm2(xy)
C1	0.5	0	0.49(5)	0.5	0.190(9)	mm2
N1	0.57(17)	0.08(16)	0.42(3)	0.25	= C1 U_{iso}	1
H1	0.583(12)	0.91719	0.56(3)	0.25	= C1 U_{iso}	m(xy)
H2	0.54(7)	0.10(8)	0.45(13)	0.25	= C1 U_{iso}	1
D1	0.60(20)	0.11(19)	0.48(9)	0.25	= C1 U_{iso}	1

Table 4.2: Structural information for partially deuterated β-$Cs_{0.1}FA_{0.9}PbI_3$-D from POLARIS data at 200 K, space group P4/mbm, lattice parameters a = 8.9084(8) Å, c = 6.3224(8) Å, wR = 2.90%. The central cation was modelled as a CH – NHD rigid molecule.

transition. As has been observed for $FAPbI_3$, it seems that $Cs_{0.1}FA_{0.9}PbI_3$ forms crystallographic twins when cooled through phase transitions, leading to large residuals and challenges identifying the absolute structure.[74]

4.2.6 Low Temperature Phase

SXRD data collected at 120 K converged to the space group Pnma with lattice parameters a = 8.8215(11) Å, b = 12.5815(13) Å, c = 8.6091(13) Å. However, unlike the higher temperature data, additional weak reflections were observed at 120 K which could be attributed to the formation of a disordered state. The emergence of disorder at low temperature agrees with previous findings for $FAPbI_3$ in the literature, in which residual entropy causes the freezing of FA cation rotation and locking of PbI_6 octahedra is a glass-like state.[93]

4.2.7 Variable Temperature Photoluminescence

A single crystal of $Cs_{0.1}FA_{0.9}PbI_3$ synthesised via the inverse solubility method was mounted in a cryostat and illuminated with an excitation wavelength of 630 nm while the temperature was varied from 290 K to 25 K. Stacked variable temperature PL spectra are shown in Figure 4-12 (a), each spectrum was fitted with a single Gaussian function subsequently used to analyse the peak PL positions and FWHM (Figure 4-13(b,c)). It should be noted that spectra taken at 290 K and 275 K were fitted using a second Gaussian term to account for photon recycling effects in the 1 mm thick

crystal.[62] These secondary peaks, due to the absorption and subsequent re-emission of PL, were not included in the peak PL position and FWHM analysis.

Peak positions extracted from Gaussian fits of the PL were plotted as a function of temperature revealing a red shift with decreasing temperature familiar to these family of hybrid halide perovskites (Figure 4-12(b)).[58,151] This shift has been attributed to stabilisation of the valence band maximum due to a combination of thermal expansion effects and electron-phonon interactions.[70,151] Below 125 K a blue shift in peak position is observed. Interestingly the blue shift at low temperatures corresponds with the transition to the disordered state as revealed through XRD and NPD measurements presented in this work. A change in PL shift at low temperature has been previously linked to disorder in $MAPbX_3$ hybrid halide perovskites, attributed to band filling effects induced by a difference in bandgap between domains of ordered and disordered cation orientations.[151]

The temperature dependence of the PL FWHM ($\Gamma(T)$) can be expressed in terms of the below:[58]

$$\Gamma(T) = \Gamma_0 + \frac{\gamma_0}{exp(\frac{E_{LO}}{K_B T}) - 1} \tag{4.1}$$

where T is temperature, K_B is the Boltzmann constant, Γ_0 is the temperature independent homogeneous broadening term γ_{LO} is the charge carrier longitudinal-optical (LO) phonon coupling strength and E_{LO} is the energy for the LO phonon. The resulting FWHM of the Gaussian fits the to steady state PL could be modelled to Equation 4.1 (blue dashed line in Figure 4-12 (c)) from which the extracted values for Γ_0, γ_{LO} and E_{LO} were 29 ± 1 meV, 30 ± 4 meV and 13 ± 1 meV respectively. There is possible grouping of the FWHM data according to phase in Figure 4-12 (c); however, the discontinuities are small and proved difficult to model separately.

Transient luminescence spectra for $Cs_{0.1}FA_{0.9}PbI_3$ were measured at seven distinct temperatures between 290 K and 50 K inclusive. The resulting spectra were modelled according to the rate equation:[46]

$$-\frac{dn}{dt} = k_1 n + k_2 n^2 + k_3 n^3 \tag{4.2}$$

where n is the photogenerated carrier density and k_i is recombination rate. Each term represents a charge carrier annihilation process following excitation, (1) being monomolecular recombination, (2) bimolecular recombination and (3) three body Auger

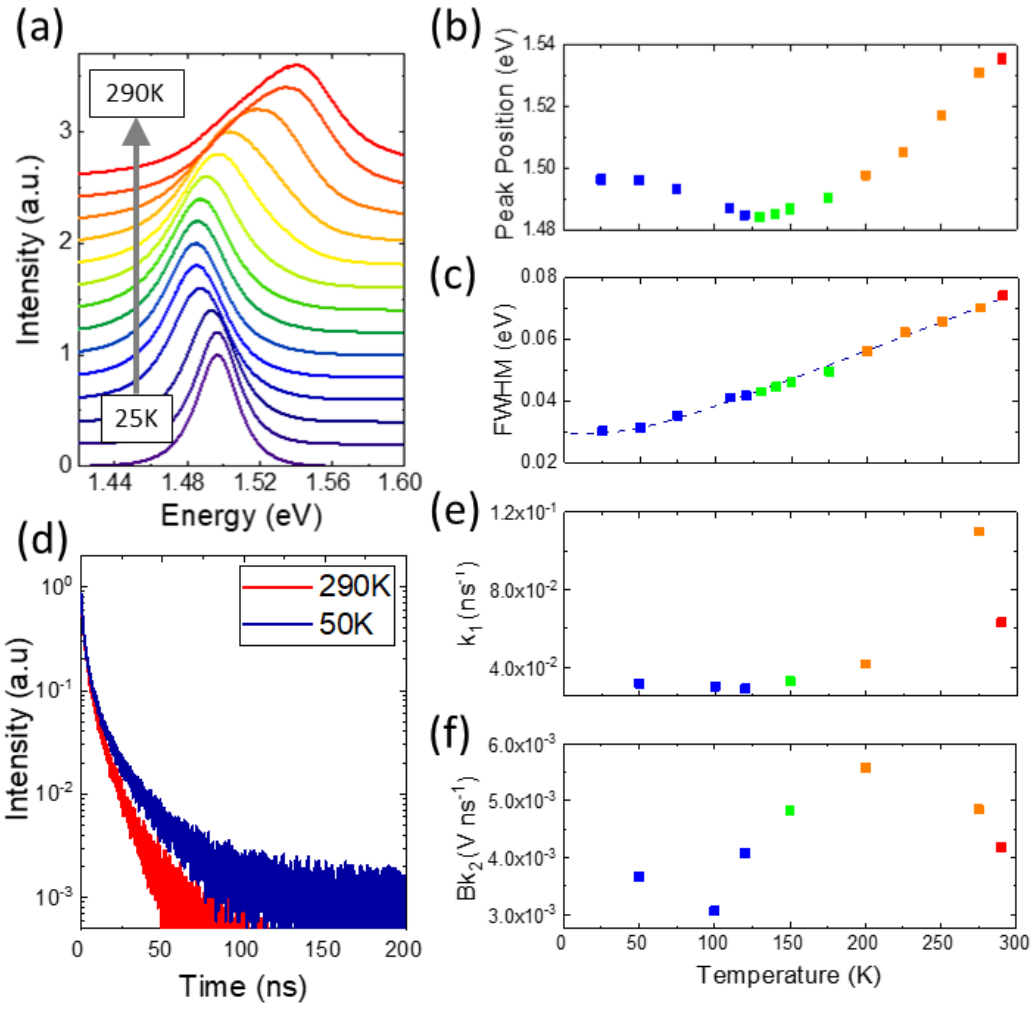

Figure 4-12: (a) Variable temperature steady state PL on a single crystal of $Cs_{0.1}FA_{0.9}PbI_3$. (b) Peak positions and (c) FWHM of the Gaussian fits of the PL as a function of temperature. (d) PL decay measured at 290 K and 50 K. (e) Extracted monomolecular recombination rate constants (k_1) and (f) effective bimolecular rate constant (Bk_2) from fits to variable temperature PL decay. Points are coloured according to the cubic α-phase (red), tetragonal β-phase (orange), orthorhombic γ-phase (green) and disordered low temperature phase (blue).

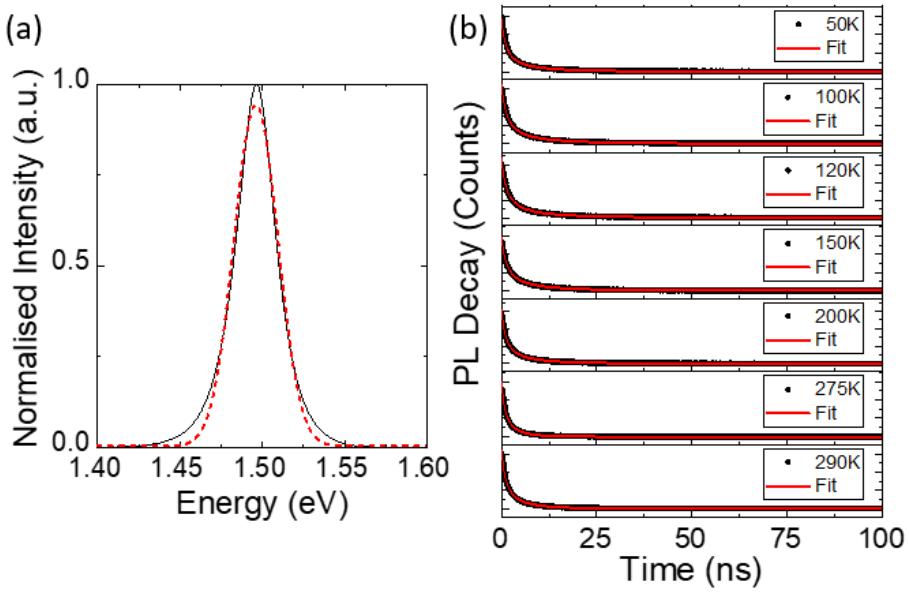

Figure 4-13: (a) Gaussian fit (red dashed line) of PL (black solid line) for a crystal of $Cs_{0.1}FA_{0.9}PbI_3$ taken at 50 K. (b) TRPL of $Cs_{0.1}FA_{0.9}PbI_3$ (black) taken between 275 K and 50 K fitted according to equation 4.2 (red)

recombination. Previous studies have shown first and second order recombination mechanisms to dominate in hybrid perovskites at moderate intensities, therefore Auger recombination was neglected.[46,68] The analytical solution of the differential equation is then given by:

$$n(t) = \frac{-k_1 e^{ck_1}}{k_2 e^{ck_1} - e^{k_1 t}} \tag{4.3}$$

where c is a constant.

The monomolecular term is predominately determined by first order Shockley-Reed (trap state mediated) recombination in hybrid halide perovskites, therefore the value of k_1 is dictated by trap-assisted recombination.[152] As displayed in Figure 4-12(e), in general, k_1 decreases with decreasing temperature; however, a significant increase is seen between 290 – 275 K. This was potentially due to domains of cubic and tetragonal phases appearing over the phase transition and acting as recombination sites. Below the 125 K transition into the disordered structure the monomolecular recombination rate increases, possibly due to disordered domains acting as recombination centers.[46]

Values of the bimolecular rate constant (k_2) could not be determined as the charge carrier density (n) was not directly measured. Assuming free carrier recombination,

the experimentally measured PL decay ($I(t)$) was taken to be proportional to $n(t)^2$ such that:

$$n(t)^2 \propto I(t). \tag{4.4}$$

Therefore only a value called Bk_2 can be extracted from the PL fitting, where B is a proportionality constant as described by Milot *et al.*[152] As B is unknown, only the value of k_1 can be directly determined. Effective bimolecular rate constants are determined as Bk_2 with units of V ns^{-1}, where V is volume. The values determined for Bk_2 (Figure 4-12 (f)) generally increase with decreasing temperature, until the transition to the low temperature disordered phase around 125 K. The reversal in trends observed for PL peak position, k_1 and Bk_2 below the 125 K transition clearly indicate the disordered nature of the FA cations and PbI_6 orientations at low temperature influence the electronic structure of the material.

4.2.8 Absorption

The percentage reflectance (R) was collected and transformed using the Kubelka-Munk model (Equation 3.13) to better represent the material absorption coefficient.[75] There is an obvious and unexpected blue shift between the measured $F(R)$ and PL for $Cs_{0.1}FA_{0.9}PbI_3$ in the combined plot shown in Figure 4-14 (a). The PL was obtained using the TCSPC set up of the Photonics and Optoeletronics group at the LMU, whereas the reflectance measurements were obtained at the University of Bath using a UV-Vis spectrometer equipped with an integrating sphere. Both instruments were correctly calibrated. Extrapolating from the edge of the $F(R)$ function (red line in Figure 4-14 (b)) provides an estimate of the material bandgap of 1.43 eV.

There is significant variation in the literature as to the position of the PL peak and absorption edge for Cs-FA lead iodide perovskites. For example, Nazarenko *et al.*[82] estimated a bang gap of 1.47 eV for $Cs_{0.1}FA_{0.9}PbI_3$, whereas Syzgantseva *et al.*[104] suggested the bandgap of Cs doped $FAPbI_3$ to take a value between 1.49 eV and 1.50 eV. Prasanna *et al.*[145] and Prathapani *et al.*[144] found bandgaps greater than 1.50 eV for Cs-FA thin films. There has been some suggestion that synthesis method can significantly affect the absorption properties measured for a material.[18] Further work is needed to probe the differences between the optical absorption properties of thin films and crystalline perovskite samples.

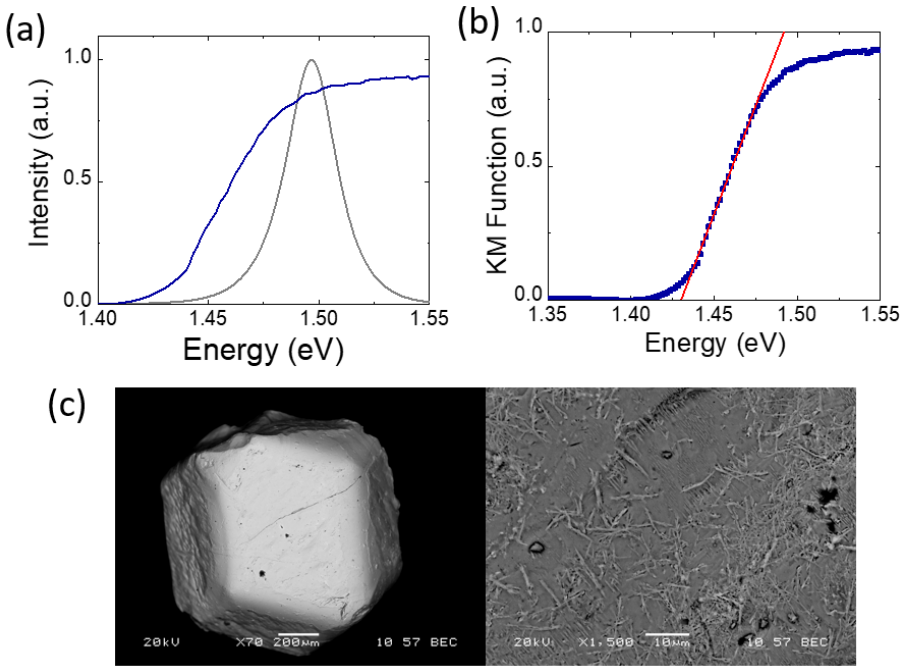

Figure 4-14: (a) PL and reflectance measurements for $Cs_{0.1}FA_{0.9}PbI_3$. The reflectance measurements have been transformed using the Kubelka-Munk (KM) function.(b) Extrapolation of the absorption edge, estimate material bandgap to 1.43 eV. (c) SEM images of the $Cs_{0.1}FA_{0.9}PbI_3$ sample used for the temperature dependent PL measurements, taken at magnifications of x 70 (left) and x 1500 (right). Needles attributed to the δ-$CsPbI_3$ and δ-$FAPbI_3$ phases can be seen.

Differences in synthesis technique cannot explain the large blue shift observed between the absorption onset and peak PL, taken of samples synthesised as part of the same batch process. SEM was used to investigate the surface properties of $Cs_{0.1}FA_{0.9}PbI_3$ crystals measured by variable temperature PL (Figure 4-14 (c)). The SEM images revealed needles attributed to δ-phases of $CsPbI_3$ and $FAPbI_3$ present on the crystal surface. From previous observations on $Cs_xFA_{1-x}PbI_3$ crystals investigated in this work, it was known that the materials phase separated over the course of a couple of weeks on exposure to atmosphere. Therefore, despite the bulk of the crystal remaining in the α-phase, the surface separated into a region rich in the higher bandgap δ-phases. Surface sensitive PL measurements would be directly affected by this, resulting in a blue shift of measured peak PL.

4.2.9 Discussion

The results of the investigation into the phase behaviour of $Cs_{0.1}FA_{0.9}PbI_3$ are summarised in Figure 4-15. Cs and FA cation mixing is more energetically favourable in the α-phase than δ-phase,[113] leading to the preferred formation of cubic α-$Cs_{0.1}FA_{0.9}PbI_3$ through synthesis by inverse solubility and precipitation from acid. Mixed Cs-FA crystals and powders remained stable in air at 20% humidity over one month, before slowly phase separating into yellow δ and black α-phase rich regions. This stability is much improved on that of α-$FAPbI_3$, which quickly transforms to δ-$FAPbI_3$ on exposure to the atmosphere.[87] Lee *et al.* attributed the improved stability of $Cs_xFA_{1-x}PbI_3$ to stronger interactions between the FA cations and I anions due to a contraction of the unit cell.[96]

A consequence of the improved stability of the mixed Cs-FA lead iodide perovskite is the desirable black α-phase becoming accessible in ambient conditions. Numerous studies have shown the tetragonal (β) to cubic (α) transition in kinetically trapped samples of α-$FAPbI_3$ to occur at 285 K.[42,74,93] However, this transition is rarely observed as formation of the hexagonal δ-$FAPbI_3$ phase is energetically favoured at room temperature.[87] The variable temperature NPD data presented in this chapter shows the tetragonal (β) to cubic (α) transition temperature was not significantly affected by the addition of 10% Cs into the $FAPbI_3$ structure, being measured at 290 K for $Cs_{0.1}FA_{0.9}PbI_3$ in this work. As described earlier in this chapter, there has been confusion whether $Cs_{0.1}FA_{0.9}PbI_3$ adopts a cubic or tetragonal structure at room temperature.[144–146] Variable NPD data and DSC data of $Cs_{0.1}FA_{0.9}PbI_3$ suggested a slow, second order transformation from the cubic α-phase to a tetragonal β-phase centered

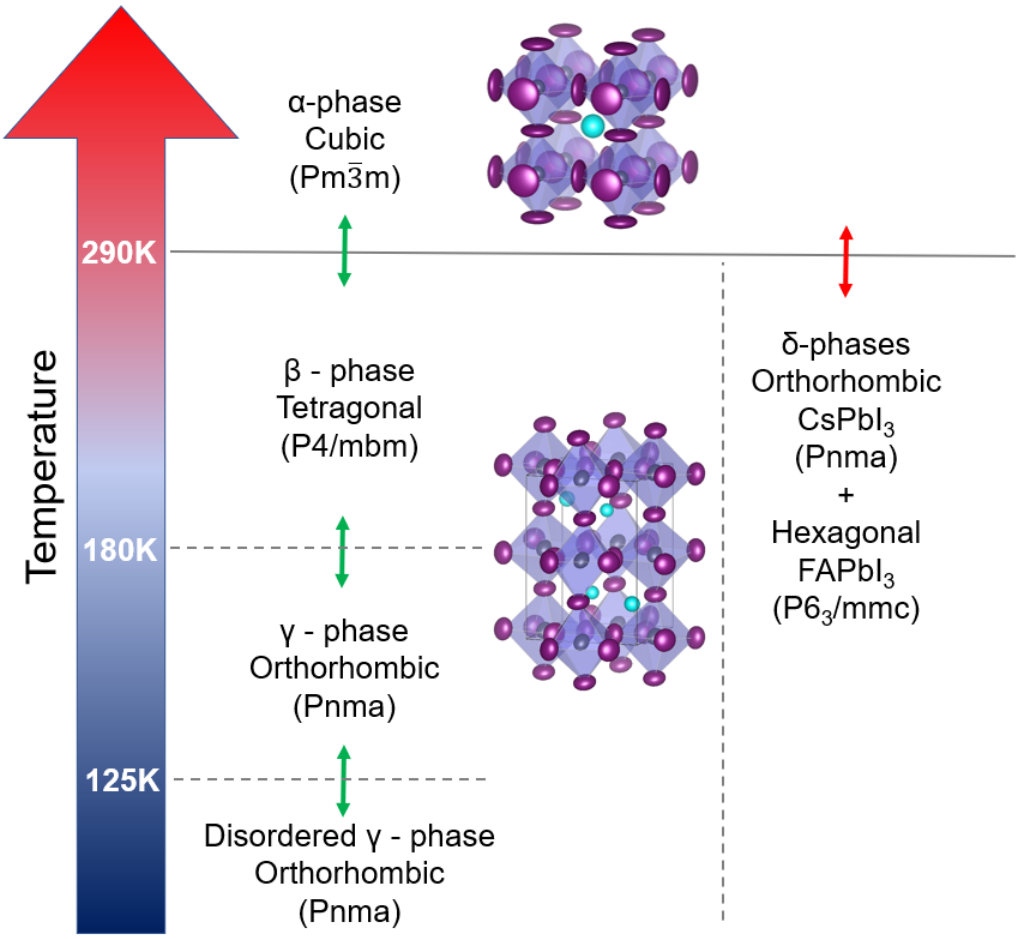

Figure 4-15: Phase transitions of $Cs_{0.1}FA_{0.9}PbI_3$ found in this work. Crystal structures were drawn in the program VESTA from SXRD data.

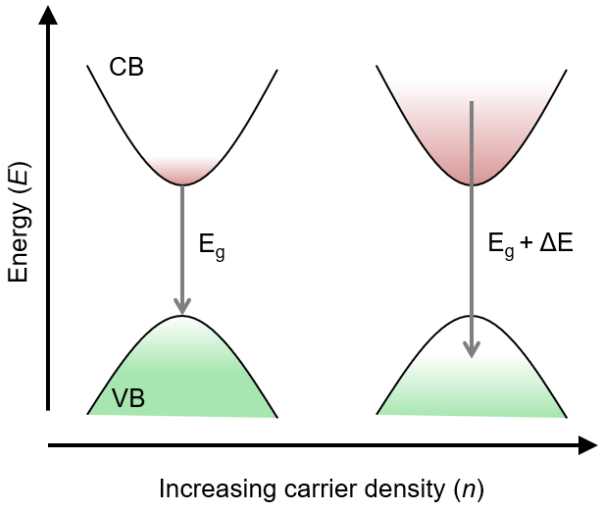

Figure 4-16: Schematic of the band filling effect, resulting in a blue shift of PL emission with increasing charge carrier density.

close to 290 K. The proximity of the cubic-tetragonal transition to room temperature, in addition to the dynamic nature of the PbI_6 octahedra, have likely been important factors in the discrepancies of the room temperature structure of $Cs_{0.1}FA_{0.9}PbI_3$ in the literature.[144–147]

Addition of the smaller Cs cation into the $FAPbI_3$ structure results in a contraction of the cuboctahedral voids formed by the corner sharing PbI_6 octahedra, resulting in geometric strain of the lead iodide framework, and leading to stronger hydrogen bonding between the amine groups of the FA cation and iodide.[146] These effects lead to the suppressed motion of the FA cation, and locked tilting of the PbI_6 octahedra at lower temperatures,[146,147] inducing the additional orthorhombic γ-phase seen in variable temperature NPD and SXRD. The appearance of this extra orthorhombic phase appears to lower the transition to a disordered state from 140 K observed in pure $FAPbI_3$, to 125 K seen in NPD and SXRD for $Cs_{0.1}FA_{0.9}PbI_3$ in this work. Therefore, in addition to increasing resistance to δ-phase formation, incorporating Cs into the $FAPbI_3$ structure has important effects resulting in the desirable cubic α-phase being accessible at room temperature, the addition of an orthorhombic phase present below 180 K and lowering of the transition temperature to the disordered state below 125 K.

The phase transition at 125 K was further supported by variable temperature PL and TRPL data, which showed a reversal in trend for peak PL position and effective bimolecular recombination rates at this temperature. The PL peak position first red shifts between 290 - 125 K, predominately due to thermal contraction effects which

increases the overlap of outer Pb and I orbitals, so decreasing the bandgap.[70] Below 125 K PL peak position blue shifts, coinciding with the disordered state suggested in the NPD and SXRD measurements. Dar *et al.* investigated the effect of orientationally disordered cations on the low temperature PL of $MAPbX_3$ thin films, demonstrating a small energy difference between domains of ordered and disordered cations.[151] At low temperatures charge transfer occurred between the ordered and disordered domains, resulting in the accumulation of charges in the disordered state, leading to a band filling effect, characterised by a blue shift in emission peak.[151] A schematic of the band filling effect is shown in Figure 4-16. A shift in the trend of effective bimolecular recombination rates extracted from TRPL measurements also corresponded to the transition to the low temperature disordered phase at 125 K. It is speculated that the presence of additional disordered domains act as recombination centers, increasing recombination rates.[46]

The phase transitions and the Cs substitution limit determined for $Cs_xFA_{1-x}PbI_3$ in this work are combined with those found for $FAPbI_3$ and $CsPbI_3$ to produce the phase diagram in Figure 4-17. It is important to note that the phase diagram was constructed using results from powder and crystal samples synthesised by the precipitation and inverse solubility methods, representing the intrinsic behaviour of these mixed cation systems.[74,88] Thin films were not investigated, and may demonstrate differing phase behaviour depending on deposition method.[18]

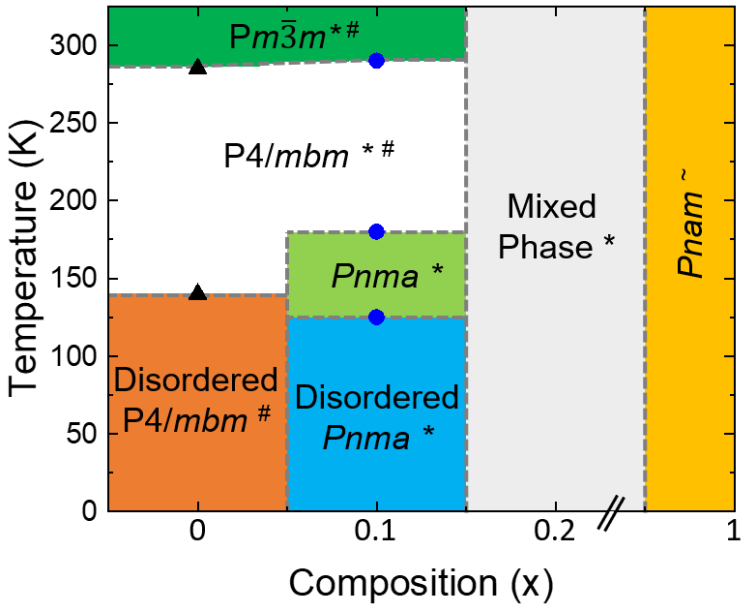

Figure 4-17: Phase diagram schematic for $Cs_xFA_{1-x}PbI_3$ powders (synthesised by the precipitation method) and single crystals (grown via inverse solubility). Space groups and transition temperatures as found in this work (blue circles and *) from variable temperature NPD data are compared with that found by Weber *et al.*[74] (black triangles and #) and Sutton *et al.*[88] (∼).

4.3 Site Substitution with Bromine in Cs-FA Lead Iodide Perovskites

4.3.1 Variable Temperature Neutron Powder Diffraction

The phase behaviour of $Cs_{0.1}FA_{0.9}Pb(I_{0.6}Br_{0.4})_3$ synthesised by the precipitation method was investigated using variable temperature NPD on the POLARIS instrument at ISIS neutron and muon source. A hydrogenous powder sample of $Cs_{0.1}FA_{0.9}Pb(I_{0.6}Br_{0.4})_3$ was cooled to 105 K and heated to 300 K at a rate of 0.4 $Kmin^{-1}$, data was continuously binned into 1 K ranges. Patterns from Bank 4, ranging between 1.5 Å and 3.69 Å are stacked according to temperature and displayed in Figure 4-18 (a).

A small continuous shift in peak position, indicating an expanding unit cell with increasing temperature, was investigated further using sequential refinement in GSAS II. A cubic model was used, adapted from that developed in the $Cs_{0.1}FA_{0.9}PbI_3$ NPD work presented earlier in this chapter. Extracted lattice parameters (a) are shown to decrease with decreasing temperature in Figure 4-18 (b). A kink in the trend is observed at 230 K, corresponding with the emergence of additional weak reflections as seen in Figure 4-18 (a). The emergence of additional peaks indicate decreasing symmetry, therefore a tetragonal β-phase was assigned below 230 K.[74,100] NPD patterns in the region indexed well to the space group P4/mbm, although the ratio of lattice parameters a to c extracted from indexing remained close to one throughout, indicating the material maintained a near cubic structure. This is similar to findings on $MAPb(Br_yCl_{1-y})_3$ perovskites which maintain a cubic structure down to 120 K.[94] It is probable that I-Br disorder affects the tilting of the PbX_6 octahedra which drives the cubic to tetragonal transition[94]

The α to β-phase transition temperature and cubic nature of the crystal structure was further supported by sequential peak fitting. The evolution of the position and FWHM of the prominent (200) reflection centered around a d-spacing of 3.15 Å was tracked. The extracted peak position and FWHM are shown as a function of temperature in Figure 4-19. Similar to that seen in the trend for lattice parameter from sequential refinement, a kink is observed in (200) peak position at 230 K. There is no obvious trend in FWHM, although values are on average 0.01 Å higher in the β phase than in the α phase. Peak broadening can be used as an indicator of peak splitting due to reducing symmetry. The small increase in FWHM below 230 K hints at a subtle change in crystal symmetry, likely due to transformation from a cubic α-phase to a pseudo-cubic tetragonal β-phase.

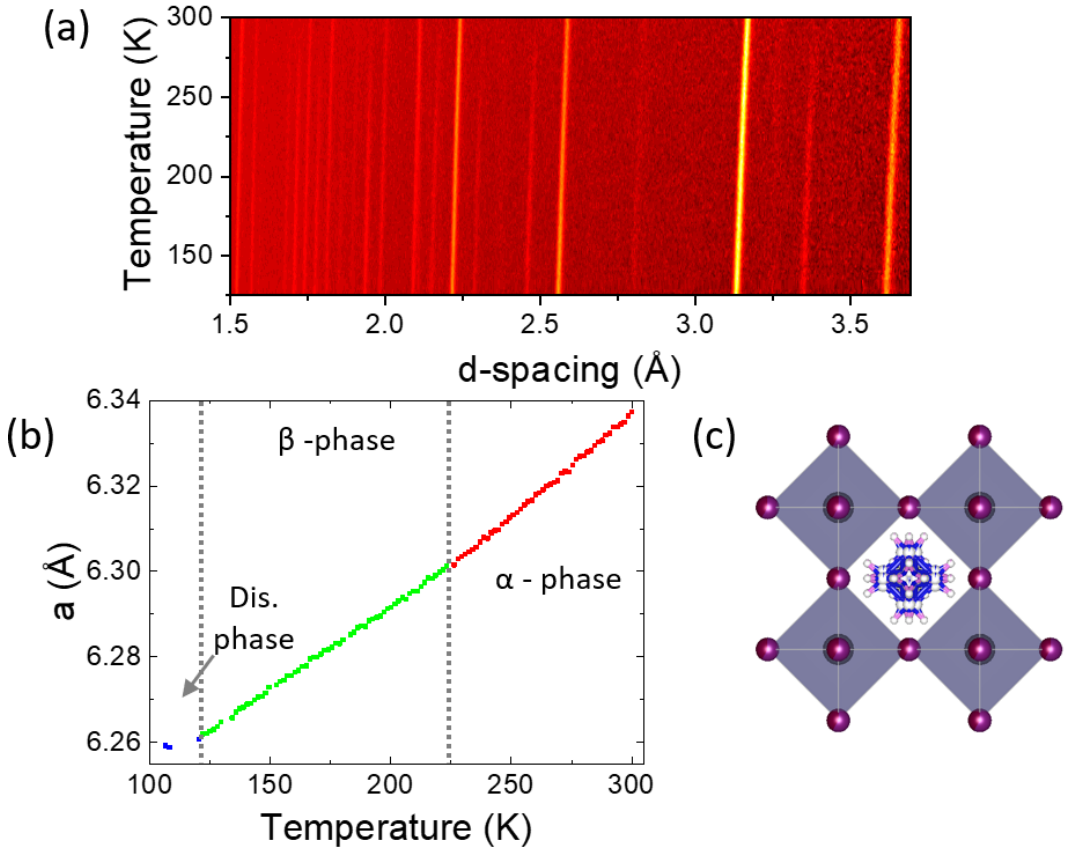

Figure 4-18: (a) Contour plot of stacked variable temperature NPD patterns on a $Cs_{0.1}FA_{0.9}Pb(I_{0.6}Br_{0.4})_3$ sample synthesised by the precipitation method and recorded on POLARIS Bank 4 at ISIS neutron and muon source. (b) Sequential refinement of a pseudo-cubic cell from 290K to 205 K. Transition temperatures were identified by kinks in the trend in lattice parameter a with temperature. (c) Cubic model used in the sequential refinement.

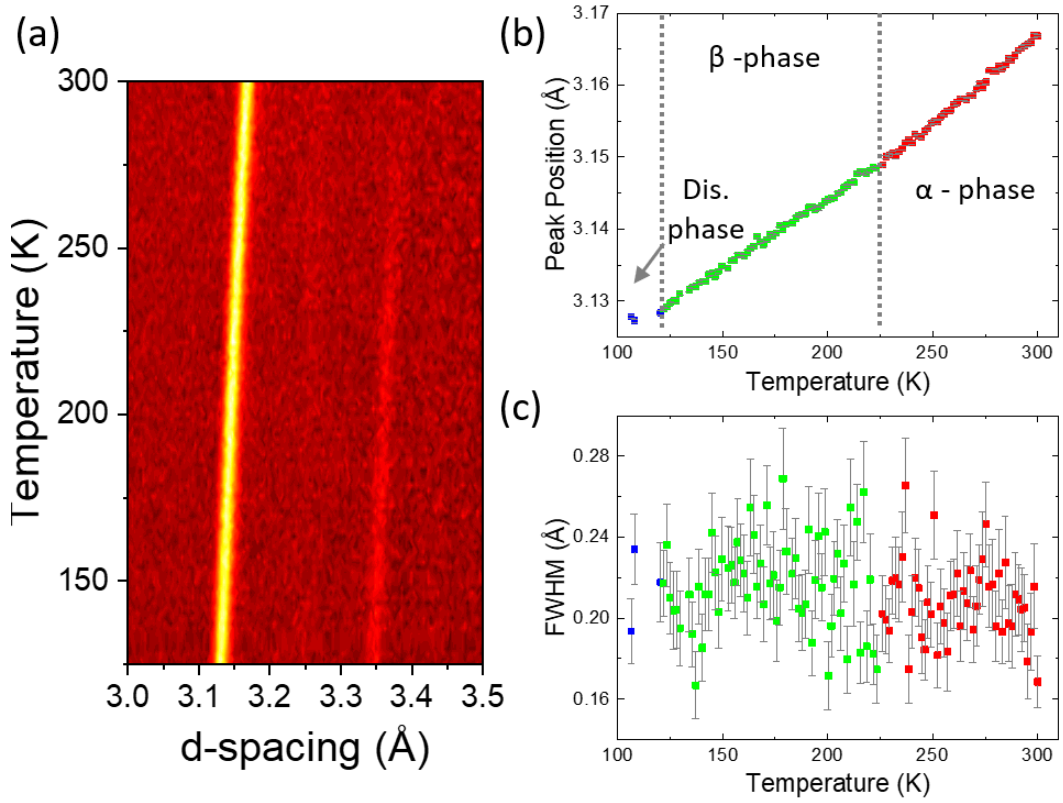

Figure 4-19: (a) Expanded contour plot from Figure 4-18 of $Cs_{0.1}FA_{0.9}Pb(I_{0.6}Br_{0.4})_3$ NPD patterns from POLARIS stacked with temperature in the range of 3.0 Å - 3.5 Å. (b) Extracted peak positions and (c) FWHM of the prominent (200) reflection centered around 3.15 Å from a sequential peak fit performed in GSAS II.

The growth of additional peaks attributed to the β-phase is gradual, first appearing in NPD patterns around 275 K and reaching peak intensity by 230 K. This is similar to the slow second order cubic to tetragonal transition observed between 275 K and 250 K in variable temperature XRD measurements on $FAPbBr_3$.[100] A further shift at 120 K in the trend of lattice parameters extracted from sequential refinement of the variable temperature NPD data suggests a further transition at low temperatures. Schueller *et al.* suggested a tetragonal (P4/*mbm*) to orthorhombic (P*nma*) transition in $FAPbBr_3$ around this temperature, although attempts to fit low temperature NPD to a simple orthorhombic model failed.[100] It is possible the low temperature phase of $Cs_{0.1}FA_{0.9}Pb(I_{0.6}Br_{0.4})_3$ is complicated by the effects of orientational disorder of the FA cations, as seen in $Cs_{0.1}FA_{0.9}PbI_3$ and $FAPbI_3$.[74]

4.3.2 Cubic Phase

The structure of $Cs_{0.1}FA_{0.9}Pb(I_{0.6}Br_{0.4})_3$ around 290 K was investigated by PXRD and NPD.

Room temperature PXRD patterns indexed best to the cubic $Pm\bar{3}m$ space group with lattice parameter $a = 6.344\,\text{Å}$. The indexed pattern is shown in Figure 4-20 (b), which also identifies impurities attributed to δ-$CsPbI_3$ (#) and δ-$FAPbI_3$ (∗). The parameters extracted from the indexed PXRD data were used as a starting point for profile fitting of NPD data acquired at 290 K.

NPD data measured at 290 K was initially fitted using the structural model obtained for cubic $Cs_{0.1}FA_{0.9}PbI_3$ presented earlier in this chapter, adapted to account for the addition of Br and a fully hydrogenous organic cation. The planar FA cation was modelled to a rigid H-C-NH_2 molecule, with ADPs of $0.244\,\text{Å}^2$, equal to that found for $Cs_{0.1}FA_{0.9}PbI_3$. The occupancies of the cation were set so as to allow 12 orientations of the FA cation within the cubo-octahedral void.[87] A Br anion was added to the halide site at (0.5, 0, 0), and the Br and I occupancies were initially set to 0.4 and 0.6 respectively to match the composition assumed from the stoichiometry used in synthesis. Lattice parameters and instrumental parameters were allowed to vary. The initial refinement converged to the space group $Pm\bar{3}m$ lattice parameter $a = 6.3376\,\text{Å}$, $wR = 2.74\%$.

In further refinements the ADPs of the C, H and N were constrained to be equal, as were the ADPs of I and Br, the position of the whole FA cation was then refined converging to give a wR of 2.54%. The occupancy of the I and Br ions were set to equal one, then allowed to vary, converging to 0.75 and 0.25 for the I and Br respectively in the final model, suggesting a true composition of $Cs_{0.1}FA_{0.9}Pb(I_{0.75}Br_{0.25})_3$. The 290 K structural model is presented in Table 4.3, giving a lattice parameter of $a = 6.337\,99(26)\,\text{Å}$ in space group $Pm\bar{3}m$, with $wR = 2.53\%$. Bromide uptake was significantly less than expected, potentially due to formation of a stabilised phase. Hoke *et al.*[153] demonstrated a preferred I:Br ratio of 8:2 in $MAPb(I_yBr_{1-y})_3$ systems, therefore a similar composition may be energetically favourable for the FA containing mixed halide systems.

The $0.112\,\text{Å}^2$ ADPs of the rigid FA cation in the mixed halide system are smaller than the $0.244\,\text{Å}^2$ measured for $Cs_{0.1}FA_{0.9}PbI_3$ in this work. However, the halide ADPs of $0.102\,\text{Å}^2$ are significantly larger than the $0.0806\,\text{Å}^2$ values for the I in $Cs_{0.1}FA_{0.9}PbI_3$. The reduced thermal motion of the FA cation is likely due to inclusion of the smaller

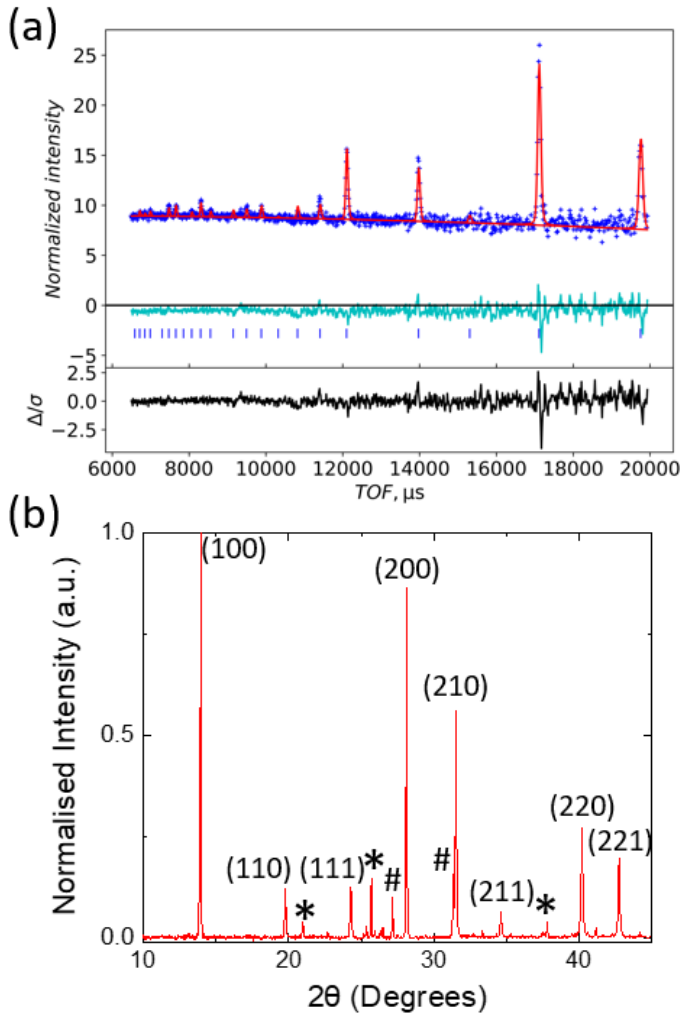

Figure 4-20: (a) Rietveld fit on $Cs_{0.1}FA_{0.9}Pb(I_{0.6}Br_{0.4})_3$ NPD data collected on POLARIS at 290 K refined to the space group $Pm\bar{3}m$, lattice parameter $a = 6.337\,99(26)$ Å, $wR = 2.53\%$. (b) PXRD data indexed to the cubic space group $Pm\bar{3}m$ with δ-$FAPbI_3$ and δ-$CsPbI_3$ impurities identified by $*$ and # respectively.

300K

Atom	x	y	z	Occupancy	U_{iso}	Symmetry
Pb1	0	0	0	1.000	0.0164(16)	m3m
I1	0.5	0	0	0.75	0.102(3)	4/mmm(x)
Br1	0.5	0	0	0.25	= I1 U_{iso}	4/mmm(x)
C1	0.5	0.562(5)	0.5	0.167	0.112(6)	4mm(y)
N1	0.682(6)	0.453(20)	0.5	0.083	= C1 U_{iso}	m(z)
H1	0.5	0.772(25)	0.5	0.167	= C1 U_{iso}	4mm(y)
H2	0.74(4)	0.61(8)	0.5	0.083	= C1 U_{iso}	m(z)
H3	0.77(3)	0.37(6)	0.5	0.083	= C1 U_{iso}	m(z)

Table 4.3: Refined model of $Cs_{0.1}FA_{0.9}PbI_3$ from NPD data at 290 K in the cubic $Pm\bar{3}m$ space group with a lattice parameter of 6.337 99(26) Å, $wR = 2.53\%$.

Br anion reducing the unit cell size, and so contracting the cuboctahedral volume occupied by the cation.[141] The reduced volume may result in stronger FA-halide interaction, as suggested by theoretical calculations for $Cs_{0.1}FA_{0.9}PbI_3$, therefore restricting the cation dynamics.[146] The increased thermal motion in the halide ions is likely due to the mismatch between the I (220 pm) and Br (198 pm) radii.[79,82,141] Inclusion of the smaller Br anion induces strain in the lead-halide framework, potentially leading to increased dynamic motion of the PbX_6 octahedra, although further high resolution variable temperature diffraction and theoretical studies would be beneficial to understand this observation.

4.4 Conclusions

The phase behaviour of $Cs_xFA_{1-x}PbI_3$ ($0 \leq x \leq 0.2$) and $Cs_{0.1}FA_{0.9}Pb(I_{0.6}Br_{0.4})_3$ perovskites were investigated primarily through variable temperature NPD and PXRD. Single crystals of $Cs_{0.1}FA_{0.9}PbI_3$ were also investigated by variable temperature PL and TRPL.

PXRD data showed contraction of the unit cell of $Cs_xFA_{1-x}PbI_3$ when compared to pure $FAPbI_3$, indicating successful Cs incorporation for x < 0.15, and EDX measurements suggested a preferred composition of $Cs_{0.12}FA_{0.88}PbI_3$ in crystals synthesised by inverse solubility.

From variable temperature NPD it was determined that inclusion of Cs results in the desirable cubic α-phase of $Cs_{0.1}FA_{0.9}PbI_3$ existing at room temperature. Despite previous studies suggesting $Cs_{0.1}FA_{0.9}PbI_3$ adopts a tetragonal structure at room temperature, peak splitting indicative to this phase is not observed in high resolution NPD data. However, the gradual second order cubic to tetragonal transition is deemed to occur around 290 K, accounting for confusion in the literature. Moreover, an additional orthorhombic phase was observed below 180 K and disorder attributed to residual entropy of the FA cation orientation appeared below 125 K. Transition to this disordered phase was suppressed in $Cs_{0.1}FA_{0.9}PbI_3$ when compared to phase pure α-$FAPbI_3$, due to effects of Cs substitution on the dynamics of the FA cation and lead iodide framework.

Variable temperature steady state PL on single crystals of $Cs_{0.1}FA_{0.9}PbI_3$ complemented results from the NPD data, suggesting transition to a low temperature state below 125 K. Below 125 K effective bimolecular recombination rates extracted from TRPL measurements increased with decreasing temperature, attributed to disordered domains behaving as recombination centers.

Transformation from a cubic α to tetragonal β-phase was also shown through variable temperature NPD on $Cs_{0.1}FA_{0.9}Pb(I_{0.6}Br_{0.4})_3$ synthesised by the precipitation method. The cubic structural model obtained at 290 K showed reduced cation motion, associated with the reduction in cuboctahedral volume due to substitution with the smaller Br anion. Transformation to the β-phase at 225 K occurred via a gradual second order transition characterised by the appearance of additional reflections in NPD patterns. The β-phase was deemed to be pseudo-cubic due to the ratio of tetragonal lattice parameters being close to one. Further work investigating the low temperature phase for potential disorder, as well as work determining the complex dynamics of the lead-

halide framework would be beneficial in understanding the superior PV performance of these mixed perovskites.

The phase behaviour of $Cs_{0.1}FA_{0.9}PbI_3$ and $Cs_{0.1}FA_{0.9}Pb(I_{0.6}Br_{0.4})_3$ were poorly understood and previous XRD studies could not model organic cation behaviour. However, this work has demonstrated the importance of modelling cation dynamics, providing important insights into the intrinsic behavior of mixed cation perovskites commonly used in photovoltaics.

Chapter 5

Cesium Methylammonium Lead Halide Perovskites

5.1 Introduction

In 2009 methylammonium lead iodide ($CH_3NH_3PbI_3$ or $MAPbI_3$) was the first hybrid halide perovskite to be used in a PV device;[12] since then, an explosion of research interest has resulted in MA containing perovskite devices challenging silicon solar cell efficiencies.[16] Research groups around the world have developed more efficient and stable perovskite solar cells by improving device architectures, as well as adding additional cations or halide anions to the A and/or X sites of the $MAPbI_3$ ABX_3 structure.[22,81,154] Adding cesium (Cs) and/or bromine (Br) into the $MAPbI_3$ template has been commonly employed as a method to enhance PV device stability and performance; however, the effect of these substitutions on the structure and phase behaviour of the perovskites has been less well studied. As introduced in Chapter 2 Section 2.5.3, the symmetry of hybrid halide perovskites decreases with decreasing temperature through a number of well known structural transitions. $MAPbI_3$ exists in the cubic $Pm\bar{3}m$ space group at high temperatures, transitioning to the tetragonal $I4/mcm$ then orthorhombic $Pnma$ structures at 327 K and 165 K respectively.[86] The central MA cation rotates freely in the cubic phase, shows rotational disorder in the *ab* plane in the tetragonal phase and is frozen in the orthorhombic phase, with only the end groups of the molecule rotating around the C-N bond.[103] Similar behaviour is observed in $MAPbBr_3$ which transitions from cubic ($Pm\bar{3}m$) to tetragonal ($P4/mmm$) to orthorhombic ($Pna2_1$) at 235 K and 148 K respectively.[94]

The behaviour of the central organic cation plays a pivotal role in the phase transitions of the material. The structure changes to optimise the hydrogen bonding between the MA cation and surrounding iodide by varying the degree of tilting of the PbI_6 octahedra. This affects the tolerance factor (t) used to define distortion in the perovskite structure.[103] For reference, Figure 5-1 shows the values of t and octahedral factors (μ) for compounds investigated in this chapter, as well as the phase pure $FAPbI_3$ and $CsPbI_3$ perovskites.

Substituting with Cs at the A-site and/or Br at the X-site of $MAPbI_3$ has been shown to induce geometric strain into the perovskite framework, directly affecting the tilts of the lead halide octahedra. Octahedral tilting determines the degree of electron orbital overlap; therefore, as well as affecting the crystallographic structure, site substitution also substantially affects the electronic and optical properties of the perovskite.[103] The changes induced by site substitution are often favourable, for example, mixed cation $Cs_xMA_{1-x}PbI_3$ compounds have demonstrated good PV performance alongside a resistance to the decomposition to PbI_2 and MAI enthalpically favoured in $MAPbI_3$.[99]

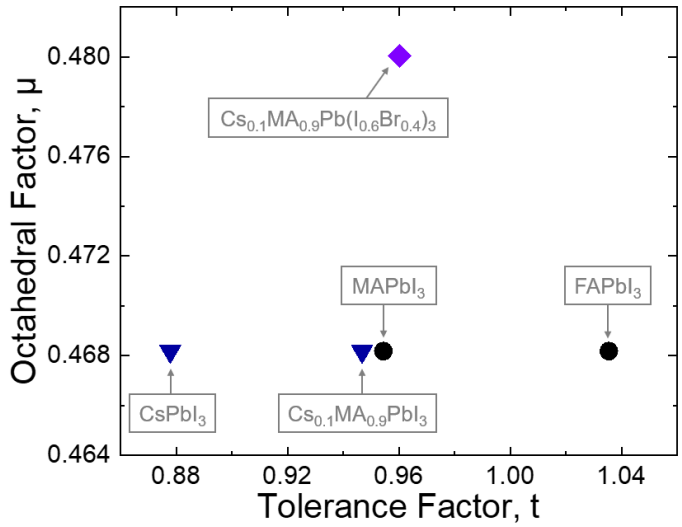

Figure 5-1: Calculated tolerance and octahedral factors for the MA containing perovskites discussed in this chapter, including those of $FAPbI_3$ and $CsPbI_3$ for reference.

Some of the best performing perovskite PV devices substitute at both the A and X site of the material, forming mixed compositions such as $Cs_xMA_{1-x}Pb(I_{1-y}Br_y)_3$.[81] These complex materials have demonstrated superior stability and precise control of the band gap depending on the chosen values of x and y.[140,155,156] However, investigations into the effect of cation and halide substitution on the phase behaviour of $Cs_xMA_{1-x}Pb(I_{1-y}Br_y)_3$ are absent. Similarly, there are few studies on the affect of Cs in $MAPbI_3$, with most research focused on $Cs_xMA_{1-x}PbBr_3$ compounds instead.[103]

Understanding the affects of site substitution on the optoelectronic and structural properties of hybrid halide perovskites is vital in the development of these materials for PV applications. $MAPbI_3$ has been studied extensively within various PV device architectures, demonstrating high charge-carrier mobilities, low exciton binding energies and the presence of free charge carriers at room temperature.[46,68,86,157,158] However, it has been shown that the local environment of the perovskite can significantly effect observed material properties; for example, the grain size determined by the substrate and deposition method used in thin film fabrication can affect charge-carrier mobilities and even the position of phase transitions.[26] Therefore, there exists some confusion when comparing perovskite optoelectronic and structural properties, as it can be difficult to determine how the characteristics change depending on the local environment. This prompted the work presented here, where the intrinsic properties of high performing perovskite compositions are investigated through a combination of diffraction and spectroscopic methods.

5.2 Phase Behaviour of Cesium Methylammonium Lead Iodide Perovskites

5.2.1 Cesium Substitution Limit

Samples of $Cs_xMA_{1-x}PbI_3$ ($0 \leq x \leq 0.4$) were synthesised as powder via the precipitation method and crystals via the inverse solubility method. In comparison to the $Cs_xFA_{1-x}PbI_3$ compositions investigated in Chapter 4, a greater resistance to degradation was observed in $Cs_xMA_{1-x}PbI_3$ ($0 \leq x \leq 0.1$) in ambient conditions, showing negligible presence of the δ-phase or PbI_2, which is a preferred degradation product of $MAPbI_3$.[80] On top of this, significantly larger single crystals of $Cs_{0.1}MA_{0.9}PbI_3$ could be grown using the inverse solubility method compared to $Cs_{0.1}FA_{0.9}PbI_3$. Crystal dimensions of 2 mm^2 (as shown in Figure 5-2 (a)) were commonly achieved.

As observed previously in thin films of $Cs_xMA_{1-x}PbI_3$,[22] a substitution limit of Cs into the $MAPbI_3$ structure was seen in crystal and powder samples. $Cs_{0.1}MA_{0.9}PbI_3$ could be routinely synthesised as the black perovskite phase, as supported by EDX measurements (Figure 5-2 (b)) demonstrating Cs incorporation throughout a cleaved crystal. EDX was used to measure Cs composition across three sites on the cleaved crystal, averaging to 2.51 $\pm$ 0.13% suggesting a true composition around $x = 0.12$. However, crystals of $Cs_{0.15}MA_{0.85}PbI_3$ showed significant growth of δ-phase impurities, as shown in Figure 5-2 (c). Impurity peaks could be assigned to δ-$CsPbI_3$ using PXRD and increased in intensity with an increasing value of x (Figure 5-3 (a)).

When attempting to grow crystals via the inverse solubility method, a yellow compound precipitated out of solution at 80°C for $Cs_xMA_{1-x}PbI_3$, $x \geq 0.15$. The precipitate was identified as δ-$CsPbI_3$ using PXRD, and could be filtered from the solution at 80°C. Perovskite crystals would then grow from the remaining precursor solution by heating to 110°C. In Figure 5-3 (b) the PXRD pattern for $Cs_{0.2}MA_{0.8}PbI_3$ grown this way is compared to that of $Cs_{0.1}MA_{0.9}PbI_3$, also grown via inverse solubility, but without the filtering step at 80°C. There is no observable shift between the peaks of the $x = 0.1$ and 0.2 samples, indicating similar Cs incorporation. This suggests excess Cs precipitated out of solution before perovskite crystallisation, indicating a substitution limit and preferred level of Cs incorporation into the $MAPbI_3$ structure. From PXRD and EDX measurements, the substitution limit of $Cs_xMA_{1-x}PbI_3$ powders and crystal samples was deemed to be $x < 0.15$, with a preferred composition of $x = 0.12$.

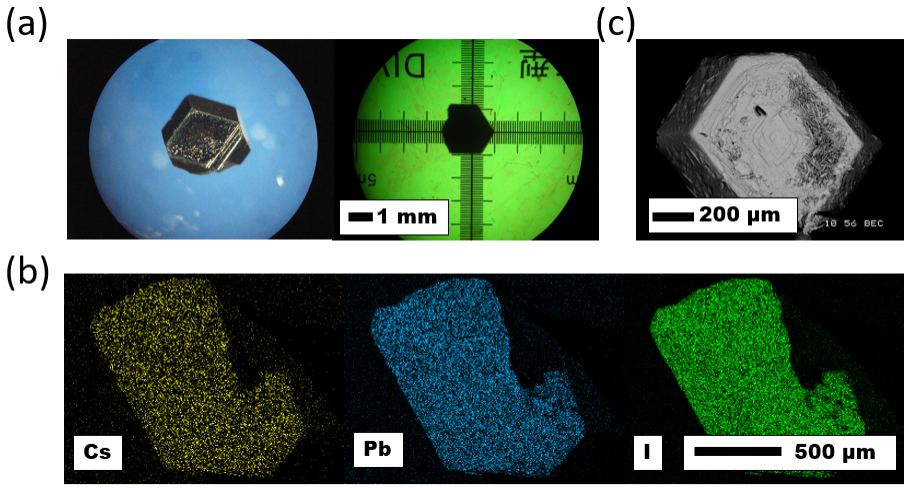

Figure 5-2: (a) Optical images of a $Cs_{0.1}MA_{0.9}PbI_3$ crystal. (b) EDX measurements of a cleaved $Cs_{0.1}MA_{0.9}PbI_3$ crystal mapping Cs, Pb and I content. Calculated weight % of Cs averaged over three sites was 2.51 ± 0.13 % compared to a calculated 2.11 %. (c) Backscattered SEM image of a $Cs_{0.15}MA_{0.85}PbI_3$ crystal showing significant growth of δ-phase needles on the right surface of the crystal.

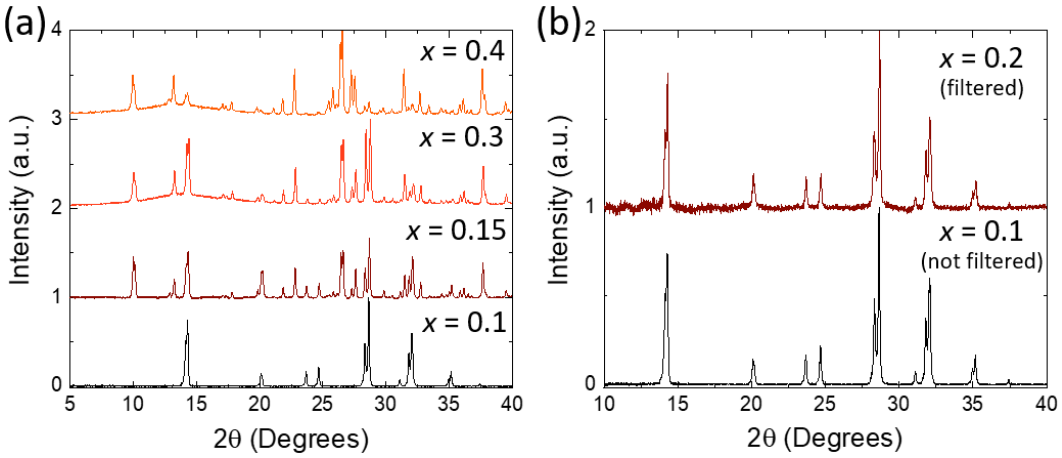

Figure 5-3: (a) PXRD patterns of $Cs_xMA_{1-x}PbI_3$, $x = 0.1$, 0.15, 0.3 and 0.4. Increasing presence of δ-$CsPbI_3$ can be tracked by the increasing intensity of the δ-phase peak centered around $2\theta = 26°$. (b) $Cs_xMA_{1-x}PbI_3$, $x = 0.1$ and 0.2 synthesised via inverse solubility. A yellow precipitate identified as δ-$CsPbI_3$ was filtered from the $x = 0.2$ precursor solution before perovskite crystals were grown, the resulting crystals were of a similar composition to that of the $x = 0.1$ samples grown without filtering.

5.2.2 Variable Temperature Neutron Powder Diffraction

The phase behaviour of $Cs_{0.1}MA_{0.9}PbI_3$ was investigated using variable temperature NPD carried out on the POLARIS instrument at the ISIS neutron and muon source, Rutherford Appleton Laboratories. Approximately 6 g of hydrogenous $Cs_{0.1}MA_{0.9}PbI_3$ was cooled *in situ* to 140 K and measured overnight at this temperature, before two three-hour collections were recorded at 240 K and 310 K. The sample was then cooled to 135 K *in situ* at a rate of 2.5 $Kmin^{-1}$ with data continuously binned into 5 K ranges between 310 K and 135 K. Due to reduced beam power from the source at ISIS, measurements between 310 K and 290 K were of poor quality, and therefore were not included in the analysis presented later in this chapter.

Patterns from the Bank 4 detector (90° to the sample) on the POLARIS instrument ranging from 1.5 Å to 3.69 Å are displayed in Figure 5-4 (a). A small continuous shift in peak position observed between 290 K and 170 K represents decreasing unit cell volume with decreasing temperature. An abrupt shift in peak position then occurs at 165 K indicating a phase change, occurring at the same temperature as the well known tetragonal to orthorhombic transition in $MAPbI_3$.[86] However, unlike $MAPbI_3$, a smearing across the phase transition is observed, with the intensity of peaks associated with the $>$ 165 K tetragonal phase reducing, as the peaks associated with the $<$ 165 K orthorhombic phase grow in. The smeared shift centered at 165 K shown in Figure 5-4 implies a slow glass-like transition, as discussed later in this chapter.

The signal-to-noise ratio is relatively poor in the variable temperature NPD data due to the fully hydrogenated sample, therefore the model used in the sequential refinement of the variable temperature data was based on that determined by the long measurement at 310 K. More details on the tetragonal model used in the refinement can be found in Section 5.2.3. Using this model, the program GSAS II[130] was used to perform a pseudo-tetragonal sequential refinement on the variable temperature NPD data between 290 K and 135 K, the extracted lattice parameters are plotted as a function of temperature in Figure 5-4 (b). The unit cell contracts along the a-axis as the temperature decreases from 290 K to 165 K. After the phase transition at 165 K, there is an abrupt change in the trend of the a and c lattice parameters, coinciding with an increase in the R-factor of the refinement indicating, a poorer fit to the tetragonal model.

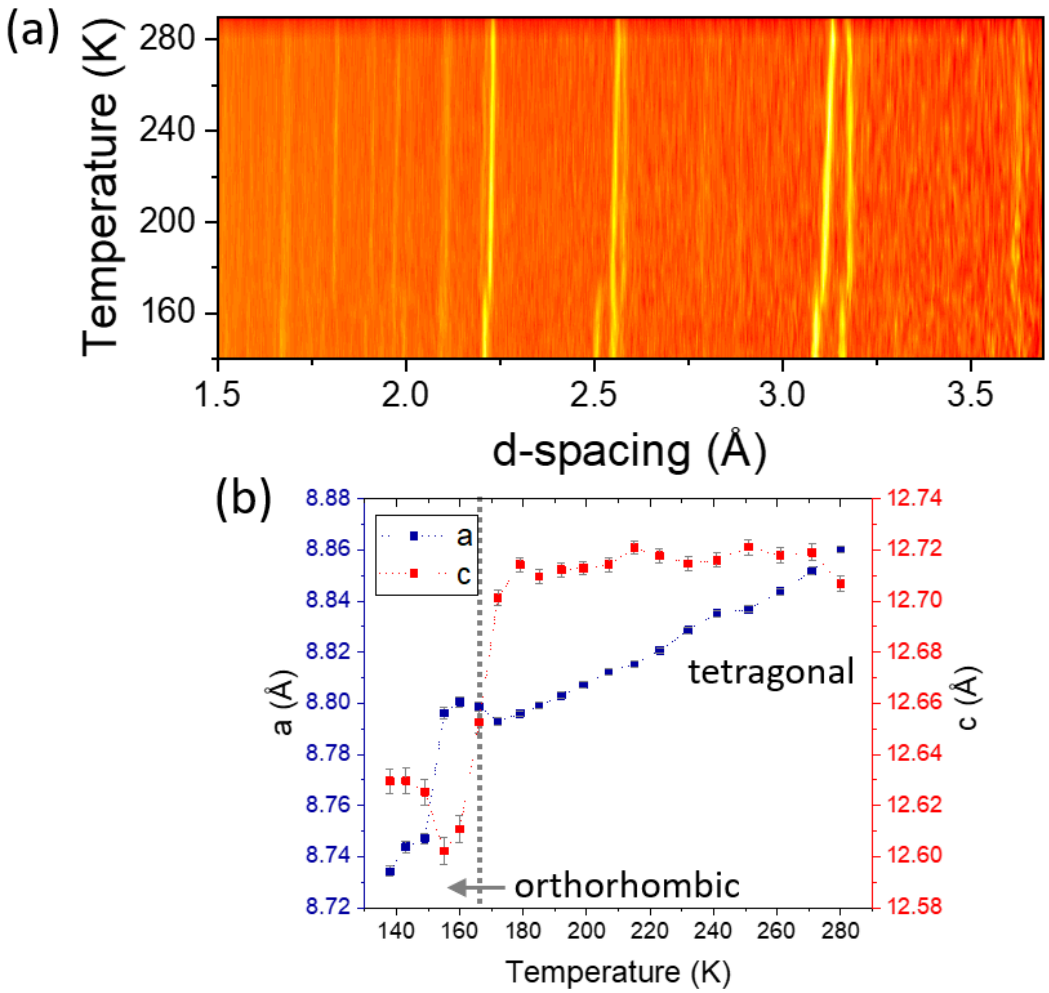

Figure 5-4: (a) Variable temperature NPD data of $Cs_{0.1}MA_{0.9}PbI_3$ recorded on Bank 4 of the POLARIS instrument at the ISIS neutron and muon source. (b) Pseudo-tetragonal refinement of the variable temperature data showing variation of the a (blue) and c (red) lattice parameters.

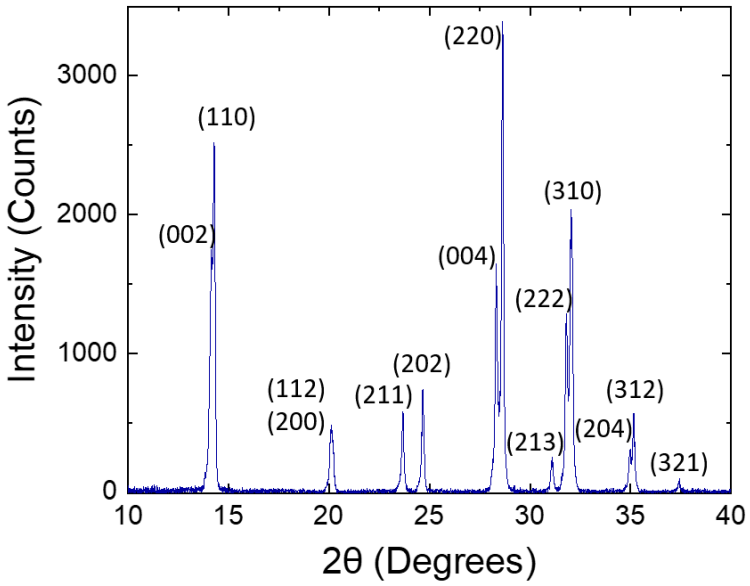

Figure 5-5: Indexed PXRD data at 293 K of a $Cs_{0.1}MA_{0.9}PbI_3$ sample synthesised by inverse solubility and ground to powder using a pestle and mortar. The background has been subtracted.

5.2.3 Tetragonal Phase

The tetragonal structure of single crystal and powder samples of $Cs_{0.1}MA_{0.9}PbI_3$ between 310 K and 165 K was characterised using PXRD, NPD and SXRD.

Phase pure samples of $Cs_{0.1}MA_{0.9}PbI_3$ synthesised by the inverse solubility method and ground using a pestle and mortar were investigated using PXRD. PXRD patterns indexed best to the tetragonal I4/*mcm* space group, with lattice parameters $a = 8.857$ Å and $c = 12.658$ Å. The indexed pattern of $Cs_{0.1}MA_{0.9}PbI_3$ collected at 293 K on a STOE STADI P diffractometer is shown in Figure 5-5. Peak broadening due to grinding effects made further refinement of the PXRD data unreliable.

A single crystal of $Cs_{0.1}MA_{0.9}PbI_3$, synthesised by the inverse solubility method, was selected for SXRD at 300 K. The structure was solved using the established tetragonal phase of $MAPbI_3$ as a model,[86] and representing the tumbling and low scattering of the organic MA cation as a single atom with large ADPs. The structure solved to the tetragonal I4/*mcm* space group with lattice parameters $a = 8.8728(5)$ Å, $c = 12.6445(11)$ Å and a residual of 6.19%.

Hydrogenous powder samples of $Cs_{0.1}MA_{0.9}PbI_3$ synthesised by the precipitation method were measured using NPD from two three-hour collections at 310 K and 240 K. The

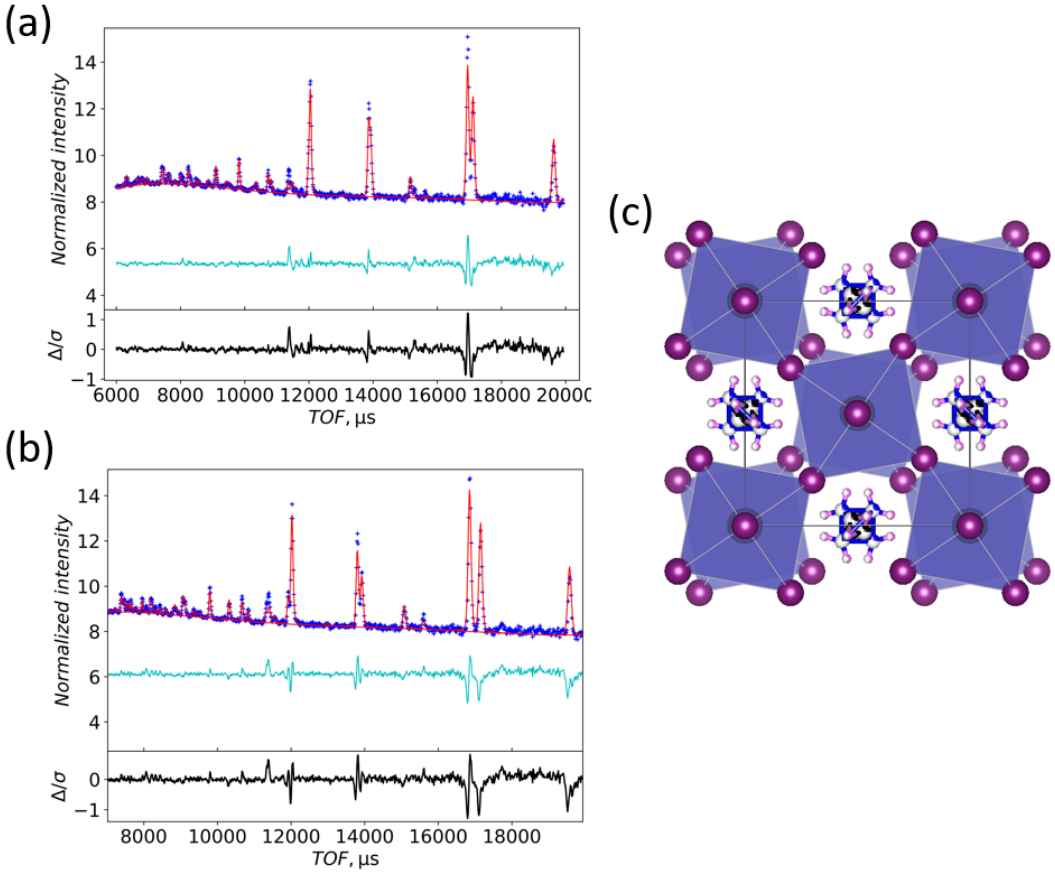

Figure 5-6: (a) Profile fit of NPD data at 310 K and (b) 240 K. Blue crosses show the observed intensities, the red line is the calculated profile and the light blue line is the difference. (c) The tetragonal model viewed along the c-axis as solved at 240 K, lead atoms are grey, iodine purple, carbon black, nitrogen blue and hydrogen pink.

structure of $MAPbI_3$ was again used as a model, with atomic positions, lattice and instrumental parameters allowed to vary. The resulting Rietveld fits converged to the tetragonal space group $I4/mcm$, shown in Figure 5-6 (a) and (b) for 310 K and 240 K respectively. At 310 K the refined lattice parameters were $a = 8.875\,70(4)$ Å and $c = 12.6759(6)$ Å with $wR = 1.08\%$ and reduced $\chi^2 = 2.26$; while at 240 K the lattice parameters converged to $a = 8.8251(4)$ Å and $c = 12.7022(6)$ Å with $wR = 1.09\%$ and reduced $\chi^2 = 2.29$. Additional crystallographic information is detailed in Table 5.1 and the tetragonal model solved at 310 K is shown in Figure 5-6 (c).

The value of a decreases while that of c increases with decreasing temperature, indicating reduced symmetry at lower temperatures. This is reflected in the peak splitting observed in the NPD patterns, which is more pronounced at lower temperatures, as

310 K

Atom	x	y	z	Occ	U_{iso}	Site
Pb1	0.5	0.5	0.5	1.00	0.0041(11)	4/m(z)
I1	0.2105(4)	0.2895(4)	0.5	1.00	0.0411(21)	mm2
I2	0.5	0.5	0.75	1.00	0.055(3)	422(z)
N1	0.4398(15)	0.0602	0.2734(21)	0.25	0.053(4)	m(xy)
H1	-0.0461(23)	0.3577(15)	0.2967(13)	0.50	0.196(7)	1
C1	0.483(5)	0.017	0.2154(28)	0.25	0.106(4)	m(xy)
H2	0.471(4)	0.029	0.3564(19)	0.50	0.192(7)	m(xy)

240 K

Atom	x	y	z	Occ	U_{iso}	Site
Pb1	0.5	0.5	0.5	1.00	0.020(1)	4/m(z)
I1	0.20065(31)	0.29935	0.5	1.00	0.0191(16)	mm2
I2	0.5	0.5	0.75	1.00	0.0337(25)	422(z)
N1	0.4340(11)	0.0660	0.2821(13)	0.25	0.020(3)	m(xy)
H1	-0.0430(21)	0.3537(12)	0.2898(12)	0.50	0.207(7)	1
C1	0.4697(12)	0.0303	0.2238(15)	0.25	0.0238(28)	m(xy)
H2	0.4591(21)	0.0409	0.3490(15)	0.50	0.167(6)	m(xy)

Table 5.1: Refined models of $Cs_{0.1}MA_{0.9}PbI_3$ using NPD in the tetragonal phase, space group I4/*mcm* at 310 K (a = 8.875 70(4) Å and c = 12.6759(6) Å with wR = 1.08% and χ^2 = 2.26) and 240 K (a = 8.8251(4) Å, c = 12.7022(6) Å with wR = 1.09% and χ^2 = 2.29).

seen in Figures 5-6 (a) and (b). The increased symmetry observed at higher temperatures indicates a trend towards a cubic perovskite phase, as observed in $MAPbI_3$, which transitions to cubic above 327 K.[86]

The MA cation ($CH_3NH_3^+$) is simplified in the tetragonal model used in the NPD profile fit, representing just two H positions at either end of the C-N cation. Modelling two H positions accounts for the likely free rotation of the H atoms around the C-N bond as observed in previous diffraction studies on methylammonium lead halide perovskites.[18,86,159] Rotation of the C-N bond is addressed by assigning the C and N positions an occupancy of 0.25, allowing the cation to occupy four different positions within the cavity formed by the PbI_6 octahedra, as seen in Figure 5-6 (c).

5.2.4 Orthorhombic Phase

The orthorhombic structure of single crystal and powder samples of $Cs_{0.1}MA_{0.9}PbI_3$ was investigated by SXRD at 150 K and 120 K, and by NPD at 140 K.

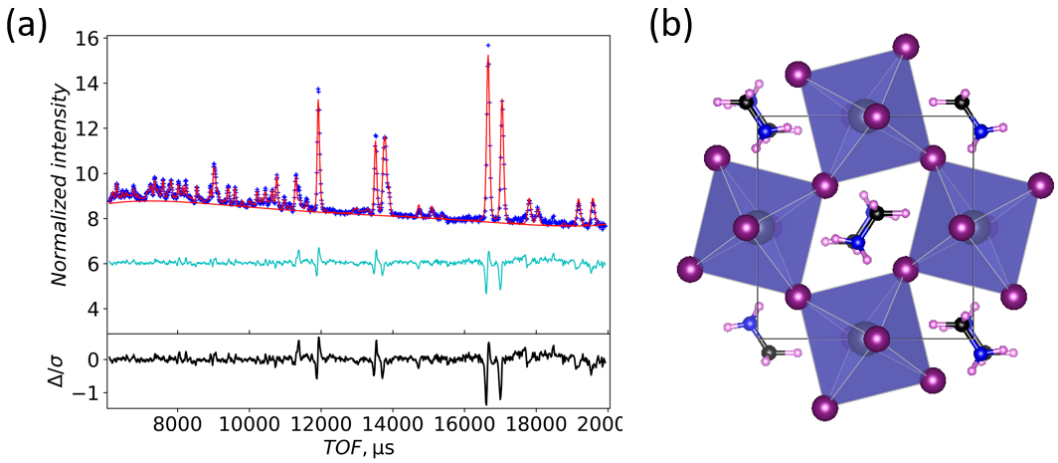

Figure 5-7: (a) Profile fit of NPD data at 140 K, blue crosses show the observed intensities, the red line is the calculated profile and the light blue line is the difference. (c) The orthorhombic model viewed along the *b*-axis as solved at 140 K, lead atoms are grey, iodine purple, carbon black, nitrogen blue and hydrogen pink.

A powder sample of hydrogenous $Cs_{0.1}MA_{0.9}PbI_3$, synthesised via the precipitation method, was measured through an eight-hour NPD collection at 140 K. The published orthorhombic structure for $MAPbI_3$ at 100 K was used as an initial model, with atomic positions, instrumental parameters and lattice parameters allowed to vary.[86] Figure 5-7 (a) shows the Rietveld fit to the NPD data and Figure 5-7 (b) the model as viewed along the *b*-axis, where Pb atoms are grey, iodine purple, carbon black, nitrogen blue and hydrogen pink. The calculated profile converged to the space group P*nma*, lattice parameters $a = 8.8605(5)$ Å, $b = 12.6278(5)$ Å, $c = 8.5944(4)$ Å with $wR = 1.13\%$ and $\chi^2 = 3.11$. Atomic positions and thermal parameters are given in Table 5.2.

A single crystal of $Cs_{0.1}MA_{0.9}PbI_3$, synthesised by the inverse solubility method, was measured using SXRD at 150 K and 120 K. The tumbling and low scattering of the organic MA cation was approximated by a single atom with a large ADPs. The best solution at 150 K converged to the orthorhombic space group P*nma*, lattice parameters $a = 8.759(2)$ Å, $b = 12.596(2)$ Å, $c = 8.689(2)$ Å and a residual of 18.0%. Twinning through the tetragonal to orthorhombic phase transition caused the high residual. At 150 K the structure could also be solved in the tetragonal I4/*mcm* solution seen at higher temperatures, indicating the probable presence of tetragonal domains due to the proximity to the phase transition centered at 165 K.

SXRD measurements at 120 K again converged to the orthorhombic space group P*nma*, with lattice parameters $a = 8.760(3)$ Å, $b = 12.578(3)$ Å, $c = 8.629(3)$ Å and a residual

140 K

Atom	x	y	z	Occ	U_{iso}	Sym
Pb1	0.5	0	0	1.00	0.008(1)	-1
I1	0.49884	0.25	-0.05290	1.00	0.009(1)	m(y)
I2	0.1885(6)	0.0171(6)	0.1877(6)	1.00	0.0156(20)	1
N1	0.9323(13)	0.75	0.0352(11)	1.00	0.0364(31)	m(y)
C1	0.9365(15)	0.25	0.0537(13)	1.00	0.0133(29)	m(y)
H1	0.936(4)	0.25	0.185(4)	1.00	0.178(16)	m(y)
H2	0.8974(27)	0.1747)16)	0.0371(25)	1.00	0.165(11)	1
H3	0.1454(17)	0.1915(11)	0.0072(18)	1.00	0.071(6)	1
H4	0.949(3)	0.75	0.138(4)	1.00	0.092(10)	m(y)

Table 5.2: Refined model of $Cs_{0.1}MA_{0.9}PbI_3$ in the orthorhombic phase, space group Pnma at using NPD data at 140 K, $a = 8.8605(5)$ Å, $b = 12.6278(5)$ Å, $c = 8.5944(4)$ Å with $wR = 1.13\%$ and $\chi^2 = 3.11$.

of 18.41%. Unlike the measurement at 150 K, reflections attributed to the tetragonal I4/mcm phase are absent, suggesting the absence of any tetragonal domains, although the residual is still high due to twinning. The data suggest the formation of multiple twins as the material undergoes a phase transition, in line with previous observations for hybrid halide perovskites and hinting at at disorder in the orientations of the MA cation and PbI_6 octahedral tilts.[74,103]

5.2.5 Variable Temperature Photoluminescence

The variable temperature behaviour of $Cs_{0.1}MA_{0.9}PbI_3$ was investigated by steady state and transient PL, illuminating a crystal with an excitation wavelength of 630 nm, while reducing the temperature from 290 K to 25 K. Figure 5-8 (a) shows the stacked PL spectra recorded as the temperature was varied. On top of the shift in peak position, a dominant feature of these spectra is their asymmetric shape due to dual PL peak emission. Previous studies on hybrid halide perovskites have suggested this dual emission to be due to the presence domains of high (tetragonal) and low (orthorhombic) temperature phases.[47,160] As discussed earlier in this chapter, SXRD measurements suggest domains of the tetragonal and orthorhombic phase form near the transition at 165 K; however, this is unlikely to be the cause of the asymmetry observed in the PL spectra. At temperatures greater or less than 10 K from the phase transition, SXRD and variable temperature NPD measurements do not indicate the presence of additional phases.

Due to the large size of the $Cs_{0.1}MA_{0.9}PbI_3$ crystal investigated, photon re-absorption

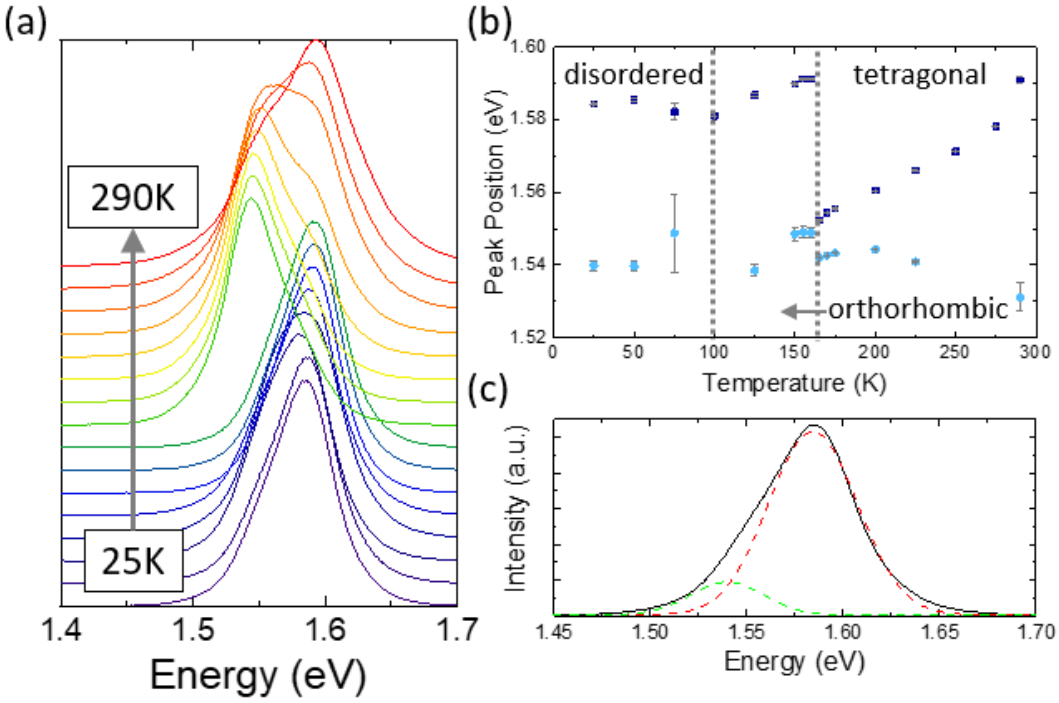

Figure 5-8: (a) Variable temperature steady state PL on a single crystal of $Cs_{0.1}MA_{0.9}PbI_3$. (b) PL peak positions extracted from Gaussian fitting of primary PL peaks (dark blue) and secondary peaks (light blue) accounting for photon recycling effects. (c) Example fit of PL spectra taken at 50 K, modelled with Gaussian functions describing primary PL (red dashed line) and secondary photon-recycling (green dashed line) contributions.

effects were determined to be the likely cause of the dual emission observed in PL spectra (Figure 5-8 (a)). Each spectrum was fitted with two Gaussian functions, one representing the real PL, while the secondary function, at a lower energy, occurred due to photon-recycling effects (absorption and then re-emission of PL photons). Figure 5-8 (b) shows the peak positions extracted from the primary (dark blue) and secondary (light blue) Gaussian fits to the variable temperature PL. An example model of the dual emission is shown in Figure 5-8 (c), where the measured spectrum at 50 K (black solid line) is fitted with primary PL (red dashed line) and secondary photon-recycling (green dashed line) contributions. It is important to note that dual PL emission in MA containing halide perovskites has also been attributed to domains of orientational disorder of the MA cation, and while unlikely to fully describe the dual emission observed in this work,[151] the phenomenon is discussed in greater detail later in this chapter.

As shown in Figure 5-8 (b), the peak position of the primary fit to the PL spectra (dark blue) red shifts from 290 K to 165 K, indicating a decreasing band gap with decreasing temperature. An abrupt discontinuity in peak position occurs between 165 K and 170 K coinciding with the tetragonal to orthorhombic phase change. The peak position then red shifts again until 100 K, when the trend changes and the PL blue shifts coinciding with the observation of disorder in the SXRD measurements.

TRPL spectra were recorded for a $Cs_{0.1}MA_{0.9}PbI_3$ crystal at 25 K, 50 K, 150 K, 200 K, 250 K and 290 K. Figure 5-8 (a) shows the normalised TRPL decay (blue lines), the tails of which were fitted according to the rate equation:

$$-\frac{dn}{dt} = k_1 n + k_2 n^2 \tag{5.1}$$

where n is the carrier density, and k_1 and k_2 are the recombination rates for monomolecular and bimolecular recombination respectively.[52] In hybrid perovskites monomolecular recombination is dominated by trap assisted recombination. As, described previously in Chapter 4, the true value of k_2 can not be calculated as the value of n was not directly measured. However, an effective value of Bk_2 could be measured, where B is a proportionality constant.[152] The extracted trap mediated (k_1) and effective bimolecular (Bk_2) recombination rates are plotted as a function of temperature in Figure 5-8 (b).

The TRPL spectra were divided into fast (< 20 ns) and slow (≥ 20 ns) decay phases, with only the slow phase modelled with Equation 5.1. This model has been shown to be a poor explanation for the fast decay phase observed in $MAPbI_3$,[161] which is likely

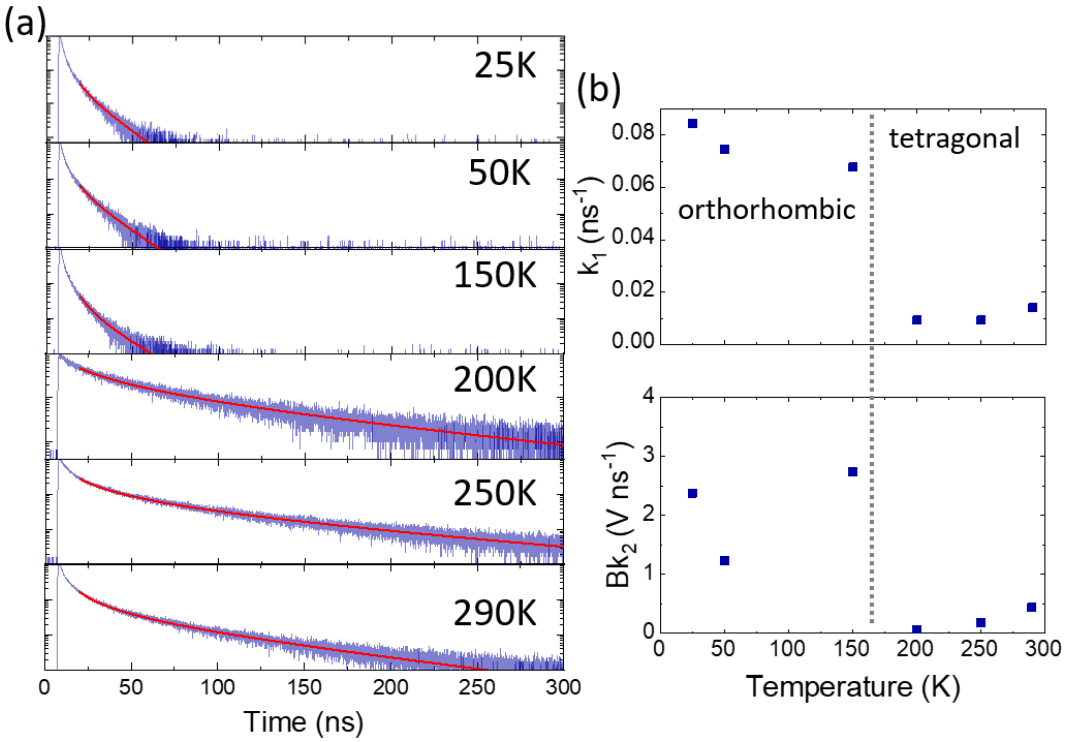

Figure 5-9: (a) Normalised TRPL spectra on a $Cs_{0.1}MA_{0.9}PbI_3$ crystal at various temperatures. The tails of the PL decay are fitted using a bimolecular decay function (red line). (b) The extracted trap state mediated (k_1) and effective bimolecular (Bk_2) recombination rates as a function of temperature.

dominated by a charge carrier diffusion process.[62] In a single crystal charge carriers generated at the point of excitation can easily diffuse through the sample, significantly reducing the charge carrier density at the point of excitation. This process dominates in the initial fast decay phase, therefore modelling to Equation 5.1 does not give a true representation of charge carrier behaviour below 20 ns.[62]

5.2.6 Absorption

UV-Vis spectroscopy was used to determine the absorption onset of $Cs_{0.1}MA_{0.9}PbI_3$. Reflectivity (R) was measured on powder perovskite samples using a spectrophotometer fitted with an integrating sphere allowing collection of specular and diffuse reflectance. Measured values of R were transformed to better resemble absorbance through the Kubelka-Munk function ($F(R)$, Equation 3.13).

The resulting normalised $F(R)$ function is plotted alongside the normalised PL taken

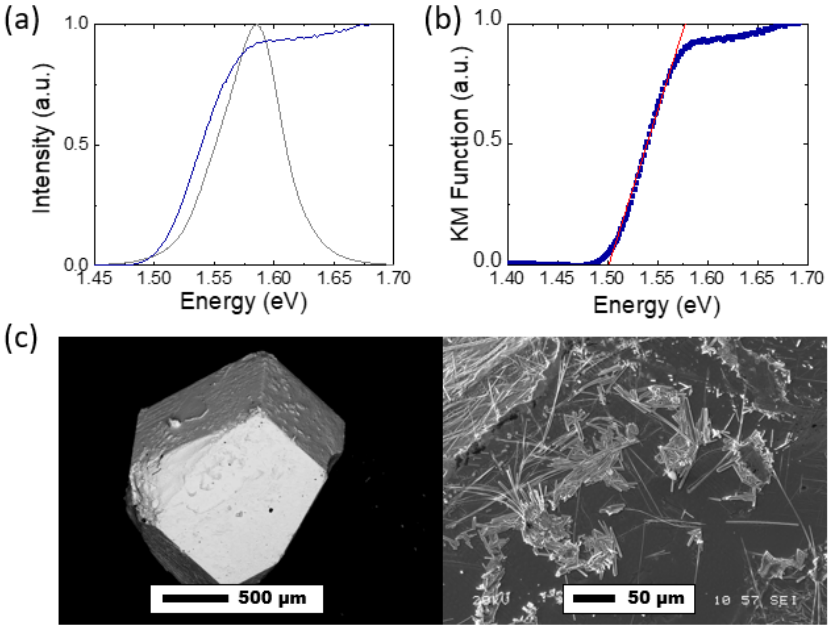

Figure 5-10: (a) PL (grey line) and reflectance transformed using the Kubelka-Munk (KM) function (blue line) of $Cs_{0.1}MA_{0.9}PbI_3$ samples. (b) Estimation of the material band gap by extrapolating from the absorption edge, suggesting a value of 1.50 eV. (c) SEM images of the $Cs_{0.1}MA_{0.9}PbI_3$ crystal used in the variable temperature PL measurements, taken at magnifications of x 45 (left) and x 300 (right). The growth of needles attributed to δ-$CsPbI_3$ can be seen on the crystal surface.

of the same compound at 25 K in Figure 5-10 (a). The band gap of the material can be estimated by extrapolating the absorption onset of the $F(R)$ function - as shown by the red line in Figure 5-10 (b) - suggesting a band gap of 1.50 eV. This contrasts with the peak PL position which was measured at energies greater than 1.55 eV in both the tetragonal and orthorhombic phases. Overlap between the absorption onset and PL peak is usually expected, often with the additional presence of a small Stokes shift, due to thermal relaxation of the exited electron before relaxation to the ground state by photo-emission.[162]

The apparent blue shift between peak PL energy and absorption onset was investigated further using SEM. Figure 5-10 (c) shows SEM images of the crystal used in PL measurements at magnifications of x 45 and x 300. The SEM images show significant growth of needles attributed to the δ-$CsPbI_3$ phase on the surface of the crystal. It is known that α-$CsPbI_3$ transforms to δ-$CsPbI_3$ in the presence of moisture, therefore, on exposure to the atmosphere, the surface of the $Cs_{0.1}MA_{0.9}PbI_3$ crystal may have separated into α and δ-phase rich regions.[88] PL measurements are inherently surface

sensitive and may have been affected by the presence of this, higher band gap, δ-phase rich region at the surface. The reflectivity measurements of the powder $Cs_{0.1}MA_{0.9}PbI_3$ would not have been as sensitive to a δ-phase rich surface, therefore resulting in recording an absorption onset at a lower energy to the PL, more in-line with the true band gap value for $Cs_{0.1}MA_{0.9}PbI_3$.

5.2.7 Discussion

The phase behaviour of $Cs_{0.1}MA_{0.9}PbI_3$ can be inferred by combining the results of the variable temperature NPD, SXRD and PL, and is summarised in Figure 5-11. The inclusion of Cs into the $MAPbI_3$ structure does not have a significant effect on the tetragonal-orthorhombic transition temperature compared to that observed in phase pure $MAPbI_3$.[86] This result is similar to that found for $Cs_{0.1}MA_{0.9}PbBr_3$ by Mozur *et al.*, which showed identical phase behaviour to $MAPbBr_3$.[103] The insignificant effect of Cs on $MAPbI_3$ phase transitions is unlike the behaviour presented in Chapter 4, which concludes that the inclusion of Cs into $FAPbI_3$ lowers the structural transition temperature to a disordered phase and introduces an orthorhombic phase. As with $Cs_{0.1}FA_{0.9}PbI_3$, inclusion of Cs into $MAPbI_3$ softens the lead iodide framework.[147] However, due to the smaller radius and increased rotational motion of the MA cation compared to FA, the affect on the octahedral tilting, and so material phase behaviour, is less pronounced. Further *ab initio* calculations on the effect of Cs incorporation on MA dynamics would be beneficial.

While variable temperature NPD data of $Cs_{0.1}MA_{0.9}PbI_3$ did not suggest any change in the tetragonal-orthorhombic transition temperature compared to $MAPbI_3$, it is proposed that inclusion of Cs did have an effect on the transition behaviour. Substitution with 10% Cs causes geometric strain in the structure due to differences in the Cs and MA cation radii, at 181 pm and 216 pm respectively.[79,81] Inclusion of the smaller Cs cation distorts the octahedral void it occupies, causing strain as the lead iodide framework optimises coordination with both the small amount of Cs and dominant organic MA cation. This strain has a small effect on the rotational motion of the MA cation resulting a glass-like phase transition, explaining the smeared appearance of the tetragonal to orthorhombic transition observed in the NPD data centered at 165 K.[103] The phase behaviour of $Cs_xMA_{1-x}PbBr_3$ perovskites has been likened to a dynamically disordered plastic crystal at high temperatures, transitioning to an orientational glass at lower temperatures.[44,103] In the context of perovskites, the term *plastic crystal* refers to a crystal with local rotational disorder but long range translational order, a

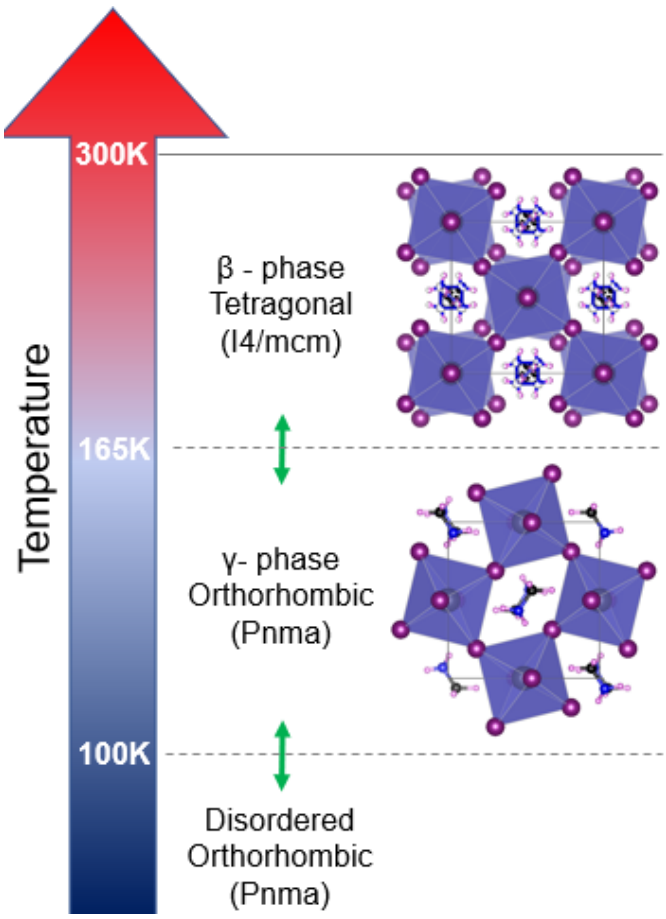

Figure 5-11: Schematic of the phase transitions in $Cs_{0.1}MA_{0.9}PbI_3$ determined by variable temperature NPD, SXRD and PL. Inclusion of Cs into the $MAPbI_3$ does not affect the tetragonal to orthorhombic transition temperature. Evidence of disorder in the orientations of the MA cation and PbI_6 octahedral tilts is observed below 100K.

good description of the dynamics of the MA cation present in the tetragonal phase of $Cs_{0.1}MA_{0.9}PbI_3$.[103]

A further disordered low temperature phase is hinted at from a change in the shift of the variable temperature PL measurements below 100 K. Dar *et al.* investigated this disorder through observing the dual PL emission exhibited by MA containing lead halide perovskites below 100 K.[151] Classical molecular dynamic simulations showed the MA cation to be kinetically trapped upon cooling, causing the formation of orientationally disordered domains. Density functional theory (DFT) calculations on $MAPbX_3$ material band gaps showed a difference in band gap between domains of ordered and disordered cation orientations, due to differences in the local electronic environment. SXRD presented in this chapter suggested the presence of disordered domains at low temperature, therefore it is possible that the 45 meV difference in the dominant and secondary PL peaks measured below 100K can be partly attributed to domain formation. However, photon reabsorption was determined to be the main contributor to secondary peak formation, as dual emission was also observed at high temperatures, in line with previous reabsorption studies on large $MAPbBr_3$ single crystals.[62]

Disorder of the MA cation can describe the difference in PL decay lifetimes observed between the tetragonal and orthorhombic phases extracted from TRPL measurements. Trap state mediated (k_1) and effective bimolecular (Bk_2) recombination rates increase on transition to the orthorhombic phase. It is likely the formation of disordered domains are able to act as recombination centres, therefore increasing PL recombination at low temperatures.[46]

Above the low temperature disordered phase ($>$ 100 K), variable temperature PL showed a blue shift in peak position with increasing temperature, an unexpected behaviour in PV semiconductors.[69] This shift was investigated further using $MAPbI_3$ crystals, grown as part of this work, and published in collaboration with the Nanostructured Materials for Optoelectronics and Energy Harvesting group at ICMAB.[70] Thermal expansion was concluded to account for 60% of the total energy shift, with 40% due to electron-phonon interactions. Thermal expansion causes a decrease in overlap between the outer Pb 6s and I 5p orbitals, resulting in a downshift of the valence band maxima in relation to the conduction band minima with increasing temperature.

5.3 Site Substitution with Bromine in Cs-MA Lead Iodide Perovskites

5.3.1 Mechanochemical Synthesis

In an attempt to simplify the synthesis of the perovskite $Cs_{0.1}MA_{0.9}Pb(I_{0.6}Br_{0.4})_3$, the mechanochemical method was investigated. Stoichiometric quantities of precursors PbI_2, $PbBr_2$, CsI, CsBr, MAI and MABr were ground together for 30 minutes using a pestle and mortar. Grinding using a ball mill was also investigated, with precursors added into a stainless steel container with grinding balls and placed in a Retsch Planetary Ball Mill. The number of grinding balls, revolutions per minute (rpm) and time in the ball mill were varied, with the best results using eight small grinding balls at 500 rpm for 30 minutes. Resulting powders were then annealed at 100°C in an oven overnight and the powder quality compared to the precipitation method through PXRD, as shown in Figure 5-12.

PXRD reflections for samples synthesised by grinding in a pestle and mortar could be assigned to the precursor salts, PbI_2, $PbBr_2$, δ-$CsPbI_3$ and small quantities of a perovskite phase. The quantity of perovskite phase present could be improved by grinding for a longer time, leading to investigation of synthesis using a ball mill. Figure 5-12 compares two powders of $Cs_{0.1}MA_{0.9}Pb(I_{0.6}Br_{0.4})_3$ synthesised by the ball mill at 500 rpm for 30 minutes and 200 rpm for 60 minutes. The higher energy 500 rpm milling process resulted in broader PXRD reflections indicating poorer crystalline quality. Karmakar *et al.*[115] used solid-state NMR spectroscopy to characterise local disorder in mixed halide perovskites synthesised through ball milling. The NMR data pointed to disorder centered at the Pb sites due to a range of Pb-X bond distances and angles.[115] This disorder contributed to the observed broadening of PXRD reflections, which decreased as the energy of the process was also decreased. However, Figure 5-12 shows the precipitation method to produce PXRD patterns with the sharpest peaks and fewest impurities, and therefore the best quality perovskite powder. The precipitation method was consequently used to produce the mixed halide samples investigated by NPD.

5.3.2 Variable Temperature Neutron Powder Diffraction

The phase behaviour of hydrogenous $Cs_{0.1}MA_{0.9}Pb(I_{0.6}Br_{0.4})_3$ was investigated using variable temperature NPD performed on the POLARIS instrument at the ISIS neutron

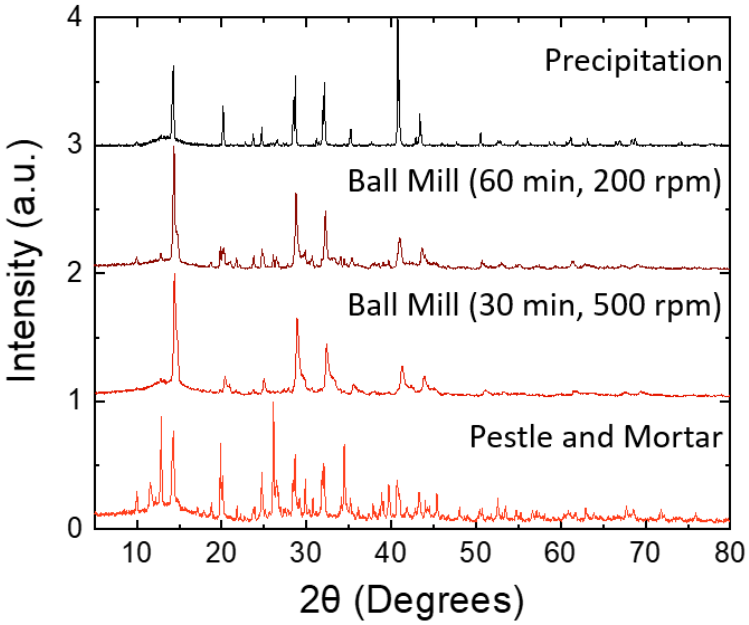

Figure 5-12: PXRD patterns for $Cs_{0.1}MA_{0.9}Pb(I_{0.6}Br_{0.4})_3$ samples synthesised mechanochemically using a pestle and mortar and a ball mill, compared with pattern achieved from the precipitation method.

and muon source. Approximately 6 g of hydrogenous $Cs_{0.1}MA_{0.9}Pb(I_{0.6}Br_{0.4})_3$ was cooled *in situ* from 300 K to 105 K at a rate of 2 $Kmin^{-1}$. The temperature was then increased to 290 K at a rate of 0.35 $Kmin^{-1}$ with data continuously binned into 3 K ranges.

Figure 5-13 (a) shows the NPD patterns from Bank 4 on POLARIS ranging from 1.50 Å to 3.69 Å. A small continuous shift to lower *d*-spacing can be seen from Figure 5-13 (a), in-line with a contracting unit cell with decreasing temperature. A lowering of symmetry with decreasing temperature can also be inferred, as the separation between the dominant split peaks, centered around 3.1 Å, increases from 290 K to 175 K. A shift in peak position is observed at 175 K, indicating a phase transition, akin to that seen in variable temperature NPD measurements on $Cs_{0.1}MA_{0.9}PbI_3$. It is likely this is a tetragonal to orthorhombic phase transition, similar to that observed in both $MAPbI_3$ and $MAPbBr_3$.[86,93]

The position of the probable tetragonal to orthorhombic phase transition at 175 K was unexpected. Recent variable temperature X-ray diffraction studies on $MAPb(I_{1-y}Br_y)_3$ compounds suggested the tetragonal-orthorhombic phase transition temperature decrease with increasing Br content.[163] This decrease in transition temperature was

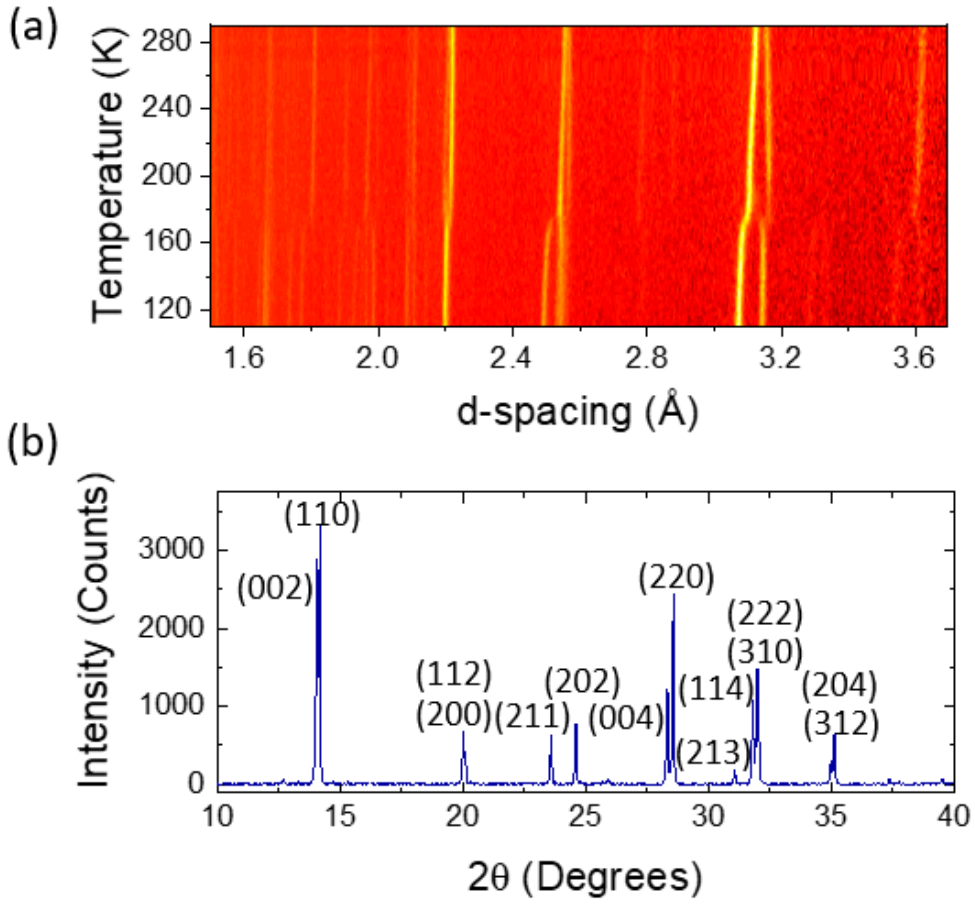

Figure 5-13: (a) Variable temperature NPD data of $Cs_{0.1}MA_{0.9}Pb(I_{0.6}Br_{0.4})_3$ recorded on the POLARIS instrument at the ISIS neutron and muon source. (b)PXRD pattern of $Cs_{0.1}MA_{0.9}Pb(I_{0.6}Br_{0.4})_3$ indexed to the tetragonal space group P4/*mmm*.

determined to be due to Br substitution increasing disorder in the crystal structure, enabling the rotational disorder of the MA cation associated with the tetragonal phase to be present at lower temperatures. The study found a transition temperature of 130 K for $MAPb(I_{0.8}Br_{0.2})_3$, 45 K lower than that measured for $Cs_{0.1}MA_{0.9}Pb(I_{0.6}Br_{0.4})_3$ in this work.[163] Crucially the mixed I/Br perovskite investigated here also contained Cs. The inclusion of Cs may lead to further geometric frustration of the lead-halide framework, restricting the rotational disorder of the organic cation, and so raising the transition temperature.[142] Further work investigating the low temperature structure and local environment of this complex mixed cation-halide perovskite is needed to understand this interesting phase behaviour.

Unfortunately, due to the poor signal-to-noise ratio due to the fully hydrogenated sample, profile fitting of the NPD data was not possible; however, PXRD data acquired at 293 K could be assigned to a tetragonal phase (Figure 5-13 (b). The PXRD pattern indexed best to the space group P4/mmm, lattice parameters $a = 8.838$ Å $c = 12.600$ Å.

Changes in the preferred tetragonal space group is determined by the distortion of the perovskite structure. Tolerance (t) and octahedral (μ) factors give an indication of the distortion, with stable structures tending to have values of $0.8 \leq t \leq 1$ and $\mu > 0.41$.[77] While the t values for $Cs_{0.1}MA_{0.9}Pb(I_{0.6}Br_{0.4})_3$ and $Cs_{0.1}MA_{0.9}PbI_3$ are the identical (both at 0.960) the value of μ is 0.012 greater for the mixed halide material. The difference is due to the inclusion of the smaller Br^- ion, and change in Pb^{2+} due to coordination with different halides.[79,82] A change in octahedral factor indicates a change in the shape and tilting of the PbX_6 corner octahedra, altering the symmetry of the structure. The PXRD data shows substitution of 40% Br at the perovskite X-site forces the structure to adopt the P4/mmm space group occupied by tetragonal $MAPbBr_3$, as opposed to the I4/mcm structure favoured by $MAPbI_3$ at 293 K.[86,93]

5.4 Conclusions

This chapter primarily investigated the phase behaviour of $Cs_{0.1}MA_{0.9}PbI_3$ perovskites through variable temperature NPD, PXRD and variable temperature PL. The substitution limit of Cs in $Cs_xMA_{1-x}PbI_3$ was also investigated using PXRD and EDX, and determined to be $x < 0.15$, with a preferred composition of $x = 0.12$.

$Cs_{0.1}MA_{0.9}PbI_3$ was shown to undergo a tetragonal to orthorhombic phase transition at 165 K, identical to the transition temperature of $MAPbI_3$. However, unlike the abrupt tetragonal-orthorhombic phase change seen in $MAPbI_3$, a glass-like transition was observed in variable temperature NPD measurements on $Cs_{0.1}MA_{0.9}PbI_3$. Incorporation of Cs into the crystal structure was determined to cause geometric strain in the lead iodide framework, subsequently affecting the dynamics of the MA cation. This effect was enough to induce a glass-like phase change, but not capable of altering the transition temperature when compared to $MAPbI_3$. Further *ab initio* calculations on the cation and lead-iodide framework dynamics would be beneficial in understanding this behaviour.

A low temperature (< 100 K) phase was inferred through variable temperature PL measurements, proposed to be due to disorder. It was suggested that disordered domains, formed due to freezing of the MA cation, caused subtle differences in the local electronic structure of $Cs_{0.1}MA_{0.9}PbI_3$, reversing the shift in PL position with temperature. However, photon reabsorption effects (present due to the size of the crystal investigated) masked evidence of disordered domain formation.

The phase behaviour of $Cs_{0.1}MA_{0.9}Pb(I_{0.6}Br_{0.4})_3$ was also investigated using variable temperature NPD. A tetragonal-orthorhombic phase transition was observed at 175 K, higher than expected for mixed I-Br perovskites. The high transition temperature was suggested to be caused by the addition of Cs frustrating the lead-halide framework; however, further work determining a full structural solution for these complex materials is needed.

The work presented in this chapter contributes to the understanding of the intrinsic properties of perovskite compounds commonly used in high performing PV devices. The detailed phase behaviour of these mixed cation-halide materials was poorly understood, but vital in the design of devices which operate over a wide range of temperatures.

Chapter 6

Formamidinium Methylammonium Lead Halide Perovskites

6.1 Introduction

The physical properties of fully inorganic cesium metal halide perovskites have been the subject of investigation for decades, although research into hybrid organic-inorganic perovskites has since eclipsed that of their inorganic counterparts.[15,24,154,164–166] A variety of organic ions have been used, including large cations such as $CH_3(CH_2)_3NH_3^+$, which enable the formation of layered materials sometimes referred to as 2D perovskites.[11,89,90,167] These 2D perovskites are formed of layers of 3D perovskite frameworks joined together by organic spacer cations, and have also shown promise in increasing the efficiency and stability of PV devices.[168] However, this work focuses on the use of smaller organic cations, capable of fitting inside the metal-halide perovskite framework, forming traditional 3D ABX_3 structures.

In 2014 Pellet *et al.* first combined the methylammonium ($CH_3NH_3^+$, MA) and formamidinium ($CH(NH_2)_2^+$, FA) cations into mixed A-site perovskite PV devices. The $FA_xMA_{1-x}PbI_3$ cells demonstrated superior PV performance when compared to pure $MAPbI_3$ or $FAPbI_3$ devices; for example, showing improved incident-photon-to-current conversion efficiency. This was determined to be caused by improved diffusion lengths because of enhanced charge carrier lifetimes in the mixed cation phase.[20] Structural studies were subsequently carried out on $FA_xMA_{1-x}Pb(I_{1-y}Br_y)_3$ materials, showing a linear dependence of lattice parameter and bandgap with cation and halide composition according to Vegard's law.[169,170] However, these studies did not determine the true composition and crystal systems of these hybrid perovskites, which were deposited as thin films in different device architectures. It is possible that cation incorporation is strongly method dependent, implying the formation of varying perovskite compositions in PV devices using the same initial precursor ratios.

The uncertainty over the up-take of cations into the perovskite structure prompted work conducted as a Master of Research degree carried out prior to this thesis, where the behaviour of bulk FA-MA lead iodide materials was investigated.[95] NMR spectroscopy compared the observed and expected ratios of MA to FA, confirming that uptake of the MA and FA cations mirrored the concentrations used in precursor solutions. A linear relationship in bandgap and lattice parameter according to Vegard's law was also observed, as shown in Figure 6-1. Structural information extracted from NPD, SXRD and PXRD measurements agreed, showing the $FA_xMA_{1-x}PbI_3$ perovskite to transition from a tetragonal to cubic structure between $x = 0.1$ and 0.2, accounting for the discrepancy in bandgap energy values observed for $x \leq 0.1$.[95]

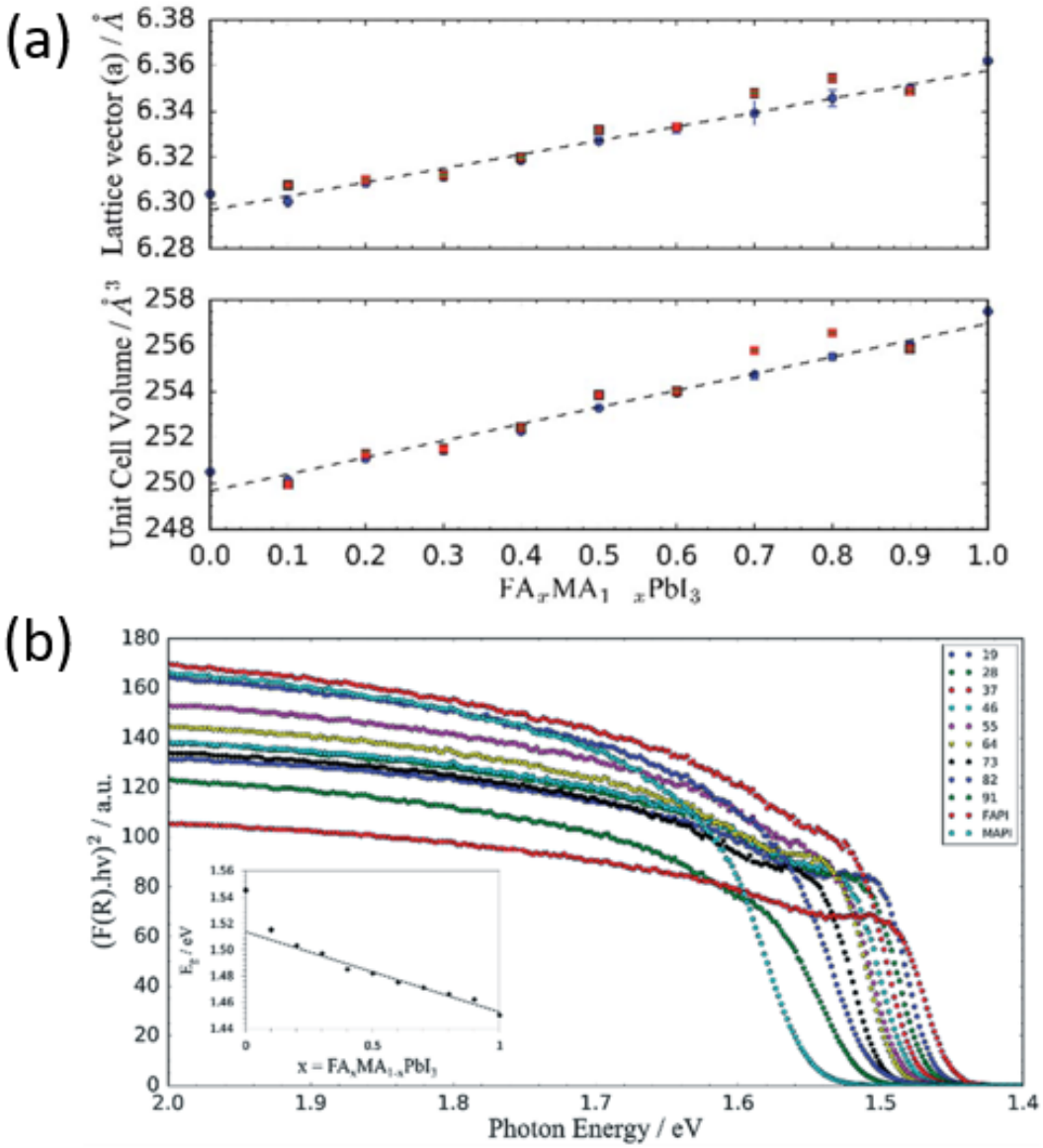

Figure 6-1: Reproduced from from Weber *et al.*[95] (a) cell parameters vs composition for $FA_xMA_{1-x}PbI_3$, black circles represent data taken from NPD, blue circles from SXRD and red squares from PXRD. (b) UV-VIS spectra for $FA_xMA_{1-x}PbI_3$ showing decreasing bandgap with increasing FA content (increasing x) with inset showing band gap values for each composition x.

As discussed in Chapter 2 Section 2.7, site substitution at the A-site of the perovskite structure improves material stability. The mixed $FA_xMA_{1-x}PbI_3$ system has shown resistance to the formation of decomposition products favoured in phase pure $MAPbI_3$ and $FAPbI_3$.[99,111] Inclusion of 10% MA into the $FAPbI_3$ structure has been shown to stabilise the desirable cubic α-phase at room temperature, and 10% substitution of FA into the $MAPbI_3$ structure reduces degradation to precursor salts and lead iodide.[95,99,111] At the time of this work, the improved material stability of these mixed cation-halide perovskites was showcased in long lived perovskite PV devices, displaying a stabilised 18% power output over 250 hours.[81]

Despite the popularity of mixed FA-MA lead halide materials in the PV community, little was known about the structural phase behaviour and intrinsic stability of these hybrid organic-inorganic perovskites. A detailed understanding of structural variations with composition and temperature is vital in the understanding of device behaviour over a range of environments. A full understanding of decomposition routes in these mixed phases is also essential in ensuring the longevity of perovskite containing devices. These important factors motivated the work presented in this chapter, which was the first to systematically study degradation in $FA_xMA_{1-x}PbI_3$ across the whole composition range ($0 \leq x \leq 1$). The results are published under item 6 of the publication list presented at the beginning of this thesis, with additional results and collaborative work also presented in this chapter.

6.2 Phase Behaviour of FA-MA Lead Iodide Perovskites

The complete phase behaviour of $FA_xMA_{1-x}PbI_3$ ($0 \leq x \leq 1$) up to 350 K was investigated in collaboration with the Nanostructured Materials for Optoelectronics and Energy Harvesting (NANOPTO) group at ICMAB. Crystals grown by the space confined technique (described in Chapter 3 Section 3.1.5) were measured at ICMAB using variable temperature PL and Raman spectroscopy. Extracted phase transition temperatures from these measurements were combined with those determined through XRD as part of the work published prior to this PhD.[95] The resulting phase diagram (Figure 6-2) was compiled by Adrián Francisco and Professor Alejandro R. Goñi.

The tetragonal phase exists at room temperature for $FA_xMA_{1-x}PbI_3$ where $x < 0.2$. The cubic phase is stabilised at room temperature with increasing FA content, although the tetragonal phase emerges below 250 K across all compositions. One of three tetragonal phases is present by 250 K, occupying the I4/mcm space group for MA rich compounds ($x < 0.3$), the P4bm space group between $x = 0.3$ and 0.5, and the P4/mbm space group for FA rich compositions ($x > 0.5$). The appearance of an additional orthorhombic phase at low temperatures is suppressed for $x \geq 0.4$. The presence of the low temperature disordered phase below 140 K, present in $FAPbI_3$ and discussed in previous chapters, is not shown in the phase diagram.[74]

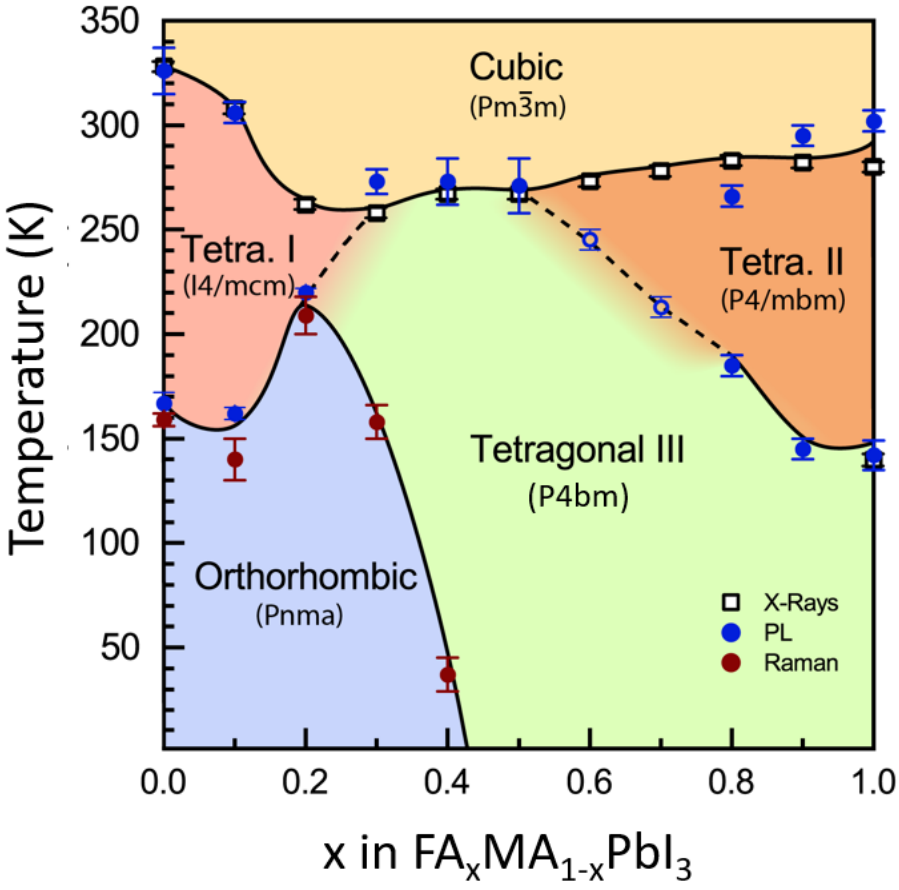

Figure 6-2: Map of metastable phases for $FA_xMA_{1-x}PbI_3$ ($0 \leq x \leq 1$). The schematic was produced by Adrián Francisco and is included with the kind permission of the NANOPTO group at ICMAB.

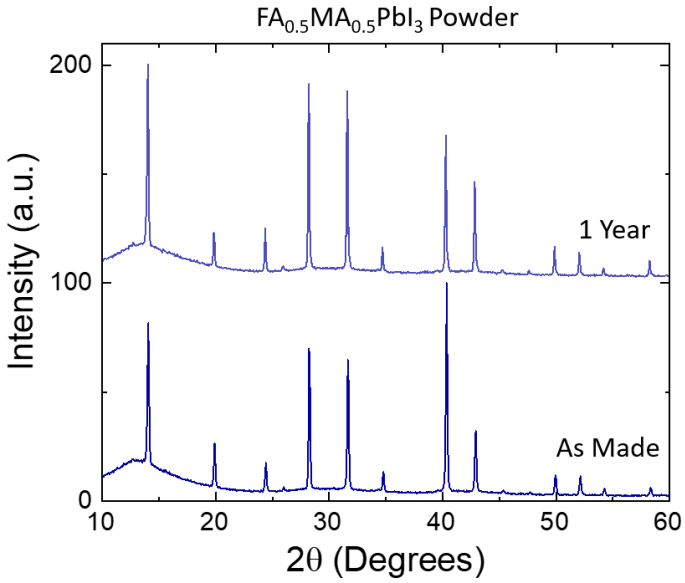

Figure 6-3: PXRD patterns of the same $FA_{0.5}MA_{0.5}PbI_3$ sample synthesised by precipitation, measured one year apart. The amorphous peak at low 2θ was due to the sample holder.

6.3 Stability of FA-MA Lead Iodide Powder

A powder sample of $FA_{0.5}MA_{0.5}PbI_3$ synthesised by the precipitation method in January 2016 was investigated during the course of this work. The as-made sample was measured using PXRD, and then measured again exactly one year on from the date of synthesis, as shown in Figure 6-3. Despite exposure to oxygen, light and an average relative humidity of 57%, the patterns appeared near identical, suggesting negligible structural degradation over one year. In contrast, one year old samples of pure $MAPbI_3$ and $FAPbI_3$, stored under the same conditions, were discoloured, suggesting degradation to MAI and PbI_2 in $MAPbI_3$ and the δ-phase of $FAPbI_3$.[17]

The measurement of the stable one-year old $FA_{0.5}MA_{0.5}PbI_3$ sample prompted an investigation into the structural integrity of mixed organic cation perovskite thin films. It is known that powder materials are more resilient to degradation than thin films,[17,171,172] therefore the following study was carried out over only ten days.

6.4 Trends in Stability of FA-MA Lead Iodide Thin Films

6.4.1 Thin Film Degradation

Films of $FA_xMA_{1-x}PbI_3$ ($0 \leq x \leq 1$, in increments of 0.1) were deposited onto clean glass substrates by spin coating. PXRD patterns of films ($0 \leq x \leq 0.8$) were collected immediately after deposition, and again after one, three, five, seven and ten days. Films were stored in the dark, at room temperature and at a controlled relative humidity ($<$ 30%), similar to conditions present in a manufacturing environment.

Figure 6-4 shows the patterns collected for films of $FA_xMA_{1-x}PbI_3$ ($0 \leq x \leq 0.5$) as synthesised (bottom trace) through to films aged for ten days (top trace). The (100) perovskite reflection can be seen in all patterns, centered around $2\theta = 14°$. An additional peak, at $2\theta = 12.7°$, emerged in patterns after aging, representing the (001) reflection for PbI_2. For $0 \leq x \leq 0.2$ the intensity of the (001) PbI_2 reflection grew rapidly, becoming more intense than the (100) perovskite peak after ten days.

Figure 6-5 shows the patterns collected for films of $FA_xMA_{1-x}PbI_3$ ($0.6 \leq x \leq 0.8$). Thin films of $x \geq 0.9$ converted to the hexagonal non-perovskite δ-$FAPbI_3$ within minutes of exposure to atmosphere, and were therefore not included in the kinetic study presented later in this chapter. The evolution of PXRD patterns suggested increasing inclusion of FA into the $MAPbI_3$ structure suppressed PbI_2 formation. At $x = 0.6$, PbI_2 growth could be blocked completely in pristine films. However, when repeating measurements on multiple $FA_{0.6}MA_{0.4}PbI_3$ samples, it was observed that small amounts of PbI_2 present in as-made films accelerated perovskite degradation. For $x \geq 0.7$ the δ-$FAPbI_3$ peak at $2\theta = 11.7°$ was immediately present, indicating instability to δ-$FAPbI_3$ formation beyond the stable $x = 0.6$ composition.

6.4.2 Kinetics of Lead Iodide Crystallisation

In order to gain a full understanding of the decomposition of mixed cation perovskites, the kinetics of formation of degradation products was considered. The Johnson-Mehl-Avrami-Kolmogorov (JMAK) approach was used. The model can be used to provide a simplified description of nucleation and subsequent crystal growth on thin film surfaces. The work was popularised by two papers published in 1939 and 1940 by Melvin Avrami, resulting in the JMAK model often being referred to as Avrami kinetics.[173–175]

The JMAK equation (often called the Avrami equation) describes the fraction of trans-

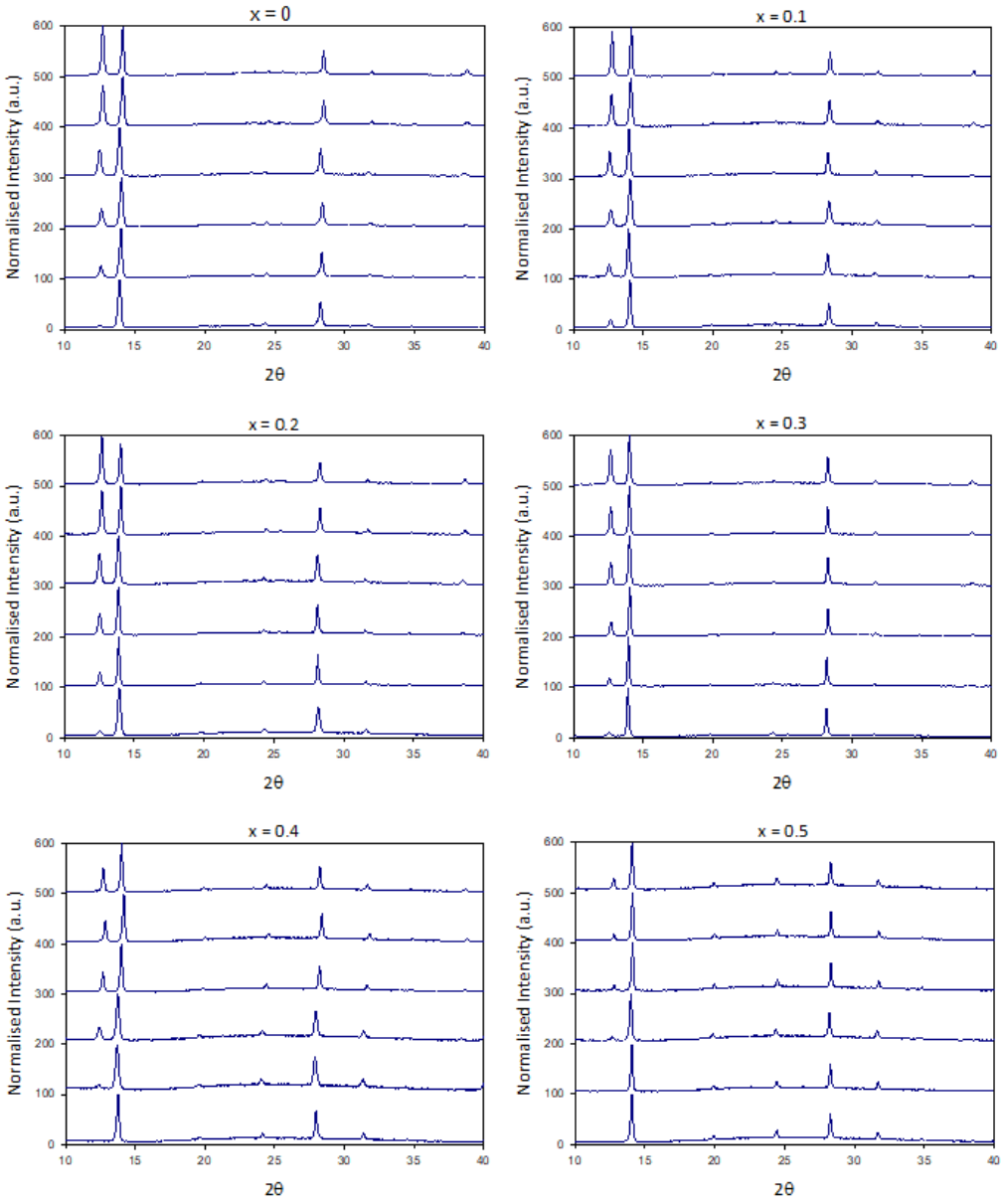

Figure 6-4: PXRD patterns of $FA_xMA_{1-x}PbI_3$ ($0 \leq x \leq 0.5$). Patterns were measured immediately after synthesis (bottom trace) and then through 1, 3, 5, 7 and 10 days (top trace). Patterns show the emergence of the (001) peak of PbI_2 at 12.7°

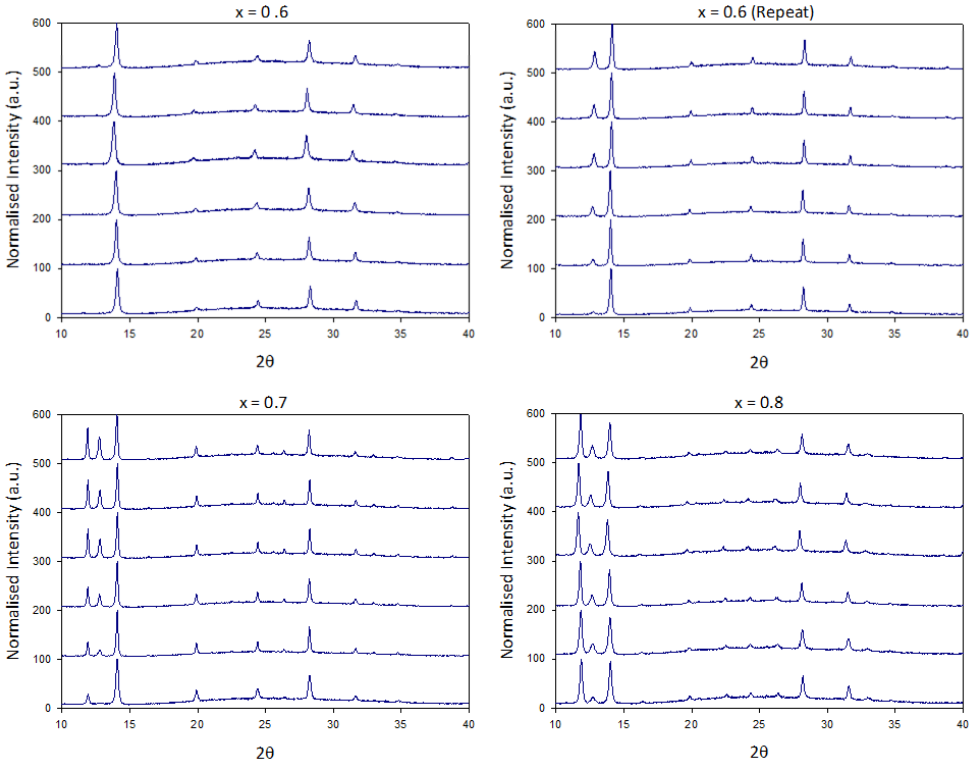

Figure 6-5: PXRD patterns of $FA_xMA_{1-x}PbI_3$ ($0.6 \leq x \leq 0.8$). Patterns were measured immediately after synthesis (bottom trace) and then through 1, 3, 5, 7 and 10 days (top trace). Patterns show the emergence of the (001) peak of PbI_2 at 12.7° and the δ-$FAPbI_3$ phase at 11.7°

formed material (α) by:

$$\alpha = 1 - e^{-(kt)^m} \tag{6.1}$$

where k is the rate constant, t is time and m is the Avrami exponent.[174,175] The value of m is dependent on the crystallisation mechanism. An m value of 2 implies *site saturation*, where all nuclei of the transformed phase are present and grow from the start of crystallisation; whereas a value of 3 implies *continuous nucleation*, where new nuclei continuously appear and grow. However, the validity of this description has been called into question, and was therefore not considered in the work presented in this chapter.[176,177]

The kinetics of the decomposition to PbI_2 in thin films of $FA_xMA_{1-x}PbI_3$ ($0 \leq x \leq 0.6$) were investigated. Films of $x \geq 0.7$ were not included in the analysis due to the significant growth of δ-$FAPbI_3$. Figure 6-6 (a) shows an example of a $FA_{0.2}MA_{0.8}PbI_3$ film degrading from black to yellow over ten days. This transformation was reflected in PXRD patterns of $FA_xMA_{1-x}PbI_3$ ($x = 0$, 0.4) highlighted in Figure 6-6 (b) which clearly shows the evolution of the (001) PbI_2 reflection over ten days, a degradation route that was suppressed in films of $FA_{0.6}MA_{0.4}PbI_3$.

Decomposition according to the following reaction was assumed:

$$MA_{1-x}FA_xPbI_3 \rightarrow (1-x)MAI + xFAI + PbI_2. \tag{6.2}$$

An attempt was made to measure the phase fraction (α) of PbI_2 present through Rietveld refinement of PXRD data for each film. However, due to the highly orientated nature of the films, values for the phase fraction resulted in large errors. Therefore, each PXRD pattern was normalised to the pattern obtained for the relevant phase pure $FA_xMA_{1-x}PbI_3$ system. The area (A) under the peak of the (001) reflection for PbI_2 was then used to approximate the phase fraction of PbI_2 present through the rearranged JMAK equation:

$$lnln\left(\frac{1}{1-A}\right) = mln(t) + mln(k) \tag{6.3}$$

where k is the rate constant, t is the age of the film, m is the Avrami exponent and A is the area under the (001) PbI_2 reflection.

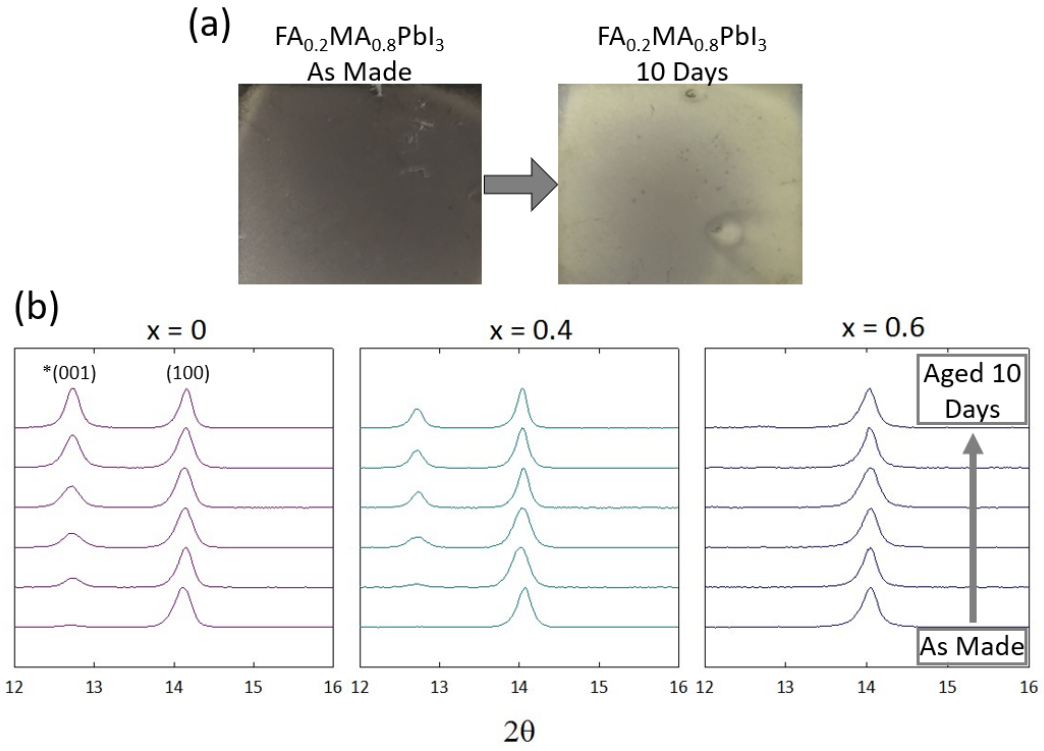

Figure 6-6: (a) Photos of a $FA_{0.2}MA_{0.8}PbI_3$ thin film as-made and aged ten days. (b) PXRD patterns of $FA_xMA_{1-x}PbI_3$ ($x = 0$, 0.4, 0.6) measured over ten days, enlarged to show (100) perovskite peak and growth of PbI_2 indicated by growth of *(001) reflection.

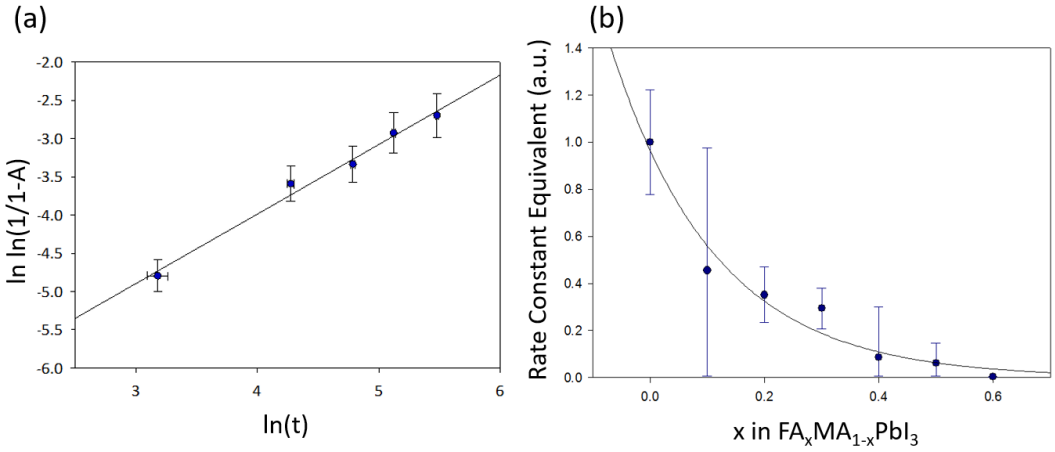

Figure 6-7: (a) Example JMAK plot for $FA_{0.5}MA_{0.5}PbI_3$, where A is the peak area under the (001) refection for PbI_2 measured in PXRD patterns taken over time t in hours. (b) Rate constant equivalents for PbI_2 growth in thin films, fitted with an exponential decay.

Values for $lnln(1/1-A)$ were plotted against $ln(t)$ to determine if the formation of PbI_2 over time was linear, indicative to JMAK kinetics. A linear dependence was observed for $0 \leq x \leq 0.3$ up to five days, after this time - due to the rapid decay of the thin films - the large peak area of the (001) PbI_2 reflection was not representative of the phase fraction of PbI_2 present. However, for $x \geq 0.4$, a linear relationship between $lnln(1/1-A)$ and $ln(t)$ was observed for the full duration of the study. JMAK kinetic plots for all $FA_xMA_{1-x}PbI_3$ ($0 \leq x \leq 0.6$) thin films can be found in Appendix D, with an example for $FA_{0.5}MA_{0.5}PbI_3$ shown in Figure 6-7 (a).

Each JMAK kinetic plot, representing formation of PbI_2 in $FA_xMA_{1-x}PbI_3$ thin films over ten days, was fitted with a linear model. The gradient and y-intercept were extracted from these models and subsequently used to calculate a rate constant (k) for PbI_2 formation, referred to here as the *rate constant equivalent*. The JMAK equation requires knowledge of the exact PbI_2 phase fraction present in order to provide a true rate of crystallisation. In this work, the area under the (001) PbI_2 reflection was used as an approximation to the phase fraction; therefore, k was not an exact value, but proportional to the true rate of PbI_2 formation. The rate constant equivalent was therefore used to illustrate the trend in the rate of PbI_2 formation across the $FA_xMA_{1-x}PbI_3$ compositions.

Rate constant equivalents were plotted for $FA_xMA_{1-x}PbI_3$ ($0 \leq x \leq 0.6$) and fitted with an exponential decay function as shown in Figure 6-7 (b). The exponential decay in the rate constant equivalent demonstrated a clear trend towards increased resistance

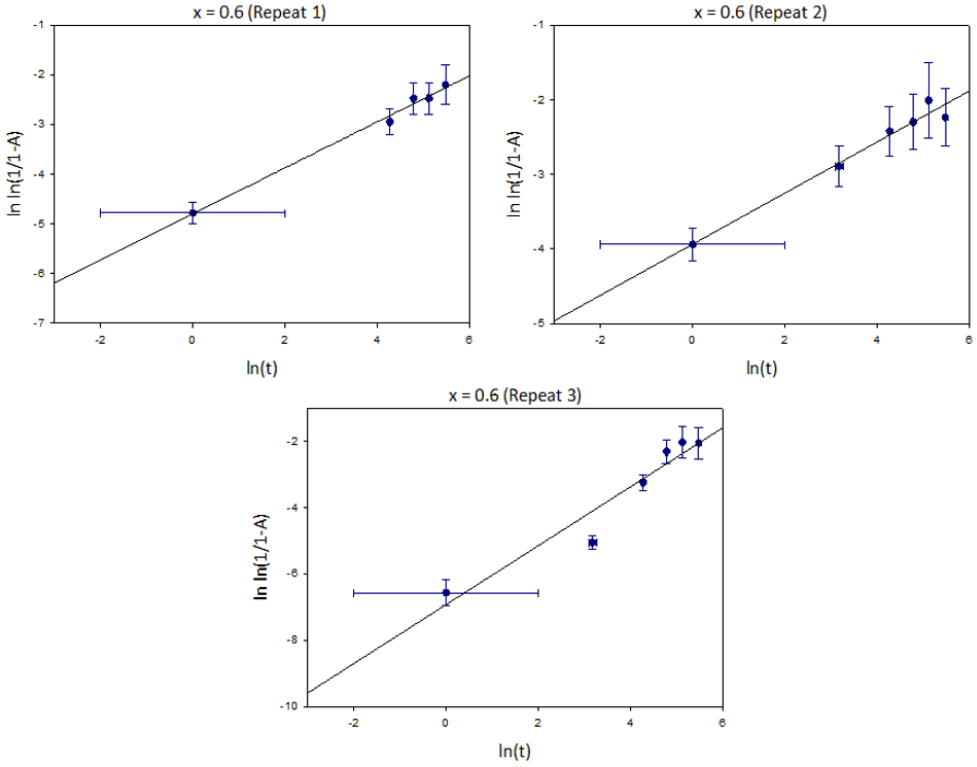

Figure 6-8: JMAK plots for the growth of PbI_2 in $FA_{0.6}MA_{0.4}PbI_3$ thin films. The rate of decomposition to PbI_2 varied depending on the phase purity of as-made films.

to PbI_2 formation in $MA_{1-x}FA_xPbI_3$ as x approached 0.6.

6.4.3 Stability Issues in Champion Composition

The presence of even trace amounts of PbI_2 in as-made films accelerated perovskite decomposition. While phase pure $FA_{0.6}MA_{0.4}PbI_3$ demonstrated negligible degradation over the ten day study, repeated measurements on samples containing various quantities of PbI_2 in as-made films showed rapid degradation. This was investigated further through the deposition of multiple $FA_{0.6}MA_{0.4}PbI_3$ films with varying amounts of PbI_2 measured in as-made samples. Films initially containing the greatest amount of PbI_2 showed rapid degradation, in some cases with the (001) PbI_2 reflection surpassing the intensity of the (100) perovskite reflection after ten days. Kinetic diagrams for PbI_2 formation in contaminated $FA_{0.6}MA_{0.4}PbI_3$ films are shown in Figure 6-8. Synthesis of pristine, phase pure perovskite thin films were vital during the deposition stage in order to successfully suppress degradation.

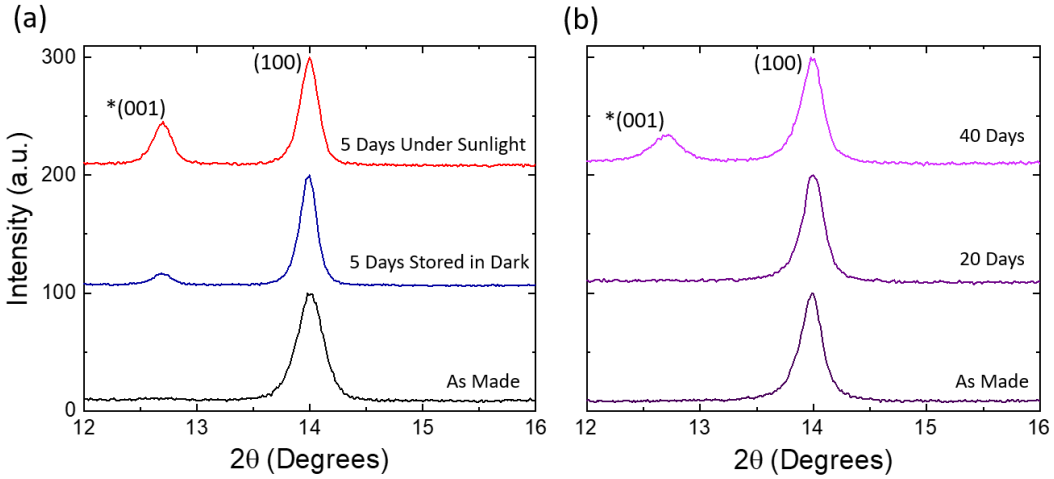

Figure 6-9: (a) $FA_{0.6}MA_{0.4}PbI_3$ films stored in the dark and under sunlight. (b) A stable $FA_{0.6}MA_{0.4}PbI_3$ sample, showing degradation only after forty days.

In addition to phase purity, storage conditions also played a pivotal role in perovskite decomposition rates. As observed in multiple studies, the perovskite thin films were sensitive to sunlight.[109,145,178,179] Films of the champion composition $FA_{0.6}MA_{0.4}PbI_3$ were compared after five days stored in the dark and five days stored under sunlight in the same dry conditions ($< 30\%$ relative humidity). The films were then measured using PXRD, the results of which are shown in Figure 6-9(a). A small amount of PbI_2 was present in the film stored in the dark, characterised by the appearance of the (001) PbI_2 reflection, although a larger proportion was present in the film stored under sunlight. The increase in PbI_2 formation under sunlight showed cation substitution did not significantly improve photo-stability.

One particularly stable film of $FA_{0.6}MA_{0.4}PbI_3$ showed no significant degradation after twenty days, with PXRD measurements indicating some degradation to PbI_2 after forty days (Figure 6-9 (b)). The range of perovskite stabilities shown in $FA_{0.6}MA_{0.4}PbI_3$ highlight the sensitivity of hybrid lead iodide perovskites to impurities and defects present in the thin film.

The use of both MA and FA cations were determined to improve the intrinsic stability of the perovskite structure, leading to investigation of decomposition routes by *ab-initio* methods.

6.4.4 Decomposition Energies

Complementary to the kinetic study described above, *ab-initio* simulations were performed by Jessica Dillon in collaboration with Professor Saiful Islam's Energy Materials Research Group at the University of Bath. The degradation energies (ΔE_{deg}) corresponding to enthalpies of formation were considered for two decomposition routes, referred to as Reaction 1 and 2:

$$\begin{aligned} \text{Reaction 1: } & FA_xMA_{1-x}PbI_3 \rightarrow xFAI + (1-x)MAI + PbI_2 \\ \text{Reaction 2: } & FA_xMA_{1-x}PbI_3 \rightarrow x(\delta FAPbI_3) + (1-x)(MAI + PbI_2) \end{aligned} \tag{6.4}$$

Starting conditions were varied between the cubic, high or low order structure of $FAPbI_3$, the tetragonal structure of $MAPbI_3$ or a 64 formula unit disordered cell. MA and FA were added to these initial structures in relevant ratios and the resulting ΔE_{deg} are plotted against composition x in Figure 6-10. These simulations suggest decomposition routes for mixed organic cation lead iodide perovskites to be less energetically favourable than pure $MAPbI_3$ and $FAPbI_3$.

6.4.5 Emergence of δ-$FAPbI_3$

As seen in Figure 6-5, PXRD patterns of $FA_xMA_{1-x}PbI_3$ (≥ 0.7) taken over ten days showed the evolution of a reflection at $2\theta = 11.7°$, representing the presence of δ-$FAPbI_3$. The appearance of this dominant decomposition pathway made modelling PbI_2 growth unfeasible. However, the kinetics of δ-$FAPbI_3$ growth could be investigated for $FA_{0.7}MA_{0.3}PbI_3$. In this case, the area under the δ-$FAPbI_3$ peak (A) was used to approximate phase fraction in the JMAK equation, and the resulting values of $lnln(1/1-A)$ were plotted against $ln(t)$ in Figure 6-11. The linear relationship implied δ-$FAPbI_3$ formation also followed JMAK kinetics at $x = 0.7$. However, at higher values of x decomposition occurred over minutes, and was therefore too fast to be considered in this study. For all $x \geq 0.7$, it was observed that the preferred direction of reaction 2 could be reversed though heating to 100°C. After a few minutes the perovskite phase re-formed, as observed in previous studies[74,87]

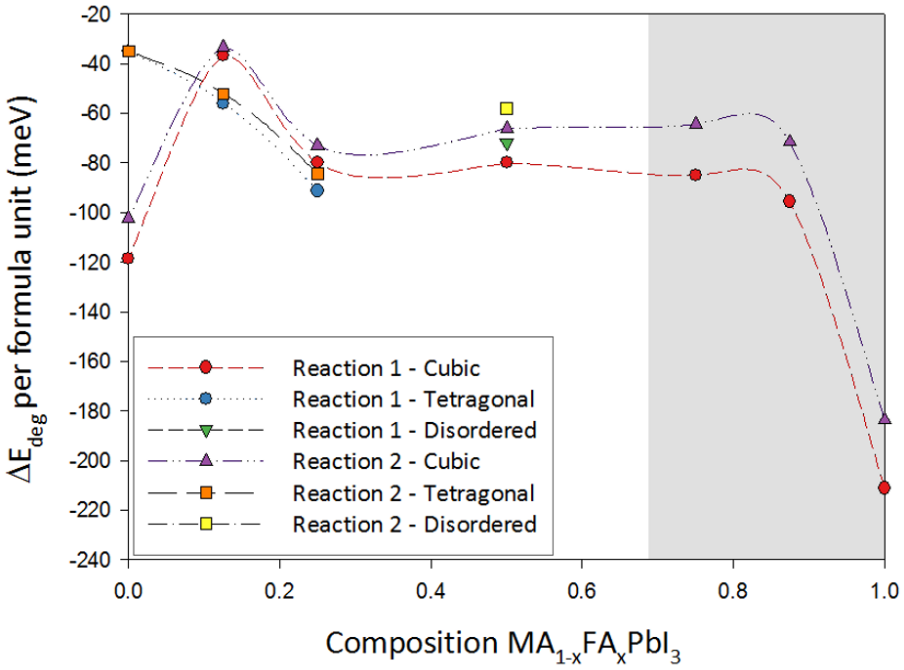

Figure 6-10: Calculated degradation energies (ΔE_{deg}) for decomposition Reactions 1 and 2. The shaded region indicates compositions of $x > 0.7$ which favour decomposition to δ-$FAPbI_3$.

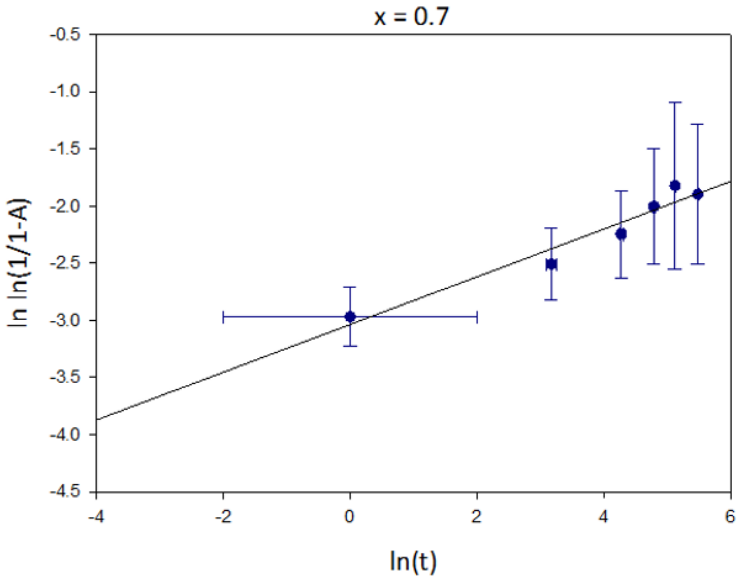

Figure 6-11: JMAK plot for the growth of δ-$FAPbI_3$ in $FA_{0.7}MA_{0.3}PbI_3$ though measuring the area under the reflection at $2\theta = 11.7°$ (A) over time in hours (t).

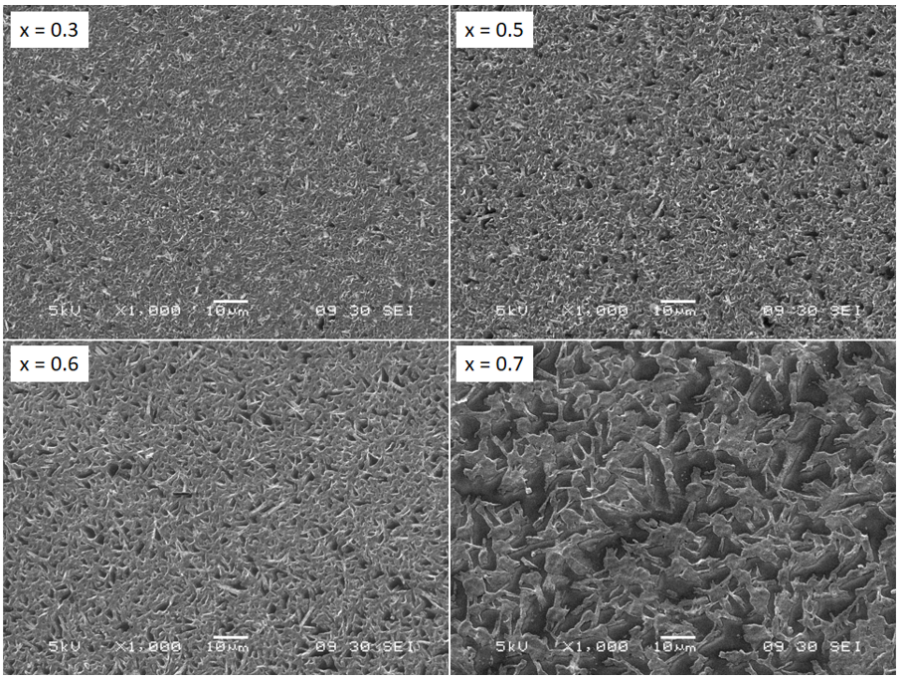

Figure 6-12: SEM images of $FA_xMA_{1-x}PbI_3$ (x = 0.3, 0.5, 0.6, 0.7) thin films.

6.4.6 Thin Film Morphology

Figure 6-12 shows secondary electron images taken at a magnification of x 1000 of $FA_xMA_{1-x}PbI_3$ thin films of composition x = 0.3, 0.5, 0.6, 0.7. Average crystallite size was measured using the program ImageJ,[121] which revealed an increase from 3.5 μm to 6 μm between compositions of x = 0.6 and 0.7 respectively, coinciding with the appearance of δ-$FAPbI_3$. A small increase of 3 μm to 3.5 μm average crystallite size was measured between x = 0.3 and 0.6. The small variation in crystallite size below the appearance of δ-$FAPbI_3$ was deemed not to significantly affect film degradation.

It is important to note film morphology has a considerable effect on the stability of thin films and improved crystallisation of perovskites onto various substrates is an active field of research.[180,181] Film morphology is determined through a number of variables such as deposition method and substrate type, as discussed later in this chapter.[181] The consideration of various deposition methods, use of a range of substrates, encapsulation and/or device fabrication offers a plethora of potential avenues of investigation into mixed cation stability, but lie beyond the scope of this investigation.

6.5 Discussion

Nagabhushana *et al.* demonstrated $MAPbI_3$ to be thermodynamically unstable, preferentially degrading into MAI and PbI_2.[99] By analogy of the degradation process shown in $MAPbI_3$, this study assumed decomposition of the mixed FA-MA cation perovskite, according to Reaction 1 (6.4) for $x < 0.7$. For compositions of $x \geq 0.7$, PXRD showed competition between the pathway forming PbI_2 and that forming the hexagonal δ-$FAPbI_3$ phase through Reaction 2 (6.4).

Reaction 1 was favoured in MA rich compositions, with the addition of FA cations slowing the rate of conversion from perovskite to PbI_2. Reaction 2 was suppressed in FA rich compositions by the addition of MA cations, as shown by the reduced intensity of δ-$FAPbI_3$ peaks in $x = 0.7$ thin films ages for ten days compared to films of $x = 0.8$. PXRD measurements showed formation of δ-$FAPbI_3$ was completely suppressed for $x \leq 0.6$, indicating degradation to occur via reaction 1 only. The preferred degradation pathways across the full composition range in $FA_xMA_{1-x}PbI_3$ are summarised schematically in Figure 6-13.

The kinetic study investigating PbI_2 formation through reaction 1 in $FA_xMA_{1-x}PbI_3$ ($0 \leq x \leq 0.6$) showed a clear reduction in degradation rate as x approached 0.6. Particularly high rates of PbI_2 formation were observed for $x \leq 0.2$, corresponding with the presence of the tetragonal $MAPbI_3$-like structure at room temperature.[95] The increase in resistance to degradation through reaction 1 was determined to be due to the stabilisation of the perovskite structure, caused by stronger interactions between the cations and iodide in the mixed phase.[80,111]

Increased stability of the mixed FA-MA cation perovskite phase was also shown in *ab initio* simulations. All the mixed $FA_xMA_{1-x}PbI_3$ ($0.1 \leq x \leq 0.6$) compositions showed less favourable energetics for decomposition via reaction 1 than pure $MAPbI_3$. When the cubic α-$FAPbI_3$ perovskite structure was considered, decomposition via reaction 1 and 2 was shown to be highly exothermic, suggesting a thermodynamically unstable structure. These thermodynamic results agreed with the experimental study measuring the kinetics of PbI_2 formation and observations of fast transformation to the δ-phase of $FAPbI_3$ rich thin films.

The results of the thermodynamic and kinetic investigations were further supported by the phase behaviour of $FA_xMA_{1-x}PbI_3$ determined in collaboration with ICMAB. Combined PL, and XRD measurements showed the cubic perovskite phase of $FA_xMA_{1-x}PbI_3$ to be stabilised at room temperature for $x \geq 0.2$. The stronger cation-iodide interaction

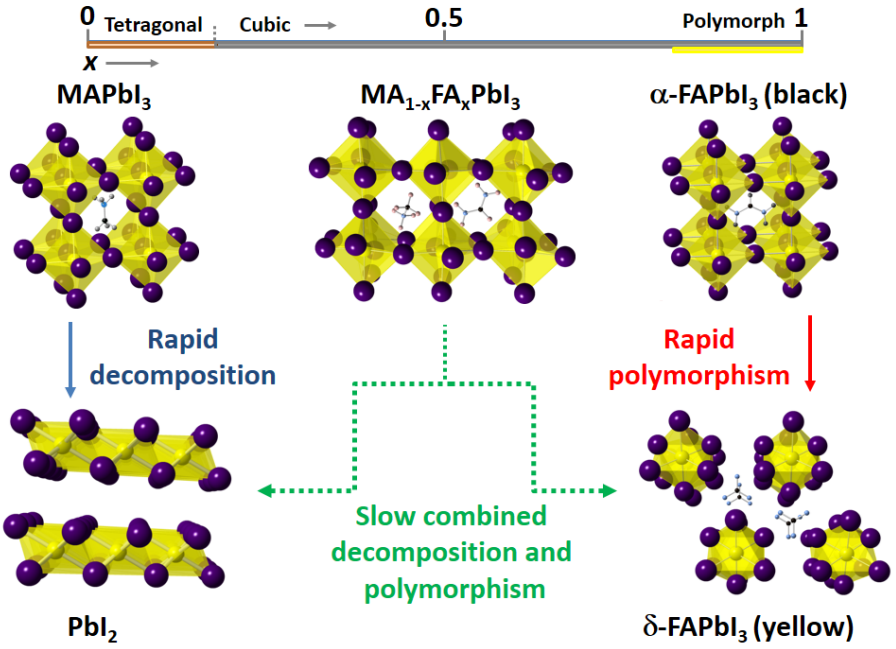

Figure 6-13: Schematic of the degradation routes in $FA_xMA_{1-x}PbI_3$ ($0 \leq x \leq 1$) at room temperature.[80]

present in these cubic phases increased material stability.

The theoretical optimum A-site cation size suggested by perovskite octahedral (μ) and tolerance (t) factors also supported the increased stability shown in the mixed FA-MA phases. Figure 6-14 shows the shift in tolerance factor achieved through site substitution at the A-site, and also indicates the region in which the ideal cubic perovskite structure forms. Outside of this region the effective size of the A-site cation is either too low or too high to form the ideal cubic perovskite structure. For low t the lead-iodide framework tilts due to the smaller cation size, forming a tetragonal structure; whereas for high t, the larger cation forces the material to adopt the non-perovskite hexagonal δ-$FAPbI_3$ structure.

One avenue not investigated, but known to have a significant effect on perovskite stability, was thin film deposition method.[181] A simple procedure was chosen, in which perovskite precursor solutions were deposited on glass substrates via the spin coating method. This was sufficient for the work presented in this chapter, which aimed to show trends in material stability rather than optimised film lifetimes. Small differences in film morphology, determined by SEM, over the compositions of interest were deemed not to have a significant impact on on decomposition kinetics. However, it is well-known

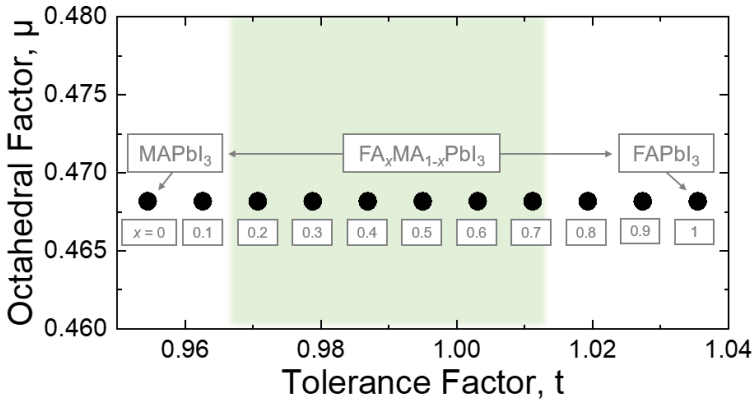

Figure 6-14: Calculated tolerance (t) and octahedral factors (μ) for $FA_xMA_{1-x}PbI_3$ ($0 \leq x \leq 1$). The shaded region area the compositional region stabilised in the cubic perovskite structure at room temperature.

that improved deposition method, use of an oxide coated substrate and/or fabrication of a full PV device can vastly improve observed perovskite lifetimes.[180,181]

Employing various deposition techniques such as spin coating,[13] dip coating,[182] ink-jet printing[183] or chemical vapour deposition[184] all have effects on the perovskite crystalline quality which affects stability. Methods capable of producing large micrometer sized crystallites generally produce more stable perovskite films.[181] Encapsulation also substantially increases the lifetime of perovskite devices. Bella *et al.* showed that by simply coating a PV device in a hydrophobic polymer, the perovskite layer could be protected against degradation over three months exposure to an Italian summer.[185]

6.6 Conclusions

This chapter investigated the trends in stability of mixed FA-MA cation perovskites. The work was the first to systematically study degradation across the whole composition range of $0 \leq x \leq 1$ in $FA_xMA_{1-x}PbI_3$. It was found that the mixed FA-MA lead iodide perovskites showed resistance to decomposition pathways favoured by pure $MAPbI_3$ and $FAPbI_3$.

Collaborative work with ICMAB revealed the phase behaviour of $FA_xMA_{1-x}PbI_3$ ($0 \leq x \leq 1$) up to 350 K. Compositions of $x \geq 0.2$ stabilised in the ideal cubic $Pm\bar{3}m$ structure at room temperature, although for $x \geq 0.7$ the mixed cation perovskites readily transformed to the hexagonal non-perovskite δ-$FAPbI_3$.

Kinetic studies on thin films of $FA_xMA_{1-x}PbI_3$ ($0 \leq x \leq 1$) used PXRD to investigate the growth of PbI_2 over a period of ten days. Thin films of $x \leq 0.2$ showed fast decomposition to PbI_2 and precursor salts (MAI and FAI), although increasing FA content slowed the rate of decomposition until $x = 0.6$, where negligible PbI_2 formation was recorded after ten days for pristine films. The quality of as-made films was found to be vital in preventing degradation, with the presence of PbI_2 impurities accelerating the rate of decomposition.

The experimentally observed improved stability of mixed FA-MA lead iodide perovskites was supported by *ab initio* studies of the decomposition reaction energies. Decomposition to PbI_2 and δ-$FAPbI_3$ was considered across all compositions of $FA_xMA_{1-x}PbI_3$ ($0 \leq x \leq 1$). The energetics of decomposition to PbI_2 and δ-$FAPbI_3$ were found to be less favourable in the mixed FA-MA cation phase when compared to pure $MAPbI_3$ and $FAPbI_3$, therefore suppressing degradation.

The increased stability shown in mixed FA-MA lead iodide perovskites was determined to be due to the stabilisation of the perovskite structure, caused by stronger interactions between the central organic cations and iodide forming the PbI_6 octahedra. The results of this work provide important information on the stability of mixed FA-MA lead iodide perovskites in moderately dry conditions, similar to those experienced during the industrial manufacture of typical PV devices.

Chapter 7

Exchange and Migration of Halide Ions in Lead Perovskites

7.1 Introduction

Compositional engineering of perovskites is a powerful tool in material design. As demonstrated throughout this thesis, site substitution at any of the A, B or X sites of the typical ABX_3 perovskite system can result in significant changes in material stability, structural properties and phase behaviour. These changes naturally extend to the photo-physical properties of perovskites, with the effects of site substitution on perovskite luminescence studied extensively in thin films and nanocrystals.[20,95,101,103,156,170] A recent development has shown post-synthesis site substitution to be possible through a technique known as *halide exchange* (also referred to as anion or ion exchange).[108] Use of this technique is particularly popular in nanocrystal research, as it allows access to mixed halide compositions which are inaccessible through typical synthetic methods.[108,186] This unusual property has important implications for devices, for example enabling the possibility of fabricating highly crystalline perovskite heterojunctions through controlled halide exchange,[187] motivating the work presented in this chapter.

In 2015 Nedelcu *et al.* first reported the chemical alteration of colloidal perovskite nanocrystals through halide exchange.[108] After synthesis it was found that the halide ratios in $CsPbX_3$ (X = Cl, Br, I) could be tuned over the entire visible spectrum simply through mixing pure nanocrystal samples in suitable ratios at 40°C in dry octadecene (ODE), Figure 7-1 shows the shift in PL achieved. Almost simultaneously Akkerman *et al.* reported that compositional tuning in halide perovskites could be achieved by the mixing of colloidal nanocrystals dispersed in toluene at room temperature.[186] Both observed fast ion exchange starting from $CsPbBr_3$ into $CsPbI_3$ or $CsPbCl_3$, although conversion directly between $CsPbI_3$ and $CsPbCl_3$ resulted in sample degradation due to the size discrepancy between the I^- and Cl^- anions.

In situ PL measurements by Nedelcu *et al.* showed transition from phase pure $CsPbBr_3$ to $CsPbI_3$ to occur over just eighteen seconds, with XRD confirming full conversion.[108] On the other hand, Akkerman *et al.* saw conversion timescales vary between seconds and hours depending on the exchange solution used.[186] It was found that the rate of anion exchange in $CsPbX_3$ nanocrystals could be increased by use of oleylammonium halides (OLA-X), compared to an exchange solution containing the lead halide precursor in toluene only.[186] In the same year, Pellet *et al.* demonstrated fast halide substitution in $MAPbX_3$ (X = Cl, Br and I) thin films through dipping in a 0.05 M precursor solution of MAX in anhydrous 2-propanol.[43] However, exchange rates varied between seconds and hours depending on film thickness.

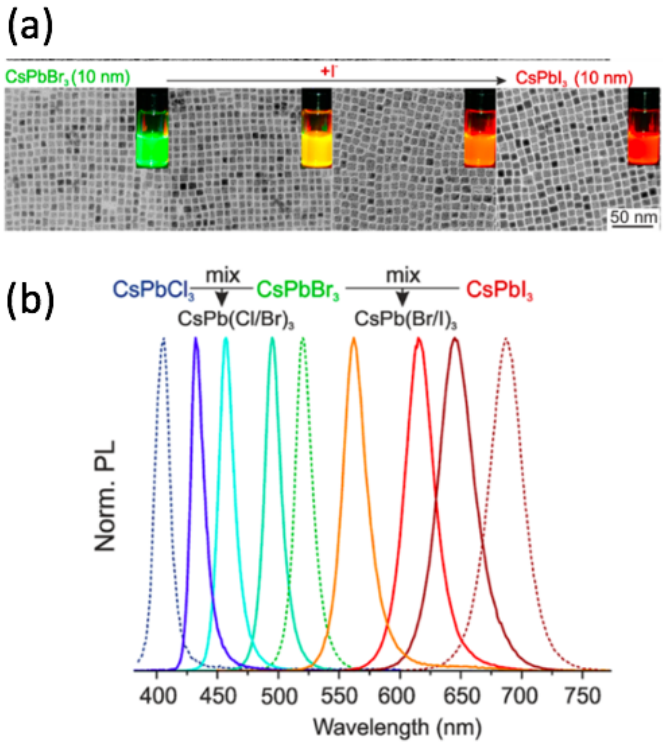

Figure 7-1: Reproduced from Nedelcu *et al.*[108] (a) Transmission electron microscopy (TEM) images of $CsPbBr_3$ to $CsPbI_3$ nanocrystals with insets showing emission under a UV lamp. (b) PL spectra of $CsPbBr_3$ nanocrystals shifting linearly on exchange with varying ratios of $CsPbI_3$ or $CsPbCl_3$.

The vacancy diffusion mechanism of anion exchange is well known in $CsPbX_3$ perovskites,[167] and has since been applied to $MAPbX_3$ structures.[43,188] The mechanism involves halide anions diffusing into the structure and occupying vacancies associated with Schottky-type defects.[189] Using this model, Lai *et al.* combined confocal PL measurements and molecular dynamics (MD) simulations to determine halide diffusivity on the order of 10^{-12} cm^2s^{-1} in $CsPbX_3$ single crystal nanowires, significantly lower than that reported in polycrystalline thin films, possibly due to reduced vacancy density.[188]

The vacancy diffusion mechanism is also crucial in the understanding of *photo-induced ion migration* within mixed halide perovskite systems. Knowledge of ionic motion in hybrid perovskites is essential in appreciating PV device operation, as the movement of ions has an important role in the understanding of undesirable effects present in perovskite PV, such as hysteresis in current-voltage scans.[189] Previous theoretical and experimental studies have shown that only the halide anions – as opposed to the Pb^{2+} or central cation – are responsible for ionic conduction via a vacancy diffusion

mechanism.[189] Further to this, work by Yoon *et al.* demonstrate the complexation constant between Pb^{2+} and Br^{-} to be seven times larger than that between Pb^{2+} and I^{-}, indicating that the Br^{-} halide to be the dominant binding species.[190]

In addition to ion exchange between solid solutions of colloidal nanocrystals, ions in mixed halide perovskites have been observed to migrate under illumination.[190] *Ion migration* in mixed I-Br PV devices has been studied experimentally, showing as distinctive shifts in the absorption and emission spectra of thin films over time. Upon illumination optical measurements reveal the formation of I and Br-rich regions, a process which reverses if the film is stored in the dark.[107,114] Yoon *et al.* postulated the formation of I and Br-rich regions through the reaction:[191]

$$\begin{aligned} n\mathrm{MAPbBr_3} + h\nu \longrightarrow (n-2m)\mathrm{MAPbBr}_x\mathrm{I}_{3-x} \\ +m\mathrm{MAPbBr}_{x-y}\mathrm{I}_{3-x+y} + m\mathrm{MAPbBr}_{x+y}\mathrm{I}_{3-x-y} \end{aligned} \tag{7.1}$$

where h is Planck's constant and ν is the frequency of the excitation source. Using cathodoluminescence imaging, Bischak *et al.* demonstrated the appearance of submicrometre scale halide-enriched clusters along grain boundaries in mixed I-Br thin films after five minutes illumination.[107] It was proposed that the strain induced on the lead halide framework from a single photoexcited charge was sufficient to overcome chemical interactions within the soft perovskite structure, enabling halide migration even at room temperature.

Understanding the dynamics of ion migration and formation of halide rich phases is important for PV performance as the phenomena can lead to charge trapping in I-rich regions. Excitation of an appropriate energy is capable of generating charge carriers in both Br and I-rich regions of a mixed halide perovskite. However, these charge carriers will migrate and preferentially recombine at the lower band gap I-rich phase, leading to dominant emission in the red region. PL studies performed by Hoke *et al.* suggest the stable I-rich cluster in these mixed I-Br compositions is $MAPb(I_{0.8}Br_{0.2})_3$.[153]

The vast majority of halide exchange and migration work has been performed using perovskite nanocrystals and thin films.[108,186–188,190,191] The increased popularity of highly crystalline mixed halide perovskites in devices, as well as the potential to create crystalline heterojunctions, prompted the work presented in this chapter. This investigation is the first to consider the effects of halide exchange and migration in perovskites grown by the popular inverse solubility method.

7.2 Halide Exchange

To investigate the potential effects of halide exchange in large perovskite crystals, samples of $MAPbBr_3$, $MAPbI_3$, $FA_{0.6}MA_{0.4}PbI_3$, $Cs_{0.1}MA_{0.9}PbI_3$ and $Cs_{0.1}FA_{0.9}PbI_3$ were selected and immersed in 80 μL of halide rich solution. To form a 2 mM I or Br-rich solution, PbX_2 (X = I or Br) was dissolved in 200 ml toluene with 2 ml oleic acid (OA) and 2 ml oleylamine (OLA). All crystals had dimensions close to 2 mm^2. The samples were then removed from the solution after four or ten days, dried and mounted onto SiO_2 substrates. The procedure is summarised in the schematic shown in Figure 7-2 and sample labels used throughout this chapter are detailed in Table 7.1.

Unlike previous reports on ion exchange, the exchange process observed in these 2 mm^2 scale crystals was slow. Nedelcu *et al.*[108] demonstrated conversion from $CsPbBr_3$ to $CsPbI_3$ nanocrystals after just eighteen seconds; however, there was no immediate colour change observed when $MAPbBr_3$ and $MAPbI_3$ crystals were first immersed in I and Br-rich solutions. A slight colour change indicative of ion exchange was observed in both $MAPbBr_3$ immersed in the I-rich solution (MAPBr-I) and $MAPbI_3$ immersed in the Br-rich solution (MAPI-Br) after 24 hours. After four days, the crystals appeared to fully convert to the characteristic orange and black of $MAPbBr_3$ and $MAPbI_3$ respectively.

Mixed cation crystals of $FA_{0.6}MA_{0.4}PbI_3$ (FAMAPI-Br), $Cs_{0.1}FA_{0.9}PbI_3$ (CsFAPI-Br) and $Cs_{0.1}MA_{0.9}PbI_3$ (CsMAPI-Br) were also immersed in the Br-rich solution, but exhibited a significantly slower exchange rate than the single cation phases. FAMAPI-Br partially changed colour when immersed in the Br solution for ten days, but showed two distinct PL peaks attributed to Br and I-rich phases. No colour change was observed in CsFAPI-Br and CsMAPI-Br after ten days immersion and, after fourteen days in solution, the crystals showed signs of degradation.

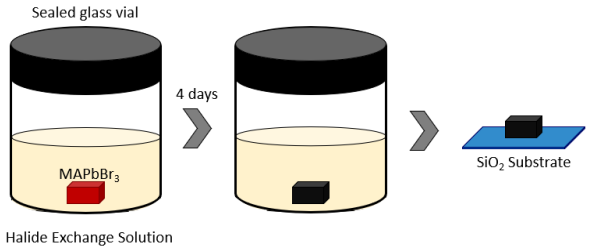

Figure 7-2: Schematic of the halide exchange procedure, using the investigation into $MAPbBr_3$ crystals immersed in an I-rich solution as an example.

Label	Original Sample	Exchange Solution Used	Time Immersed (days)
MAPBr-I	$MAPbBr_3$	I-rich	4
MAPI-Br	$MAPbI_3$	Br-rich	4
FAMAPI-Br	$FA_{0.6}MA_{0.4}PbI_3$	Br-rich	10
CsMAPI-Br	$Cs_{0.1}MA_{0.9}PbI_3$	Br-rich	14
CsFAPI-Br	$Cs_{0.1}FA_{0.9}PbI_3$	Br-rich	14

Table 7.1: Sample labels used throughout this chapter. Perovskite crystals were immersed in 2 mM solutions PbX_2 (X = I or Br) in toluene, with 2 ml OA and 2 ml OLA.

7.2.1 Photoluminescence

Investigations into the effects of halide exchange were conducted using PL at the Chair for Photonics and Optoelectronics, Ludwig Maximilian University of Munich (LMU).

MAPBr-I: $MAPbBr_3$ exchanged with I

The PL of MAPBr-I was measured and compared to that of $MAPbI_3$ and $MAPbBr_3$, as shown in Figure 7-3. Each spectrum was fitted with a single Gaussian function, giving peak positions of 1.70 eV, 1.61 eV and 2.31 eV for MAPBr-I, $MAPbI_3$ and $MAPbBr_3$ respectively. The measured FWHM of 0.11 eV was larger for MAPBr-I, than the 0.09 eV measured for the $MAPbBr_3$ crystal before immersion in the I-rich exchange solution.

The dominant composition could be estimated using the PL of $MAPbBr_3$ and $MAPbI_3$ as references, and assuming a linear blue shift in PL peak position as y increases in $MAPb(I_{1-y}Br_y)_3$, a well known property of mixed cation perovskites.[108,149,186] From this, a value of 0.13 for y was inferred, suggesting a composition of $MAPb(I_{0.87}Br_{0.13})_3$.

MAPI-Br: $MAPbI_3$ exchanged with Br

Figure 7-4 shows the PL measured for MAPI-Br compared to $MAPI_3$ and $MAPBr_3$ crystals. A peak position and FWHM of 1.68 eV and 0.12 eV were measured by fitting the dominant MAPI-Br spectrum with a single Gaussian function. The composition was estimated to be $MAPb(I_{0.91}Br_{0.09})_3$, similar to that found in MAPBr-I. Unlike MAPBr-I, an additional peak (position 2.49 eV and FWHM 0.21 eV) was seen in the MAPI-Br PL, attributed to a thin film of an orange Br-rich compound which formed on the crystal surface. The film could be easily removed revealing a black perovskite phase underneath, although the reduced PL intensity and high energy position of this second peak suggested formation of a Br-rich phase on the crystal surface, which PXRD measurements showed to be amorphous.

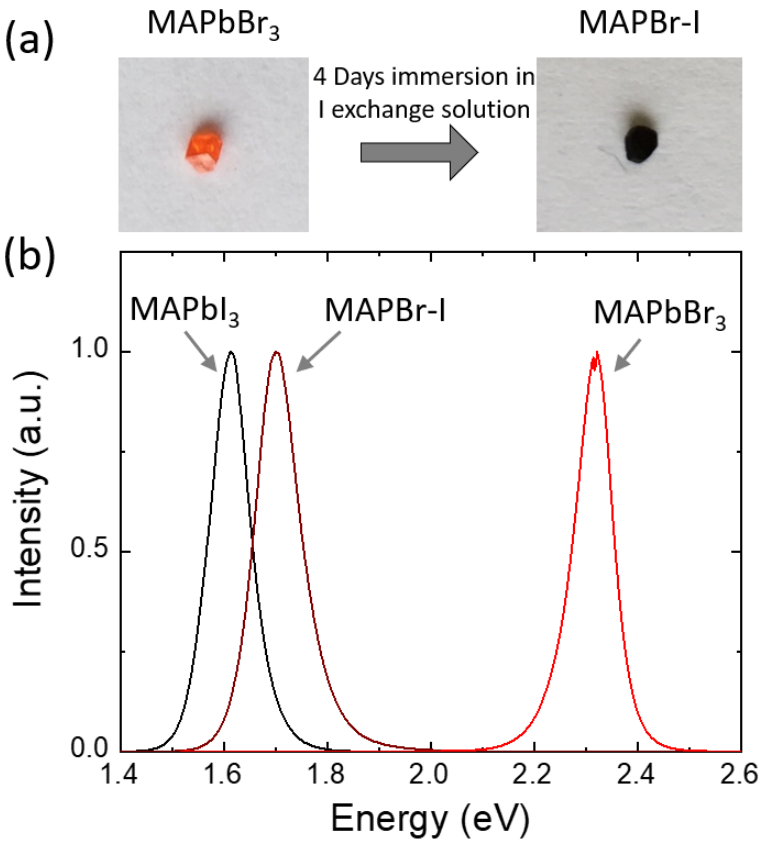

Figure 7-3: (a) Photos of the 2 mm $MAPbBr_3$ crystal before and after immersion in an I exchange solution (b) PL of $MAPbBr_3$, $MAPbI_3$ and MAPBr-I.

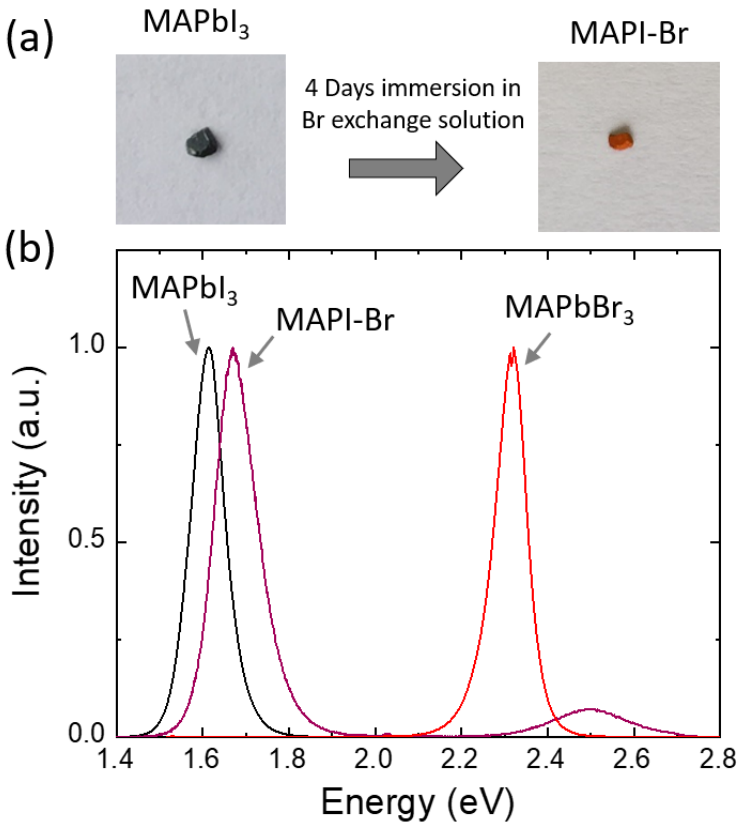

Figure 7-4: (a) Photos of the 2 mm $MAPbI_3$ crystal before and after immersion in a Br exchange solution (b) PL of MAPI-Br with $MAPbBr_3$ and $MAPbI_3$ for reference.

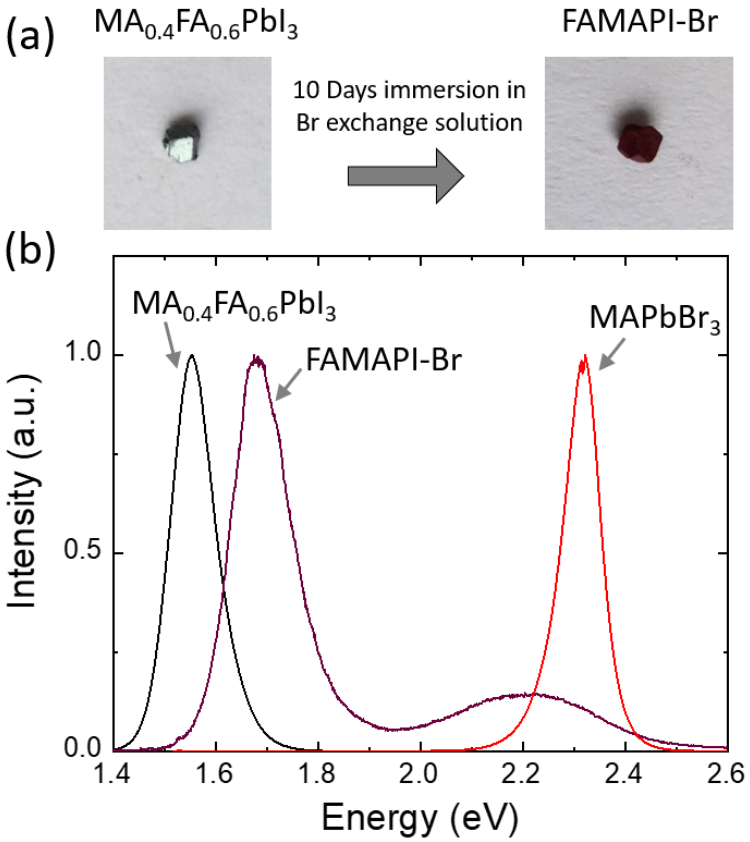

Figure 7-5: (a) Photos of the 2 mm $FA_{0.6}MA_{0.4}PbI_3$ crystal before and after immersion in a Br exchange solution (b) PL of FAMAPI-Br with $MAPbBr_3$ and $FA_{0.6}MA_{0.4}PbI_3$ for reference.

FAMAPI-Br: $FA_{0.6}MA_{0.4}PbI_3$ exchanged with Br

PL spectra of FAMAPI-Br, $FA_{0.6}MA_{0.4}PbI_3$ and $MAPbBr_3$ are shown in Figure 7-5. The dominant peak positions and FWHM were measured to be 1.56 eV and 0.11 eV for $FA_{0.6}MA_{0.4}PbI_3$, and 1.69 eV and 0.14 eV for FAMAPI-Br. Similar to MAPI-Br, a secondary peak was measured at higher energy in FAMAPI-Br, with a position of 2.19 eV and FWHM of 0.35 eV. However, an orange Br-rich film was not seen on the FAMAPI-Br crystal surface. It was proposed that this second peak could be attributed to a broad range of Br-rich perovskite phases forming domains near the crystal surface, as the intensity of this secondary peak varied with excitation position. Interestingly, the dominant peak PL position for FAMAPI-Br (1.69 eV) was similar to those measured for MAPBr-I (1.70 eV) and MAPI-Br (1.68 eV), indicating a preferred ratio of the mixed I-Br phase formed regardless of the initial composition.

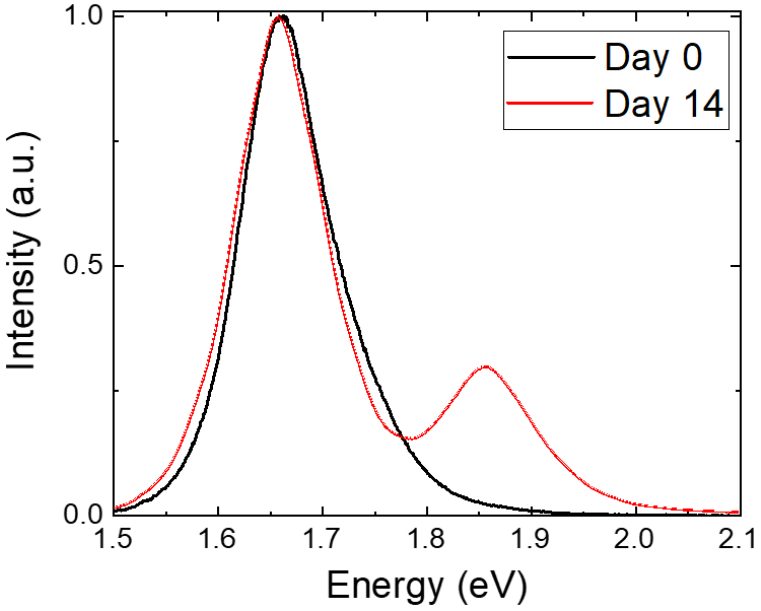

Figure 7-6: PL of MAPBr-I measured when first removed from the exchange solution (black) and after fourteen days stored in air at $< 30\%$ humidity (red).

Phase Stability

There was no change in PL properties of MAPBr-I crystals after three days storage in the dark at less than 30% humidity. This agrees with stability measurements made by Akkerman *et al.* on halide exchanged $CsPbX_3$ nanocrystals.[186] However, after fourteen days an additional PL peak, centered at 1.86 eV, formed (Figure 7-6). The peak represents the appearance of a Br-rich phase. Phase separation into I and Br-rich regions is a characteristic typically seen in mixed halide thin films.[114]

7.2.2 Chemical Analysis

Chemical analysis of samples through EDX and PXRD was conducted at the University of Bath on return from the LMU.

Energy Dispersive X-ray Spectroscopy

EDX spectroscopy was used to obtain chemical maps showing the distribution of I and Br in a cleaved crystal of MAPBr-I (Figure 7-7). Strikingly, the EDX maps reveal halide exchange occurred at the crystal surface only, with very little I detected elsewhere in the crystal, which maintained a near phase pure $MAPbBr_3$ composition throughout. This suggests halide exchange in perovskite single crystals is a slow and inefficient pro-

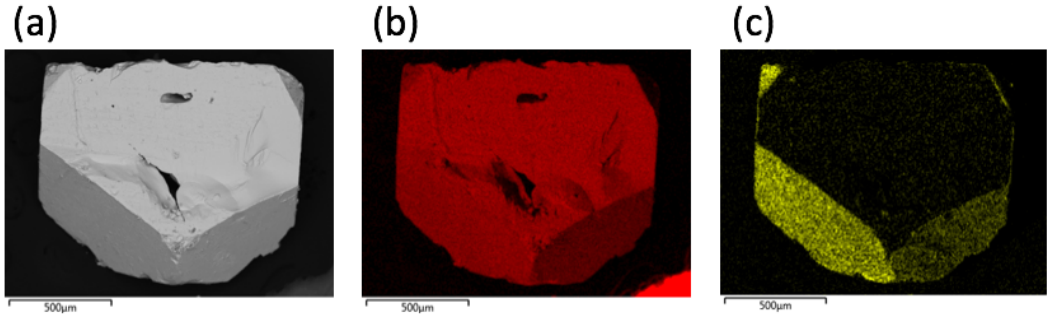

Figure 7-7: (a) Backscattered SEM image of a cleaved MAPBr-I crystal and EDX maps of (b) Br and (c) I distribution.

cess, affecting only the crystal surface before the exchange solution causes degradation. Surface sensitive PL was capable of detecting mixed I-Br phases present on the crystal; however, it is apparent this mixing did not extend through any significant volume of the crystal.

Powder X-ray Diffraction

PXRD data were acquired for $MAPbBr_3$ and MAPBr-I samples ground using a pestle and mortar. Figure 7-8 shows the resulting patterns indexed to the same unit cell in the cubic space group $Pm\bar{3}m$, with lattice parameter $a = 5.935\,\text{Å}$. Surprisingly, there were no additional peaks or peak splitting observed due to the presence of iodide in the sample. It is possible most of the volatile iodide escaped the structure during grinding as discussed later in this chapter. These results are contrary to that seen in literature for nanocrystals and thin films, which suggest fast and complete halide exchange, resulting in transformation of the material structure.[108]

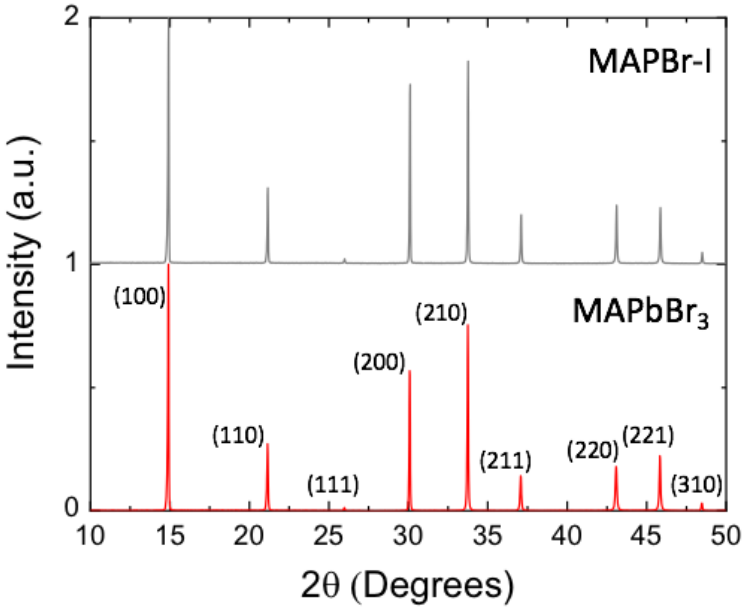

Figure 7-8: PXRD patterns for $MAPbBr_3$ (red) and MAPBr-I (grey) crystals ground using a pestle and mortar, indexed to a cubic unit cell in the space group $Pm\bar{3}m$, lattice parameter $a = 5.935$ Å.

7.3 Ion Migration

Under continuous illumination, using an excitation wavelength of 500 nm, the PL position of MAPBr-I crystals red shifted. To map this shift, spectra were first obtained every twelve seconds for ten minutes. The most significant shift was seen within the first sixty seconds and was further measured by obtaining PL spectra every 1.5 seconds for one minute using an exposure time of 800 ms, as shown in Figure 7-9 (a), which also shows the increase in PL intensity with continued illumination. The PL position could also be *recovered* after eight minutes of the sample being kept in the dark (Figure 7-9 (b)).

As shown in Figure 7-9 (b), the PL position recovered after a few minutes in the dark. The PL of MAPBr-I was measured after five minutes continuous illumination (red spectrum in Figure 7-9 (b)), before being allowed to recover in the dark at which point PL was measured again after two minutes (green spectrum) and eight minutes (purple spectrum) using an exposure time of one second. The PL peaks were approximated with a single Gaussian function with an extracted position of 1.70 eV and FWHM of 0.11 eV after five minutes continuous illumination. The PL shifted to 1.74 eV and broadened to a FWHM of 0.14 eV after eight minutes dark recovery. The majority of PL recovery occurs in the first two minutes, with the position restored to the original value after eight minutes. Because of this, all samples were allowed at least ten minutes of dark recovery time before PL shift under continuous illumination was measured.

The series of spectra shown in Figure 7-9 (a) were fitted with single Gaussian functions, and the resulting peak positions are plotted as a function of time in Figure 7-10. Using this approach, a red shift of 0.044 eV from 1.755 eV to 1.711 eV was measured. This could be fitted to the bi-exponential decay function in the program Origin defined as:

$$y = y_0 + A_1 e^{-k_1 t} + A_2 e^{-k_2 t} \tag{7.2}$$

where y_0 and $A_{1,2}$ are constants, t is time and k_1 and k_2 are the rates for the fast and slow decay components respectively. Measured decay rates for the PL shift are $k_1 = 0.341\ s^{-1}$ and $k_2 = 0.039\ s^{-1}$.

An improved fit could be obtained using two Gaussian functions representing an I-rich (lower energy) and Br-rich (higher energy) phase as shown in Figure 7-11 (a). The separate I-rich (black) and Br-rich (red) peak positions and FWHM were plotted as a function of time and modelled to the biexponential decay equation 7.2. The peak

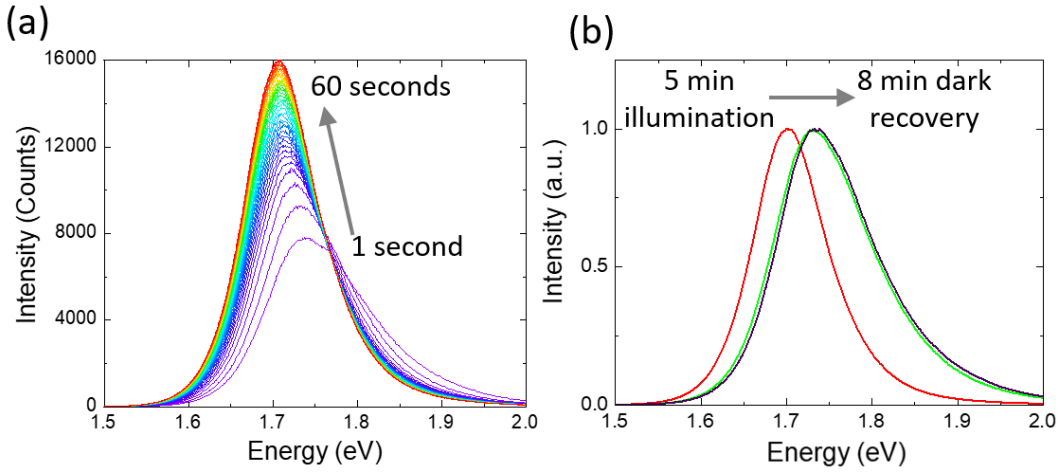

Figure 7-9: (a) PL of MAPBr-I evolving over one minute continuous illumination. (b) The PL of MAPBr-I was measured after five minutes continuous illumination (red), before the sample was measured after two minutes (green) and eight minutes (purple) dark recovery.

associated with a Br-rich phase red shifted 0.07 eV (from 1.80 eV to 1.73 eV). A smaller red shift was seen in the more dominant I-rich peak (from 1.73 eV to 1.70 eV). The Br-rich phase decayed faster than the I-rich phase. Extracted decay rates for the PL shift were $k_1 = 0.516\ s^{-1}$ and $k_2 = 0.046\ s^{-1}$ for the Br-rich phase, and $k_1 = 0.261\ s^{-1}$ and $k_2 = 0.034\ s^{-1}$ for the I-rich phase. A sharper decay was observed for the FWHM in both phases, with extracted decay rates of $k_1 = 1.030\ s^{-1}$ and $k_2 = 0.041\ s^{-1}$ for the Br-rich phase, and $k_1 = 0.558\ s^{-1}$ and $k_2 = 0.036\ s^{-1}$ for the I-rich phase.

Due to the well known linear shift in perovskite PL energy depending on cation and halide ratios,[95,108,186] it was possible to estimate the composition of these illuminated samples. After continuous illumination the composition the MAPBr-I samples was measured to be equivalent to $MAPb(I_{0.87}Br_{0.13})_3$. However, the initial PL position suggested a composition of approximately $MAPb(I_{0.8}Br_{0.2})_3$, identical to the stable I-Br suggested by Hoke *et al.*[153]

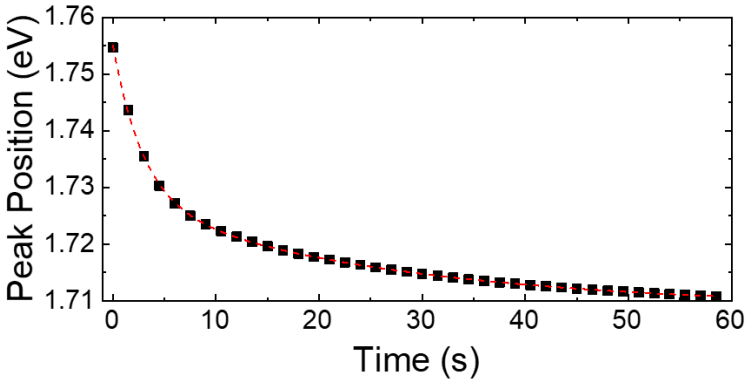

Figure 7-10: Evolution of peak position of the PL of MAPBr-I over the first 60 seconds of illumination at 500 nm fitted with single Gaussian functions, and modelled with a biexponential function (red dashed line).

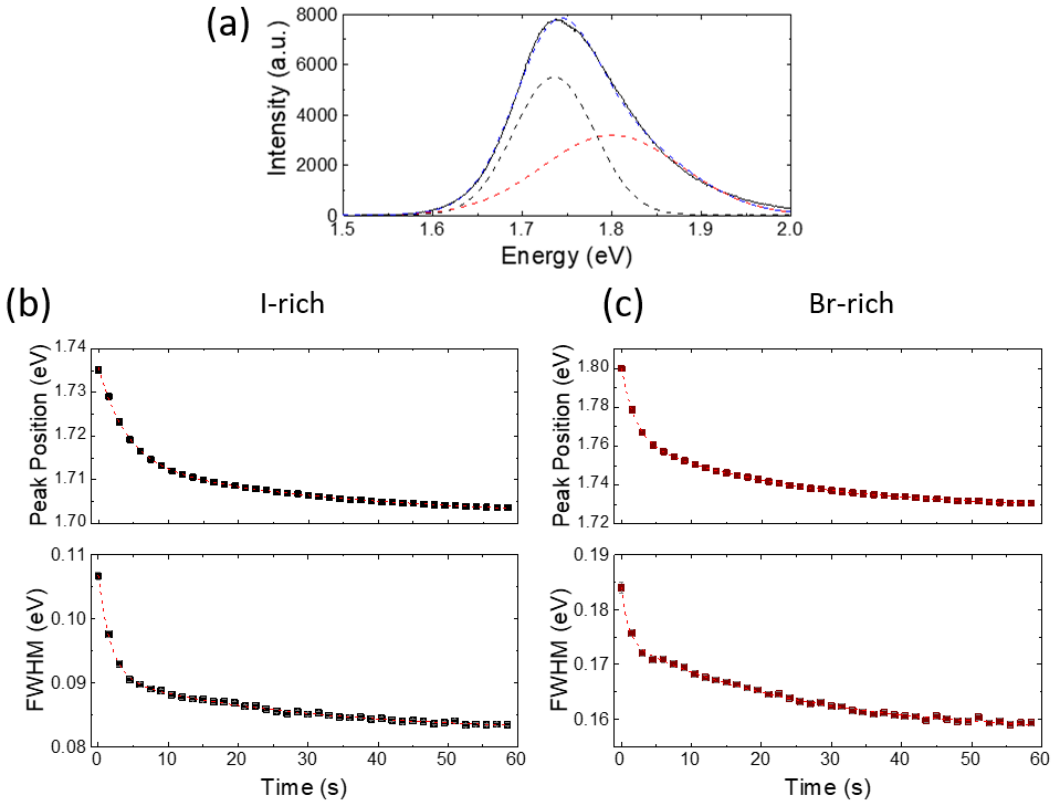

Figure 7-11: (a) Example PL spectrum of MAPBr-I sample (black solid line) fitted with two Gaussian functions representing an I-rich (black dashed line) and Br-rich (red dashed line). The evolution of the peak position and FWHM of the I-rich (b) and Br-rich (c) phases are modelled to biexponential decays

7.4 Discussion

Halide Exchange

The mechanism by which halide exchange occurs was proposed to be the well known vacancy assisted diffusion mechanism.[108,114,189] Figure 7-12 shows a schematic of the process occurring for the MAPBr-I sample, in which a $MAPbBr_3$ crystal was immersed in an I-rich solution.

A significant result of the work presented in this chapter was the resistance to anion exchange shown in mixed cation lead halide perovskites. While crystals of $MAPbBr_3$ and $MAPbI_3$ reacted with exchange solutions within four days, samples of $FA_{0.6}MA_{0.4}PbI_3$ required ten days in solution to show any significant color change associated with successful exchange. $Cs_{0.1}FA_{0.9}PbI_3$ and $Cs_{0.1}MA_{0.9}PbI_3$ degraded in solution before any significant halide exchange was observed. The mixed cation compositions were specifically targeted because of their improved material stability as demonstrated in Chapters 4, 5 and 6. $FA_{0.6}MA_{0.4}PbI_3$ and $Cs_{0.1}FA_{0.9}PbI_3$ were also selected due to their proximity to the ideal tolerance factor of one, as shown in Figure 7-13.[80,95]

The lack of exchange in Cs containing crystals and broad PL of FAMAPI-Br samples indicate site substitution of the cation reduces the rate of halide exchange between Br and I anions. It was proposed that the stabilised crystal structures of these mixed cation perovskites result in stronger hydrogen bonding between the organic cations and iodide in the PbI_6 octahedra.[87,95,146,147] The stronger interaction between the organic cation and lead iodide framework requires a greater activation energy to initiate halide exchange via the vacancy assisted diffusion mechanism. This has implications for photo-induced ion migration, which occurs via the same mechanism, and has been attributed to problems of phase segregation, charge trapping and hysteresis in PV devices.[114] Further work determining the precise mechanism and reduced exchange kinetics in these mixed cation systems would be beneficial to improve our understanding of the effect of site substitution on vacancy assisted anion diffusion, which has important consequences for hybrid perovskite device operation.[189]

Moving on to consider the single cation $MAPbX_3$ crystals, it was clear that the Br to I exchange was more efficient than the I to Br process. A single broad peak was observed at 1.70 eV in PL measurements for MAPBr-I, whereas a second, low intensity peak was seen at 2.49 eV for MAPI-Br associated with a Br-rich capping layer. This is unlike observations on thin films, which show an increased rate of reaction when $MAPbI_3$ films are exchanged in a Br-rich solution, as opposed to $MAPbBr_3$ films in an I-rich

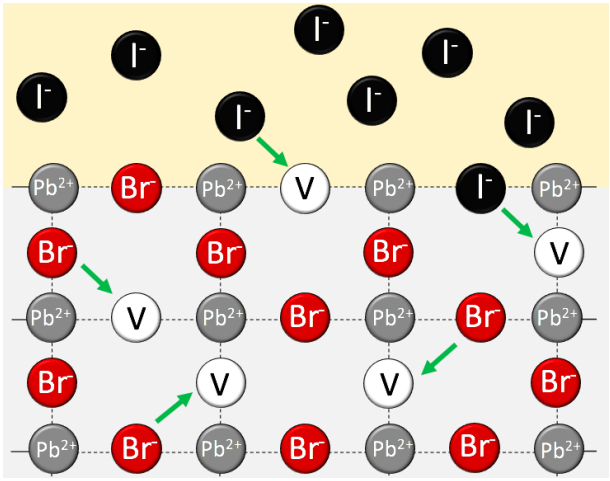

Figure 7-12: Schematic of the proposed ion diffusion mechanism occurring in this work, adapted from Yoon *et al.*[114] Here a crystal of $MAPBr_3$ is shown immersed in an I-rich exchange solution.

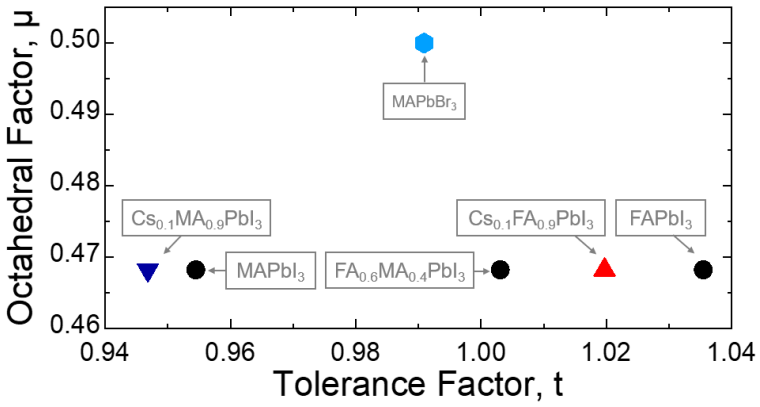

Figure 7-13: Calculated octahedral factors (μ) and tolerance factors (t) for the materials investigated in this chapter.

solution.[43] In the case of $MAPbI_3$ films immersed in Br-rich solutions, XRD measurements suggest full conversion from $MAPbI_3$ to $MAPbBr_3$ within five minutes, proposed to be facilitated by favourable thermodynamics and limited by iodide diffusion.[43] However, it has also been shown that I to Br exchange is unsuccessful when single crystals of $MAPbI_3$ grown by chemical vapor deposition were immersed in a Br-rich solution, causing chemical etching of the $MAPbI_3$ surface. For work presented in this chapter, it is possible that the bromide reacted with the $MAPbI_3$, forming a non-perovskite complex on the crystal surface. The contrary behaviour observed between thin films and single crystals highlight the importance of further studies into halide exchange in crystalline perovskites. Increased halide diffusion path lengths and reduced defect densities in high quality perovskite crystals have substantial effects on anion diffusion which has been widely studied in thin film perovskite devices.[108,186,188,189]

At the time of this work, no study had investigated the stability of the mixed halide phase formed through halide exchange beyond two days.[186] Phase separation, similar to that previously observed in $MAPb(I_{1-y}Br_y)_3$ thin films, was seen in MAPBr-I after fourteen days. Crystals were stored in air, therefore oxidation of $MAPbI_3$-rich regions was possible. This degradation process involves oxygen diffusing into the crystal structure, forming a superoxide species on exposure to light which can deprotonate the MA cation resulting in the formation of molecular iodine according to the reaction:[171]

$$4CH_3NH_3PbI_3 + O_2 \longrightarrow 4PbI_2 + 2I_2 + 2H_2O + 4CH_3NH_2. \tag{7.3}$$

The volatile molecular iodine was lost, resulting in an increased Br concentration in the mixed halide perovskite. The phase instability demonstrated in this work has important implications for single crystalline heterojunctions synthesised by anion exchange, which would have to be protected from oxidation for use in potential devices.

Loss of iodine could also account for the fact that PXRD measurements on MAPBr-I showed no additional peaks associated with an I-rich phase. The smaller crystallites produced by grinding the sample allowed a shorter diffusion pathway for oxygen, enabling fast oxidation in I-rich regions. However, the apparent absence of an I-rich phase could also be accounted for by the small volume fraction of the halide exchanged area, as seen in EDX measurements.

I-rich areas were very small in relation to the whole MAPBr-I crystal, as shown in EDX measurements, which demonstrated iodide to be present on the crystal surface only. The colour change of orange to black of the MAPBr-I crystal indicated the initial

depth of the anion exchanged region to be at least 100 - 500 nm, corresponding with the absorption depth of visible light in $MAPbI_3$.[187] The slow halide diffusion may be a result of the high complexation constant between Pb^{2+} and Br^-, resulting in bromide substitution with iodide being unfavourable.[190] It is clear diffusion of iodide into the $MAPbBr_3$ structure is inefficient in large perovskite crystals, suggesting compositional tuning post-synthesis in crystals or thick crystalline thin films is not effective.

Photo-induced Ion Migration

The mechanism responsible for the shift in PL observed with illumination was determined to be photo-induced ion migration facilitated by the vacancy assisted diffusion mechanism, similar to that seen in halide exchange. Upon illumination, energy provided by the excitation source enables halide diffusion, forming I and Br-rich regions in the case of MAPBr-I samples, as shown schematically in Figure 7-14.[107] The initial broad PL of MAPBr-I could be fitted to two Gaussian functions representing an I and Br-rich region, where the position and FWHM of both shifted according to a biexponential decay. The biexponential nature of this shift suggested the presence of an initial fast and subsequent slow diffusion process. The rate of change in the Br-rich PL peak was faster than that observed in the I-rich peak, therefore it was proposed than an initial fast diffusion of bromide anions occurred before a slower diffusion of iodide ions forming separate halide rich regions. However, these diffusion rates are likely to be highly dependent on diffusion path lengths and defect densities determined by method of synthesis. Alternative rate constants for I-Br photo-induced anion migration have been measured in mixed halide thin films, in which faster rate constants were measured for iodide.[190] It is clear the local environment of the anions has a greater affect on photo-induced ion migration than properties intrinsic to the I-Br mixed halide perovskites.

The PL from I-rich regions increased in intensity due to a cascade of photo-generated charge carriers recombining preferentially in the lower bandgap region.[153] This is due to holes becoming trapped the I-rich regions, as the valance band of $MAPbI_3$ rich regions occupies the lowest energy state out of the $MAPbBr_3$ and $MAPb(I_{1-y}Br_y)_3$ regions present in the sample, therefore leading to I-rich regions acting as recombination centers.[190]

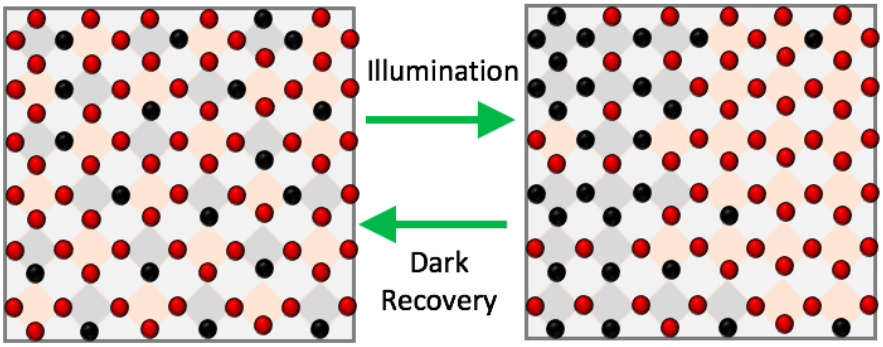

Figure 7-14: Schematic of the reversible phase separation of $MAPb(I_xBr_{1-x})_3$, forming I (black) and Br-rich (red) regions under continuous illumination, based on the mechanism described by Bischak *et al.*[107]

7.5 Conclusions

Halide exchange and migration were investigated in perovskites grown by inverse solubility. $MAPbBr_3$ crystals immersed in an I-rich exchange solution (referred to as MAPBr-I samples) showed a distinctive colour change from orange to black over four days. PL measurements confirmed transformation into a mixed halide phase resembling $MAPb(I_{0.87}Br_{0.13})_3$, although EDX and PXRD measurements showed iodide exchange did not occur throughout the bulk of the crystal. The mixed phase was only present in the first few hundred nanometres of the crystal surface.

MAPBr-I samples also showed evidence of photo-induced ion migration through a red shift in PL over one minute under continuous illumination. The shift could be modelled as a biexponential process occurring over Br and I-rich regions, with the PL intensity from the I-rich area increasing due to preferential recombination at a lower bandgap. The biexponential nature of the shift in PL energy in I and Br-rich regions was speculated to be due to initial fast diffusion of bromide followed by diffusion of iodide; however, conflicting measurements have been made using thin films. It was determined that ion diffusion path lengths and defect densities - which are highly dependant on crystal quality - have greater effects on ion migration than the intrinsic properties of mixed I-Br perovskites.

$MAPbI_3$ crystals immersed in a Br-rich solution (referred to as MAPI-Br samples) showed evidence of a Br-rich capping layer forming over the crystal surface. This limitation agreed with previous observations on crystals grown by chemical vapor deposition, but disagreed with studies on thin films, which showed fast halide exchange

between Br anions and $MAPbI_3$ thin films.[43,188] Illustrating further discrepancies between polycrystalline thin films and single crystals.

Notably, mixed cation perovskites demonstrated a resistance to halide exchange, with $FA_{0.6}MA_{0.4}PbI_3$ requiring ten days in solution to show any color change and mixed Cs-FA and Cs-MA perovskites degrading before color change due to halide exchange was observed. The increased resistance was proposed to be due to a reduced rate of exchange caused by the stabilised crystal structures of these mixed cation perovskites increasing the activation energy required to initiate halide exchange via the vacancy assisted diffusion mechanism. This has important consequences in PV devices, as protection against photo induced anion migration - which proceeds via the same vacancy diffusion mechanism - has the potential to improve device stability. Further work is needed to determine the precise effect of cation substitution on intrinsic halide diffusion in these highly crystalline materials, providing further insights into long term device stability.

It was concluded that post-synthesis compositional tuning in large perovskite crystals was ineffective due to the inefficiency of halide exchange, coupled with long term phase segregation due to loss of iodide.

Chapter 8

Conclusions

There is a great need for new materials in the drive towards affordable and sustainable energy generation for all. Chapter 1 outlined solar energy as part of the solution in combating climate change, and introduced perovskites as a class of materials making swift progress towards low-cost, high efficiency, thin film commercial photovoltaic (PV) technology. Methylammonium lead iodide ($CH_3NH_3PbI_3$ or $MAPbI_3$) and formamidinium lead iodide ($CH(NH_2)_2PbI_3$ or $FAPbI_3$) were presented as the archetypal hybrid (organic-inorganic) PV perovskites with an ABX_3 structure type. However, instabilities in $MAPbI_3$ and $FAPbI_3$ have led to the use of site substitution at any of the A, B or X-sites in an effort to improve PV device lifetimes. The effect of this site substitution on the fundamental behaviour of these hybrid halide perovskites was poorly understood and, therefore, formed the primary motivation for the work presented in this thesis.

Mixed A and/or X-site hybrid halide perovskites were synthesised as simple thin films deposited on a substrate via spin coating, as powder by solvothermal and precipitation techniques, and as crystals by the inverse solubility method. Known methods of perovskite crystallisation were developed further to produce high quality single crystals with tunable dimensions for use in spectroscopic and single crystal X-ray diffraction measurements. Bulk material (powder and single crystal) was primarily investigated throughout this work in order to focus on the intrinsic properties of the perovskites, away from the (sometimes significant) influence of PV device architecture.

Variable temperature neutron powder diffraction (NPD), carried out on the POLARIS instrument at the ISIS neutron and muon source, was employed to investigate the phase behaviour of $Cs_{0.1}FA_{0.9}PbI_3$, and $Cs_{0.1}FA_{0.9}Pb(I_{0.6}Br_{0.4})_3$ (Chapter 4), as well as $Cs_{0.1}MA_{0.9}PbI_3$ and $Cs_{0.1}MA_{0.9}Pb(I_{0.6}Br_{0.4})_3$ (Chapter 5). X-ray diffraction (powder and single crystal) conducted at the University of Bath, and variable temperature photoluminescence (PL) conducted at the Ludwig Maximilian University of Munich (LMU), complemented NPD measurements on mixed cation lead iodide phases $Cs_{0.1}FA_{0.9}PbI_3$ and $Cs_{0.1}MA_{0.9}PbI_3$.

The desirable cubic α-phase was found to be accessible at room temperature in mixed Cs-FA perovskites, with the Cs stabilising the $FAPbI_3$ structure and so resisting transformation into the undesirable non-perovskite δ-phase usually seen at ambient conditions in $FAPbI_3$. Compared to pure $FAPbI_3$, inclusion of Cs also induced the formation of an orthorhombic phase in $Cs_{0.1}FA_{0.9}PbI_3$ below 180 K and lowered the transition to the disordered state to 125 K. The complex $Cs_{0.1}FA_{0.9}Pb(I_{0.6}Br_{0.4})_3$ composition showed reduced cation motion associated with a reduction in cuboctahedral volume due to inclusion of the smaller bromide anion. Variable temperature NPD revealed

this mixed cation mixed halide material to maintain a pseudo-cubic structure through to 105 K, an important and highly desirable property for PV devices operating over a wide range of temperatures.

In contrast to the Cs-FA system, the addition of Cs into the $MAPbI_3$ structure was shown to have little effect on the phase transition temperatures. However, the nature of the tetragonal to orthorhombic transition changed from an abrupt to a slower glass-like transition due to additional strain present in the lead halide framework of the Cs-MA system. Interestingly, the observed tetragonal to orthorhombic phase transition in $Cs_{0.1}MA_{0.9}Pb(I_{0.6}Br_{0.4})_3$ was higher than expected for mixed I-Br perovskites, and further work investigating the effect of Cs substitution on the dynamics of the mixed I-Br framework - which drives these phase transitions - would be beneficial.

Building on previous work determining the phase behaviour of FA-MA lead iodide systems, trends in the stability of $FA_xMA_{1-x}PbI_3$ across the full composition range ($0 \leq x \leq 1$) were presented in Chapter 6. Powder X-ray diffraction (PXRD) was employed to investigate decomposition by determining the kinetics of lead iodide crystallisation in the mixed FA-MA perovskites deposited as thin films. Inclusion of increasing amounts of FA into the $MAPbI_3$ structure was shown to increase resistance to decomposition, the most stable composition being $FA_{0.6}MA_{0.4}PbI_3$. However, greater quantities of FA resulted in fast transition to the non-perovskite δ-$FAPbI_3$ phase. The quality of as-made films was found to be vital in preventing decomposition.

Finally, the effects of halide exchange in hybrid organic-inorganic lead iodide crystals were investigated through PL, PXRD and energy-dispersive X-ray spectroscopy (EDX). $MAPbBr_3$ crystals were immersed in an I-rich solution, with PL suggesting a preferred composition of $MAPb(I_{0.87}Br_{0.13})_3$ forming after four days immersion. However, subsequent PXRD and EDX measurements showed exchange to occur at the crystal surface only, demonstrating post-synthesis compositional tuning to be unfeasible in large perovskite crystals, unlike their nanocrystal counterparts. Mixed FA-MA cation perovskites showed increased resistance to halide exchange, with no exchange observed in Cs-FA and Cs-MA lead iodide perovskites. Stabilised crystal structures of the mixed cation materials was determined to reduce the rate of halide exchange via the vacancy diffusion mechanism, an important result for PV devices combating undesirable photo-induced ion migration, which proceeds via the same mechanism.

The novel results presented in this thesis highlight the importance of an in-depth understanding of site substitution in the popular hybrid halide perovskites. Successful PV devices must demonstrate an ability to function across a large range of temperatures,

as commercial solar cells are commonly subjected to significant temperature differences due to the environments in which they are used. Site substituted perovskite devices may generate impressive power conversion efficiencies in laboratories, but without an understanding of these substitutions on fundamental material phase behaviour, PV devices may fail. The structural phase behaviour of Cs and Br substituted organic lead iodide perovskites, presented in Chapters 4 and 5, provide important information for the practical performance of devices. As demonstrated in this work, phase transitions can cause significant differences to material structural and optoelectronic properties, affecting device operation, and should therefore be avoided over known operating temperatures.

Resistance to decomposition and ion migration through site substitution (as presented in Chapters 6 and 7) are also important in the long term development of perovskite devices. Knowledge of an already thermodynamically stable composition and materials able to resist photo-induced ion migration (a common problem in perovskite PV) provide a foundation from which devices can be developed.

Perovskite materials are rapidly being developed for use in commercial solar cells, with incorporation into silicon tandem devices being the likely first step. However, many challenges remain in perovskite materials research which will dictate the direction of future investigations. Reducing toxicity, by eliminating lead through substitution with a suitable metal cation, remains a key challenge. Significant work has gone into stabilising lead-tin perovskite alloys, although the efficiencies and lifetimes of these PV devices are consistently lower than their lead counterparts. A better understanding of charge-carrier dynamics in these alloys would be effective in optimising device design. Leading on directly from work presented in this thesis, further investigations into the lattice dynamics of mixed cation *and* halide perovskites would be beneficial. Greater understanding of the behaviour of a mixed I-Br lead framework would add insight into the nature of experimentally determined phase transitions.

If the material properties of these complex site-substituted perovskites can be optimised, then there exists great potential for the large scale manufacture of highly efficient, thin film perovskite photovoltaic technologies.

References

[1] United Nations, "Transforming our world: The 2030 agenda for sustainable development," *UN General Assembly*, pp. 1–41, 2015.

[2] F. Creutzig, P. Agoston, J. C. Goldschmidt, G. Luderer, G. Nemet, and R. C. Pietzcker, "The underestimated potential of solar energy to mitigate climate change," *Nature Energy*, vol. 2, no. 9, p. 17140, 2017.

[3] E. Kabir, P. Kumar, S. Kumar, A. A. Adelodun, and K. H. Kim, "Solar energy: potential and future prospects," *Renewable and Sustainable Energy Reviews*, vol. 82, pp. 894–900, 2018.

[4] IRENA, "Renewable power generation costs in 2017 - Key findings and executive summary," *International Renewable Energy Agency*, pp. 1–16, 2018.

[5] D. S. Philips and W. Warmuth, "Fraunhofer ISE: Photovoltaics Report," Tech. Rep. March, Fraunhofer ISE, 2019.

[6] Z. Wang, Z. Song, Y. Yan, S. Liu, and D. Yang, "Perovskite - a perfect top cell for tandem devices to break the S-Q limit," *Advanced Science*, vol. 6, no. 7, p. 1801704, 2019.

[7] K. A. Bush, A. F. Palmstrom, Z. J. Yu, M. Boccard, R. Cheacharoen, J. P. Mailoa, D. P. McMeekin, R. L. Hoye, C. D. Bailie, T. Leijtens, I. M. Peters, M. C. Minichetti, N. Rolston, R. Prasanna, S. Sofia, D. Harwood, W. Ma, F. Moghadam, H. J. Snaith, T. Buonassisi, Z. C. Holman, S. F. Bent, and M. D. McGehee, "23.6%-Efficient monolithic perovskite/silicon tandem solar cells with improved stability," *Nature Energy*, vol. 2, no. 4, pp. 1–7, 2017.

[8] K. Momma and F. Izumi, "VESTA: A three-dimensional visualization system for electronic and structural analysis," *Journal of Applied Crystallography*, vol. 41, no. 3, pp. 653–658, 2008.

[9] G. Rose, "Beschreibung einiger neuen Mineralien des Urals," *Annalen der physik*, vol. 124, no. 12, pp. 551–573, 1839.

[10] C. Moller, "Crystal structure and photoconductivity of cesium plumbohalides," *Nature*, vol. 182, p. 1436, 1958.

[11] D. Weber, "$CH_3NH_3PbX_3$, ein Pb(II)-system mit kubischer perowskitstruktur," *Zeitschrift für Naturforschung B*, vol. 33, no. 12, pp. 1443–1445, 1978.

[12] A. Kojima, K. Teshima, Y. Shirai, and T. Miyasaka, "Organometal halide perovskites as visible-light sensitizers for photovoltaic cells," *Journal of the American Chemical Society*, vol. 131, no. 17, pp. 6050–6051, 2009.

[13] M. M. Lee, J. Teuscher, T. Miyasaka, T. N. Murakami, and H. J. Snaith, "Efficient hybrid solar cells based on meso-superstructured organometal halide perovskites," *Science*, vol. 338, no. 6107, pp. 643–648, 2012.

[14] H. S. Kim, C. R. Lee, J. H. Im, K. B. Lee, T. Moehl, A. Marchioro, S. J. Moon, R. Humphry-Baker, J. H. Yum, J. E. Moser, M. Grätzel, and N. G. Park, "Lead iodide perovskite sensitized all-solid-state submicron thin film mesoscopic solar cell with efficiency exceeding 9%," *Scientific Reports*, vol. 2, no. 591, pp. 1–7, 2012.

[15] Editorial, "A decade of perovskite photovoltaics," *Nature Energy*, vol. 4, no. 1, p. 1, 2019.

[16] M. A. Green, Y. Hishikawa, E. D. Dunlop, D. H. Levi, J. Hohl-Ebinger, M. Yoshita, and A. W. Ho-Baillie, "Solar cell efficiency tables (Version 53)," *Progress in Photovoltaics: Research and Applications*, vol. 27, no. 1, pp. 3–12, 2019.

[17] N. Aristidou, I. Sanchez-Molina, T. Chotchuangchutchaval, M. Brown, L. Martinez, T. Rath, and S. A. Haque, "The role of oxygen in the degradation of methylammonium lead trihalide perovskite photoactive layers," *Angewandte Chemie*, vol. 54, no. 28, pp. 8208–8212, 2015.

[18] C. C. Stoumpos, C. D. Malliakas, and M. G. Kanatzidis, "Semiconducting tin and lead iodide perovskites with organic cations: Phase transitions, high mobilities, and near-infrared photoluminescent properties," *Inorganic Chemistry*, vol. 52, no. 15, pp. 9019–9038, 2013.

[19] G. E. Eperon, G. M. Paternò, R. J. Sutton, A. Zampetti, A. A. Haghighirad, F. Cacialli, and H. J. Snaith, "Inorganic caesium lead iodide perovskite solar cells," *Journal of Materials Chemistry A*, vol. 3, no. 39, pp. 19688–19695, 2015.

[20] N. Pellet, P. Gao, G. Gregori, T. Y. Yang, M. K. Nazeeruddin, J. Maier, and M. Grätzel, "Mixed-organic-cation perovskite photovoltaics for enhanced solar-light harvesting," *Angewandte Chemie*, vol. 53, no. 12, pp. 3151–3157, 2014.

[21] M. T. Klug, A. Osherov, A. A. Haghighirad, S. D. Stranks, P. R. Brown, S. Bai, J. T. Wang, X. Dang, V. Bulović, H. J. Snaith, and A. M. Belcher, "Tailoring metal halide perovskites through metal substitution: influence on photovoltaic and material properties," *Energy and Environmental Science*, vol. 10, no. 1, pp. 236–246, 2017.

[22] R. G. Niemann, L. Gouda, J. Hu, S. Tirosh, R. Gottesman, P. J. Cameron, and A. Zaban, "Cs incorporation into $CH_3NH_3PbI_3$ perovskite: substitution limit and stability enhancement," *Journal of Materials Chemistry A*, vol. 4, no. 45, pp. 17819–17827, 2016.

[23] A. K. Jena, A. Kulkarni, and T. Miyasaka, "Halide perovskite photovoltaics: background, status, and future prospects," *Chemical Reviews*, vol. 119, no. 5, pp. 3036–3103, 2019.

[24] H. J. Snaith, "Perovskites: The emergence of a new era for low-cost, high-efficiency solar cells," *Journal of Physical Chemistry Letters*, vol. 4, no. 21, pp. 3623–3630, 2013.

[25] M. I. Saidaminov, A. L. Abdelhady, G. Maculan, and O. M. Bakr, "Retrograde solubility of formamidinium and methylammonium lead halide perovskites enabling rapid single crystal growth," *Chemical Communications*, vol. 51, no. 100, pp. 17658–17661, 2015.

[26] C. Stavrakas, S. J. Zelewski, K. Frohna, E. P. Booker, K. Galkowski, K. Ji, E. Ruggeri, S. Mackowski, R. Kudrawiec, P. Plochocka, and S. D. Stranks, "Influence of grain size on phase transitions in halide perovskite films," *Advanced Energy Materials*, vol. 9, no. 35, p. 1901883, 2019.

[27] S. Braunger, L. E. Mundt, C. M. Wolff, M. Mews, C. Rehermann, M. Jošt, A. Tejada, D. Eisenhauer, C. Becker, J. A. Guerra, E. Unger, L. Korte, D. Neher, M. C. Schubert, B. Rech, and S. Albrecht, "$Cs_xFA_{1-x}Pb(I_{1-y}Br_y)_3$ Perovskite compositions: the appearance of wrinkled morphology and its impact on solar

cell performance," *Journal of Physical Chemistry C*, vol. 122, no. 30, pp. 17123–17135, 2018.

[28] C. Hamaguchi, "Energy band structures of semiconductors," in *Basic Semiconductor Physics*, pp. 1–27, Springer, 2 ed., 2017.

[29] C. Kittel, *Introduction to Solid State Physics*. Wiley, 8 ed., 2005.

[30] R. Wolfson, *Essential University Physics*. Pearson, 3 ed., 2014.

[31] M. Riordan and L. Hoddeson, *Crystal fire: the invention of the transistor and the birth of the information age*. Norton, 1 ed., 1998.

[32] K. W. Boer and U. W. Pohl, "Properties and growth of semiconductors," in *Semiconductor Physics*, pp. 1–26, Springer, 2014.

[33] S. J. Fonash, *Solar Cell Device Physics*. Elsevier, 2 ed., 2010.

[34] A. Mohammad Bagher, "Types of solar cells and application," *American Journal of Optics and Photonics*, vol. 3, no. 5, p. 94, 2015.

[35] C. H. Henry, "Limiting efficiencies of ideal single and multiple energy gap terrestrial solar cells," *Journal of Applied Physics*, vol. 51, no. 8, pp. 4494–4500, 1980.

[36] W. Shockley and H. J. Queisser, "Detailed balance limit of efficiency of p-n junction solar cells," *Journal of Applied Physics*, vol. 32, no. 3, pp. 510–519, 1961.

[37] G. F. Brown and J. Wu, "Third generation photovoltaics," *Laser and Photonics Reviews*, vol. 3, no. 4, pp. 394–405, 2009.

[38] M. L. Petrus, J. Schlipf, C. Li, T. P. Gujar, N. Giesbrecht, P. Müller-Buschbaum, M. Thelakkat, T. Bein, S. Hüttner, and P. Docampo, "Capturing the sun: a review of the challenges and perspectives of perovskite solar cells," *Advanced Energy Materials*, vol. 7, no. 16, pp. 1–27, 2017.

[39] Oxford PV, *Oxford PV perovskite solar cell achieves 28% efficiency*. Retrieved from https://www.oxfordpv.com/news/oxford-pv-perovskite-solar-cell-achieves-28-efficiency, Accessed 20/04/2019.

[40] F. Brivio, K. T. Butler, A. Walsh, and M. Van Schilfgaarde, "Relativistic quasiparticle self-consistent electronic structure of hybrid halide perovskite photovoltaic absorbers," *Physical Review B*, vol. 89, no. 15, pp. 1–6, 2014.

[41] K. Galkowski, A. A. Mitioglu, A. Surrente, Z. Yang, D. K. Maude, P. Kossacki, G. E. Eperon, J. T. Wang, H. J. Snaith, P. Plochocka, and R. J. Nicholas, "Spatially resolved studies of the phases and morphology of methylammonium and formamidinium lead tri-halide perovskites," *Nanoscale*, vol. 9, no. 9, pp. 3222–3230, 2017.

[42] D. H. Fabini, C. C. Stoumpos, G. Laurita, A. Kaltzoglou, A. G. Kontos, P. Falaras, M. G. Kanatzidis, and R. Seshadri, "Reentrant structural and optical properties and large positive thermal expansion in perovskite formamidinium lead iodide," *Angewandte Chemie*, vol. 55, no. 49, pp. 15392–15396, 2016.

[43] N. Pellet, J. Teuscher, J. Maier, and M. Grätzel, "Transforming hybrid organic inorganic perovskites by rapid halide exchange," *Chemistry of Materials*, vol. 27, no. 6, pp. 2181–2188, 2015.

[44] J. Even, L. Pedesseau, C. Katan, M. Kepenekian, J. S. Lauret, D. Sapori, and E. Deleporte, "Solid-state physics perspective on hybrid perovskite semiconductors," *Journal of Physical Chemistry C*, vol. 119, no. 19, pp. 10161–10177, 2015.

[45] J. Jimenez and J. W. Tomm, *Spectroscopic Analysis of Optoelectronic Semiconductors*. Springer, 1 ed., 2016.

[46] L. M. Herz, "Charge-carrier dynamics in organic-inorganic metal halide perovskites," *Annual Review of Physical Chemistry*, vol. 67, pp. 65–89, 2016.

[47] C. Wehrenfennig, G. E. Eperon, M. B. Johnston, H. J. Snaith, and L. M. Herz, "High charge carrier mobilities and lifetimes in organolead trihalide perovskites," *Advanced Materials*, vol. 26, no. 10, pp. 1584–1589, 2014.

[48] C. S. Ponseca, T. J. Savenije, M. Abdellah, K. Zheng, A. Yartsev, T. Pascher, T. Harlang, P. Chabera, T. Pullerits, A. Stepanov, J. P. Wolf, and V. Sundström, "Organometal halide perovskite solar cell materials rationalized: Ultrafast charge generation, high and microsecond-long balanced mobilities, and slow recombination," *Journal of the American Chemical Society*, vol. 136, no. 14, pp. 5189–5192, 2014.

[49] S. D. Stranks, V. M. Burlakov, T. Leijtens, J. M. Ball, A. Goriely, and H. J. Snaith, "Recombination kinetics in organic-inorganic perovskites: excitons, free charge, and subgap states," *Physical Review Applied*, vol. 2, no. 3, pp. 1–8, 2014.

[50] Y. Yamada, T. Nakamura, M. Endo, A. Wakamiya, and Y. Kanemitsu, "Near-band-edge optical responses of solution-processed organic–inorganic hybrid per-

ovskite $CH_3NH_3PbI_3$ on mesoporous TiO_2 electrodes," *Applied Physics Express*, vol. 7, no. 3, p. 032302, 2014.

[51] H. H. Telle, A. G. Urena, and R. J. Donovan, *Laser Chemistry*. Wiley, 1 ed., 2007.

[52] J. S. Manser and P. V. Kamat, "Band filling with free charge carriers in organometal halide perovskites," *Nature Photonics*, vol. 8, no. 9, pp. 737–743, 2014.

[53] K. Wu, A. Bera, C. Ma, Y. Du, Y. Yang, L. Li, and T. Wu, "Temperature-dependent excitonic photoluminescence of hybrid organometal halide perovskite films," *Physical Chemistry Chemical Physics*, vol. 16, no. 41, pp. 22476–22481, 2014.

[54] K. Tanaka and T. Kondo, "Bandgap and exciton binding energies in lead-iodide-based natural quantum-well crystals," *Science and Technology of Advanced Materials*, vol. 4, no. 6, pp. 599–604, 2003.

[55] V. D'Innocenzo, G. Grancini, M. J. P. Alcocer, A. R. S. Kandada, S. D. Stranks, M. M. Lee, G. Lanzani, H. J. Snaith, and A. Petrozza, "Excitons versus free charges in organo-lead tri-halide perovskites," *Nature Communications*, vol. 5, p. 3586, 2014.

[56] J. Even, L. Pedesseau, and C. Katan, "Analysis of multivalley and multibandgap absorption and enhancement of free carriers related to exciton screening in hybrid perovskites," *Journal of Physical Chemistry C*, vol. 118, no. 22, pp. 11566–11572, 2014.

[57] H. Zhu, K. Miyata, Y. Fu, J. Wang, P. P. Joshi, D. Niesner, K. W. Williams, S. Jin, and X. Y. Zhu, "Screening in crystalline liquids protects energetic carriers in hybrid perovskites," *Science*, vol. 353, no. 6306, pp. 1409–1413, 2016.

[58] A. D. Wright, C. Verdi, R. L. Milot, G. E. Eperon, M. A. Pérez-Osorio, H. J. Snaith, F. Giustino, M. B. Johnston, and L. M. Herz, "Electron-phonon coupling in hybrid lead halide perovskites," *Nature Communications*, vol. 7, no. May, p. 11755, 2016.

[59] D. W. DeQuilettes, W. Zhang, V. M. Burlakov, D. J. Graham, T. Leijtens, A. Osherov, V. Bulović, H. J. Snaith, D. S. Ginger, and S. D. Stranks, "Photo-induced halide redistribution in organic-inorganic perovskite films," *Nature Communications*, vol. 7, no. May, p. 11683, 2016.

[60] D. Shi, V. Adinolfi, R. Comin, M. Yuan, E. Alarousu, A. Buin, Y. Chen, S. Hoogland, A. Rothenberger, K. Katsiev, Y. Losovyj, X. Zhang, P. A. Dowben, O. F. Mohammed, E. H. Sargent, and O. M. Bakr, "Low trap-state density and long carrier diffusion in organolead trihalide perovskite single crystals," *Science*, vol. 347, no. 6221, pp. 519–522, 2015.

[61] Y. Yang, Y. Yan, M. Yang, S. Choi, K. Zhu, J. M. Luther, and M. C. Beard, "Low surface recombination velocity in solution-grown $CH_3NH_3PbBr_3$ perovskite single crystal," *Nature Communications*, vol. 6, p. 7961, 2015.

[62] B. Wenger, P. K. Nayak, X. Wen, S. V. Kesava, N. K. Noel, and H. J. Snaith, "Consolidation of the optoelectronic properties of $CH_3NH_3PbBr_3$ perovskite single crystals," *Nature Communications*, vol. 8, no. 1, p. 590, 2017.

[63] Q. Dong, Y. Fang, Y. Shao, P. Mulligan, J. Qiu, L. Cao, and J. Huang, "Electron-hole diffusion lengths in solution-grown $CH_3NH_3PbI_3$ single crystals," *Science*, vol. 347, no. 6225, pp. 967–970, 2015.

[64] G. Walters, B. R. Sutherland, S. Hoogland, D. Shi, R. Comin, D. P. Sellan, O. M. Bakr, and E. H. Sargent, "Two-photon absorption in organometallic bromide perovskites," *ACS Nano*, vol. 9, no. 9, pp. 9340–9346, 2015.

[65] B. Wu, H. T. Nguyen, Z. Ku, G. Han, D. Giovanni, N. Mathews, H. J. Fan, and T. C. Sum, "Discerning the surface and bulk recombination kinetics of organic–inorganic halide perovskite single crystals," *Advanced Energy Materials*, vol. 6, no. 14, pp. 1–9, 2016.

[66] M. I. Saidaminov, A. L. Abdelhady, B. Murali, E. Alarousu, V. M. Burlakov, W. Peng, I. Dursun, L. Wang, Y. He, G. MacUlan, A. Goriely, T. Wu, O. F. Mohammed, and O. M. Bakr, "High-quality bulk hybrid perovskite single crystals within minutes by inverse temperature crystallization," *Nature Communications*, vol. 6, no. May, pp. 1–6, 2015.

[67] H. Wei, Y. Fang, P. Mulligan, W. Chuirazzi, H. H. Fang, C. Wang, B. R. Ecker, Y. Gao, M. A. Loi, L. Cao, and J. Huang, "Sensitive X-ray detectors made of methylammonium lead tribromide perovskite single crystals," *Nature Photonics*, vol. 10, no. 5, pp. 333–339, 2016.

[68] T. W. Crothers, R. L. Milot, J. B. Patel, E. S. Parrott, J. Schlipf, P. Müller-Buschbaum, M. B. Johnston, and L. M. Herz, "Photon reabsorption masks intrin-

sic bimolecular charge-carrier recombination in $CH_3NH_3PbI_3$ perovskite," *Nano Letters*, vol. 17, no. 9, pp. 5782–5789, 2017.

[69] Y. Varshni, "Temperature dependence of the energy gap in semiconductors," *Physica*, vol. 34, no. 1, pp. 149–154, 1967.

[70] A. Francisco-López, B. Charles, O. J. Weber, M. I. Alonso, M. Garriga, M. Campoy-Quiles, M. T. Weller, and A. R. Goñi, "The equal footing of thermal expansion and electron-phonon interaction in the temperature dependence of lead halide perovskite band gaps," *The Journal of Physical Chemistry Letters*, vol. 10, no. 11, pp. 2971–2977, 2019.

[71] W. Clegg, *X-Ray Crystallography.* Oxford University Press, 2 ed., 2015.

[72] W. Clegg, *Crystal structure determination.* Oxford University Press, 1 ed., 1996.

[73] L. Priester, "Defects in the grain boundary structure," in *Grain Boundaries: From Theory to Engineering*, vol. 2, pp. 155–146, Springer, 2013.

[74] O. J. Weber, D. Ghosh, S. Gaines, P. F. Henry, A. B. Walker, M. S. Islam, and M. T. Weller, "Phase behavior and polymorphism of formamidinium lead iodide," *Chemistry of Materials*, vol. 30, no. 11, pp. 3768–3778, 2018.

[75] M. T. Weller and N. A. Young, *Characterisation methods in inorganic chemistry.* Oxford University Press, 1 ed., 2017.

[76] V. M. Goldschmidt, "Die gesetze der krystallochemie," *Die Naturwissenschaften*, vol. 14, no. 21, pp. 477–485, 1926.

[77] Z. Li, M. Yang, J. S. Park, S. H. Wei, J. J. Berry, and K. Zhu, "Stabilizing perovskite structures by tuning tolerance factor: formation of formamidinium and cesium lead iodide solid-state alloys," *Chemistry of Materials*, vol. 28, no. 1, pp. 284–292, 2016.

[78] G. Kieslich, S. Sun, and A. K. Cheetham, "An extended tolerance factor approach for organic-inorganic perovskites," *Chemical Science*, vol. 6, no. 6, pp. 3430–3433, 2015.

[79] W. Travis, E. N. Glover, H. Bronstein, D. O. Scanlon, and R. G. Palgrave, "On the application of the tolerance factor to inorganic and hybrid halide perovskites: A revised system," *Chemical Science*, vol. 7, no. 7, pp. 4548–4556, 2016.

[80] B. Charles, J. Dillon, O. J. Weber, M. S. Islam, and M. T. Weller, "Understanding the stability of mixed A-cation lead iodide perovskites," *Journal of Materials Chemistry A*, vol. 5, no. 43, pp. 22495–22499, 2017.

[81] M. Saliba, T. Matsui, J. Y. Seo, K. Domanski, J. P. Correa-Baena, M. K. Nazeeruddin, S. M. Zakeeruddin, W. Tress, A. Abate, A. Hagfeldt, and M. Grätzel, "Cesium-containing triple cation perovskite solar cells: Improved stability, reproducibility and high efficiency," *Energy and Environmental Science*, vol. 9, no. 6, pp. 1989–1997, 2016.

[82] O. Nazarenko, S. Yakunin, V. Morad, I. Cherniukh, and M. V. Kovalenko, "Single crystals of caesium formamidinium lead halide perovskites: Solution growth and gamma dosimetry," *NPG Asia Materials*, vol. 9, no. 4, pp. 373–8, 2017.

[83] C. J. Howard and H. T. Stokes, "Group-theoretical analysis of octahedral tilting in perovskites," *Acta Crystallographica Section B*, vol. 58, no. 3, pp. 565–565, 2002.

[84] P. M. Woodward, "Octahedral tilting in perovskites. I. geometrical considerations," *Acta Crystallographica Section B*, vol. 53, no. 1, pp. 32–43, 1997.

[85] A. M. Glazer, "The classification of tilted octahedra in perovskites," *Acta Crystallographica Section B*, vol. 28, no. 11, pp. 3384–3392, 1972.

[86] M. T. Weller, O. J. Weber, P. F. Henry, A. M. Di Pumpo, and T. C. Hansen, "Complete structure and cation orientation in the perovskite photovoltaic methylammonium lead iodide between 100 and 352 K," *Chemical Communications*, vol. 51, no. 20, pp. 4180–4183, 2015.

[87] M. T. Weller, O. J. Weber, J. M. Frost, and A. Walsh, "Cubic perovskite structure of black formamidinium lead iodide, α-$[HC(NH_2)_2]PbI_3$, at 298 K," *Journal of Physical Chemistry Letters*, vol. 6, no. 16, pp. 3209–3212, 2015.

[88] R. J. Sutton, M. R. Filip, A. A. Haghighirad, N. Sakai, B. Wenger, F. Giustino, and H. J. Snaith, "Cubic or orthorhombic? revealing the crystal structure of metastable black-phase $CsPbI_3$ by theory and experiment," *ACS Energy Letters*, vol. 3, pp. 1787–1794, 2018.

[89] D. B. Mitzi, "Templating and structural engineering in organic-inorganic perovskites," *Journal of the Chemical Society, Dalton Transactions*, vol. 1, pp. 1–12, 2001.

[90] T. Baikie, Y. Fang, J. M. Kadro, M. Schreyer, F. Wei, S. G. Mhaisalkar, M. Graetzel, and T. J. White, "Synthesis and crystal chemistry of the hybrid perovskite $(CH_3NH_3)PbI_3$ for solid-state sensitised solar cell applications," *Journal of Materials Chemistry A*, vol. 1, no. 18, p. 5628, 2013.

[91] Y. Kawamura, H. Mashiyama, and K. Hasebe, "Structural study on cubic–tetragonal transition of $CH_3NH_3PbI_3$," *Journal of the Physical Society of Japan*, vol. 71, no. 7, pp. 1694–1697, 2002.

[92] T. Y. Yang, G. Gregori, N. Pellet, M. Grätzel, and J. Maier, "The significance of ion conduction in a hybrid organic-inorganic lead-iodide-based perovskite photosensitizer," *Angewandte Chemie*, vol. 54, no. 27, pp. 7905–7910, 2015.

[93] T. Chen, W.-L. Chen, B. J. Foley, J. Lee, J. P. C. Ruff, J. Y. P. Ko, C. M. Brown, L. W. Harriger, D. Zhang, C. Park, M. Yoon, Y.-M. Chang, J. J. Choi, and S.-H. Lee, "Origin of long lifetime of band-edge charge carriers in organic–inorganic lead iodide perovskites," *Proceedings of the National Academy of Sciences*, vol. 114, no. 29, pp. 7519–7524, 2017.

[94] M. C. Alvarez-Galván, J. A. Alonso, C. A. López, E. López-Linares, C. Contreras, M. J. Lázaro, F. Fauth, and M. V. Martínez-Huerta, "Crystal Growth, structural phase transitions, and optical gap evolution of $CH_3NH_3Pb(Br_{1-x}Cl_x)_3$ Perovskites," *Crystal Growth and Design*, vol. 19, no. 2, pp. 918–924, 2019.

[95] O. J. Weber, B. Charles, and M. T. Weller, "Phase behaviour and composition in the formamidinium-methylammonium hybrid lead iodide perovskite solid solution," *Journal of Materials Chemistry A*, vol. 4, no. 40, pp. 15375–15382, 2016.

[96] J. W. Lee, D. H. Kim, H. S. Kim, S. W. Seo, S. M. Cho, and N. G. Park, "Formamidinium and cesium hybridization for photo- and moisture-stable perovskite solar cell," *Advanced Energy Materials*, vol. 5, no. 20, p. 1501310, 2015.

[97] E. J. Juarez-Perez, L. K. Ono, and Y. Qi, "Thermal degradation of formamidinium based lead halide perovskites into sym-triazine and hydrogen cyanide observed by coupled thermogravimetry - mass spectrometry analysis," *Journal of Materials Chemistry A*, vol. 7, pp. 16912–16919, 2019.

[98] E. P. Favvas and A. Mitropoulos, "What is spinodal decomposition," *Engineering Science and Technology Review*, vol. 1, pp. 25–27, 2008.

[99] G. P. Nagabhushana, R. Shivaramaiah, and A. Navrotsky, "Direct calorimetric verification of thermodynamic instability of lead halide hybrid perovskites," *Pro-*

ceedings of the National Academy of Sciences, vol. 113, no. 28, pp. 7717–7721, 2016.

[100] E. C. Schueller, G. Laurita, D. H. Fabini, C. C. Stoumpos, M. G. Kanatzidis, and R. Seshadri, "Crystal structure evolution and notable thermal expansion in hybrid perovskites formamidinium tin iodide and formamidinium lead bromide," *Inorganic Chemistry*, vol. 57, no. 2, pp. 695–701, 2018.

[101] D. B. Mitzi, C. D. Dimitrakopoulos, and L. L. Kosbar, "Structurally tailored organic-inorganic perovskites: Optical properties and solution-processed channel materials for thin-film transistors," *Chemistry of Materials*, vol. 13, no. 10, pp. 3728–3740, 2001.

[102] A. R. Denton and N. W. Ashcroft, "Vegard's Law," *Physical Review A*, vol. 43, no. 6, pp. 3161–3164, 1991.

[103] E. M. Mozur, A. E. Maughan, Y. Cheng, A. Huq, N. Jalarvo, L. L. Daemen, and J. R. Neilson, "Orientational glass formation in substituted hybrid perovskites," *Chemistry of Materials*, vol. 29, no. 23, pp. 10168–10177, 2017.

[104] O. A. Syzgantseva, M. Saliba, M. Grätzel, and U. Rothlisberger, "Stabilization of the perovskite phase of formamidinium lead triiodide by methylammonium, Cs, and/or Rb doping," *Journal of Physical Chemistry Letters*, vol. 8, no. 6, pp. 1191–1196, 2017.

[105] D. J. Kubicki, D. Prochowicz, A. Hofstetter, S. M. Zakeeruddin, M. Grätzel, and L. Emsley, "Phase segregation in Cs-, Rb- and K-doped mixed-cation $(MA)_x(FA)_{1-x}PbI_3$ hybrid perovskites from solid-state NMR," *Journal of the American Chemical Society*, vol. 139, no. 40, pp. 14173–14180, 2017.

[106] T. Zhang, M. Yang, E. E. Benson, Z. Li, J. Van De Lagemaat, J. M. Luther, Y. Yan, K. Zhu, and Y. Zhao, "A facile solvothermal growth of single crystal mixed halide perovskite $CH_3NH_3Pb(Br_{1-x}Cl_x)_3$," *Chemical Communications*, vol. 51, no. 37, pp. 7820–7823, 2015.

[107] C. G. Bischak, C. L. Hetherington, H. Wu, S. Aloni, D. F. Ogletree, D. T. Limmer, and N. S. Ginsberg, "Origin of reversible photoinduced phase separation in hybrid perovskites," *Nano Letters*, vol. 17, no. 2, pp. 1028–1033, 2017.

[108] G. Nedelcu, L. Protesescu, S. Yakunin, M. I. Bodnarchuk, M. J. Grotevent, and M. V. Kovalenko, "Fast anion-exchange in highly luminescent nanocrystals of

cesium lead halide perovskites ($CsPbX_3$, X = Cl, Br, I)," *Nano Letters*, vol. 15, no. 8, pp. 5635–5640, 2015.

[109] W. Rehman, D. P. McMeekin, J. B. Patel, R. L. Milot, M. B. Johnston, H. J. Snaith, and L. M. Herz, "Photovoltaic mixed-cation lead mixed-halide perovskites: Links between crystallinity, photo-stability and electronic properties," *Energy and Environmental Science*, vol. 10, no. 1, pp. 361–369, 2017.

[110] A. M. Leguy, Y. Hu, M. Campoy-Quiles, M. I. Alonso, O. J. Weber, P. Azarhoosh, M. Van Schilfgaarde, M. T. Weller, T. Bein, J. Nelson, P. Docampo, and P. R. Barnes, "Reversible hydration of $CH_3NH_3PbI_3$ in films, single crystals, and solar cells," *Chemistry of Materials*, vol. 27, no. 9, pp. 3397–3407, 2015.

[111] A. Binek, F. C. Hanusch, P. Docampo, and T. Bein, "Stabilization of the trigonal high-temperature phase of formamidinium lead iodide," *Journal of Physical Chemistry Letters*, vol. 6, no. 7, pp. 1249–1253, 2015.

[112] T. Zhang, X. Meng, Y. Bai, S. Xiao, C. Hu, Y. Yang, H. Chen, and S. Yang, "Profiling the organic cation-dependent degradation of organolead halide perovskite solar cells," *Journal of Materials Chemistry A*, vol. 5, no. 3, pp. 1103–1111, 2017.

[113] C. Yi, J. Luo, S. Meloni, A. Boziki, N. Ashari-Astani, C. Grätzel, S. M. Zakeeruddin, U. Röthlisberger, and M. Grätzel, "Entropic stabilization of mixed A-cation ABX_3 metal halide perovskites for high performance perovskite solar cells," *Energy and Environmental Science*, vol. 9, no. 2, pp. 656–662, 2016.

[114] S. J. Yoon, M. Kuno, and P. V. Kamat, "Shift happens. How halide ion defects influence photoinduced segregation in mixed halide perovskites," *ACS Energy Letters*, vol. 2, no. 7, pp. 1507–1514, 2017.

[115] A. Karmakar, A. M. Askar, G. M. Bernard, V. V. Terskikh, M. Ha, S. Patel, K. Shankar, and V. K. Michaelis, "Mechanochemical synthesis of methylammonium lead mixed-halide perovskites: unraveling the solid-solution behavior using solid-state NMR," *Chemistry of Materials*, vol. 30, no. 7, pp. 2309–2321, 2018.

[116] Q. Zhang and F. Saito, "Mechanochemical synthesis of $LaMnO_3$ from La_2O_3 and Mn_2O_3 powders," *Journal of Alloys and Compounds*, vol. 297, no. 1-2, pp. 99–103, 2000.

[117] D. Prochowicz, K. Sokołowski, I. Justyniak, A. Kornowicz, D. Fairen-Jimenez, T. Friščić, and J. Lewiński, "A mechanochemical strategy for IRMOF as-

sembly based on pre-designed oxo-zinc precursors," *Chemical Communications*, vol. 51Prochowi, no. 19, pp. 4032–4035, 2015.

[118] A. Poglitsch and D. Weber, "Dynamic disorder in methylammoniumtrihalogenoplumbates (II) observed by millimeter-wave spectroscopy," *The Journal of Chemical Physics*, vol. 87, no. 11, pp. 6373–6378, 1987.

[119] Y. Dang, Y. Liu, Y. Sun, D. Yuan, X. Liu, W. Lu, G. Liu, H. Xia, and X. Tao, "Bulk crystal growth of hybrid perovskite material $CH_3NH_3PbI_3$," *CrystEngComm*, vol. 17, no. 3, pp. 665–670, 2015.

[120] Y. X. Chen, Q. Q. Ge, Y. Shi, J. Liu, D. J. Xue, J. Y. Ma, J. Ding, H. J. Yan, J. S. Hu, and L. J. Wan, "General Space-Confined On-Substrate Fabrication of Thickness-Adjustable Hybrid Perovskite Single-Crystalline Thin Films," *Journal of the American Chemical Society*, vol. 138, no. 50, pp. 16196–16199, 2016.

[121] C. T. Rueden, J. Schindelin, M. C. Hiner, B. E. DeZonia, A. E. Walter, E. T. Arena, and K. W. Eliceiri, "ImageJ2: ImageJ for the next generation of scientific image data," *BMC Bioinformatics*, vol. 18, no. 1, pp. 1–26, 2017.

[122] J. Xie, "Stereomicroscopy: 3D imaging and the third dimension measurement," *Agilent Technologies*, pp. 1–8, 2011.

[123] W. Zhou, R. P. Apkarian, and Z. L. Wang, "Fundamentals of Scanning Electron Microscopy," in *Scanning Microscopy for Nanotechnology*, ch. 1, pp. 1–40, Springer, 2007.

[124] A. UI-Hamid, "Microchemical Analysis in the SEM," in *A Beginners' Guide to Scanning Electron Microscopy*, p. 265, Springer, 1 ed., 2018.

[125] O. V. Dolomanov, L. J. Bourhis, R. J. Gildea, J. A. K. Howard, and H. Puschmann, "OLEX2: A complete structure solution, refinement and analysis program," *Journal of Applied Crystallography*, vol. 42, no. 2, pp. 339–341, 2009.

[126] G. M. Sheldrick, "Crystal structure refinement with SHELXL," *Acta Crystallographica Section C: Structural Chemistry*, vol. 71, no. Md, pp. 3–8, 2015.

[127] A. L. Spek, "Structure validation in chemical crystallography," *Acta Crystallographica Section D: Biological Crystallography*, vol. 65, no. 2, pp. 148–155, 2009.

[128] W. Bragg and W. Bragg, "The reflection of X-rays by crystals," *Royal Society*, vol. 88, no. 605, 1913.

[129] M. M. Woolfson, *An introduction to X-ray crystallography*. Cambridge University Press, 1997.

[130] B. H. Toby and R. B. Von Dreele, "GSAS-II: The genesis of a modern open-source all purpose crystallography software package," *Journal of Applied Crystallography*, vol. 46, no. 2, pp. 544–549, 2013.

[131] ISIS neutron and muon source, *How ISIS works*. Retrieved from https://www.isis.stfc.ac.uk/Pages/How-ISIS-works–in-depth.aspx, Accessed 30/08/2019.

[132] R. I. Smith, S. Hull, and A. R. Armstrong, "Polaris powder diffractometer at ISIS," *Materials Science Forum*, vol. 180, pp. 1000–1002, 1994.

[133] R. E. Dinnebier, A. Leineweber, and J. Evans, *Rietveld Refinement Practical Powder Diffraction Pattern Analysis using TOPAS*. De Gruyer, 1 ed., 2018.

[134] G. S. Pawley, "Unit-cell refinement from powder diffraction scans," *Journal of Applied Crystallography*, vol. 14, no. 6, pp. 357–361, 1981.

[135] A. Le Bail, "Whole powder pattern decomposition methods and applications: A retrospection," *Powder Diffraction*, vol. 20, no. 4, pp. 316–326, 2005.

[136] H. M. Rietveld, "The Rietveld method," *Physica Scripta*, vol. 89, no. 9, 2014.

[137] C. S. Kumar, *UV-VIS and Photoluminescence Spectroscopy for Nanomaterials Characterization*. Springer, 1 ed., 2013.

[138] M. Wahl, "Time-correlated single-photon counting on a chip," tech. rep., Pico Quant, 2014.

[139] J. Mooney and P. Kambhampati, "Get the basics right: Jacobian conversion of wavelength and energy scales for quantitative analysis of emission spectra," *Journal of Physical Chemistry Letters*, vol. 5, no. 20, p. 3497, 2014.

[140] D.-P. Zhan, L.-Q. Xie, Z.-Q. Tian, J.-W. Yan, B.-W. Mao, L. Chen, H.-X. Lin, Z.-A. Nan, and T. Wang, "Understanding the cubic phase stabilization and crystallization kinetics in mixed cations and halides perovskite single crystals," *Journal of the American Chemical Society*, vol. 139, no. 9, pp. 3320–3323, 2017.

[141] G. E. Eperon, S. D. Stranks, C. Menelaou, M. B. Johnston, L. M. Herz, and H. J. Snaith, "Formamidinium lead trihalide: A broadly tunable perovskite for

efficient planar heterojunction solar cells," *Energy and Environmental Science*, vol. 7, no. 3, pp. 982–988, 2014.

[142] D. H. Fabini, T. A. Siaw, C. C. Stoumpos, G. Laurita, D. Olds, K. Page, J. G. Hu, M. G. Kanatzidis, S. Han, and R. Seshadri, "Universal dynamics of molecular reorientation in hybrid lead iodide perovskites," *Journal of the American Chemical Society*, vol. 139, no. 46, pp. 16875–16884, 2017.

[143] L. Protesescu, S. Yakunin, S. Kumar, J. Bär, F. Bertolotti, N. Masciocchi, A. Guagliardi, M. Grotevent, I. Shorubalko, M. I. Bodnarchuk, C. J. Shih, and M. V. Kovalenko, "Dismantling the "red Wall" of colloidal perovskites: highly luminescent formamidinium and formamidinium-cesium lead iodide nanocrystals," *ACS Nano*, vol. 11, no. 3, pp. 3119–3134, 2017.

[144] S. Prathapani, P. Bhargava, and S. Mallick, "Electronic band structure and carrier concentration of formamidinium-cesium mixed cation lead mixed halide hybrid perovskites," *Applied Physics Letters*, vol. 112, no. 9, pp. 1–5, 2018.

[145] R. Prasanna, A. Gold-Parker, T. Leijtens, B. Conings, A. Babayigit, H. G. Boyen, M. F. Toney, and M. D. McGehee, "Band gap tuning via lattice contraction and octahedral tilting in perovskite materials for photovoltaics," *Journal of the American Chemical Society*, vol. 139, no. 32, pp. 11117–11124, 2017.

[146] D. Ghosh, A. R. Smith, A. B. Walker, and M. S. Islam, "Mixed A-cation perovskites for solar cells: atomic-scale insights into structural distortion, hydrogen bonding and electronic properties," *Chemistry of Materials*, vol. 30, no. 15, pp. 5194–5204, 2018.

[147] D. Ghosh, P. Walsh Atkins, M. S. Islam, A. B. Walker, and C. Eames, "Good vibrations: locking of octahedral tilting in mixed-cation iodide perovskites for solar cells," *ACS Energy Letters*, vol. 2, no. 10, pp. 2424–2429, 2017.

[148] F. Lédée, G. Trippé-Allard, H. Diab, P. Audebert, D. Garrot, J. S. Lauret, and E. Deleporte, "Fast growth of monocrystalline thin films of 2D layered hybrid perovskite," *CrystEngComm*, vol. 19, no. 19, pp. 2598–2602, 2017.

[149] D. P. Mcmeekin, G. Sadoughi, W. Rehman, G. E. Eperon, M. Saliba, M. T. Hörantner, A. Haghighirad, N. Sakai, L. Korte, B. Rech, M. B. Johnston, L. M. Herz, and H. J. Snaith, "A mixed-cation lead mixed-halide perovskite absorber for tandem solar cells," *Science*, vol. 351, no. 6269, pp. 151–156, 2016.

[150] C. Yi, J. Luo, S. Meloni, A. Boziki, N. Ashari-Astani, C. Grätzel, S. M. Zakeeruddin, U. Röthlisberger, and M. Grätzel, "Entropic stabilization of mixed A-cation ABX_3 metal halide perovskites for high performance perovskite solar cells," *Energy and Environmental Science*, vol. 9, no. 2, pp. 656–662, 2016.

[151] M. I. Dar, N. Arora, S. M. Zakeeruddin, M. Grätzel, G. Jacopin, S. Meloni, A. Boziki, U. Rothlisberger, and A. Mattoni, "Origin of unusual bandgap shift and dual emission in organic-inorganic lead halide perovskites," *Science Advances*, vol. 2, no. 10, p. e1601156, 2016.

[152] R. L. Milot, R. J. Sutton, G. E. Eperon, A. A. Haghighirad, J. Martinez Hardigree, L. Miranda, H. J. Snaith, M. B. Johnston, and L. M. Herz, "Charge-carrier dynamics in 2D hybrid metal-halide perovskites," *Nano Letters*, vol. 16, no. 11, pp. 7001–7007, 2016.

[153] E. T. Hoke, D. J. Slotcavage, E. R. Dohner, A. R. Bowring, H. I. Karunadasa, and M. D. McGehee, "Reversible photo-induced trap formation in mixed-halide hybrid perovskites for photovoltaics," *Chemical Science*, vol. 6, no. 1, pp. 613–617, 2015.

[154] M. Grätzel, "The light and shade of perovskite solar cells," *Nature Materials*, vol. 13, no. 9, pp. 838–842, 2014.

[155] R. E. Beal, D. J. Slotcavage, T. Leijtens, A. R. Bowring, R. A. Belisle, W. H. Nguyen, G. F. Burkhard, E. T. Hoke, and M. D. McGehee, "Cesium lead halide perovskites with improved stability for tandem solar cells," *Journal of Physical Chemistry Letters*, vol. 7, no. 5, pp. 746–751, 2016.

[156] H. F. Zarick, N. Soetan, W. R. Erwin, and R. Bardhan, "Mixed halide hybrid perovskites: A paradigm shift in photovoltaics," *Journal of Materials Chemistry A*, vol. 6, no. 14, pp. 5507–5537, 2018.

[157] K. H. Wang, L. C. Li, M. Shellaiah, and K. W. Sun, "Structural and photophysical properties of methylammonium lead tribromide ($MAPbBr_3$) single crystals," *Scientific Reports*, vol. 7, no. 1, pp. 1–14, 2017.

[158] S. D. Stranks, G. E. Eperon, G. Grancini, C. Menelaou, M. J. P. Alcocer, T. Leijtens, L. M. Herz, A. Petrozza, and H. J. Snaith, "Electron-hole diffusion lengths exceeding 1 micrometer in an organometal trihalide perovskite absorber," *Science*, vol. 342, no. October, pp. 341–345, 2013.

[159] I. P. Swainson, R. P. Hammond, C. Soullière, O. Knop, and W. Massa, "Phase transitions in the perovskite methylammonium lead bromide, $CH_3ND_3PbBr_3$," *Journal of Solid State Chemistry*, vol. 176, no. 1, pp. 97–104, 2003.

[160] C. Wehrenfennig, M. Liu, H. J. Snaith, M. B. Johnston, and L. M. Herz, "Charge carrier recombination channels in the low-temperature phase of organic-inorganic lead halide perovskite thin films," *Applied Materials*, vol. 2, no. 8, p. 081513, 2014.

[161] P. K. Nayak, D. T. Moore, B. Wenger, S. Nayak, A. A. Haghighirad, A. Fineberg, N. K. Noel, O. G. Reid, G. Rumbles, P. Kukura, K. A. Vincent, and H. J. Snaith, "Mechanism for rapid growth of organic-inorganic halide perovskite crystals," *Nature Communications*, vol. 7, p. 13303, 2016.

[162] M. Fox, *Optical Properties of Solids*. Oxford University Press, 2 ed., 2010.

[163] F. Lehmann, A. Franz, D. M. Többens, S. Levcenco, T. Unold, A. Taubert, and S. Schorr, "The phase diagram of a mixed halide (Br, I) hybrid perovskite obtained by synchrotron X-ray diffraction," *RSC Advances*, vol. 9, no. 20, pp. 11151–11159, 2019.

[164] M. Mori and H. Saito, "An X-ray study of successive phase transitions in $CsSnBr_3$," *Journal of Physics C: Solid State Physics*, vol. 19, no. 14, pp. 2391–2401, 1986.

[165] J. F. Ackerman, G. M. Cole, and S. L. Holt, "The physical properties of some transition metal compounds of the ABX3 type," *Inorganica Chimica Acta*, vol. 8, no. C, pp. 323–343, 1974.

[166] S. F. Hoefler, G. Trimmel, and T. Rath, "Progress on lead-free metal halide perovskites for photovoltaic applications: a review," *Monatshefte fur Chemie*, vol. 148, no. 5, pp. 795–826, 2017.

[167] J. Mizusaki, K. Arai, and K. Fueki, "Ionic conduction of the perovskite-type halides," *Solid State Ionics*, vol. 11, no. 3, pp. 203–211, 1983.

[168] C. C. Stoumpos, D. H. Cao, D. J. Clark, J. Young, J. M. Rondinelli, J. I. Jang, J. T. Hupp, and M. G. Kanatzidis, "Ruddlesden-popper hybrid lead iodide perovskite 2D homologous semiconductors," *Chemistry of Materials*, vol. 28, no. 8, pp. 2852–2867, 2016.

[169] T. J. Jacobsson, J. P. Correa-Baena, E. Halvani Anaraki, B. Philippe, S. D. Stranks, M. E. Bouduban, W. Tress, K. Schenk, J. Teuscher, J. E. Moser,

H. Rensmo, and A. Hagfeldt, "Unreacted PbI_2 as a double-edged sword for enhancing the performance of perovskite solar cells," *Journal of the American Chemical Society*, vol. 138, no. 32, pp. 10331–10343, 2016.

[170] Z. Yang, C. C. Chueh, P. W. Liang, M. Crump, F. Lin, Z. Zhu, and A. K. Jen, "Effects of formamidinium and bromide ion substitution in methylammonium lead triiodide toward high-performance perovskite solar cells," *Nano Energy*, vol. 22, pp. 328–337, 2016.

[171] N. Aristidou, C. Eames, I. Sanchez-Molina, X. Bu, J. Kosco, M. Saiful Islam, and S. A. Haque, "Fast oxygen diffusion and iodide defects mediate oxygen-induced degradation of perovskite solar cells," *Nature Communications*, vol. 8, no. May, pp. 1–10, 2017.

[172] M. A. Green and A. Ho-Baillie, "Perovskite solar cells: The birth of a new era in photovoltaics," *ACS Energy Letters*, vol. 2, no. 4, pp. 822–830, 2017.

[173] M. Fanfoni and M. Tomellini, "The Johnson-Mehl-Avrami-Kohnogorov model: A brief review," *Il Nuovo Cimento D*, vol. 20, no. 7-8, pp. 1171–1182, 1998.

[174] M. Avrami, "Kinetics of phase change. I: General theory," *The Journal of Chemical Physics*, vol. 7, no. 12, pp. 1103–1112, 1939.

[175] M. Avrami, "Kinetics of phase change. II Transformation-time relations for random distribution of nuclei," *The Journal of Chemical Physics*, vol. 8, no. 2, pp. 212–224, 1940.

[176] M. Castro, F. Domínguez-Adame, A. Sánchez, and T. Rodríguez, "Model for crystallization kinetics: Deviations from Kolmogorov-Johnson-Mehl-Avrami kinetics," *Applied Physics Letters*, vol. 75, no. 15, pp. 2205–2207, 1999.

[177] C. Michaelsen, M. Dahms, and M. Pfuff, "Comment on crystallization kinetics," *Physical Review B - Condensed Matter and Materials Physics*, vol. 53, no. 17, pp. 11877–11877, 1996.

[178] M. I. Asghar, J. Zhang, H. Wang, and P. D. Lund, "Device stability of perovskite solar cells – A review," *Renewable and Sustainable Energy Reviews*, vol. 77, no. April, pp. 131–146, 2017.

[179] T. Leijtens, G. E. Eperon, N. K. Noel, S. N. Habisreutinger, A. Petrozza, and H. J. Snaith, "Stability of metal halide perovskite solar cells," *Advanced Energy Materials*, vol. 5, no. 20, pp. 1–23, 2015.

[180] T. Leijtens, K. Bush, R. Cheacharoen, R. Beal, A. Bowring, and M. D. McGehee, "Towards enabling stable lead halide perovskite solar cells; Interplay between structural, environmental, and thermal stability," *Journal of Materials Chemistry A*, vol. 5, no. 23, pp. 11483–11500, 2017.

[181] A. Sharenko and M. F. Toney, "Relationships between lead halide perovskite thin-film fabrication, morphology, and performance in solar cells," *Journal of the American Chemical Society*, vol. 138, no. 2, pp. 463–470, 2016.

[182] J. Burschka, N. Pellet, S. J. Moon, R. Humphry-Baker, P. Gao, M. K. Nazeeruddin, and M. Grätzel, "Sequential deposition as a route to high-performance perovskite-sensitized solar cells," *Nature*, vol. 499, no. 7458, pp. 316–319, 2013.

[183] Z. Wei, H. Chen, K. Yan, and S. Yang, "Inkjet printing and instant chemical transformation of a $CH_3NH_3PbI_3$/nanocarbon electrode and interface for planar perovskite solar cells," *Angewandte Chemie*, vol. 53, no. 48, pp. 13239–13243, 2014.

[184] Q. Chen, H. Zhou, Z. Hong, S. Luo, H. S. Duan, H. H. Wang, Y. Liu, G. Li, and Y. Yang, "Planar heterojunction perovskite solar cells via vapor-assisted solution process," *Journal of the American Chemical Society*, vol. 136, no. 2, pp. 622–625, 2014.

[185] F. Bella, G. Griffini, J. P. Correa-Baena, G. Saracco, M. Grätzel, A. Hagfeldt, S. Turri, and C. Gerbaldi, "Improving efficiency and stability of perovskite solar cells with photocurable fluoropolymers," *Science*, vol. 354, no. 6309, pp. 203–206, 2016.

[186] Q. A. Akkerman, V. D'Innocenzo, S. Accornero, A. Scarpellini, A. Petrozza, M. Prato, and L. Manna, "Tuning the optical properties of cesium lead halide perovskite nanocrystals by anion exchange reactions," *Journal of the American Chemical Society*, vol. 137, no. 32, pp. 10276–10281, 2015.

[187] N. T. Shewmon, H. Yu, I. Constantinou, E. Klump, and F. So, "Formation of Perovskite Heterostructures by Ion Exchange," *ACS Applied Materials and Interfaces*, vol. 8, no. 48, pp. 33273–33279, 2016.

[188] M. Lai, A. Obliger, D. Lu, C. S. Kley, C. G. Bischak, Q. Kong, T. Lei, L. Dou, N. S. Ginsberg, D. T. Limmer, and P. Yang, "Intrinsic anion diffusivity in lead halide perovskites is facilitated by a soft lattice," *Proceedings of the National*

Academy of Sciences of the United States of America, vol. 115, no. 47, pp. 11929–11934, 2018.

[189] C. Eames, J. M. Frost, P. R. Barnes, B. C. O'Regan, A. Walsh, and M. S. Islam, "Ionic transport in hybrid lead iodide perovskite solar cells," *Nature Communications*, vol. 6, no. May, pp. 2–9, 2015.

[190] S. J. Yoon, K. G. Stamplecoskie, and P. V. Kamat, "How lead halide complex chemistry dictates the composition of mixed halide perovskites," *Journal of Physical Chemistry Letters*, vol. 7, no. 7, pp. 1368–1373, 2016.

[191] S. J. Yoon, S. Draguta, J. S. Manser, O. Sharia, W. F. Schneider, M. Kuno, and P. V. Kamat, "Tracking iodide and bromide ion segregation in mixed halide lead perovskites during photoirradiation," *ACS Energy Letters*, vol. 1, no. 1, pp. 290–296, 2016.

Appendix A

Reactant Quantities for Perovskite Synthesis

The reactant quantities used in perovskite synthesis are detailed in this appendix. Brief descriptions of the methods presented are:

- Solvothermal - precursors added to a stainless steel autoclave and heated in an oven.
- Precipitation - precipitation from acid in a three-necked round bottom flask flushed with nitrogen and heated using an oil bath.
- Inverse solubility - high temperature crystallisation in sealed glass vials heated using an oil bath.
- Thin film - deposition of thin films onto glass substrates via spin coating.

x	MAI (mg)	FAI (mg)	$Pb(OAc)_2.3H_2O$ (mg)	HI, 1M (ml)
0	256	0	612	1.613
0.1	230	27.0	611	1.609
0.2	204	55.2	609	1.606
0.3	178	82.7	608	1.603
0.4	153	110	607	1.599
0.5	127	137	606	1.596
0.6	101	164	604	1.593
0.7	75.8	191	603	1.589
0.8	50.4	218	602	1.586
0.9	25.2	245	601	1.583
1	0	272	599	1.579

Table A.1: Synthesis of $MA_{1-x}FA_xPbI_3$ via the solvothermal method.

x	MAI (mg)	FAI (mg)	PbI_2 (mg)	HI (ml)
0	256	0	734	1.613
0.1	230	27.0	742	1.610
0.2	204	55.2	741	1.606
0.3	178	82.7	739	1.603
0.4	153	110	737	1.600
0.5	127	137	736	1.596
0.6	101	164	734	1.593
0.7	75.8	191	733	1.590
0.8	50.4	218	731	1.586
0.9	25.2	245	729	1.583
1	0	272	728	1.580

Table A.2: Synthesis of $FA_xMA_{1-x}PbI_3$ via precipitation.

x	CsI (mg)	FAI (mg)	PbI_2 (mg)	HI (ml)
0.1	40.5	241.2	718.4	1.558
0.15	60.3	226.2	713.5	1.548
0.2	79.9	211.5	708.7	1.537
0.3	118.2	182.6	699.2	1.517
1	360.4	0	639.6	1.387

Table A.3: Synthesis of $Cs_xFA_{1-x}PbI_3$ via precipitation.

x	CsI (mg)	MAI (mg)	PbI_2 (mg)	HI (ml)
0.05	20.8	241.6	737.6	1.6
0.1	41.2	227.1	731.7	1.587
0.15	61.4	212.8	725.9	1.575
0.2	81.2	198.7	720.2	1.562
0.25	100.7	184.8	714.5	1.55

Table A.4: Synthesis of $Cs_xMA_{1-x}PbI_3$ via precipitation.

CsI (mg)	FAI (mg)	PbI_2 (mg)	$PbBr_2$ (mg)	HI (ml)	HBr (ml)
44.4	264.4	315.0	376.2	1.025	0.683

Table A.5: Synthesis of $Cs_{0.1}FA_{0.9}Pb(I_{0.6}Br_{0.4})_3$ via precipitation.

CsI (mg)	MAI (mg)	PbI_2 (mg)	$PbBr_2$ (mg)	HI (ml)	HBr (ml)
45.3	249.4	321.5	383.9	1.046	0.697

Table A.6: Synthesis of $Cs_{0.1}MA_{0.9}Pb(I_{0.6}Br_{0.4})_3$ via precipitation.

CsI (mg)	FAI (mg)	MAI (mg)	PbI_2 (mg)	$PbBr_2$ (mg)	HI (ml)	HBr (ml)
42.2	208.6	39.5	557.7	151.9	1.299	0.325

Table A.7: Synthesis of $Cs_{0.1}(FA_{0.83}MA_{0.17})Pb(I_{0.83}Br_{0.17})_3$ via precipitation.

x	MAI (mg)	FAI (mg)	PbI_2 (mg)	GBL (ml)
0	256.4	0	743.6	1.613
0.1	230.3	27.7	742	1.610
0.2	204.3	55.2	740.5	1.606
0.3	178.4	82.7	738.9	1.603
0.4	152.6	110	737.4	1.600
0.5	126.9	137.3	735.9	1.596
0.6	101.3	164.4	734.4	1.593
0.7	75.8	191.4	732.8	1.590
0.8	50.4	218.2	731.3	1.763
0.9	25.2	245	729.8	1.759
1	0	271.7	728.3	1.755

Table A.8: Synthesis of $FA_xMA_{1-x}PbI_3$ via inverse solubility. 1M precursor solutions were used for $x \leq 0.7$ and 0.9M for $x \geq 0.8$.

x	CsI (mg)	FAI (mg)	PbI_2 (mg)	GBL (ml)
0.1	40.5	241.2	718.4	1.731
0.15	60.3	226.2	713.5	1.72
0.2	79.9	211.5	708.7	1.708
0.3	118.2	182.6	699.2	1.685

Table A.9: Synthesis of $Cs_xFA_{1-x}PbI_3$ via inverse solubility.

x	CsI (mg)	MAI (mg)	PbI_2 (mg)	GBL (ml)
0.05	20.8	241.6	737.6	1.6
0.1	41.2	227.1	731.7	1.587
0.15	61.4	212.8	725.9	1.575
0.2	81.2	198.7	720.2	1.562
0.25	100.7	184.8	714.5	1.55

Table A.10: Synthesis of $Cs_xMA_{1-x}PbI_3$ via inverse solubility.

x	FABr (mg)	MABr (mg)	$PbBr_2$ (mg)	DMF (ml)
0	0	233.8	766.2	2.088
0.1	26	209.8	764.2	2.082

Table A.11: Synthesis of $FA_xMA_{1-x}PbBr_3$ via inverse solubility.

x	MAI (mg)	FAI (mg)	PbI_2 (mg)	DMF (ml)
0	256.4	0	743.6	2.688
0.1	230.3	27.7	742	2.683
0.2	204.3	55.2	740.5	2.677
0.3	178.4	82.7	738.9	2.672
0.4	152.6	110	737.4	2.666
0.5	126.9	137.3	735.9	2.660
0.6	101.3	164.4	734.4	2.655
0.7	75.8	191.4	732.8	2.649
0.8	50.4	218.2	731.3	2.644
0.9	25.2	245	729.8	2.639
1	0	271.7	728.3	2.633

Table A.12: $FA_xMA_{1-x}PbI_3$ thin film fabrication.

Appendix B

Additional Experimental Details

B.1 Chapter 4: Cesium Formamidinium Lead Halide Perovskites

$Cs_{0.1}FA_{0.9}PbI_3$ powder samples were synthesised by precipitation from acid according to the method detailed in Chapter 3.

$Cs_{0.1}FA_{0.9}PbI_3$ crystals were grown by inverse solubility according to the method described in Chapter 3.

$Cs_{0.1}FA_{0.9}Pb(I_{0.6}Br_{0.4})_3$ powder samples were synthesised by precipitation from acid according to the method detailed in Chapter 3.

FAI-D powder. Part-deuterated FAI was synthesised by Dr James Tellum at the ISIS deuteration facility. Hydrogenous FAI was dissolved in a large excess of D_2O under an argon atmosphere and stirring for 60 minutes, the D_2O was then evaporated and the sample dried under vacuum. The extent of deuteration was determined by the disappearance of the NH resonance in 1H NMR spectrum. Only partial deuteration of the cation could be achieved resulting in the composition $CH(ND_2)_2I$.

$Cs_{0.1}FA_{0.9}PbI_3$-D powder. With the aim of producing a multi-gram sample of part-deuterated $Cs_{0.1}FA_{0.9}PbI_3$, 0.405 g of dried CsI, 2.412 g of FAI-D and 7.184 g of dried PbI_2 were dissolved in 25.97 ml of dimethyl sulfoxide (DMSO-d6, from Merk 99.9% atom % D) and drop cast onto a preheated glass dish at 150°C on a hot plate in a dry box. As the solvent evaporated a black solid formed which was subsequently dried on the hotplate for a further 120 minutes. The sample was sealed under nitrogen and

stored below 5°C to reduce H-D exchange.

Powder X-ray diffraction (PXRD) data were collected on a Bruker Advance D8 diffractometer and a STOE STADI P (Debye-Scherrer geometry) using CuKα radiation (λ = 1.540 60 Å). Indexing and peak fitting were carried out in GSAS-II on $Cs_{0.1}FA_{0.9}PbI_3$ samples synthesised via inverse solubility (ground using a pestle and mortar) and $Cs_{0.1}FA_{0.9}PbI_3$ and $Cs_{0.1}FA_{0.9}Pb(I_{0.6}Br_{0.4})_3$ samples made using the precipitation method.

Single crystal X-ray diffraction (SXRD) data were collected on a RIGAKU SuperNova dual tube Eos S2 CCD diffractometer using Mo (λ = 0.7107 Å) radiation. Suitable single crystals of $Cs_{0.1}FA_{0.9}PbI_3$ synthesized via inverse solubility were selected and measured at 300 K using an exposure of 10 s/frame, the sample was then cooled and measured at 175 K, 150 K and 120 K using an increased exposure of 20 s/frame. The data analysis was conducted by Dr Lauren Hatcher using the programs Olex2, ShelXL and PLATON.

Neutron powder diffraction (NPD) was carried out on the POLARIS instrument at the ISIS Neutron and Muon Source, Rutherford Appleton Laboratories. Approximately 6 g of $Cs_{0.1}FA_{0.9}PbI_3$–D and hydrogenous $Cs_{0.1}FA_{0.9}Pb(I_{0.6}Br_{0.4})_3$-H were loaded separately into a 5 mm vanadium sample can under argon and sealed using an indium O-ring. The $Cs_{0.1}FA_{0.9}PbI_3$–D sample was cooled to 100 K in the instrument cryofurnace and data were collected over 2 hours. The sample was subsequently heated at 1 K/min to 175 K, where a second 2-hour collection was recorded, before being cooled to 110 K at 1 K/min. Variable temperature diffraction data were recorded with an exposure time of 5 mins at a ramp rate of 0.2 K/min. A final 2-hour collection was measured at 300 K. The $Cs_{0.1}FA_{0.9}Pb(I_{0.6}Br_{0.4})_3$-H sample was cooled to 105 K and subsequently heated to 300 K at 0.4K/min, with data collected continuously and binned into 1 K ranges.

Energy-dispersive X-ray (EDX) spectroscopy was carried out using a Jeol JSM-6480LV SEM equipped with an Oxford INCA X-Act SDD X-ray detector using an accelerating voltage of 20kV.

Differential Scanning Calorimetry (DSC) measurements were carried out on $Cs_{0.1}FA_{0.9}PbI_3$ samples grown via inverse solubility and precipitation using a TA Instruments DSC Q20. Samples were cycled between 225 K and 420 K at a rate of 2 K/min.

UV-Visible Absorption (UV-Vis) spectroscopy was carried out using a Perking Elmer Lambda 750s spectrophotometer fitted with a 60 mm integrating sphere. Powder samples of $Cs_{0.1}FA_{0.9}PbI_3$ were loaded into a PTFE powder sample holder fitted with a

fused silica window. Reflectivity was measured and transformed to resemble absorbance using the Kubelka-Munk function.

Steady state and transient photoluminescence (PL) measurements were conducted using an in-house time-correlated single photon counter (TCSPC) set up at the Ludwig Maximillian University of Munich, described in detail in Chapter 3. A suitable crystal of $Cs_{0.1}FA_{0.9}PbI_3$ grown by inverse solubility was selected and mounted onto a silica substrate in a CryoVac cryostat. PL and TRPL measurements were then taken between 290 K and 25 K.

B.2 Chapter 5: Cesium Methylammonium Lead Halide Perovskites

$Cs_xMA_{1-x}PbI_3$ and $Cs_{0.1}MA_{0.9}Pb(I_{0.6}Br_{0.4})_3$ powder samples were synthesised by precipitation from acid according to the method detailed in Chapter 3.

$Cs_xMA_{1-x}PbI_3$ crystals were grown by inverse solubility according to the method described in Chapter 3.

$Cs_{0.1}MA_{0.9}Pb(I_{0.6}Br_{0.4})_3$ powder samples were synthesised by the mechanochemical method described in Chapter 3.

Energy-dispersive X-ray (EDX) spectroscopy was carried out using a Jeol JSM-6480LV SEM equipped with an Oxford INCA X-Act SDD X-ray detector. $Cs_xMA_{1-x}PbI_3$ crystals grown by inverse solubility were cleaved and mounted onto SEM stubs using carbon tape. Samples were left in a vacuum overnight to allow off-gassing of the carbon tape before measuring. An accelerating voltage of 20 keV was used and the chemical composition was analysed at three separate sites on each crystal using the software INCA and AZTEC, which were also used to produce a chemical map of the whole sample showing the distribution of Cs, Pb and I.

Powder X-ray diffraction (PXRD) data were collected on a Bruker Advance D8 and a STOE STADI P diffractometer using CuKα radiation ($\lambda = 1.540\,60$ Å). Phase identification and indexing were carried out in GSAS II on $Cs_xMA_{1-x}PbI_3$ samples synthesised by inverse solubility (ground using a pestle and mortar) and precipitation, as well as $Cs_{0.1}MA_{0.9}Pb(I_{0.6}Br_{0.4})_3$ powder made by precipitation.

Single crystal X-ray diffraction (SXRD) data were collected on a RIGAKU SuperNova dual tube Eos S2 CCD diffractometer using Mo radiation ($\lambda = 0.7107$ Å). A suitable

crystal of $Cs_{0.1}MA_{0.9}PbI_3$ grown by inverse solubilty was selected and measured at 300K using an exposure of 20 s/frame, then at 150 K and 120 K at 20 s/frame. Data analysis was conducted by Dr Lauren Hatcher using the programs Olex2 and ShelXL.

Neutron powder diffraction (NPD) experiments were carried out by Prof. Paul Henry and myself on the POLARIS instrument at the ISIS neutron and muon source, Rutherford Appleton Laboratories. Approximately 6 g of hydrogenous $Cs_{0.1}MA_{0.9}PbI_3$ and $Cs_{0.1}MA_{0.9}Pb(I_{0.6}Br_{0.4})_3$ powder, synthesised by the precipitation method, were loaded into 5 mm vanadium sample cans and sealed using an indium O-ring. The $Cs_{0.1}MA_{0.9}PbI_3$ sample was cooled *in situ* to 140 K and measured overnight at this temperature, before two three-hour collections were recorded at 240 K and 310 K. The sample was then cooled to 135 K *in situ* at a rate of 2.5 $Kmin^{-1}$ with data continuously binned into 5 K ranges between 310 K and 135 K. Due to reduced beam power from the source at ISIS, measurements between 310 K and 290 K were of poor quality, and therefore were not included in the analysis presented later in this chapter. The $Cs_{0.1}MA_{0.9}Pb(I_{0.6}Br_{0.4})_3$ sample was cooled *in situ* from 300K to 105K at a rate of 2 $Kmin^{-1}$, then the temperature was increased to 290 K at a rate of 0.35 Kmin[1] with data continuously binned into 3 K ranges. Profile fitting and sequential refinements were carried out using the program GSAS II.

UV-Visible Absorption (UV-Vis) spectroscopy was carried out using a Perkin Elmer Lambda 750 s spectrophotometer fitted with a 60 mm integrating sphere. Powder samples of $Cs_{0.1}MA_{0.9}PbI_3$ synthesised by the inverse solubility method (ground by pestle and mortar) were loaded into a PTFE powder sample holder fitted with a fused silica window. Reflection measurements were recorded and background subtracted, before being transformed to resemble absorbance using the Kubelka-Munk function.

Steady state and transient photoluminescence (PL) measurements were conducted using the TCSPC set up at the Ludwig Maximillian University of Munich, described in detail in Chapter 3. A suitable crystal of $Cs_{0.1}MA_{0.9}PbI_3$ grown by inverse solubility was selected and mounted on a silica substrate in a CryoVac cryostat. PL and TRPL measurements were then taken between 290 K and 25 K.

B.3 Chapter 6: Formamidinium Methylammonium Lead Halide Perovskites

Precursor synthesis of methylammonum ioidide (MAI) was carried out for this work. 16.62 ml of HI (57 wt %) was reduced using 1.5 wt % H_3PO_2 and added slowly to 10.891 ml of aqueous CH_3NH_2 (40 wt %) under stirring in an ice bath for one hour. Rotary evaporation was used to remove the H_2O and the resulting MAI was recrystallised in hot ethanol before being oven dried overnight.

Thin film deposition of $FA_xMA_{1-x}PbI_3$ onto cleaned glass substrates was carried out according to the method detailed in Chapter 3.

Powder X-ray diffraction (PXRD) data were collected on a Bruker Advance D8 diffractometer using Cu-Kα radiation (λ = 1.540 60 Å). The diffraction angle was scanned from values of 2θ between 10° and 50° using a step size of 0.016°. Patterns were analysed using the EVA diffraction suite.

Scanning electron microscopy (SEM) images were taken of $FA_xMA_{1-x}PbI_3$ thin films (x = 0.3, 0.5, 0.6, 0.7) using a Jeol JSM-6480LV SEM. An accelerating voltage of 5 kV was used to obtain secondary electron (SE) images of the films at a magnification of x 1000.

Ab-initio simulation was performed by Jessica Dillon in collaboration with Saiful Islam's Energy Materials Research Group at the University of Bath. The code VASP58 was used to investigate the energetics of $FA_xMA_{1-x}PbI_3$. A pseudo-cubic cell of XXX atoms was modelled, along with PAW pseudopotentials, a GGA+VdW (OptB86b) exchange-correlation function, a plane wave cut off energy of 520 eV and k-point sampling at the gamma point. Forces were converged to less than 0.01 eVÅ^{-1} for structure relaxation.

B.4 Chapter 7: Exchange and Migration of Halide Ions in Lead Perovskites

$MAPbBr_3$, $MAPbI_3$, $FA_{0.6}MA_{0.4}PbI_3$, $Cs_{0.1}MA_{0.9}PbI_3$ and $FA_{0.1}MA_{0.9}PbI_3$ crystals were grown by inverse solubility according to the method described in Chapter 3.

Halide exchange solutions were made by Dr He Huang at the Ludwig Maximilian University of Munich by dissolving PbX_2 (X = I or Br) in 200 ml toluene with 2 ml

oleic acid (OA) and 2 ml oleylamine (OLA) to form a 2 mM I or Br-rich solution.

Steady state photoluminescence (PL) measurements were conducted using an in-house time-correlated single photon counter (TCSPC) set up at the Ludwig Maximillian University of Munich, described in detail in Chapter 3. Samples were mounted onto silica substrates and fixed to the sample stage using Apezion grease.

Powder X-ray diffraction (PXRD) data were collected on a STOE STADI P using CuKα radiation ($\lambda = 1.540\,60$ Å). Indexing and peak fitting were carried out in GSAS-II on $MAPbBr_3$ and MAPBr-I samples ground using a pestle and mortar.

Energy-dispersive X-ray (EDX) spectroscopy was carried out using a Jeol JSM-6480LV SEM equipped with an Oxford INCA X-Act SDD X-ray detector using an accelerating voltage of 20 kV.

Appendix C

Surface Roughness Measurements

During the final stages of writing this thesis, atomic force microscopy (AFM) imaging was performed on a $MAPbI_3$ single crystal to be included with a publication in collaboration with ICMAB (item 3 in the publications list presented at the beginning of this thesis).

Measurements were performed using a Digital Instruments Nanoscope IIIa scanning probe microscope in tapping mode using a Nanoworld soft tapping AFM probe. A $MAPbI_3$ crystal grown by inverse solubility was selected and the surface roughness of three areas (1 μm^2, 2 μm^2 and 5 μm^2) were measured.

The roughness average (R_a) and root mean square roughness (R_q) for the three areas are shown Table C.1. The 5 μm^2 area image contained features (shown in optical image in Figure C-2 (a)) typical of the crystals grown by the inverse solubilty method, and significantly increase the surface roughness measured.

Area of Interest (μm^2)	R_a (nm)	R_q (nm)
1	1.25	1.58
2	1.31	1.64
5	4.40	6.07

Table C.1: Roughness average (R_a) and root mean square roughness (R_q) for surface of $MAPbI_3$ crystal.

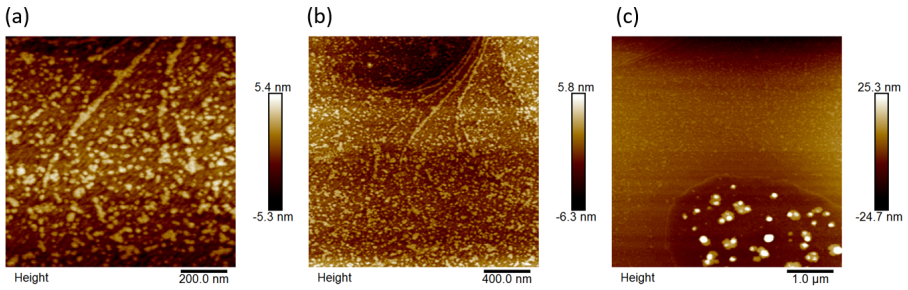

Figure C-1: AFM images of MAPbI3 crystal surface of areas (a) 1 μm^2, (b) 2 μm^2 and (c) 5 μm^2. Features reaching 25 nm were typical throughout the surface, appearing in clusters and significantly increasing the surface roughness measured.

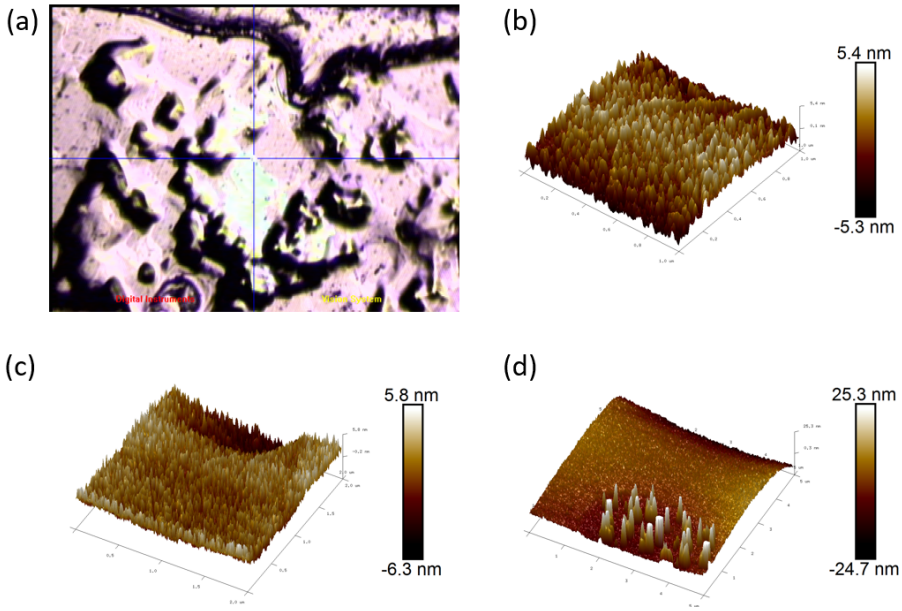

Figure C-2: (a) Optical image of crystal surface measured in AFM (15 μm^2 area), with 3D images of measurements taken of areas (b) 1 μm^2, (c) 2 μm^2 and (d) 5 μm^2.

Appendix D

JMAK Kinetic Plots

Kinetic plots based on the Johnson-Mehl-Avrami-Kolmogorov (JMAK) equation, modelling the growth of PbI_2 in thin films of $FA_xMA_{1-x}PbI_3$ ($0 \leq x \leq 0.5$) are presented below. $FA_{0.6}MA_{0.4}PbI_3$ was presented in the main text. In the plots below $lnln(1/1-A)$ is plotted against $ln(t)$, where t is time in hours and A is the peak area under the (001) PbI_2 reflection recorded in X-ray diffraction measurements. The gradient and intercept of the linear fits for these JMAK plots were extracted and subsequently used to calculate approximate values for crystallisation rate constant.

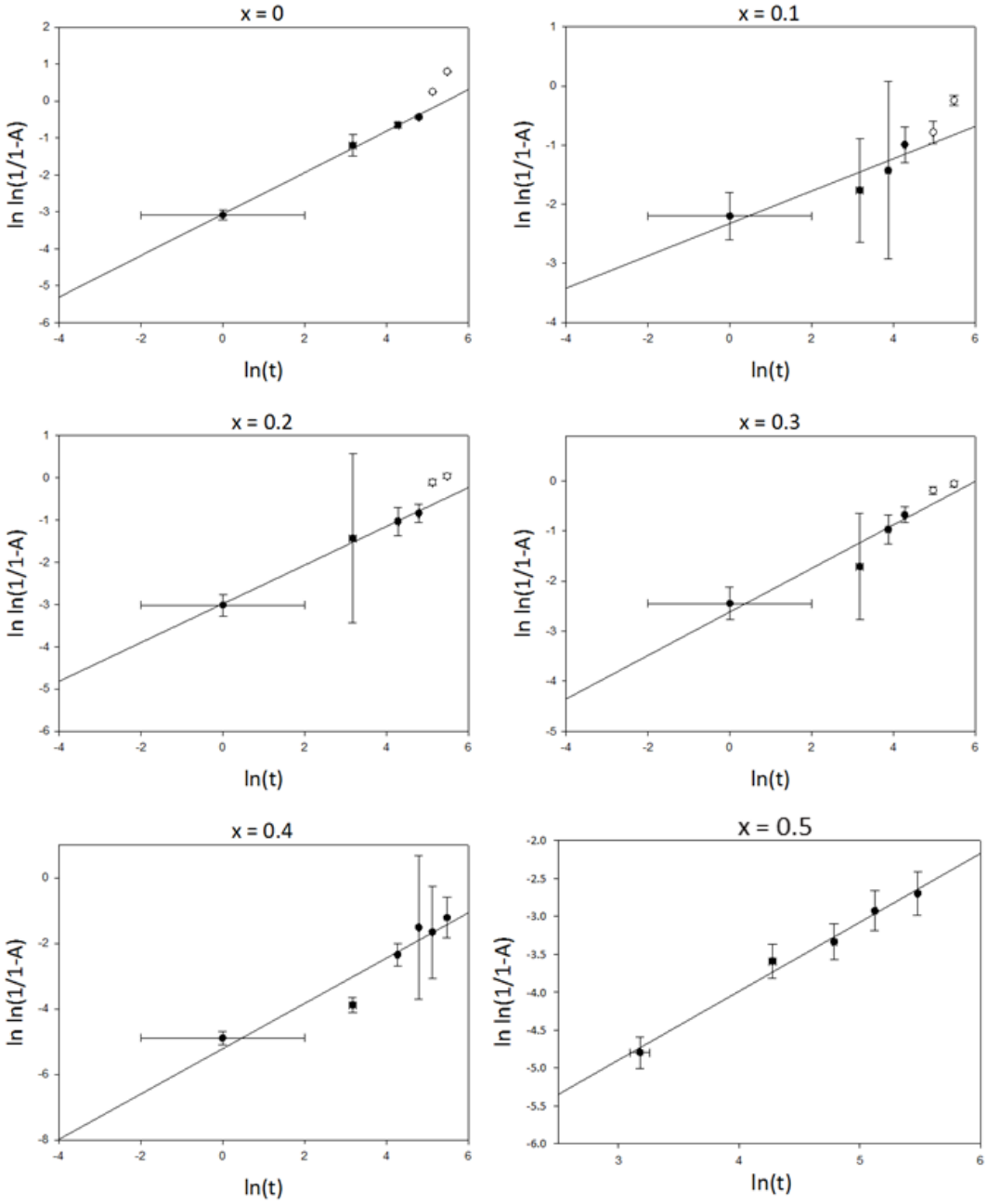

Figure D-1: JMAK plots for $FA_xMA_{1-x}PbI_3$ ($0 \leq x \leq 0.5$), measuring area under the (001) PbI_2 reflection (A) over time in hours (t).

Appendix E

Error Analysis for JMAK Kinetics

The error bars plotted as part of relationship between rate constant of lead iodide formation and value of x in $MA_{1-x}FA_xPbI_3$ were calculated as follows. Peak areas of the (001) reflection for PbI_2 used to approximate the phase fraction of PbI_2 in the thin films were read with an error of ± 20%, the time of the measurement had an error of ± 2 hours. The Johnson-Mehl-Avrami-Kolmogorov (JMAK) equation,

$$\alpha = 1 - exp(-(kt)^m) \tag{E.1}$$

where α is the phase fraction of product, k is the rate constant, t is the time and m is the Avrami exponent, can be rearranged to give:

$$lnln\left(\frac{1}{1-A}\right) = mln(t) + mln(k). \tag{E.2}$$

Here α is substituted for A, representing the peak area of the (001) PbI_2 reflection. Therefore the errors on $lnln(\frac{1}{1-A})$ and $ln(t)$ are, respectively:

$$\alpha_{lnln(\frac{1}{1-A})} = \frac{\alpha_A}{(1-A)ln\left(\frac{1}{1-A}\right)} \tag{E.3}$$

$$\alpha_{ln(t)} = \frac{\alpha_t}{t}. \tag{E.4}$$

Equation E.2 implies a linear relationship if $lnln(1/1-A)$ is plotted against $ln(t)$, where m is the gradient and $y_0 = mln(k)$ the intercept. These kinetic plots were made using SigmaPlot and fitted using regression analysis. The gradient, intercept and their standard errors were extracted using this fit. From the gradient (m) and intercept (y_0) a value of the rate constant k could be calculated through,

$$k = exp\left(\frac{y_0}{m}\right). \tag{E.5}$$

It is important to note this value of k is not absolute due to the approximating PbI_0 phase fraction as peak area. The error on this value of k was calculated through:

$$\alpha_k = \left(\frac{y_0}{m}\right) exp\left(\frac{y_0}{m}\right) \sqrt{\left(\frac{\alpha_{y_0}}{y_0}\right)^2 + \left(\frac{\alpha_m}{m}\right)^2}. \tag{E.6}$$